The role of the small G-protein R-Ras in vascular function and blood pressure control

KAYA JANE OLCZAK

A thesis submitted to Queen Mary University of London in partial fulfilment of the requirements of the Degree of Doctor of Philosophy

Clinical Pharmacology and Precision Medicine

William Harvey Research Institute

Faculty of Medicine and Dentistry

Queen Mary University of London

Statement of Originality

I, Kaya Jane Olczak, confirm that the research included within this thesis is my own work or that where it has been carried out in collaboration with, or supported by others, that this is duly acknowledged below and my contribution indicated. Previously published material is also acknowledged below.

I attest that I have exercised reasonable care to ensure that the work is original, and does not to the best of my knowledge break any UK law, infringe any third party's copyright or other Intellectual Property Right, or contain any confidential material.

I accept that the College has the right to use plagiarism detection software to check the electronic version of the thesis.

I confirm that this thesis has not been previously submitted for the award of a degree by this or any other university.

The copyright of this thesis rests with the author and no quotation from it or information derived from it may be published without the prior written consent of the author.

Signature:

Date: 06.01.2023

Details of collaboration

This work was supported by the British Heart Foundation – Award number: FS/18/64/34185

Thank you to the following groups and individuals for their contributions:

- Slide preparation and picrosirius red staining performed by Nadia Rahman, Pathology services (Cancer Research UK Barts Centre Institute, QMUL).
- RNA sequencing performed by Dr. Charles Mein, Dr. Nadiya Mahmud, and Dr. Ewa Wozniak at the Genome Centre, Blizard Institute, QMUL.
- Phosphoproteomics performed by Dr. Vinothini Rajeeve and Ms. Ruth Otunsola (Cutillas group, Cancer Research UK Barts Centre Mass Spectrometry Facility, QMUL).
- *RRAS* association analysis performed by Dr. Helen Warren, Clinical Pharmacology, QMUL.

Relevant publications

Olczak, K. J., Taylor-Bateman, V., Nicholls, H. L., Traylor, M., Cabrera, C. P., & Munroe, P. B. (2021). Hypertension Genetics Past, Present and Future Applications. *Journal of Internal Medicine*, *290*(6), 1130–1152. https://doi.org/10.1111/joim.13352

Olczak, K.J., Ahmed, F., Munroe, P.B. (2023), 'Chapter 22: Disorders Manifesting with Systemic Hypertension' in Kumar et al., Clinical Cardiovascular and Genomic Medicine - Principles and Practice. Amsterdam, Netherlands: Elsevier. [Awaiting publication]

Abstract

Elevated blood pressure, termed hypertension, is a major risk factor for cardiovascular mortality. Despite decades of research the pathogenesis of hypertension remains unclear. Genome-wide association studies have identified genes contributing to the polygenic nature of blood pressure. A meta-analysis of Exome chip genotypes from >300,000 individuals identified a rare missense single nucleotide variant, rs61760904, associated with a large effect on systolic blood pressure, located in an exon in the small GTPase R-Ras. R-Ras is highly expressed in the vasculature and is implicated in cardiovascular processes. This thesis investigated the potential role of R-Ras in blood pressure control.

The CRISPR-Cas9 RrasDEL-415 knockout mouse model was specifically generated for this project. The blood pressure phenotype of these mice was characterised using radiotelemetry. Young R-Ras knockout mice exhibited blood pressure comparable to wild-type littermates, at baseline and with angiotensin II-induced hypertension. However, systolic blood pressure was significantly elevated in the aged R-Ras knockout mouse. This age-related phenotype in the R-Ras knockout mouse was explored in humans using an age-stratified association analysis of the *RRAS* variant in ~500,000 individuals from the UK Biobank. Individuals homozygous for the rare variant aged ≥50 years had higher mean systolic blood pressure (+14.6 mmHg) compared to individuals <50 years (+9.7 mmHg).

This motivated the hypothesis that compensatory mechanisms were masking the impact of R-Ras on blood pressure control *in vivo* in the young mouse. Phosphoproteomic analysis of the young mouse aorta revealed significant downregulation of pathways related to blood pressure control with R-Ras knockout – notably, ‘cAMP signaling’ and ‘Vascular smooth muscle contraction’.

The work presented in this PhD thesis supports a role of R-Ras in vascular mechanisms of blood pressure control, and in the age-related pathogenesis of hypertension in humans. Future work, notably repeating phosphoproteomics of the aged R-Ras knockout mouse aorta, is essential to delineate the exact mechanisms responsible.

Acknowledgements

First and foremost, a huge thank you to my supervisors Professor Patricia B Munroe and Professor Andrew Tinker. This PhD has not been an easy ride, mainly due to circumstances out of our control, but the unwavering optimism and trust shown by you both kept me going through to the very end.

I would like to acknowledge everyone in the Tinker, Munroe, and Hobbs lab groups – the kindness and support shown from all three groups has been indispensable. If I were to list everyone here this acknowledgements section will be a thesis in its own right. Therefore, I will shout out Dr. Qadeer Aziz, who always made me laugh, even when I was wildly frustrated practicing those radiotelemetry surgeries. Thank you to Dr. Aisah Aubdool for being not only a friend but a mentor – you are an inspirational woman, and I cannot wait to see what you achieve. Dr. Josh Dignam and Dr. Vanessa Lowe, you two were my favourite distractions, and I am so grateful for those ridiculous office chats. Dr. Aled Jones, computer whiz and all-round genius, thank you for solving my R/ woes. Dr. Helen Warren, thank you for putting the cherry on top of this thesis with the *RRAS* association analysis. and finally, Dr. Keat-Eng Ng, thank you for being my lab mum and keeping me so well fed these past years.

Throughout everything leading up to and during this PhD, my family and my friends have been my rock. Dada, words cannot express how grateful I am for you supporting me through this entire journey. I fundamentally could not have achieved what I have without you. Fooza, Mamek, Babcia, Kalinka, the four most important women in my life, thank you for providing constant affirmation that I can in fact one day become Dr. Booba. and Toby, you now fall in that category too. Finally, my incredible friends – Sasha, Lexi, Lucy, Louis, Alasdair (not necessarily in that order) – you got me through the lowest of lows, perhaps without even realising it. Thank you.

I am eternally grateful to the British Heart Foundation, their volunteers, and their donators, who funded this PhD project and without whom none of this could have been possible.

Last but *certainly* not least, thank you to all the mice who contributed to this PhD research with the greatest sacrifice of all.

Dziadek, to dla ciebie

Table of contents

List of figures

List of tables

Abbreviations

ΔΔG	Relative stability change
A	Adenosine
ACCORD	Action to Control Cardiovascular Risk in Diabetes
ACE	Angiotensin converting enzyme
ACh	Acetylcholine
ACTB	Beta actin
ADCY6	Adenylate cyclase type 6
ADCY9	Adenylate cyclase type 9
ADMA	Assymetric dimethylargine
Akt	Protein kinase B
AKT1	AKT Serine/Threonine Kinase 1
ANGI	Angiotensin I
ANGII	Angiotensin II
ANOVA	Analysis of variance
ANP	Atrial natriuretic peptide
APS	Ammonium persulfate
AT1R	Angiotensin receptor type 1
AT2R	Angiotensin receptor type 2
ATF4	Activating Transcription Factor 4
ATP	Adenosine triphosphate
AU	Arbitrary units
BCA	Bicinchoninic acid
BH4	Tetrahydrobiopterin
BMI	Body mass index
BNP	Brain natriuretic peptide
BP	Blood pressure
bp	Base pair
bpm	Beats per minute
BRAF	V-raf murine sarcoma viral oncogene
BRIGHT	British Genetics of Hypertension
BSA	Bovine serum albumin
C	Cytosine
C	Carbamidomethyl
Ca^{2+}	Calcium

CAAX	Cys-A-A-X
$CaCl_2$	Calcium chloride
CALIBER	CArdiovascular research using LInked Bespoke studies and Electronic health Records
CaM	Calmodulin
cAMP	Cyclic adenosine monophosphate
cDNA	Complementary DNA
cGMP	Cyclic guanosine monophosphate
CHO	Chinese hamster ovary cells
CI	Confidence interval
CNP	C-type natriuretic peptide
CO	Cardiac output
CO_2	Carbon dioxide
CPI-17	C-kinase potentiated protein Phosphatase 1 inhibitor, molecular mass 17 kDa
C_q	Quantification cycle
CRC	Concentration response curve
C_t	Cycle threshold
Cu	Copper
CV	Cardiovascular
CVD	Cardiovascular disease
D	aspartate
D-PBS	Dulbecco's phosphate buffered saline
DAG	Diacylglycerol
DAPI	4′,6-diamidino-2-phenylindole
DASH	Dietary Approaches to Stop Hypertension
DBP	Diastolic blood pressure
DDAH1	Dimethylarginine dimethylaminohydrolase-1
DE	Differential expression
DMSO	Dimethyl sulfoxide
DNA	Deoxyribonucleic acid
dNTPs	Deoxynucleotide triphosphates
dsDNA	Double stranded DNA
DSI	Data Sciences International
EC	Endothelial cell
EC_{50}	Half maximal effective concentration

ECM	Extracellular matrix
EDTA	Ethylenediaminetetraacetic acid
EGM	Endothelial Cell Growth Medium
eNOS	Endothelial nitric oxide
Epac	Exchange protein directly activated by cAMP
ERK1/2	Extracellular signal-related kinase 1/2
ES	Enrichment score
ET1	Endothelin 1
FAK	Focal adhesion kinase
FBS	Fetal bovine serum
FDR	False discovery rate
FLNa	Filamin A
FPR	false positive rate
FRET	Fluorescence resonance energy transfer
G	Guanine
g	grams
GAP	GTPase activating proteins
GDP	Guanosine diphosphate
GEF	Guanine nucleotide exchange factor
GFP	Green fluorescent protein
GPCR	G-protein coupled receptor
GSEA	Geneset enrichment analysis
GTP	Guanosine triphosphate
GWAS	Genome wide association study
h	Hour
HBSS	Hanks' Balanced Salt Solution
HCAEC	Human coronary artery endothelial cell
HCl	Hydrochloric acid
HEPES	4-(2-hydroxyethyl)-1-piperazineethanesulfonic
HET	Heterozygous
HEV	High endothelial venule
HR	Heart rate
HRP	Horse-radish peroxidase
HUVEC	Human Umbilical Vein Endothelial Cells
IC	Intracellular
IC_{50}	Half maximal inhibitory concentration

ICBP	International Consortium for Blood Pressure Genome-Wide Association Studies
ILK	Integrin-linked kinase
IMPC	International Mouse Phenotyping Consortium
IP_3	Inositol triphosphate
IRAG1	Inositol 1,4,5-Triphosphate Receptor Associated 1
K	Lysine
K_{ATP}	ATP-sensitive potassium channel
KCl	Potassium chloride
kDa	Kilodalton
KEGG	Kyoto Encyclopedia of Genes and Genomes
KH_2PO_4	Potassium dihydrogen phosphate
KO	Knockout
KSEA	Kinase substrate enrichmnent analysis
L	Litres
L-NAME	N(gamma)-nitro-L-arginine methyl ester
Lats1/2	Large tumor suppressor kinase 1/2
LB	Luria-Bertani
LC MS/MS	Liquid chromatography with tandem mass spectrometry
LMM	Linear mixed model
Log2(abspep)	Log2 absolute peptide
Log2FC	Log 2 (Fold Change)
M	Methionine
M3AChR	Muscarinic acetylcholine receptor M3
MAP	Mean arterial pressure
MAPK	Mitogen-activated protein kinase
MEK1/2	Mitogen-activated protein kinase kinase 1/2
$MgSO_4$	Magnesium sulfate
min	Minutes
MLC	Myosin light chain
MLC-P	Phosphorylated myosin light chain
MLCK	Myosin light chain kinase
MLCP	Myosin light chain phosphatase
mmHg	Millimetres of mercury
MMP	Matrix metalloproteinase
MPNST	Malignant peripheral nerve sheath tumours

mQH_2O	Milli-Q water
mRNA	Messenger RNA
MS	Mass spectrometry
mTOR	Mechanistic target of rapamycin
MVP	Million Veteran Program
MYL9	Myosin light polypeptide 9 regulatory
MYLK	Myosin light polypeptide kinase
MYPT1	Myosin phosphatase target subunit 1
N	Newtons
N	Asparagine
N-term Q	N-terminal Gln
NaCl	Sodium chloride
NADPH	Nicotinamide adenine dinucleotide phosphate
$NaHCO_3$	Sodium bicarbonate
NaOH	Sodium hydroxide
NCD	Non-communicable diseases
NEB	New England Biolabs
NES	Normalised enrichment score
NGS	Next generation sequencing
NICE	National Institute for Health and Care excellence
NIH	National Institutes of Health
NO	Nitric oxide
no_mod	No modification
NPRA	Natriuretic peptide receptor type A
NPRB	Natriuretic peptide receptor type B
NPRC	Natriuretic peptide receptor type C
ns	Non-significant
NS	Nervous system
nt	Nucleotide
ORP3	OSBPL3 oxysterol binding protein like
P	Proline
PBS	Phosphate Buffered Saline
PCA	Principal component analysis
PCR	Polymerase chain reaction
PDE	Phosphodiesterase
peNOS	Phospho-eNOS

PESCAL	Peak Statistic Calculator
Phospho(ST)	Phosphorylation on Serine or Threonine
Phospho(Y)	Phosphorylation on Tyrosine
PI3K	Phosphatidylinositol-3 kinase
PIP_2	Phosphatidylinositol 4,5-biphosphate
PIP_3	Phosphatidylinositol (3,4,5)-trisphosphate
PKA	Protein kinase A
PKACA	cAMP-dependent protein kinase catalytic subunit alpha
PKC	Protein kinase C
PKCA	Protein kinase C alpha
PKC	Protein kinase C
PLC	Phospholipase C
PolyPhen-2	Polymorphism Phenotyping v2
PP	Pulse pressure
ppm	Parts per million
PROVEAN	Protein Variation Effect Analyzer
PTM	Post-translational modification
PVDF	Polyvinylidene difluoride
QC	Quality control
QMUL	Queen Mary University of London
qPCR	Real-time quantitative chain reaction
QTL	Quantitative trait loci
RAAS	Renin angiotensin aldosterone system
RAC1	Ras-related C3 botulinum toxin substrate 1
RalGDS	Ral guanine nucleotide dissociation stimulator
RASA3	Ras GTPase-activating protein 3
RhoA	Ras homolog family member A
RIN	RNA integrity number
R_{Max}	Maximum response
RMSD	Root-mean-square deviation
RNA	Ribonucleic acid
RNA-seq	RNA sequencing
ROCK	Rho-associated protein kinase
ROS	Reactive oxide species
rpm	Revolutions per minute
RT	Reverse transcription

RyR	Ryanodine receptor
S	Serine
SBP	Systolic blood pressure
SCAF1	SR-Related CTD Associated Factor 1
scRNA-seq	Single cell RNA-seq
SD	Standard deviation
SDS	Sodium dodecyl sulfate
SEM	Standard error of mean
SERCA	Sarco/endoplasmic reticulum Ca2+-ATPase
sGC	Soluble guanylate cyclase
SI/II	Switch region I/II
SIFT	Sorting Intolerant from Tolerant
SKAT-O	Optimal unified SNP-set Kernel Association Test
SNP	Single nucleotide polymorphism
SNS	Sympathetic nervous system
SNV	Single nucleotide variant
SPRINT	Systolic Blood Pressure Intervention Trial
SR	Sarcoplasmic reticulum
ssDNA	Single stranded DNA
SVR	Systemic vascular resistance
T	Thymine
T	Threonine
TAE	Tris Acetate-EDTA
TAZ	Transcriptional co-activator with PDZ binding motif
TEAD	Transcriptional enhanced associate domain
TEMED	*N,N,N',N'*-Tetramethylethylenediamine
TGF-β	Transforming growth factor β
TiO2	Titanium dioxide
TNFα	Tumour necrosis factor alpha
TNS2	Tensin-2
TxA2	Thromboxane A2
U46619	9,11-dideoxy-9α,11α-methanoepoxy-prosta-5Z,13E-dien-1-oic acid
UKB	UK Biobank
UMOD	Uromodulin
UT	Untransfected
UTR	Untranslated region

V	Volts
VEGF	Vascular endothelial growth factor
VEGFA	Vascular endothelial growth factor A
VEGFR	Vascular endothelial growth factor receptor
VEP	Variant Effect Predictor
VGCC	Voltage-gated calcium channel
VSM	Vascular smooth muscle
VSMC	Vascular smooth muscle cell
WHRI	William Harvey Research Institute
WR	Working reagent
WT	Wild-type
XIC	Extracted ion chromatogram
Y	Tyrosine
YAP1	Yes-associated protein 1

Chapter 1. Introduction

Elevated arterial blood pressure (BP), termed hypertension, is a chronic condition and a major risk factor for cardiovascular (CV) disease, including stroke and myocardial infarction [1–9]. Hypertension is preventable in many cases, however the prevalence of hypertension is rising worldwide due to the ageing population and the normalisation of sedentary lifestyles and unhealthy diets, among other factors [4–6]. Despite extensive research, BP regulation and hypertension remain poorly understood leading to issues with adherence to anti-hypertensive therapies across patients [7,10]. A better understanding of hypertension pathophysiology is necessary to aid more personalised disease management across individuals, facilitate high-risk population screening, and for the identification of novel drug targets. Studies into the genetic architecture of BP traits and hypertension have identified over 2000 genetic variants in the human genome associated with BP regulation, providing new insights into mechanisms contributing to BP. Variation in the *RRAS* gene, encoding for the small G-protein R-Ras, has been demonstrated to be associated with systolic BP (SBP) across populations [11–13]. This study aims to investigate the potential role of R-Ras in BP control.

1.1. The Cardiovascular system

The CV system is composed of the heart, systemic and pulmonary vasculature and lymphatic system and functions to deliver oxygen and nutrients to organs from the heart and remove waste from organs via the blood. The systemic vasculature is divided into the arterial and venous system, the arterial system being primarily responsible for blood distribution and BP control. The primary function of arterial vessels depends on their size and structure (Table 1.1). The aorta is the largest arterial vessel and delivers blood directly from the heart to other large arteries and smaller arterioles, including the mesenteric, carotid and renal arteries, which distribute blood to organ systems [14]. Small resistance arterioles are responsible for BP control; they have fewer layers of vascular smooth muscle (VSM) in comparison to larger arteries, and have sensitive endothelium responsive to chemical and mechanical stimuli in the blood, triggering mechanisms regulating VSM tone [14].

Table 1.1. Arterial vessel size and function.

Vessel type	Diameter (mm)	Function
Aorta	25	Blood distribution
Large arteries	1.0 – 10.0	Blood distribution
Small arteries	0.2 – 1.0	Blood distribution and BP regulation
Arterioles	0.01 – 0.2	BP regulation

BP: blood pressure. Adapted from Klabunde, R. E. (2021) Cardiovascular physiology concepts. Philadelphia: Wolters Kluwer [14].

Haemodynamics describes the factors controlling blood flow in the CV system, particularly the arterial system. During a cardiac cycle, when the ventricles contract blood is ejected into the arterial system and the pressure inside arteries increases due to an expansion in blood volume (systole); this is denoted by SBP. Diastolic BP (DBP) describes the pressure when ventricles are relaxed and the pressure in the arteries is at its lowest (diastole). SBP and DBP are used to calculate the average pressure in the arteries during a cardiac cycle, denoted as mean arterial pressure (MAP) (Figures 1.1 and 1.2). The pulse pressure (PP) represents the force generated by a single heart contraction [14]. SBP and DBP are equivalent to the maximum and minimum PP respectively (Figure 1.1), and PP is therefore calculated as the difference between SBP and DBP (Figure 1.2) [14]. MAP is also measured and it is a product of cardiac output (CO) and systemic vascular resistance (SVR) (Figure 1.2) [14]. Arterial BP is measured in millimetres of mercury (mmHg) using a BP sphygmomanometer, and is denoted as SBP over DBP [14].

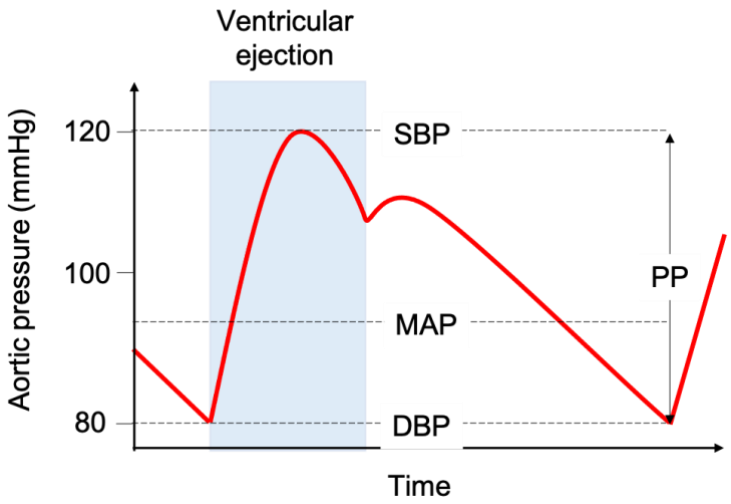

Figure 1.1. Characteristics of the pulse pressure wave. Changes in aortic pressure during a single cardiac cycle in a normotensive patient. [14]

$$MAP = DBP + 1/3\ (SBP - DBP)$$

$$MAP = CO \times SVR$$

$$PP = SBP - DBP$$

Figure 1.2. Blood pressure formulas. [14]

Haemodynamic factors are independent of each other and constantly fluctuating. In normotensive individuals, BP control systems function to compensate for changes in CO, SVR and MAP. In hypertensive individuals, BP control systems become dysregulated resulting in haemodynamic imbalance and BP elevation.

1.2. Hypertension

1.2.1. A brief history of hypertension

The circulatory system was first described by William Harvey in 1628, in his published "*Exercitatio Anatomica de Motu Cordis et Sanguinis in Animalibus".* A century later the English Clergyman Stephan Hales first measured BP in a horse using his invention the manometer. In 1896 Scipione Riva-Rocci refined non-invasive BP measurement and developed the mercury sphygmomanometer, a version of what we use today. The mercury sphygmomanometer was only useful for SBP measurement until Nikolai Kortkoff defined audible sounds used to distinguish SBP and DBP in 1905, eponymously named Kortkoff sounds [15]. At this time, the impact of elevated BP on population health was underestimated and anti-hypertensive medications were sparse, with severe side effects (sodium thiocyanate) or limited efficacy (phenobarbital) [16]. Recognition of the significance of hypertension is attributed to the death of Franklin D. Roosevelt in 1945 due to severe BP elevation (reaching 300/190 mmHg). This catapulted BP to the forefront of CV research and urged the succeeding president, Harry Truman, to sign in to law the National Heart Act [16]. This law established the National Heart Institute (now known as the National Heart, Lung and Blood Institute) and prompted the launch of the Framingham Heart Studies in 1947, the first longitudinal studies of its kind, with an initial focus on ischaemic heart disease [16]. The first major findings were published in 1957 and included the characterisation of hypertension as >160/95 mmHg. The Framingham studies eventually led to a series of publications consistently highlighting high BP as a risk factor for CVD including stroke [1,17], coronary heart disease [2], heart failure [8] and general CV morbidity and mortality [9].

1.2.2. Clinical definitions of hypertension

The European Society of Cardiology/European Society of Hypertension Guidelines in 2018 characterised hypertension clinically as 140/90 mmHg in patients below 80 years [7]. Current treatment strategies in Europe aim to achieve a goal BP below 140/90 mmHg, however clinical trials suggest benefits in lowering SBP further to 120 mmHg. The SPRINT (Systolic Blood Pressure Intervention Trial) study demonstrated a reduction in SBP to 120 mmHg in non-diabetic patients over 50 years significantly reduced incidence of fatal and non-fatal cardiovascular events compared to a target of 140 mmHg [3]. Reflective of this, the clinical threshold for hypertension in the USA was amended to 130/80 mmHg in 2017 [18]. However, lowering SBP to 120 mmHg vs 140 mmHg requires more intensive treatment and additional drug combinations increasing the likelihood of serious adverse events [3,19]. Physicians have

argued the harm associated with a target of 120 mmHg may outweigh the benefits, particularly in elderly patients [20]. The most recent guidelines in the UK therefore remain at 140/90 mmHg [7].

1.2.3. Epidemiology

Hypertension is the leading risk factor responsible for all-cause mortality and accounts for 9.4 million annual deaths worldwide [5]. The Global Burden of Disease study, a major comparison risk assessment spanning 1990 to 2015, calculated high BP to have the highest disease burden compared to other risk factors including smoking, body mass index (BMI) and drug use [5]. The NCD (non-communicable diseases) Risk Factor Collaboration performed a longitudinal study focusing on BP trends in 19.1 million participants with raised BP from 200 countries, from 1975 to 2015 [6]. The global estimated number of adults with raised BP increased from 594 million to 1.13 billion over these 41 years due to a combination of factors including population growth and ageing. Little global change in SBP values were observed (1975 – 2015; men: 126.6 mmHg – 127.0 mmHg, women: 123.9 mmHg – 122.3 mmHg), yet trends within and between regions changed significantly. Notably, high income countries in Western and Asia Pacific region were leading in high BP prevalence in 1975, but prevalence notably declined over the years, and mid income countries and low income countries in central and eastern Europe, sub-Saharan Africa and South Asia saw the highest mean BP values in 2015 [6]. In high income countries changes in risk factors, improved treatment and detection are partly responsible for the decrease in BP, despite an elevation in BMI [21]. In contrast, higher levels of salt and less fresh fruit in Eastern European diets, and malnutrition and under-treatment in South Asian and sub-Saharan African countries, could explain the modern increase in high BP prevalence [6]. The 2013 Prospective Urban Rural Epidemiology study also attributed the rise of elevated BP in low income countries, particularly in Africa, to lack of awareness, treatment and control of hypertension [22]. In lower-mid income countries including China, Colombia and Iran, urbanisation has been associated with the adoption of unhealthy diets and sedentary lifestyles [22] contributing to the rise in BP prevalence in these regions [6]. Low income countries had the lowest rate of antihypertensive use reflective of the lack of accessibility to treatment, in terms of affordability, drug inventory, and distance to clinics for patients [22].

1.2.4. Hypertension as a risk factor in cardiovascular disease

Since the Framingham Heart Studies [1,2,8,17], numerous large-scale analyses have repeatedly demonstrated the correlation between elevated BP and CV events. In 2002, the Prospective Studies Collaboration published a landmark meta-analysis of 61 studies assessing the incidence of CVD in the context of elevated BP, with corrections for sex and age [23]. Results demonstrated a positive correlation between 10 mmHg increases in SBP and DBP and increased mortality from stroke, ischaemic heart disease, heart failure, inflammatory heart disease and atherosclerosis [23]. This has been replicated in more recent large-scale studies analysing correlations between hypertension and a range of CV events, including the 2015 NCD study aforementioned [6], the 2014 CALIBER (CArdiovascular research using LInked Bespoke studies and Electronic health Records) study [24], and a meta-analysis of 123 MEDLINE trials [4]. The Prospective Studies Collaboration study calculated a 20 mmHg difference in SBP equated to the same hazard as 10 mmHg in DBP [23], with very similar results in the CALIBER study (20 mmHg SBP v 11 mmHg DBP) [24]. Prior to the study it was believed that the threshold of SBP as a risk factor for CV events sat between 140 to 160 mmHg, however this theory has been contradicted and there is evidence for a log linear relationship between 10 mmHg differences in SBP and the hazard ratio, even with values as low as 115 mmHg [4,23].

The CALIBER study, a 5 year follow up study of 1.25 million patients, utilised electronic health records allowing generalisation of the population and not limited to those enrolled in trials [24]. This large-scale study demonstrated variation in the relationship between age and BP elevation according to disease, supporting the idea that BP functions via different mechanisms to increase risk of CVD. For example, the risk of angina, myocardial infarction and heart failure is higher in patients aged 30 – 59 years compared to 60 years and above with increasing SBP. Furthermore, the impact of higher SBP and DBP values on CV risk is generally weaker at older ages. Notably, the risk of abdominal aortic aneurysm has a strong positive correlation with increases in SBP in patients aged 30 – 59 years, yet this is markedly diminished in patients aged 60 years and above, although this correlation is maintained with DBP. Nonetheless, SBP appears to have a greater impact on CV risk overall [24].

Ettehad *et al*., were the first investigators to assess the impact of raised BP on CV risk in the context of co-morbidities [4]. In a meta-analysis of 123 studies with over 600,000 participants including patients with co-morbidities including diabetes, prior CV events and chronic kidney disease investigators found lowering BP reduced the hazard ratio of major CV events by 20%, and all-cause mortality by 13% for every 10 mmHg, reflecting results from the Prospective Studies Collaboration study [23] and CALIBER [24]. This meta-analysis importantly added

insight to the relationship between BP and disease as they found higher-risk groups still have the same reduction in hazard ratio with decrease in BP, consistent with results from the SPRINT trial [3]. Co-morbidities did appear to influence efficacy of different drugs for risk reduction; for example, calcium channel blockers appeared less efficacious in treatment of heart failure compared to diuretics but were superior in stroke prevention. However, these results may be confounded by treatment choice dependent on prior CV events, and prevalence of combination therapies [4].

Elevated BP also impacts other organ systems including the kidneys. This was exemplified in a Northern Californian cohort where investigators found patients with BP of 140/90 mmHg had a 2.6 fold chance of developing end-stage renal disease compared with normotensive patients, in both diabetic and non-diabetic subjects [25]. However the risk is more complex than this; meta-analyses have shown that lowering BP with medication does not affect the hazard risk on renal failure [4] and end-stage renal disease [26], and has actually been shown to potentially cause adverse effects including acute kidney injury [3]. Moreover, end-stage renal disease risk was unaffected by decreasing SBP in the SPRINT [3] and ACCORD (Action to Control Cardiovascular Risk in Diabetes) trials [19]. This is potentially due to the complexity of renal failure, which is a manifestation of multiple mechanisms both lowering and increasing BP. Nonetheless, patients with chronic kidney disease appeared to have less risk reduction with every 10 mmHg decrease in BP than those without [4].

1.2.5. Pathogenesis of hypertension

Arterial BP is a product of systemic vascular resistance and circulatory fluid volume, which are influenced by several physiological mechanisms in the CV system and in major organ systems, including the nervous system (NS), the kidneys, and the immune system (Figure 1.3). Dysregulation of these BP control mechanisms contributes to the pathogenesis of hypertension.

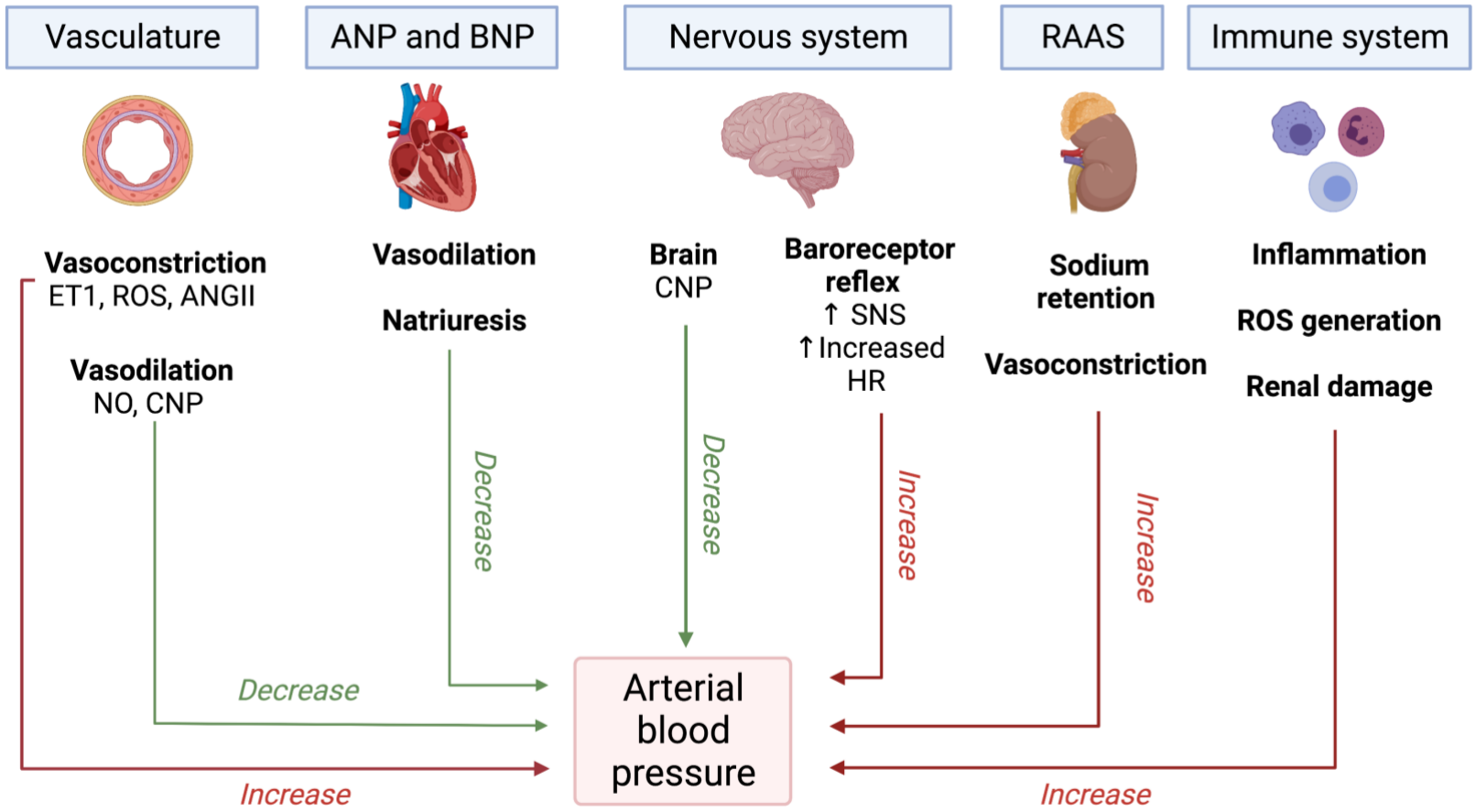

Figure 1.3. Mechanisms of blood pressure control. BP is regulated in response to changes in haemodynamic factors by multiple control systems throughout the body. Diagram created with Biorender.com.

1.2.5.1. The vasculature

Systemic vascular resistance is influenced by the lumen diameter, dependent on vascular tone, and the structural and mechanical characteristics of the vessel. Vascular tone is governed by vasoconstriction and vasodilation, largely mediated by the endothelial and VSM cell layers (Figures 1.4 and 1.5). Vascular tone is important in the acute phase of vasocontraction in response to chemical and mechanical stimuli, including vasodilatory molecule nitric oxide (NO) and vasoconstrictor endothelin 1 (ET1). In contrast, chronic haemodynamic changes promote structural and compositional changes in the VSM and external layers of the vasculature, characterised by vascular remodelling and an increased media to lumen ratio. This section describes how these vascular changes contribute to the pathogenesis of hypertension.

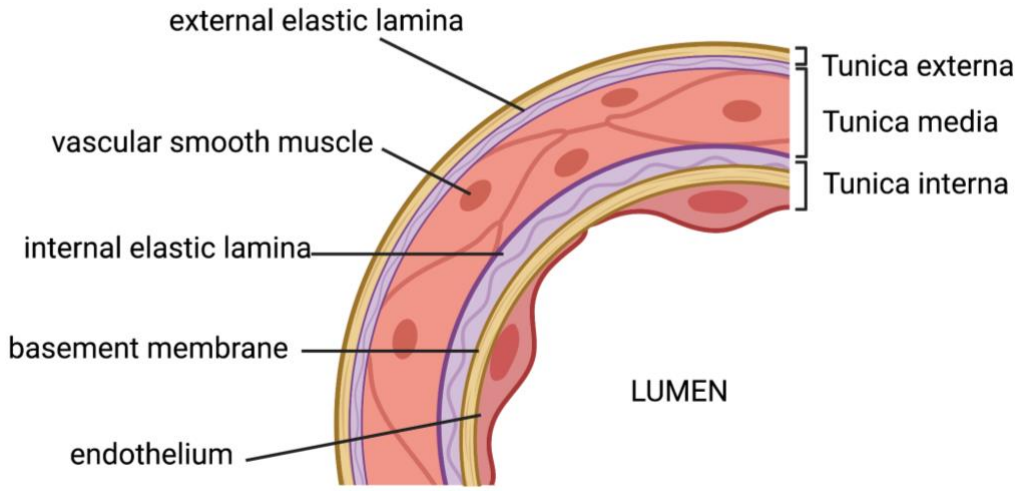

Figure 1.4. Cross section of a blood vessel. Diagram created with Biorender.com.

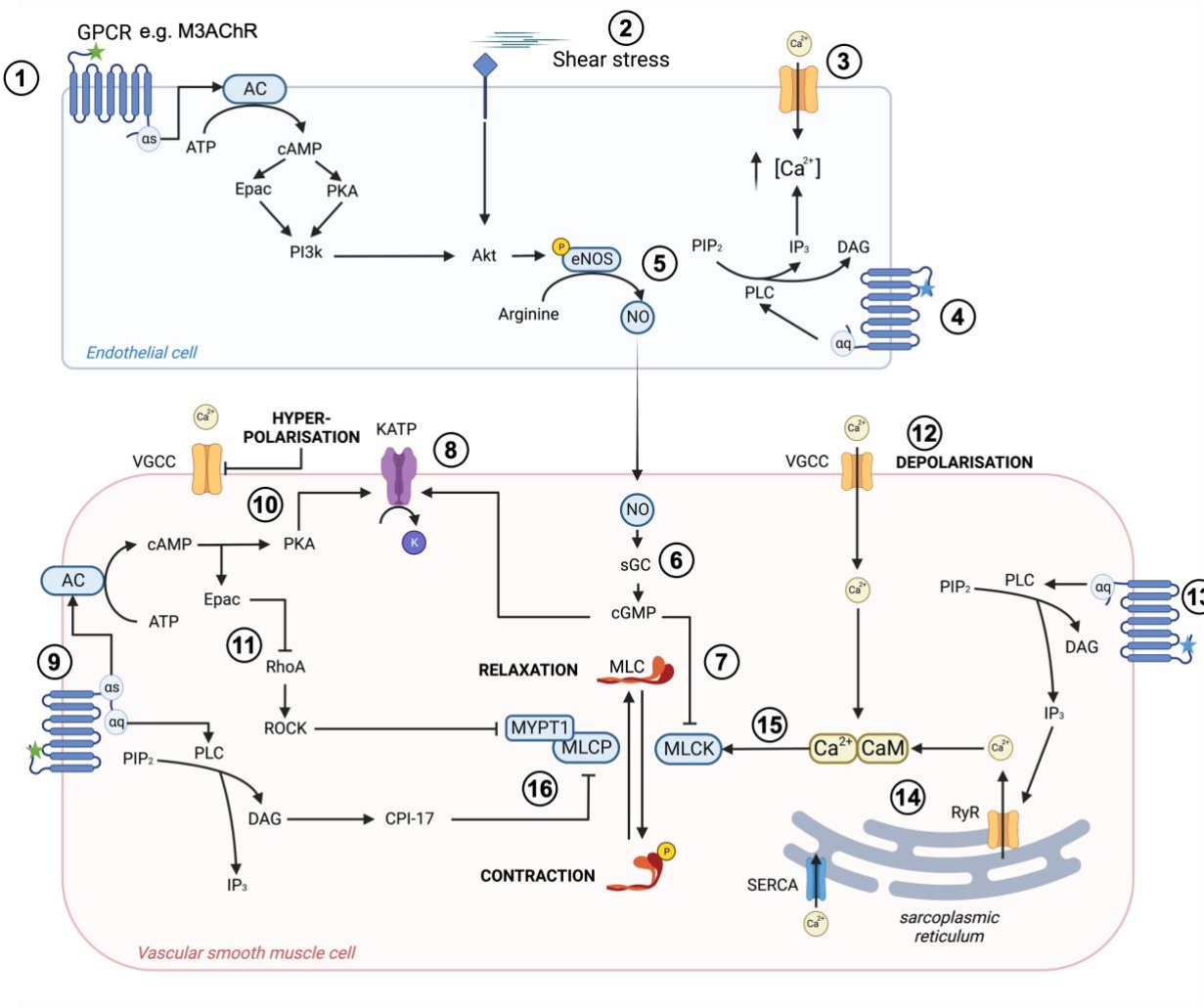

Figure 1.5. Cell signalling in endothelial and vascular smooth muscle cells to regulate vascular tone. Activation of Akt by (1) Gαs-coupled receptor signaling or (2) shear stress acting on mechanoreceptors results in phosphorylation of eNOS at Ser1177. eNOS activation also results from increased IC calcium levels via (3) calcium channel influx or (4) Gαq-coupled receptor mediated activation of PIP_2 signaling. (5) eNOS in its active phosphorylated state catalyses the formation of NO from L-arginine. (6) NO diffuses out of ECs into VSMCs, where it potentiates cGMP formation by activating sGC. VSMC relaxation is promoted via (7) cGMP-mediated inhibition of MLCK and (8) activation of K_{ATP} channels, inducing hyperpolarisation and inhibiting VGCC opening. (9) Gαs-coupled signalling promotes VSMC relaxation via (10) K_{ATP} channel activation and (11) inhibition of RhoA/ROCK signalling. An increase in IC Ca^{2+} results from (12) membrane depolarisation, VGCC opening and subsequent Ca^{2+} influx, and (13) Gαq-coupled receptor activation (14) inducing Ca^{2+} release from internal stores. This results in (15) Ca^{2+}-calmodulin complex formation and subsequent MLCK activation to induce VSMC contraction. (16) Gαq-coupled signalling also inhibits MLCP, facilitating MLC

phosphorylation, myosin crossbridge formation, and subsequent VSMC contraction. Image created with Biorender.com.

1.2.5.1.1. The endothelium

The endothelium is comprised of a monolayer of endothelial cells lining the lumen of the vessel (Figure 1.4). In a healthy vessel, the endothelium releases endothelium-derived relaxing factors, most notably NO, and endothelium-derived constricting factors, such as ET1 and angiotensin II (ANGII), to regulate vascular tone via effects on the VSM layer. In pathophysiological conditions, endothelial dysfunction, characterised by an imbalance of these factors and formation of oxidative species, promotes vasoconstriction resulting in an increase in BP.

In 1980, Furchgott and Zawadski identified an endothelium-derived molecule that triggered relaxation of the VSM in a rabbit aorta, originally denoted Endothelium-derived relaxing factor [27]. This molecule was later proved to be the free radical gas NO [28,29]. Since, the importance of NO signalling has been demonstrated throughout the CV system, notably in vasodilatation of blood vessels [27–29], inhibition of vascular smooth muscle cell (VSMC) proliferation, regulation of vascular permeability [30,31] and inhibition of platelet and monocyte adhesion and activation [32].

NO is synthesised in and released from ECs, before diffusing into VSMCs where it exerts its effects on VSMC relaxation and proliferation via cyclic guanosine monophosphate (cGMP) signalling (Figure 1.5). Formation of NO from the amino acid L-arginine is catalysed by the constitutively active enzyme endothelial nitric oxide synthase (eNOS). eNOS activation requires the endothelium-derived cofactor tetrahydrobiopterin (BH4) [32]. The phosphorylation status of eNOS is influenced by various pathways initiated by mechanical and chemical stimuli (Figure 1.5). In a healthy system, basal phosphorylation of eNOS ensures a continuous release of low levels of NO from the endothelium, maintaining vascular tone and permeability and ultimately BP [33–36].

Endothelial dysfunction plays a prominent role in hypertension pathophysiology and is characterised by diminished NO bioavailability. eNOS null mice exhibit a hypertensive phenotype [33], and this phenotype is replicated in rats via inhibition of NO production by application of eNOS inhibitor L-NAME (N(gamma)-nitro-L-arginine methyl ester) [6]. Furthermore, diminished NO signalling results in disinhibition of VSMC proliferation reflected in intimal thickening observed in hypertensive blood vessels [37].

1.2.5.1.2. Vascular smooth muscle

VSM contraction is triggered by cross-bridge formation of myosin heads with actin filaments to generate force. This is dependent on phosphorylation of the myosin ATPase, myosin light chain 20 (MLC_{20}). MLC_{20} is phosphorylated at S19 by myosin light chain kinase (MLCK) [38–40]. Various calcium-dependent and calcium-independent mechanisms influence the phosphorylation status of MLC_{20} (Figure 1.5).

Calcium-dependent mechanisms rely on an increase in intracellular (IC) Ca^{2+} levels (Figure 1.5). This can be elicited via membrane depolarisation resulting in Ca^{2+} influx via voltage-gated calcium channels (VGCCs) on the membrane, notably L-type channels [41]. Alternatively, Ca^{2+} efflux from internal stores, including the sarcoplasmic reticulum (SR), is triggered by Gαq-coupled IP_3/DAG signalling [38,42,43]. Free Ca^{2+} forms a complex with the calcium binding protein calmodulin (CaM), together activating MLCK [38]. In contrast, VSM relaxation is triggered by a decrease in IC Ca^{2+} levels causing dissociation of the Ca^{2+}-CaM complex, MLCK deactivation, and dephosphorylation of MLC_{20} by MLC phosphatase (MLCP) (Figure 1.5) [38,44]. Decreases in IC Ca^{2+} result from a multitude of pathways including inactivation of L-type calcium channels [45], activation of the Na^{+}-Ca^{2+}exchanger, and uptake into the SR via the Ca^{2+} ATPase (SERCA) [46].

Calcium-independent mechanisms of VSM contraction regulate calcium sensitivity of MLC_{20}, mainly via DAG/PLC/PKC and RhoA/ROCK signalling (Figure 1.5). Whereas IP_3 stimulates release of Ca^{2+} from the SR, diacylglycerol (DAG) acts as a second messenger to activate Protein Kinase C (PKC), and C-kinase potentiated protein Phosphatase 1 inhibitor, molecular mass 17 kDa (CPI-17). PKC induces phosphorylation of CPI-17 which inhibits MLCP, thus facilitating contraction [47]. Likewise, Ras homolog family member A (RhoA) and Rho-associated protein kinase (ROCK) have been shown to phosphorylate CPI-17 to mediate contraction [47]. RhoA/ROCK-mediated contraction is largely dependent on calcium sensitization by ROCK, via direct phosphorylation of myosin phosphatase target subunit (MYPT1), or indirectly via phosphorylation of Zipper-interacting protein kinase [48]. MYPT1 phosphorylation disrupts binding of MLCP to MLC, reducing phosphatase activity. In contrast, cAMP signalling inhibits vasoconstriction via calcium-independent mechanisms in VSM. Activation of Gs-coupled receptors stimulates increases in cAMP levels, activating the cAMP-sensing protein Epac (activating exchange protein directly activated by cAMP). Epac stimulates Rap1-dependent Ca^{2+} desensitisation and relaxation, inhibiting RhoA, and disinhibiting MLCP activity [49]. cAMP has also been shown to activate ATP-sensitive potassium channels (K_{ATP}) by stimulating PKA-dependent phosphorylation and leading to hyperpolarisation and consequent vasorelaxation (Figure 1.5) [50].

In hypertension, vascular reactivity and VSM contraction is increased due to dysregulation of calcium-dependent and independent mechanisms [40]. Indeed, calcium channel blockers are more effective in lowering BP and SVR in hypertensive than normotensive humans [51] and rats [52,53], in part due to increased expression and phosphorylation of L-type calcium channels. RhoA/ROCK activation is increased in animal models of hypertension [54,55], and in humans [56,57], influencing ROCK-dependent contraction and vessel remodelling. MYPT1 phosphorylation is also upregulated in patients with essential hypertension [57].

1.2.5.1.3. Vascular remodelling

Vascular remodelling is a hallmark characteristic of hypertension [58]. Chronic haemodynamic changes result in adaptation of structural and mechanical properties of the vasculature. In pathogenic conditions, like hypertension, these changes are maladaptive [40,58]. In resistance arteries, increased SVR is related to structural alterations, characterised by VSMC proliferation and hypertrophy, decreased lumen diameter, and lumen stenosis. Large arteries such as the aorta exhibit increased stiffness and loss of elasticity [58]. Furthermore, increased arterial stiffness and hypertension appear causally interrelated [59].

The extracellular matrix (ECM) is composed of elastins, collagens, glycoproteins, and prostaglandins, linked via integrins to form a three-dimensional dynamic network [60]. The ECM is essential for the structural integrity of the vessel wall [60]. The composition of the ECM varies by layer in the vascular wall. The inner basement membrane is predominantly composed of collagen, laminin, and fibronectin, facilitating anchoring of ECs in the tunica media. In the internal elastic lamina, elastin is arranged in concentric circles with VSMCs to facilitate contraction and dilation of the VSM layer. In the tunica adventitia, fibrillar collagens provide strength and limit vasodilation (Figure 1.4). Proteases, including matrix metalloproteinases (MMPs), hydrolyse ECM proteins to regulate VSM turnover [58].

In hypertensive conditions, VSMCs switch from a quiescent, low turnover phenotype with high expression of contractile proteins, to a dedifferentiated phenotype with high expression of factors associated with cell growth, migration, and fibrosis. In hypertension, accumulation of dedifferentiated smooth muscle cells in the vascular wall stimulates media thickening, neointimal hyperplasia, and vascular stiffness [40]. Prolonged vasoconstriction further stimulates ECM reorganisation and actin polymerisation over time [40]. Increased local production of ANGII and transforming growth factor-β (TGF-β) by the VSM in response to increases in cyclic stretch and stress increases the rate of synthesis of the ECM, thus increasing wall thickness [61]. Bersi and colleagues demonstrated loss of elasticity, fibrosis and collagen deposition, and wall thickening in the thoracic aorta in ANGII-induced

hypertensive mice [65]. Integrins also contribute to adventitial thickening in hypertensive conditions. In the ANGII-induced hypertension mouse model, elimination of the α1 subunit of the α1β1 integrin, a major receptor for collagen, attenuated wall thickening of the carotid artery [62]. Furthermore, MMPs are downregulated in hypertensive patients, resulting in enhanced collagen deposition and fibrosis [63].

1.2.5.1.4. Oxidative stress

Oxidative stress contributes to dysregulation of vascular tone and vascular remodelling in hypertension via the formation of reactive oxide species (ROS). ROS are generated by enzymes including nicotinamide adenine dinucleotide phosphate (NADPH) and cyclooxygenase, and their activity is upregulated by factors including systemic inflammation, vascular stretch and tobacco smoking [64]. In the endothelium, ROS production reduces the bioavailability of NO, by oxidising BH4 and shifting eNOS to a conformation favouring ROS production [32]. ROS also bind directly to NO to decrease its bioavailability, leading to the generation of the pro-inflammatory peroxynitrite and enhancing ROS production in a feedback cycle [64,65]. This is evident in the vasculature of hypertensive mice, which exhibit elevated oxidised BH4 and ROS production, concurrent with decreased NO levels [32]. Further, ROS have been shown to increase vascular tone via stimulation of ET1 in the VSM and ECs [64]. Upregulation of vascular ROS production contributes to VSMC growth and remodelling, decreasing compliancy of arteries and further promoting the development of hypertension [37]. ROS generation is also linked to ANGII, a key peptide in the renin-angiotensin aldosterone system (RAAS) (see section 1.2.5.2). Endothelial ANGII has been shown to activate epidermal growth family receptors present on VSMCs and in kidneys, promoting vascular NAPDH production and ultimately VSM hypertrophy [66]. In hypertensive human males, ANGII-induced ROS production is elevated, as measured with CM-H2DCFDA fluorescence assays [37]. Doughan *et al.,* showed ANGII-induced mitochondrial hydrogen peroxide production was blocked by inhibition of NOS, NAPDH and PKC, and K_{ATP} channels in isolated mitochondria and bovine arterial endothelial cells, suggesting a PKC-dependent pathway of ANGII induced mitochondrial dysfunction and ROS production via activation of NAPDH oxidase in ECs [67].

1.2.5.2. The renin angiotensin aldosterone system

The RAAS regulates pressure-volume homeostasis in the kidneys and is arguably the most integral BP regulatory mechanism. Prorenin is produced continuously in renal juxtaglomerular cells and is cleaved to its active form of renin in conditions of low BP or decreased sodium load detected by macula densa cells in the distal convoluted tubule [68]. Renin is released

into the interstitial space where it cleaves hepatic angiotensinogen to form angiotensin I (ANGI) [69]. The ubiquitously expressed angiotensin converting enzyme converts ANGI to ANGII in the plasma and tissues including the kidneys, adrenal cortex, arterial vasculature, and the brain. ANGII has a short plasma half-life of 1 – 2 mins prior to degradation by peptidases into its less active forms, angiotensin III and IV [68], and therefore primarily exerts its effects locally in tissues via G protein coupled receptors (GPCRs) angiotensin receptor 1 (AT1R) and angiotensin receptor 2 (AT2R). Early studies in rats demonstrated block of AT1R and AT2R inhibited ANGII induced effects on BP elevation and VSMC hypertrophy respectively [70], demonstrating differential roles for the angiotensin receptors. In the kidneys, ANGII upregulates activity of the Na^+/H^+ exchanger and Na^+/K^+-ATPase transporter to facilitate sodium reabsorption, elevating BP by promoting the movement of blood into the extracellular space and increasing circulating blood volume [68]. ANGII also stimulates the release of the steroid hormone aldosterone from the zona glomerulosa in adrenal cortex via AT1R [71]. Aldosterone binds renal mineralocorticoid receptors to induce activation of the epithelial sodium channel promoting renal sodium reabsorption in the cortical collecting duct of the kidneys [68]. Aldosterone further induces endothelial dysfunction and vasoconstriction via GPCRs independent of its renal actions [72]. ANGII generation also occurs in the vasculature, promoting endothelial dysfunction and vasoconstriction via AT1R activation [68,73–75]. In the central nervous system, ANGII stimulates thirst by binding the hypothalamus and increases water reabsorption in the kidney by promoting the release of antidiuretic hormone from the posterior pituitary, increasing circulatory fluid volume. ANGII also decreases the sensitivity of the baroreceptor reflex to diminish the response to elevations in blood volume [76]. Finally, ANGII has been linked with ROS and inflammation in hypertension, as discussed in sections 1.2.5.1.4. and 1.2.5.5., respectively.

1.2.5.3. The baroreceptor reflex

Arthur Guyton and colleagues first identified specialised mechanoreceptors, termed baroreceptors, located around the arterial tree and concentrated in the carotid sinus [77]. In conditions of increased circulatory volume, baroreceptors detect arterial stretch and trigger signals sent via nerve bundles in the carotid sinus to the brain to reduce activity of the sympathetic nervous system (SNS), reducing heart rate and thereby BP [77]. The importance of the baroreceptor reflex in BP control was initially demonstrated in dogs; block of the baroreceptor reflex and subsequent rapid blood transfusion to increase circulatory blood volume resulted in an uncontrollable elevation of BP compared to dogs with the reflex intact [78]. Research in patients [79] and animal models [76] supports SNS hyperactivity in

hypertensive conditions, and in the context of co-morbidities including obesity [80] and renal disease [81].

1.2.5.4. Natriuretic peptides

Natriuretic peptides, namely ANP (atrial natriuretic peptide), BNP (brain natriuretic peptide) and CNP (C-type natriuretic peptide) are hormones important in BP control. Conditions of elevated blood volume, atrial, ventricular and vascular wall stretch, and increased BP triggers the release of the endocrine mediators ANP and BNP to decrease BP. Natriuretic peptide receptor type A (NPRA) and type B (NPRB) are membrane bound guanylate cyclase receptors and when activated by ANP and BNP activate guanylyl cyclase signalling leading to BP lowering mechanisms including natriuresis (excretion of sodium in the urine), the baroreceptor reflex, and vasodilation [82]. ANP and BNP preferably bind NPRA receptors, which are located primarily on the VSM, ECs, and in organ systems related to BP control including the kidneys, adrenal glands, and the NS [83,84]. BNP null rats have hypertension and associated phenotypes including arterial fibrosis and end organ damage [85]. Genetic studies have identified numerous variants in genes encoding ANP and BNP, and their precursors pro-ANP and pro-BNP, associated with SBP, DBP, and hypertension [86]. Genetic variants detected in hypertensive patients are associated with decreased levels of ANP and BNP, highlighting the BP lowering properties of this hormonal system [87]. However, later stages of hypertension were found to be associated with elevated BNP levels, although this is hypothesised to result from cardiac stress associated with high BP [88]. The endopeptidase neprilysin acts to inactivate ANP and BNP, and is a target of the combination drug LCZ696, clinically known as Sacubilitril/Valsartan, which acts as a dual angiotensin receptor and neprilysin inhibitor. Numerous trials have shown LCZ696 decreases BP in elderly patients with a greater efficacy than the angiotensin receptor blocker olmesartan alone [89], and valsartan alone [90]. LCZ696 has further shown to have effects on cardiac hypertrophy independent of its effects on BP [91], and is also indicated in other CV disease including heart failure [92]. An ongoing clinical trial is looking into its efficacy in resistant hypertension (ClinicalTrials.gov Identifier: NCT04637152).

ANP and BNP have been extensively investigated in respect to CV mechanisms, but there is less research on the more recently identified CNP [93]. Unlike ANP and BNP which are solely produced in the heart, CNP is localised throughout the body, including in the brain [94], ECs and blood plasma [95], cardiomyocytes [96] and fibroblasts [97]. Mounting evidence has implicated CNP in BP control at the level of peripheral vasculature, particularly with endothelial control via NPRB Gi-coupled signalling [93]. The primary function of the natriuretic peptide receptor type C (NPRC) was initially believed to be internalisation and degradation of

natriuretic peptides, negatively regulating their actions [98]. However, mounting evidence has indicated functional roles of NPRC via CNP, for example endothelial production of NO via a calcium dependent pathway as demonstrated in isolated rat aortas [99]. CNP has also been linked to hypertension in animal models, where endothelial specific deletion of CNP in mice resulted in elevated BP [100], and in human genomic studies with the identification of variants in CNP [101] and its endoproteinase furin associated with hypertension [102], and NPRC receptor variants associated with SBP [11,86,103,104], DBP [86,105] and hypertension [86]. Further, CNP has also been shown to be involved in other BP related CV processes including cardiac hypertrophy, inflammation, angiogenesis and vascular remodelling [93].

1.2.5.5. Inflammation

Numerous studies in rodents and hypertensive patients have highlighted an association between inflammation and hypertension, although the exact mechanisms remain unclear. Elevated levels of activated monocytes and monocyte-derived cells were measured in ANGII-induced hypertensive mice in response to increased mechanical stress; this was inhibited by scavenging of hydrogen peroxide and addition of NO, supporting a link between ROS, inflammation and endothelial dysfunction [106]. Chemokines are also linked to ANGII-induced hypertension and elevated ROS production in rodents. CXCR2 inhibition in rats led to a decrease in BP leading the authors to suggest CXCR2 as a potential therapeutic target [107]. Rodent models have also shown the role of CCR2 in hypertension and oxidative stress and hypertrophy [108,109] and renal damage [110] dependent on monocyte function. Guzik *et al.,* demonstrated the role of T cells, but not B cells, in ANGII and salt-induced hypertension in mice via production of cytokine tumour necrosis factor alpha (TNFα) and ROS production [111], and patients with hypertension have higher renal infiltration of CD4+ and CD8+ T cells [112]. Hypertensive patients also have elevated levels of inflammatory markers, including C-reactive protein and TNFα [113]. Contradictorily, drugs treating inflammation including cyclosporine and non-steroidal anti-inflammatory drugs increase BP, highlighting the complexity of BP control and hypertension pathogenesis [114].

1.2.6. Hypertension risk factors

Hypertension is categorised as primary (or essential) hypertension, i.e. without determined cause, or secondary hypertension, as a result of a pre-existing disease (Table 1.2).

Table 1.2. Causes of hypertension.

Primary Hypertension (90%)	Secondary Hypertension (10%)
Lifestyle factors (50 – 70%) • Diet • Lack of physical exercise • Alcohol and tobacco use • Stress	Monogenic disorders Diabetes Kidney disease Thyroid disease
Genetics (30 – 50%)	

1.2.6.1. Lifestyle risk factors

Lifestyle factors play a prominent role in the pathogenesis of primary hypertension and nonpharmacological intervention targeting these factors is often the first line treatment of primary hypertension, including alterations in diet, reductions in sodium intake and tobacco and alcohol use, and physical exercise.

1.2.6.1.1. Sodium

Sodium levels in the blood have long been associated with regulation of BP, and high levels of salt in the diet are linked with the onset of hypertension [115,116] and CVD including stroke [117]. Hypertensive patients often display heightened responses to sodium due to pre-existing dysregulation of compensatory mechanisms [118]. These patients are termed salt sensitive, and this can be a result of genetic factors (e.g. monogenic disorders of hypertension), environmental factors, or both (e.g. in the case of obesity) [119]. Studies in rats have found high salt diet impairs NO release and elevates ROS production, thus causing endothelial dysfunction [120]. Sodium has also been linked to inflammation and the microbiome; in mice a high salt diet depletes gut microbiota and treatment with *Lactobacillus muriinus* prevents salt-induced exacerbation of salt-sensitive hypertension via T helper 17 cell modulation driving autoimmunity [121].

1.2.6.1.2. Diet

Multiple studies have described an optimal diet for BP control. A meta-analysis of randomised controlled trials evaluating the DASH diet (Dietary Approaches to Stop Hypertension), a diet rich in vegetables, fruit and low-fat dairy, found a significant reduction in SBP and DBP in normotensive subjects, with an even greater reduction in hypertensive subjects [122]. The Framingham heart study in the 1960s identified the relationship between body weight and BP [123], and more recent analyses showed the prevalence of hypertension in obese individuals is 3 fold higher than in subjects with a normal BMI [124]. Elevations in BP in obese patients are partly due to sensitisation of the baroreceptor reflex [125], increased SNS activity thereby stimulating RAAS activation and ANGII production, and further with endothelial dysfunction [124]. Increasing physical activity levels is demonstrated to reduce BP in both hypertensive and normotensive and independent of BMI [126], and studies in older patients found that increased aerobic exercise increased NO release from endothelial cells, corresponding to a decrease in BP [127].

1.2.6.1.3. Alcohol

A link between alcohol consumption and hypertension was first reported in French soldiers during World War II [128]. Since, hundreds of studies have explored the relationship between levels of alcohol consumption and hypertension risk, and the influence of ethnicity and gender [129–132]. Notably, a meta-analysis of epidemiological studies using 17,059 participants from the Third National Health and Nutrition Examination Study in the US found African Americans had higher odds of developing hypertension than White and Mexican American populations. Furthermore, the same study found the risk of developing hypertension was only significant in White and Mexican American men and women consuming high levels of alcohol, but not with mild and moderate alcohol consumption [131]. This study did not find a sex-specific association of alcohol intake with hypertension risk, in contrast to a meta-analysis of prospective studies conducted in the US and Japan which identified a protective effect of moderate alcohol consumption in women, but not in men [129]. However, this protective effect in women was not observed in a more recent meta-analysis which included some of the same prospective cohorts [128]. Despite conflicting literature, it is well-established that heavy alcohol consumption (above 2 drinks per day) increases odds of hypertension [128–130,132]. The mechanisms by which alcohol affects BP have been elucidated in rodent models; rats chronically administered with ethanol have decreased baroreceptor sensitivity [133], increased VSM contraction [134], and attenuated vasodilation [135,136]. Tirapelli *et al*., found a reduction in post translational expression of eNOS in rat aortas thereby reducing NO

formation [136], and alcohol has also been linked to vascular ROS production [137] and decreased bioavailability of NO via the formation of peroxynitrite catalysed by eNOS.

1.2.6.1.4. Smoking

The relationship between smoking and hypertension is also unclear. Tobacco use is a well-established risk factor in CVD, although studies in hypertensive subjects have been contradictory with smoking sometimes shown to lower or increase BP compared to smokers, and in some case with no impact at all [124]. In the context of hypertension however, it appears smoking is more relevant in increasing the CV risk related to hypertension rather than changes in BP [138].

1.2.6.1.5. Stress

In conditions of acute stress, elevated BP results from enhanced SNS activity [139]. Chronic stress is also associated with maintained elevations in BP and hypertension, and with hypertension related pathologies including atherosclerosis [140].

1.2.6.1.6. Ageing

Hypertension is more prevalent in the older population. The 2015 National Health and Nutrition Examination Survey reported 70% of adults over 65 years as hypertensive, with numbers predicted to rise due to the ageing population [141]. Indeed, hypertension is often viewed as a disease of accelerated vascular ageing. Several factors contribute to age-related progression of BP, including arterial stiffness [142–144], vascular dysfunction [143], and inflammation [143,145]. The prevalence of arterial stiffness and hypertension concomitantly increases with age [142,144,146]. Ageing large arteries exhibit wall thickening and loss of elasticity, resulting in increased pulse wave velocity; this is a marker of arterial stiffness [144]. Elevated pulse wave velocity results in an increase SBP with little change in DBP, and therefore isolated systolic hypertension is the most common form in the aged population [147]. Ageing is also associated with enhanced elastin degradation and accumulation of collagen in the ECM. This is potentiated by MMPs, as demonstrated in aged rats [148], and in the ageing human aorta, via upregulation of the MMP2-activating enzyme calpain-1 [149]. Bruno and colleagues reported age-dependent increases in the media to lumen ratio and collagen deposition in small resistance arteries, exacerbated in hypertensive patients [143]. Vascular tone is also dysregulated in small resistance arteries with age. Gq/11 and Gq/12-coupled receptor expression is elevated in mesenteric arteries of aged mice, and inhibition decreased myogenic tone via PLC/Ca^{2+} and ROCK signalling [150]. NO availability is decreased in small arteries of older individuals, resulting in blunted endothelial-mediated vasodilation and ROS

production [143]. Finally, low-grade chronic inflammation associated with age is linked to hypertension pathogenesis via ROS formation, and elevated SNS activity [151].

1.2.6.2. Genetics of hypertension

Genetics plays a prominent role in the pathogenesis of primary and secondary hypertension (Table 1.2). In 1949, Page documented the multifaceted nature of hypertension as a result of the dysregulation of four integral systems: CV, renal, endocrine, and neural [152]. The genetic contribution to hypertension was recognised 32 years later in revision of the Mosaic Theory of Hypertension [153], following evidence from a multitude of familial studies [154–156] and the characterisation of rare monogenic disorders of hypertension [157,158]. With a consensus on the existence of a genetic component of BP, the Platt vs. Pickering debate of the 1950s considered whether hypertension was a monogenic or polygenic disorder [159]. Platt argued that rare monogenic disorders of hypertension were evidence for a monogenic nature. In contrast, Pickering postulated the Gaussian, rather than bimodal, distribution of BP throughout the population suggested BP is determined by a collection of genes and further recognised hypertension as a quantitative trait with a normal distribution, opposing the previous suggestion of hypertension as a qualitative trait distinct to normotensive BP [159]. Later studies supported the polygenic nature of hypertension and estimated the heritability of clinical SBP and DBP to be 15 – 40% and 15 – 30% respectively [154], with rare monogenic disorders representing an extreme end of the distribution.

The Human Genome Project provided the catalyst for advances in gene mapping in the 1990s [160]. Linkage analysis was a key tool in the early years, where microsatellite genetic markers were tested for co-segregation with a trait in families, the results of these studies provided chromosomal locations of genes for traits [161]. Investigation into families with monogenic disorders of hypertension using linkage analysis facilitated the identification of the first BP associated genes and highlighted the role of renal and adrenal pathways in BP control [157]. Yet monogenic forms of hypertension account for a very small percentage of hypertensive cases, and in a bid to elucidate genes involved in polygenic forms of hypertension a series of candidate-gene linkage studies were carried out in familial cohorts [162–168]. These studies yielded some promising results; however, these were often contradictory across cohorts with no single candidate gene consistently showing strong linkage with hypertension. Candidate-gene studies were generally underpowered as they relied on familial cohorts for which recruitment is difficult, and there was a lack replication data [169]. Furthermore, candidate genes were selected based on previously characterised BP pathways restricting the

identification of novel BP genes. At the turn of the 21st century, genome-wide linkage analyses were deployed with the aim of identifying loci anywhere in the genome – a hypothesis free approach. Various genome-wide linkage analyses were undertaken in relatively large cohorts including the Framingham Heart Study [170], the Family Blood Pressure Program [171,172] and the British Genetics of Hypertension (BRIGHT) study [173]. These studies successfully identified a number of quantitative trait loci (QTLs; regions of DNA linked to variations in the phenotype) associated with hypertension, some of which were validated in follow-up studies [174–176]. The identification of broad QTL regions on five chromosomes led the BRIGHT study researchers to propose hypertension as an "oligogenic" disorder, in which a small number of genes located in these regions provide the largest effect on the trait, with additional genes exerting smaller effects [173]. Nonetheless, interpreting linkage analysis results presented challenges and limitations; the QTLs identified spanned broad regions of DNA making the identification of the responsible gene difficult [161]. Furthermore, there was a lack of power to identify single nucleotide variants (SNVs) associations with small effects [177].

The complete sequencing of the human genome in 2003 [160], paired with the development of single nucleotide polymorphism (SNP) chip arrays enabled cost-efficient high-throughput genotyping of selected variants, and powered the first genome wide association studies (GWAS) [178–183]. SNPs are SNVs which are present in over 1% of individuals in the population. In GWAS SNPs distributed across the genome are tested for association with traits or diseases. GWASs have benefits over linkage analyses and candidate gene studies as they are unbiased, permit larger sample sizes, and enable meta-analyses improving statistical power [184]. The first GWAS for BP and hypertension was accomplished by the Wellcome Trust Case Control Consortium in 2007, and analysed genotype data of 2000 individuals for 7 diseases, including hypertension, diabetes, and coronary artery disease, with a set of common controls [185] . However, the results of this study demonstrated no genetic variants with large effects on BP or hypertension [185]. Two meta-analyses of GWAS carried out in 2009 identified 13 novel BP loci reaching genome-wide significance of $P < 5 \times 10^{-8}$, using ~30,000 individuals. These studies provided the first validated loci for BP [180,186]. In 2011, the International Consortium for Blood Pressure Genome-Wide Association Studies (ICBP) identified a further 16 novel loci associated with BP traits, namely SBP, DBP, PP, and hypertension, in a meta-analysis of 29 studies [86]. The combination with the 13 previously reported loci explained a very small proportion of genetic variance of BP. Variants identified were common with small effect sizes on BP traits, and often found in non-coding (intronic or intergenic) regions of the genome [86,180,186]. These results demonstrated the need for even greater participant numbers to optimise the power of analysis and identify low frequency and

rare variants with significant effect sizes mapping to exonic genomic regions, to explain more variation in the phenotype.

SNP arrays include only a small proportion of the variants present in the genome, and do not include rare variants with minor allele frequencies (MAFs) below 1%. The development of SNP reference panels, including the 1000 Genomes Project [187] and the Haplotype Reference Consortium [188], enabled imputation and estimation of the effects of associated variants not featured on arrays. In tandem with SNP arrays, the establishment of accessible large-scale Biobanks (e.g. UK Biobank) containing not only genetic data but a variety of phenotypic and health-related data [189] have improved the statistical power of GWAS and enabled the detection of both common and rare BP variants [12,13,103,190]. Rare variants with large effects have more potential than common variants to provide insight into disease pathogenesis and act as genetic markers (Figure 1.6).

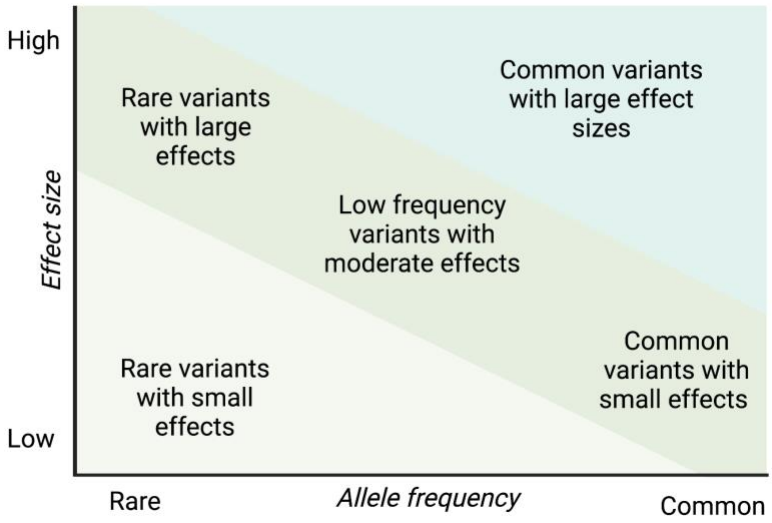

Figure 1.6. Relationship between allele frequency and effect size of rare and common variants. Adapted from Tam *et al.,* 2019 [191].

In 2011 the Exome chip was launched [192]; an array of predominantly rare and low frequency variants mostly located in exonic (coding) regions. Four years later, a trans-ethnic meta-analysis of Exome chip data with replication in European and South Asian ancestries was published and identified the first rare exonic variants associated with BP traits with effect sizes greater than that observed with common variants (>1.5 mmHg per allele), mapped to four genes: *RBM47, COL21A1, DBH,* and *RRAS,* our gene of interest. In the same year, an

additional trans-ethnic study reported a rare variant of the *NPR1* gene, associated with a +1.1 mmHg increase in SBP; this gene is a drug target for hypertension with a clinical trial ongoing [193]. Nonetheless, the collective number of loci identified at this point accounted for 2.8% of the genetic heritability of BP. It was not until 2018 that the impact of large-scale Biobanks was truly demonstrated, with the identification of over 500 novel loci in a single study 1 million individuals of European descent, doubling the total explained heritability from less than 3% to ~6% [194]. This study was closely followed by a large-scale GWAS meta-analysis of over 750,000 participants of mixed-ancestry from UK Biobank (UKB) and Million Veteran Program (MVP) data in 2019, identifying a further 53 novel rare variants associated with BP traits [104]. The study with the largest number of participants to date was carried out in 2020, including 1.3 million individuals using Exome chip data with replication in trans-ethnic individuals identified an additional 106 novel loci, of which 87 were rare variants. These analyses focused on identifying rare variants with larger effect sizes on BP. More recently in 2022, a single-stage GWAS meta-analysis combining genetic data from over 1 million individuals from UKB, ICBP, MVP and the BioVU Vanderbilt DNA databank, investigated common variants with a MAF ≥1% to assess the percentage heritability explained in BP traits, and identified over 2000 independent signals. When translated into a polygenic risk score, these loci and secondary signals explained 41.2% of the common heritability of SBP [195], exemplifying the power of large-scale meta-analyses. To date, over 1200 loci have been significantly associated with BP, with continuous efforts being made to further unravel the genetic architecture of BP (Figure 1.7).

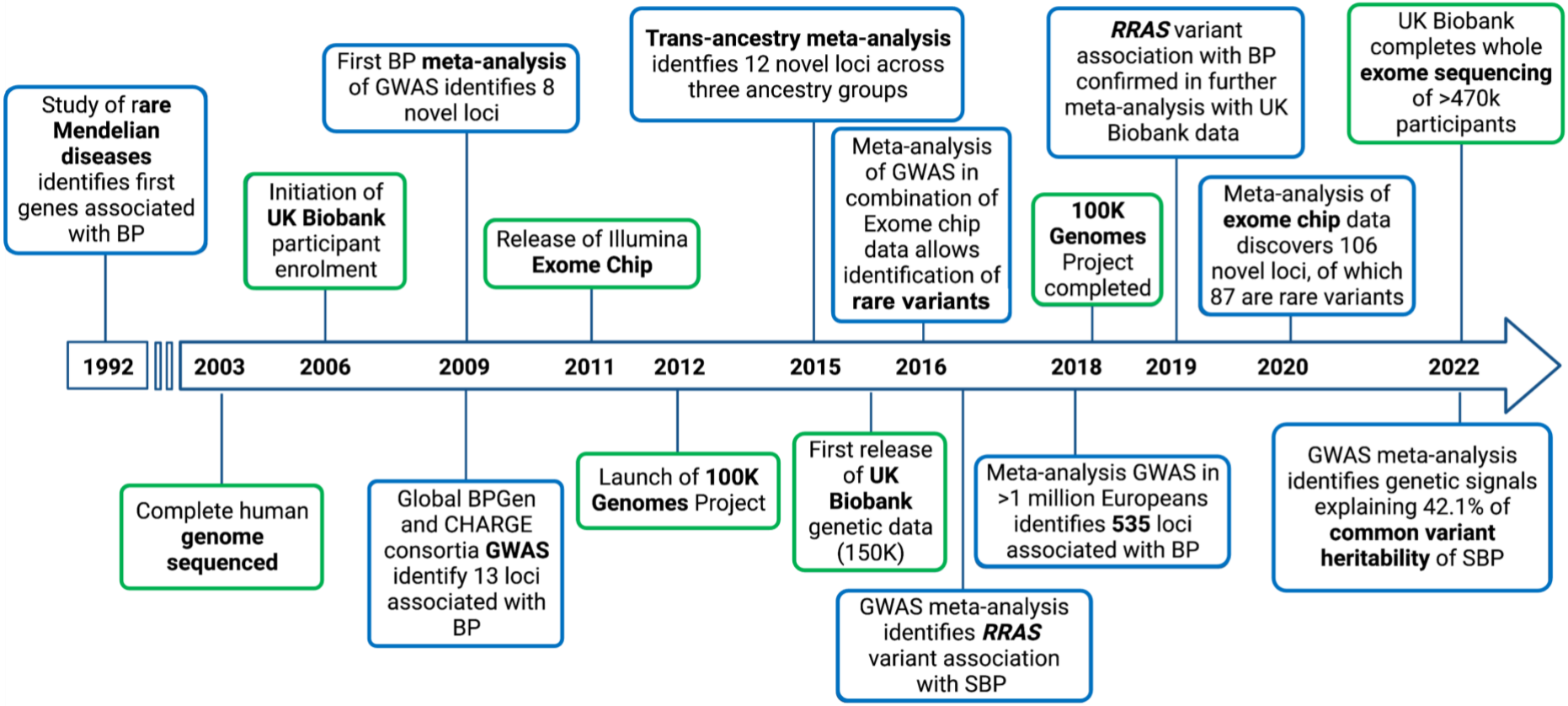

Figure 1.7. Timeline of important blood pressure genetic discoveries (blue) and release of genetic resources (green). [86,103–105,179,182,185,186,190,195–199]

1.2.7. Current BP treatments

The current National Institute for Health and Care excellence (NICE) guidelines in the UK aim to lower BP to <140/80 mmHg in hypertensive patients aged under 80 years, and <150/90 mmHg in patients aged 80 years and over [200]. Life-style changes, including improved diet and exercise and reduced alcohol and tobacco use, are recommended for all hypertensive patients. Lifestyle modifications alone in many patients do not reduce BP, and drug treatment is often necessary to sufficiently lower BP (Table 1.3).

Table 1.3. Drugs used in the treatment of hypertension

Drug class	Mechanism of action	Example
AT1R inhibitors	Inhibit activation of RAAS preventing vasoconstriction and endothelial dysfunction	Losartan
Angiotensin ACE inhibitors		Captopril
Thiazide diuretics	Block sodium-chloride symporter of distal convoluted tubule in kidney causing increased water excretion in urine lowering blood volume	Chlortalidone
Calcium channel blockers	Cause vasodilation via inhibition of calcium influx in vascular smooth muscle	Verapamil
Beta-blockers	Inhibit β-adrenergic receptors in heart to reduce cardiac output	Propranolol
Alpha-blockers	Vasodilation via inhibition of α1-adrenergic receptors in VSM	Doxazosin

Drugs are listed in order of treatment steps as outlined in the NICE clinical guidelines for hypertension management in adults [7,10,200].

Interindividual variation exists in patient response to the anti-hypertensive drugs, largely dependent on age and ethnic background, in addition to issues with patient adherence [10,11]. Moreover, patients often require combination therapies to reach BP target levels. Current

NICE guidelines take into account ethnic background and co-morbidities, namely type II diabetes, to inform treatment choice [200]. Nonetheless, in 2017 over ¼ of adults aged over 18 years in England had hypertension [200], and data from the US only indicates 50% of hypertensive patients were satisfactorily treated in 2012 [201]. Together these issues highlight a need to design more efficacious and personalised medicines.

1.3. R-Ras

In 2016, a trans-ancestry meta-analysis of over 300,000 participants from European and South Asian Ancestry first identified rare genetic variants with modest effect sizes on BP traits [11] (Figure 1.7). This study identified 30 novel loci including the SNV rs61760904 reaching genome-wide significance with a positive effect size of 1.51 mmHg/T allele on SBP. This rare variant was mapped to the *RRAS* gene (Figure 1.8), encoding the small G-protein R-Ras, with a predicted amino acid change from an arginine (D) to an asparagine (N) at position 133 (D133N). This association was subsequently confirmed in a meta-analysis of UKB and the MVP data published in 2019 [104], and most recently in a meta-analysis of over 1.3 million individuals [12]. In the recently released Genebass database of rare variant associations of over 4,529 phenotypes in exome data from UK Biobank [202], SKAT-O (optimal unified SNP-set Kernel Association Test) testing of variants in the gene including the rs61760904 missense variant showed significant association with the phenotypes 'Hypertension' ($p = 5.96x10^{-10}$), and 'Systolic blood pressure, automated reading' ($p = 3.41x10^{-7}$) [202]. rs61760904 was the most significantly associated variant, and gene based testing indicated no association with the *SCAF1* gene, the neighbouring gene to *RRAS* [202]. Altogether, this data is supportive of rs61760904 as the potential causal variant, and R-Ras as a promising candidate gene.

Numerous studies have indicated a role of R-Ras in cardiovascular physiology, including vasodilation and vascular remodelling. Furthermore, R-Ras is expressed in arteries, including the aorta [203], and endothelial and smooth muscle cell lines [204]. Coupled with genome-wide significant association with SBP, this suggests involvement of R-Ras in BP control and hypertension.

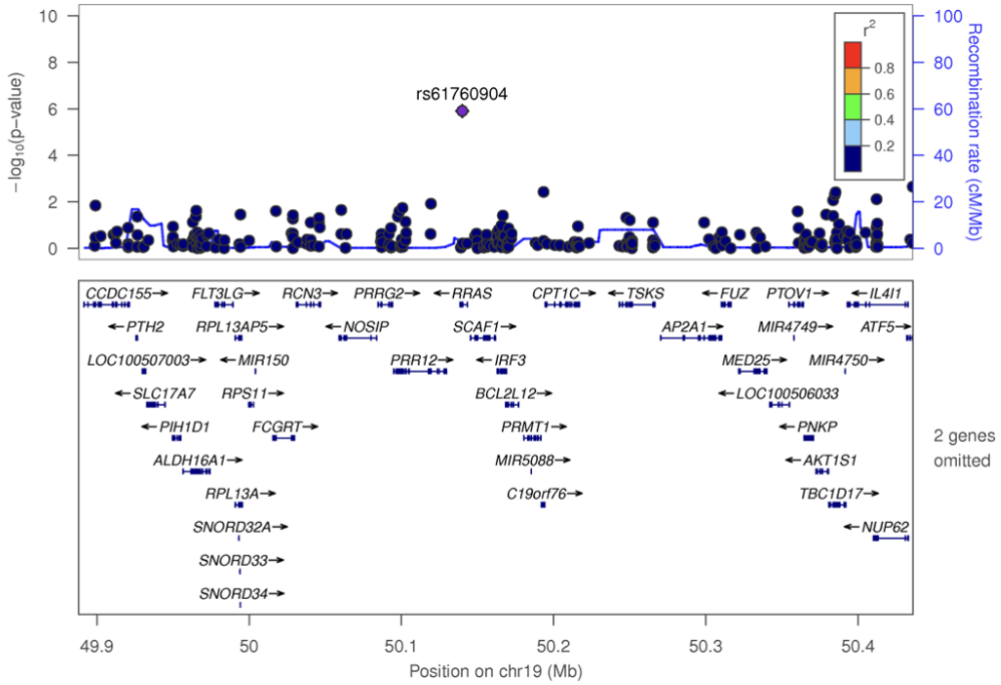

Figure 1.8. Regional association plot of chromosome 19 and the systolic blood pressure-associated variant, rs61760904, identified in the meta-analysis using Exome-chip data. Figure adapted from Surendran *et al.,* 2016 [103].

1.3.1. The Ras superfamily

The Ras superfamily is comprised of over 150 small GTPases that share common enzymatic activity and play vital roles in signalling in mammalian cells (Figure 1.9) [205–207]. Ras proteins share a conserved GTP-binding core of ~20 kDa formed of 5 guanine nucleotide consensus sequence elements which bind phosphate, Mg^{2+} and guanine to aid the GDP-GTP cycle (GDP: guanosine diphosphate, GTP: guanosine triphosphate) [206–209]. Ras proteins have 2 switch regions (SI; Ras residues 30 – 38, SII; 59 – 76) involved in effector binding specificity and conformational changes during cycle. The Ras and Rho of proteins possess a hypervariable carboxyl terminal region terminating in a Cys-A-A-X (CAAX) binding motif, which undergoes post-translational modifications including prenylation and palmitoylation, and is essential for targeting the proteins to the membrane to enable activation and inactivation by specific guanine nucleotide exchange factors (GEFs) and GTPase activating proteins (GAPs) respectively [209–214] (Figure 1.10).

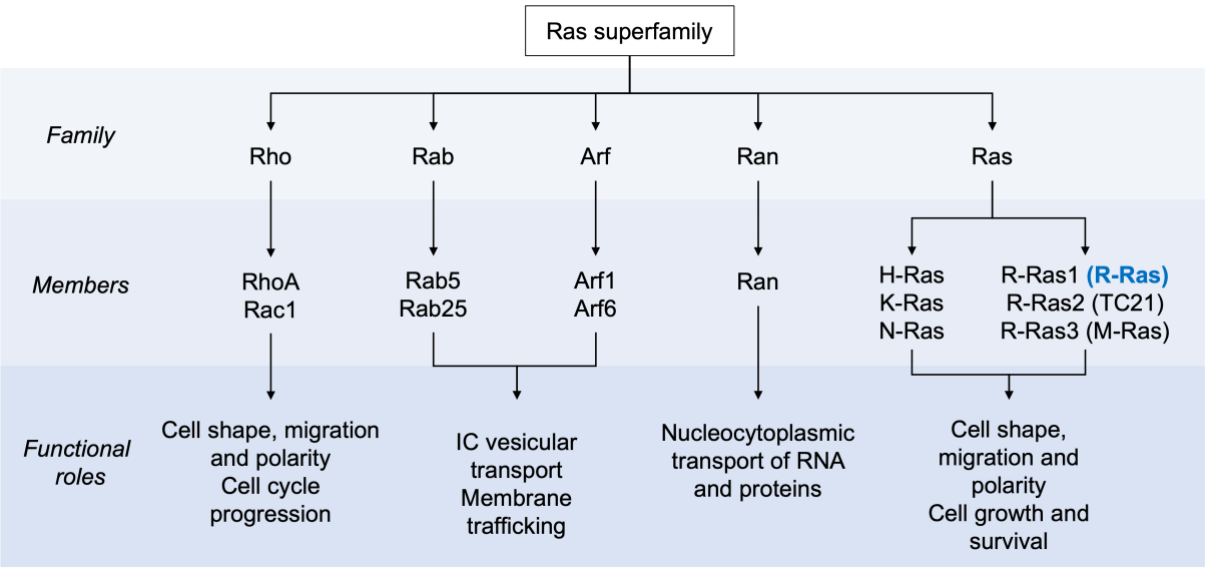

Figure 1.9. The Ras superfamily. Over 150 small GTPases make up the Ras superfamily, divided into families based on structure, sequence homology and functional similarities [205–207,209].

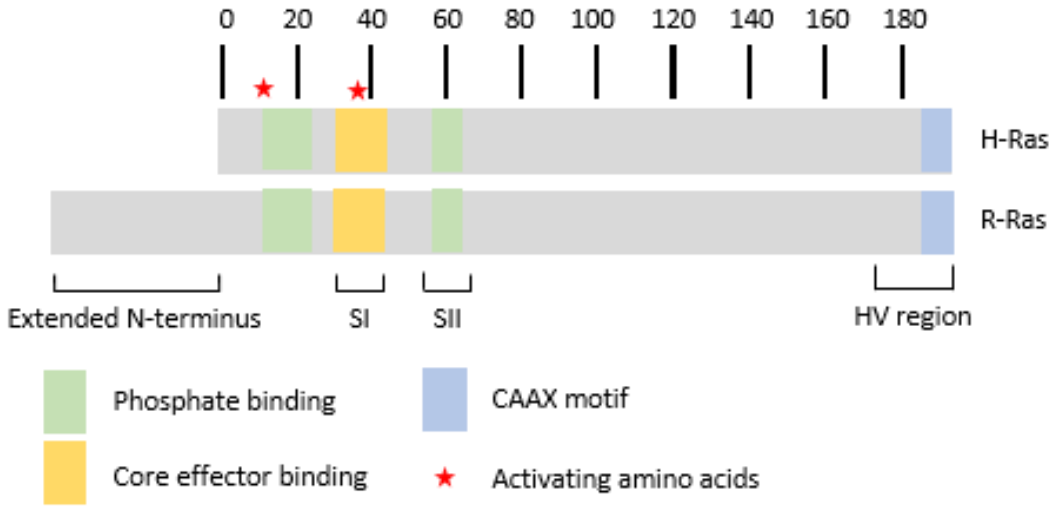

Figure 1.10. The Ras family structure. The Ras family share conserved functional regions, including switch regions, a hypervariable region at the C-terminus, the CAAX motif and motifs for phosphate binding and core effector binding. R-Ras has an extended N-terminus compared to other Ras family proteins [204,215–217].

Ras proteins cycle between an inactive GDP-bound state and an active GTP-bound state [45, 54-57]. This process is regulated by specific GEFs and GAPs (Figure 1.11). GEFs catalyse the release of GDP enabling GTP binding and conversion of the protein into the active GTP-bound state. GAPs support intrinsic GTPase activity and stimulate GTP hydrolysis to convert Ras proteins to the inactive GDP-bound state [205,209,218–221]. As listed in Table 1.4, members of the Ras family interact with different GEFs and GAPs resulting in diversity in signalling between Ras proteins [205,213,218,219,222–225].

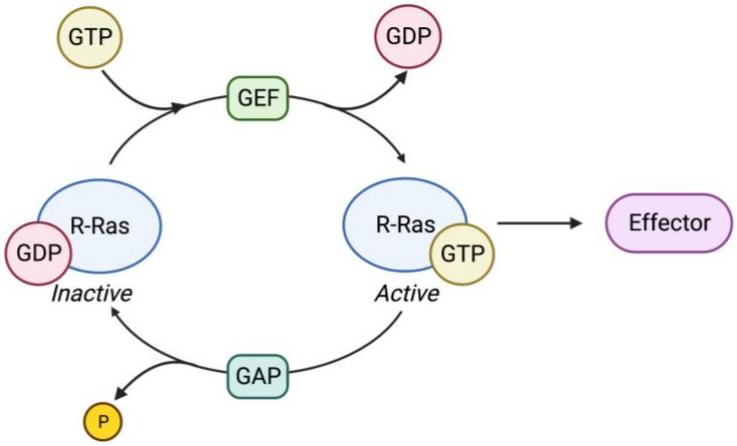

Figure 1.11. The R-Ras GTP-GDP cycle.

Table 1.4. Ras family GEFs and GAPs.

Ras protein	GEFs	GAPs
H-Ras	RasGRF1, RasGRF2, CalDAG-GEFII, CalDAG-GEFIII, SOS, PDZ-GEF1, RasGRP4	p130a, NF1
K-Ras	RasGRF1, CalDAG-GEFI, CalDAG-GEFII, CalDAG-GEFIII, SOS, Rap1GDS1	p130a, NF1
N-Ras	RasGRF1, CalDAG-GEFI, CalDAG-GEFII, CalDAG-GEFIII, SOS	p130a, NF1
R-Ras	RasGRF1, CalDAG-GEFI, CalDAG-GEFII, CalDAG-GEFIII	p130a, NF1, R-RasGAP, Plexin-B1

1.3.2. The Ras family

The Ras (Ras sarcoma) family is known as the founding family of the Ras superfamily and is further divided into H-Ras, K-Ras, N-Ras proteins, and the R-Ras family (Figure 1.9) [206,207,211,224]. H-Ras, K-Ras, and N-Ras proteins are widely recognised as oncogenic proteins and share an 85% sequence homology. Lowe *et al.,* in 1987 identified an additional Ras family GTPase based on hybridization with an H-Ras probe and subsequent cloning studies [210,211]. This protein, denoted R-Ras, shares 55% sequence homology with the Ras family GTPases [211,226]. H-Ras, K-Ras and N-Ras are proteins of 189 – 190 amino acids in length and are formed of 4 coding exons and intron regions. In contrast, R-Ras is 218 amino acid protein composed of 6 exons, with an extended N-terminus of 26 amino acids [210,211,226]. R-Ras also has a distinct proline-rich PXXP sequence enabling binding to the adaptor protein Nck and subsequent regulation of integrin signalling (Figure 1.10) [227]. Following the discovery of R-Ras (R-Ras1), two additional closely related proteins, TC21 (R-Ras2) and M-Ras (R-Ras3), were identified together forming a distinct branch of classic Ras proteins (Figure 1.9) [228]. R-Ras and TC21 share similarities in effector coupling and downstream signalling pathways, notably PI3K/Akt [225,229]. In contrast, M-Ras is regulated

by classic Ras GAPs and GEPs [225] and, unlike R-Ras and TC21, potentiates MEK/ERK signalling [229]. This thesis focuses on the *RRAS* gene, encoding the R-Ras1 protein, denoted as R-Ras throughout.

1.3.3. R-Ras signalling

Ras proteins modulate a diverse array of signalling pathways via interactions with different effector molecules (Figure 1.12). H-, K-, and N-Ras proteins are recognised as oncogenic proteins, and are the most commonly mutated proteins in cancer [211,224]. They play a large role in cancer via activation of the MAP kinase (MAPK) pathways, particularly ERK signalling pathways, heavily involved in cell growth and proliferation [224]. R-Ras signalling is less defined, and there is conflicting evidence in differential cell systems, summarised in Figure 1.12. Notably, it is debated as to whether R-Ras interacts with ERK1 signalling; experiments undertaken in CHO cells [230], J774 macrophages, and PC12 cells oppose this [231], however, more recent work by Fremin *et al.,* in 2016 suggests ERK1 phosphorylates R-Ras at the S201 residue [232]. Likewise, experiments exploring the link between R-Ras and MAPK signalling in different cell systems also yield conflicting results; R-Ras appears to activate MAPK in NIH3T3 cells [233] but has no effect on MAPK activation in Cos-7 cells [224]. Nevertheless, it is well established that R-Ras activation initiates PI3K/Akt signalling [217,224,230,231,234–239].

R-Ras activation is mediated by various receptor systems, including GPCRs [240], tyrosine kinase receptors [212,218,241], semaphorin-plexin signalling [238,239] and Notch receptor signalling [242] (Figure 1.12). Notably, activation of the Gαq-coupled muscarinic acetylcholine receptor M3 (M3AChR) potentiates R-Ras activation, dependent on Epac [240,243]. Likewise, Semaphorin-4D, an axon guidance protein which binds the plexin B1-receptor, has been shown to induce growth cone collapse via inhibition of R-Ras activation and subsequent inhibition of PI3K and GSK-β3 signalling in hippocampal neurons cultured from rat embryos [238].

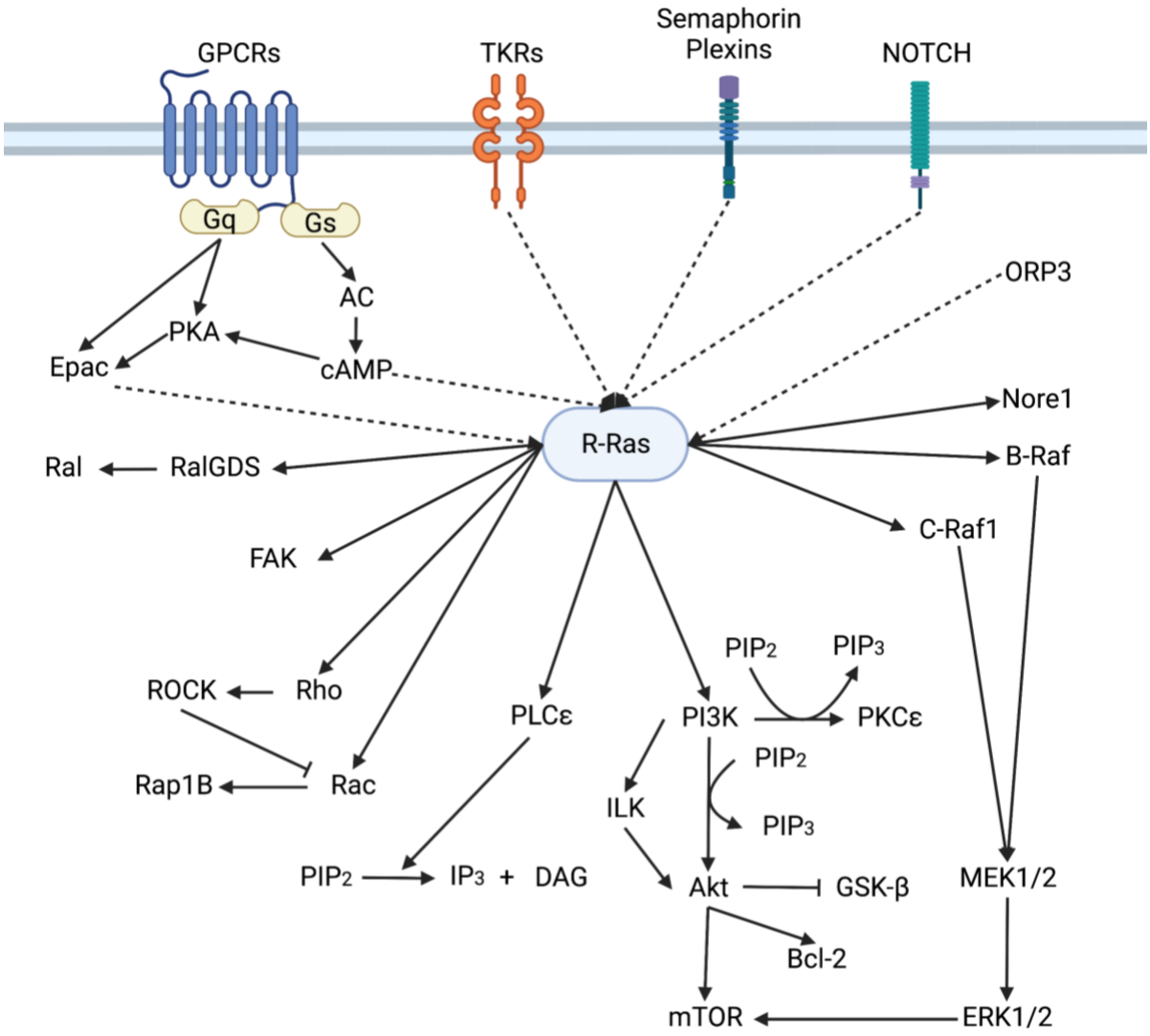

Figure 1.12. R-Ras signalling overview. Solid arrows indicate activation downstream of R-Ras, dotted arrows indicate upstream effector activation of R-Ras. [11,212,217,218,224,231–245].

1.3.4. R-Ras function

The generation of a R-Ras knockout (KO) mouse model by Komatsu *et al.,* in 2005 [208], in combination with *ex vivo* and *in vitro* assays and the use of constitutively active and dominant negative mutants of R-Ras (R-Ras38V and R-Ras43N, respectively), has provided insight into cellular, physiological, and pathological roles of R-Ras (Table 1.5). R-Ras has been identified to play key roles in basic cellular functions including cell spreading, adhesion and migration. These cellular functions rely heavily on bi-directional signalling molecules, the integrins.

Table 1.5. Primary physiological functions of R-Ras.

Function	Mechanism	References
Integrin activation	Reverses H-Ras mediated integrin inhibition	[226,246]
Cell migration	Promotes cell spreading, adhesion and migration via integrins and calcium-dependent actin-binding protein modulation	[208,233,235,247]
Vascular permeability	Interacts with actin binding protein filamin-A and Epac to maintain permeability Inhibits VEGF-induced permeability Promotes blood vessel maturation and stability	[208,216,217,248,249]
Angiogenesis	Inhibits VEGF-induced angiogenesis via VEGFR2 inhibition Promotes blood vessel maturation and stability Promotes cardiac angiogenesis via DDAH1	[208,217,250,251]
Nervous system development	Promotes growth cone collapse, neural tube formation and oligodendrite differentiation	[238,239,245]
Immune response	Mediates T cell priming and trafficking and autoimmunity	[252–255]

1.3.4.1. Integrins

R-Ras is demonstrated to activate integrins composed of specific α and β subunits. Notably, R-Ras activates α2 but not α5-containing integrins to promote migration of breast epithelial cells via PI3K and PKC signalling, independent of MAPK [256]. Expression of R-Ras38V in 32D [236] and CHO cell lines failed to activate β3 integrins [257]. In contrast, a separate study in CHO lines demonstrated an R-Ras38V-mediated activation of αIIbβ3, but no change in expression [226]. The scaffold protein SHANK3 was shown to inhibit β1 integrin activation by sequestering R-Ras in HEK293 cells [258]. R-Ras-mediated activation of the β1-integrin has also been demonstrated to act downstream of oxysterol-binding protein-related protein 3

(ORP3) [259,260]. Further, numerous studies have demonstrated R-Ras reversal of H-Ras mediated integrin suppression. H-Ras-mediated inhibition of integrin activation via ERK signalling was demonstrated in CHO cells, and this was reversed by R-Ras via PI3K and Notch signalling cascades, independent of ERK [208,230,242]. Overall, it is well established that R-Ras signalling results in integrin activation, linking R-Ras signalling to advanced processes as discussed below.

1.3.4.2. Cell shape change, adhesion, and migration

Cell migration is a fundamental process in both physiological and pathophysiological systems [257]. The cell undergoes an initiation stage of spreading and adhesion to the extracellular matrix resulting in the formation of cell protrusions [241,257]. These protrusions extend and form new attachments to the extracellular matrix concomitant to the release of attachments at the rear of the cell facilitating directional movement [227,241]. A vast number of IC signalling pathways mediate this process. Notably, integrin signalling is essential in adhesion, and the small GTPases Cdc42, Rac and RhoA are indicated to mediate actin polymerization to allow spreading and formation of protrusions [215,241].

R-Ras influences these signalling pathways to encourage cell spreading and adhesion via regulation of the actin cytoskeleton. In cultured cortical neurons, R-Ras-induced activation of the actin-binding multidomain adaptor protein, afadin, facilitated F-actin binding and formation of axonal protrusions [229]. R-Ras-mediated reorganisation of the actin cytoskeleton in the epithelial cell line, MCF10A, was demonstrated to be dependent on PLCε signalling [247]. R-Ras38V-expressing cells lose polarisation and spread to a greater extent than control cells and exhibit a ruffling lamellipodia phenotype, as demonstrated in numerous cell lines [214,231,232,235,237,247]. In Cos-7 cells R-Ras38V was shown to colocalize with β1-integrins and regulate integrin clustering in these characteristic ruffles to promote cell adhesion [214]. Activation of R-Ras by ORP3 has been shown to regulate cell adhesion via Akt phosphorylation and subsequent β1 integrin activity [260]. Further, R-Ras is proposed to activate Rac1 via PI3K/Akt signalling [236] promoting IP_3-dependent calcium mobilization and calcium-dependent modulation of actin-binding proteins and membrane trafficking [235,247].

Research exploring the role of R-Ras in cell migration yields inconsistent results depending on the cell system used. Cell migration relies on the formation of filopodia, however, it has been demonstrated in MCF10A cells [247], T47D cells [261] and in fibroblasts [235] that expression of R-Ras38V inhibits filopodia formation and promotes a ruffling lamellipodia phenotype. Furthermore, R-Ras transfection into human coronary artery endothelial cells

(HCAECs) inhibited platelet-derived growth factor-induced migration [188]. In contrast, two separate studies in the human breast cancer cell line T47D showed constitutively active R-Ras to induce migration across collagen, in an α2β1 dependent manner [256,261,262]. Likewise, in a human cervical carcinoma cell line, C33A, R-Ras promoted migration across collagen [263]. In *vitro* studies in mouse fibroblasts have also demonstrated R-Ras modulation of cell extension generation involved in early stages of cell migration by the actin binding protein Flightless I via GAPs Rasgap^{10} [264,265].

1.3.4.3. Angiogenesis

Cell adhesion and migration underlie the formation of new blood vessels, termed angiogenesis. Angiogenesis occurs throughout the body in physiological and pathophysiological systems e.g. embryonic development and tumour growth [248]. An anti-angiogenic role of R-Ras has been exemplified in *in vivo* tumour formation and *ex vivo* matrigel plug assays in R-Ras null mice. Further, R-Ras38V-transfected human umbilical vein endothelial cells (HUVECs) exhibit attenuated vascular endothelial growth factor (VEGF)-induced angiogenesis *in vitro* [208].

R-Ras also promotes the formation of mature, stable blood vessels via a few independent pathways. Blood vessel stability is governed by tight regulation of vascular permeability by the vascular endothelium. Small molecules passively cross the endothelial barrier, however, passage of large molecules of >40 kDa depends on active processes, such as actin polymerization and reorganization of the cytoskeleton, and the formation of transcellular and paracellular gap junctions [30,31,216,248,266]. The paracellular adherens junction, composed mostly of adhesion molecule VE-Cadherin, is critical in maintenance of vascular permeability. Pro-angiogenic stimuli, including VEGF, stimulate hyperphosphorylation and internalisation of VE-Cadherin via a cAMP dependent pathway, dissolving junctions and increasing the permeability of the vessel, thus destabilising it and encouraging angiogenesis [248,267,268]. R-Ras is suggested to inhibit the effects of VEGF on angiogenesis and vascular permeability via inhibition of internalization, phosphorylation and therefore activation of VEGF receptor 2 (VEGFR) [259,261,267,268], as exemplified by observed hyperphosphorylation of VEGFR2 in null mice [261]. Furthermore, in retinas of null mice the vessels formed were “leaky”, and immunostaining for VE-Cadherin in the blood vessel endothelium was reduced compared to the wild-type (WT) animals [262]. Conditional KO demonstrated this retinal development was dependent on R-Ras localised in pericytes [269]. Studies in a mouse model of ischaemia demonstrated interplay between Akt/GSK-3β and R-Ras signalling to maintain vascular

permeability, independent of VEGF [217]. This is achieved via the non-muscle actin binding protein Filamin A (FLNa), which interacts with β-integrins to maintain permeability. Loss of communication between R-Ras and FLNa enhances vascular permeability via cAMP signalling, as decreased R-Ras or FLNa expression in HCAECs mimicked increased vascular permeability observed with forskolin-induced cAMP production [249]. R-Ras also regulates vascular permeability via interactions with the inducible guanine nucleotide exchange factor Epac. Epac enhances endothelial barrier integrity by binding to and stimulating cAMP activity (Figure 1.12), resulting in Rac1 activation and subsequent stabilisation of actin and redistribution of adherens and tight junctions [248]. In HEK293 cells, Epac is demonstrated to play a role in R-Ras activation induced by M3AChR Gq-coupled signalling, dependent on cAMP signalling [240]. Epac has also been shown to induce eNOS phosphorylation and subsequent NO production in HUVECs [240], although it has not yet been explored as to whether R-Ras is also involved in this.

R-Ras also appears to inhibit hyperplasia of VSM in blood vessels; in a mouse model of restenosis, VSM hyperplasia is inhibited in the R-Ras null mouse compared to WT [208]. This R-Ras-mediated inhibition of proliferation is replicated in HCAECs [208] and in rat glioma cells [241].

Finally, the R-Ras/Akt/GSK-3β signalling axis is suggested to play a role in exercise induced cardiac angiogenesis via dimethylarginine dimethylaminohydrolase-1 (DDAH1). Exercise-induced angiogenesis in WT mice was concurrent with increased protein levels of DDAH1, R-Ras, Akt and GSK-3β, and this effect was ablated in DDAH1 null mice. DDAH1 degrades assymetric dimethylargine (ADMA), a major inhibitor of NOS, thereby increasing NO bioavailability. In this study, changes in eNOS protein expression were in line with elevated R-Ras expression with exercise, and reductions with DDAH1 KO, however a potential link between the R-Ras and NO pathways has not been looked into [251]. ADMA accumulation is linked to endothelial cell apoptosis, a process linked to angiogenesis and maturation of blood vessels. Takino *et al.,* found R-Ras inhibited Bax-induced apoptosis of HUVECs, downstream of RasGRP, further evidencing a link between R-Ras and angiogenesis and potentially with DDAH1 [270].

1.3.4.4. Nervous system development

R-Ras signalling is implicated in NS development. In its active state, the serine/threonine protein kinase GSK-3β induces collapse of the actin-based extension of a developing neurite, termed a growth cone, which is essential in the development of the NS [238,239,245]. GSK-

3β is inactivated via PI3K/Akt signalling, and in a developing NS the Sema4D-Plexin-B1 complex inactivates PI3K to disinhibit GSK-3β allowing collapse of the growth cone. R-Ras activates PI3K/Akt, and thus plays a role in inactivating GSK-3β and preventing collapse (Figure 1.12) [245]. Likewise, expression of R-Ras38V in the neuronal growth factor-stimulated PC12 cell line inhibited Sema4D-induced neurite retraction [245]. R-Ras also interacts with Eph receptors, a class of protein tyrosine kinases, to aid NS development [241,271]. Silencing RNA studies show EphB2/R-Ras mediated inhibition of glioma cell proliferation in an organotypic rat brain slice, via MAPK signalling [241]. R-Ras appears to play a role in neural tube formation via interactions with VANGL Planar Cell Polarity Protein [272]. Finally, *in vitro* and *in vivo* studies have suggested an essential role of R-Ras role in oligodendrocyte differentiation, which is essential for axonal myelination and effective transmission of neural impulses [273,274].

1.3.4.5. The immune system

The immune system serves to protect the body from pathogens. The innate immune system acts as the first line of defence and recruits phagocytic cells, including macrophages, dendritic cells, and neutrophils, which engulf and destroy pathogens upon contact. If the innate immune response fails to contain the pathogen spread, the adaptive immune response is activated. Unlike the innate immune response, which is non-specific, the adaptive immune response acquires a memory of specific pathogens, in the form of antigen-specific receptors expressed on T and B cells [275].

Evidence for the role of R-Ras in the innate immune response is inconsistent; *in vitro* studies in HCAECs found R-Ras38V enhanced monocyte adhesion and increased R-Ras activity corresponded to increased expression of connectin segment-1 fibronectin and α5β1 integrins, which are mediators of monocyte entry into atherosclerotic regions, dependent on Akt activation [276]. Conversely, *in vivo* studies in atherosclerotic plaques of R-Ras null mice found the same F4/80-positive macrophage levels as WT [208].

R-Ras is more established in the adaptive immune response, and studies have proposed a role of R-Ras in T cell priming and trafficking. In response to infection, naïve T cells are trafficked to the lymph nodes via high endothelial venules (HEV) for specialisation. In WT mice, R-Ras is upregulated in the endothelium of HEVs after pathogen inoculation [252]. R-Ras null mice have smaller lymph nodes and disorganised HEVs [253], and in EC-specific inducible R-Ras KO mice pathogen-induced naïve T cell trafficking to lymph nodes is attenuated [252]. Moreover, Singh *et al.,* found bone marrow derived dendritic cells from R-

Ras null mice exhibit impaired T cell priming and proliferation [254]. R-Ras is also associated with autoimmunity; in a model of experimental autoimmune encephalomyelitis characterised by hypermyelination, R-Ras null mice had an attenuated disease phenotype, in tandem with upregulation of regulatory T cells and reduction in CD4+ and CD8+ T cells [255]. Together these studies identify a role of R-Ras in T cell regulation of the adaptive immune response, however, there has been no evidence for R-Ras in B cells.

1.3.4.6. Pathological roles of R-Ras

The other members of the Ras family, H-Ras, K-Ras and N-Ras are acknowledged as oncogenes, and are mutated in various cancers [209]. However, the role of R-Ras in cancer pathology is disputed. For example, Bcl2, a pro-apoptopic protein downregulated in numerous cancers including melanoma, breast and lung cancers, associates with R-Ras, as demonstrated in coimmunoprecipitation studies in the NIH3T3 fibroblast cell line [233] and in the cervical cancer derived HeLa cell line [256], but with opposing evidence in bone marrow-derived lymphoblast FDC-P1 cells [273] or the similarly murine bone-marrow derived 32D cell line [277]. However, R-Ras38V expression in the human breast carcinoma cell line T47D induces migration of cells across collagen, an important process in the formation of tumours [256]. More recently, R-Ras has been shown to colocalise with the TGF-β receptor-interacting protein in colorectal cancer cells, implicating R-Ras in TGF-β oncogenic signalling via MAPK/ERK pathways [278]. Further, induction of skin carcinomas using DMBA/TPA in the R-Ras null mouse resulted in a reduction in the number of tumours formed, as well as a delay in tumour formation [271] indicating an oncogenic role of R-Ras. OPR3, an upstream effector of R-Ras promoting β1-integerin activity, is also overexpressed in some cancers suggesting this pathway may contribute to an oncogenic role of R-Ras [260]. More recently, R-Ras was linked to development of malignant peripheral nerve sheath tumours (MPNSTs) which are characterised by loss of the GAP neurofrombin 1 (NF1). R-Ras is normally inactivated by NF1 but was found to be constitutively active in MPNSTs. Phosphoproteomic analysis further identified alteration in ROCK1 and cortactin signalling pathways, suggesting R-Ras promotes actin reorganisation to facilitate pathogenic MPNST cell migration [279] .

RASopathies, including Noonan syndrome, are a family of neural developmental disorders associated with cardiac defects, including pulmonary stenosis, atrial septal defects, and hypertrophic cardiomyopathy, and predisposition to malignancies, among other co-morbidities. Noonan syndrome is characterised by dysregulation of RAS signalling via enhanced activation of Ras family members H-Ras, K-Ras, and N-Ras, and upstream

modulators [280]. Although R-Ras has not been directly linked to Noonan syndrome pathogenesis, activating mutations in *RRAS* were recently identified in two patients with clinical features overlapping with Noonan syndrome, but lacking characteristics for a definitive diagnosis. One patient carried an alanine to glycine substitution mutation (R-RasA163G), and one patient carried a *de novo* three-nucleotide duplication (c.116_118dup, p.Gly39dup) mutation. The R-RasA163G patient exhibited pulmonary stenosis, although other cardiac abnormalities were absent. *In silico* and *in vitro* studies demonstrated these mutations enhanced GTPase activity by maintaining R-Ras in its GTP-bound active state, thus dysregulating MEK/ERK signalling downstream [280]. Nonetheless, these cases are extremely rare, and evidence is otherwise lacking for causal R-Ras mutations in RASopathies.

1.4. The Rras-DEL415 KO mouse model

With strong genetic support of the missense rs61760904 variant in the *RRAS* gene associated with elevated SBP [11,104,281], DBP [281] and PP [104,281], R-Ras presented as a promising candidate for follow up functional studies. A R-Ras KO mouse model, Rras-DEL415, was specifically generated for this project via CRISPR-Cas9 on a C57BL/6N background by MRC Harwell (UK) in conjunction with the International Mouse Phenotyping Consortium (IMPC). Inactivation of *Rras* in these mice is caused by deletion of 415 nucleotide bases, including critical exon 3 and exon 4, to create a KO allele (Figure 1.13). Exon loss was validated by MRC Harwell using a WT loss of allele assay with a Dot1l internal control.

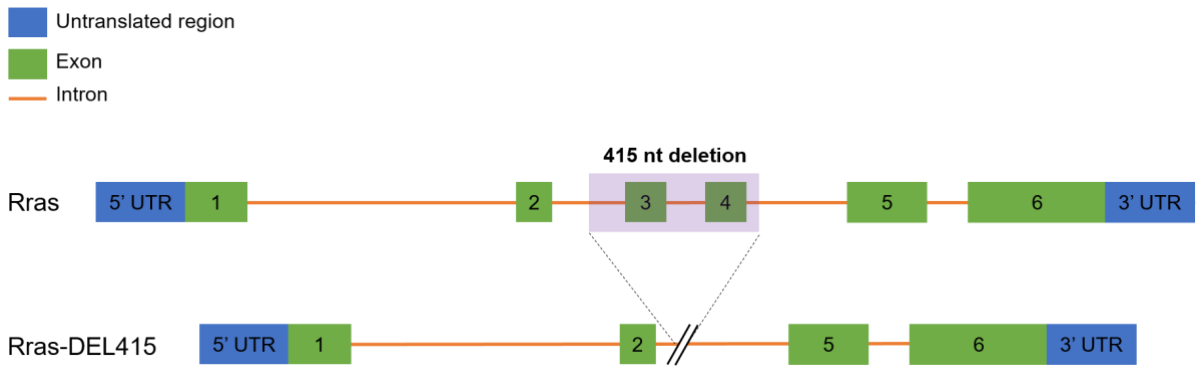

Figure 1.13. Generation of the *Rras* KO allele, Rras-DEL415.

Previous *in vivo* exploration of R-Ras function has predominantly been in the R-Ras KO mouse model generated by Komatsu and colleagues [208]. This model utilised a gene-trap vector inserted between exons 4 and 5 to inactivate the *Rras* gene, using the C57BL6/129Sv strain.

Studies in this mouse model have demonstrated R-Ras to play major roles in angiogenesis and maturation of blood vessels [297,320,321], smooth muscle restenosis [297], and tumour formation [322]. The same group later used a Cre/LoxP mouse for a pericyte-conditional *Rras* KO, highlighting a role of R-Ras in development of the retinal vasculature [269]. This study is the first to use the Rras-DEL415 global knockout mouse model, generally referred to as R-Ras KO in this thesis. Since its generation, IMPC has reported significant phenotypes of the Rras-DEL415 mouse, including decreased circulating calcium levels, and increased serum albumin and triglyceride levels. However, the BP phenotype of these mice has not been measured. Interestingly, the Mouse Genome Informatics (MGI) resource (MGI:5438689, [429]) reported decreased B cell number, and increased CD4+ and CD8+ T cell numbers phenotypes in the Komatsu *et al.,* model; these phenotypes have not been reported by the IMPC for Rras-DEL415 [338], however, it appears lymphocyte levels have not been investigated and therefore a similar phenotype may be present.

Although the rs61760904 *RRAS* variant is predicted to encode for a D133N mutation, a R-Ras KO mouse model was used in this thesis to identify the essential roles of R-Ras in BP control. Pilot experiments assessing the BP phenotype in R-Ras KO mice using radiotelemetry found an elevated SBP and MAP phenotype in R-Ras KO mice (Figure 1.14). In support of the genetic data, these findings formed the motivation behind this PhD study investigating the potential role of R-Ras in BP control and hypertension.

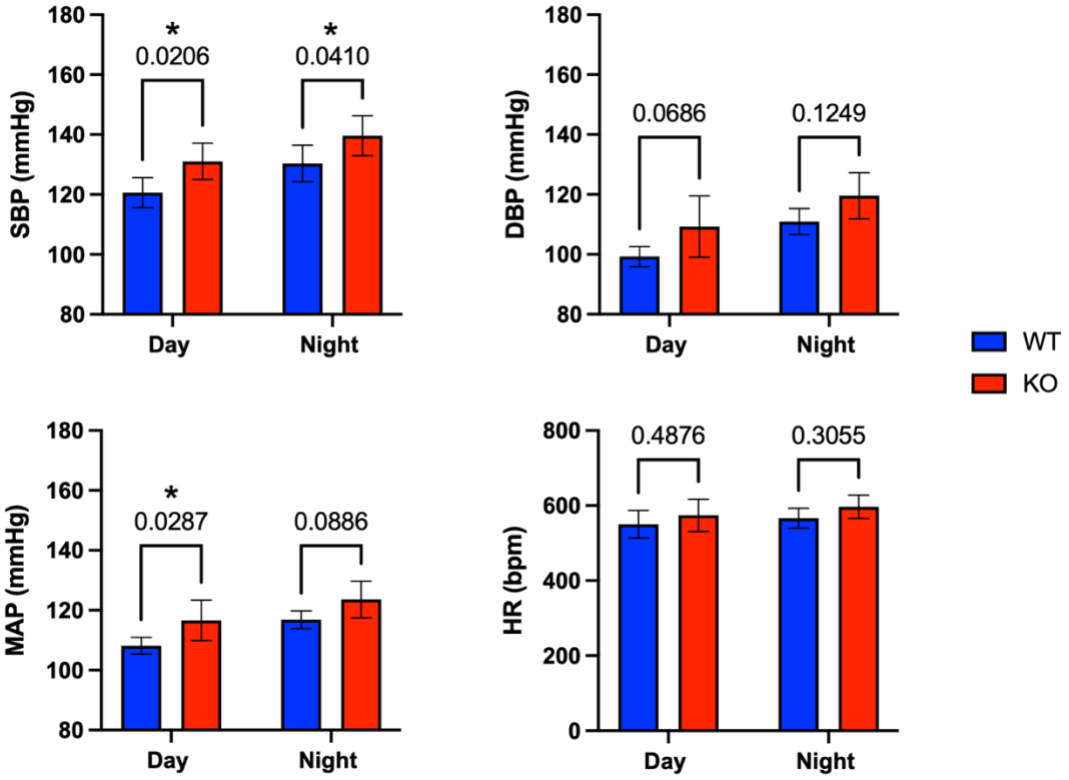

Figure 1.14. Pilot radiotelemetry data demonstrates an elevated BP phenotype in R-Ras KO mice aged 12 months. WT and R-Ras KO mice were implanted with radiotelemetry probes and their BP and HR measured for 2 days diurnally. WT *n* = 5, KO *n* = 6. Data is analysed using a two-way ANOVA with Sidak's multiple comparisons test. P values are displayed as numerical values, and asterisks indicate significance ($p < 0.05$).

1.5. Hypothesis and aims

R-Ras is known to activate PI3k/Akt signalling and is highly expressed in endothelial cells in the vasculature. Furthermore, R-Ras signalling is implicated in physiological mechanisms related to BP control, namely angiogenesis [37, 47-50, 101], vascular permeability [47-51, 101] and VSM hyperplasia [37, 47]. Therefore, I hypothesised that R-Ras would regulate vascular tone via activation of the PI3K/Akt signalling axis in endothelial cells to promote formation of the vasodilatory molecule, NO (Figure 1.15).

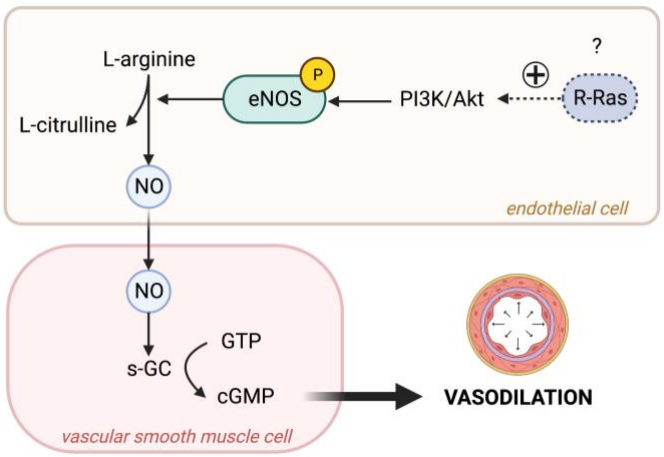

Figure 1.15. Proposed R-Ras signalling in the vasculature to regulate vasodilation via nitric oxide production.

The hypothesis therefore stated:

“The small G-protein R-Ras interacts with signalling pathways in vascular endothelial and smooth muscle cells to promote blood vessel dilation, and the exonic variant modifies R-Ras function leading to increases in blood pressure”.

The specific aims of this PhD were to:

1. Predict the impact of the SBP-associated exonic variant rs61760904 on R-Ras protein expression and function,
2. Explore the influence of R-Ras on BP phenotype and organ systems *in vivo* with a knock-out mouse model,
3. Investigate R-Ras signalling in the vasculature, and
4. Translate findings from the Rras-DEL415 mouse model to humans via genetic analyses of the exonic variant using UK Biobank genetic data.

Chapter 2. Materials and Methods

2.1. Computational and genetic statistical methods

2.1.1. Protein structure analysis

R-Ras full length protein structure prediction was performed using the RoseTTAFold method via the Robetta server (https://robetta.bakerlab.org/). RoseTTAFold uses a “three-track” neural network, which considers patterns in protein sequence, amino acid interactions, and potential 3D structure of proteins [282]. PyMol 2.5 (The PyMOL Molecular Graphics System, Version 2.5, Schrödinger, LLC) was used to compare the 3D models of R-Ras and mutant R-Ras. Root-mean-square deviation (RMSD) of atomic positions was calculated using PyMOL with the code “cealign PDB1, PDB2 etc.” to assess alignment. An RMSD value of 0 Å equates to a perfect alignment.

2.1.2. Variant damage prediction

The impact of the rs61760904 variant D133N (the BP variant), and two additional variants D133P (an R-Ras variant that disrupts secondary structure) and D133K (an R-Ras variant with an opposite charge), on R-Ras protein function were predicted using bioinformatic tools listed in Table 2.1.

Table 2.1. Variant damage prediction tools used to predict the impact of D133N, D133K and D133P amino acid substitutions on R-Ras function.

Prediction tool	Input	Prediction method	URL
ConSurf	FASTA	Sequence	https://consurf.tau.ac.il/
Missense3D-DB	UniProt ID	Structural	http://missense3d.bc.ic.ac.uk/missense3d/
PolyPhen-2	FASTA	Combined	http://genetics.bwh.harvard.edu/pph2/
PROVEAN	FASTA	Sequence	http://provean.jcvi.org
MUPro	FASTA	Structural	http://mupro.proteomics.ics.uci.edu/
MutPred2	FASTA	Combined	http://mutpred.mutdb.org/
SNAP2	FASTA	Combined	https://rostlab.org/services/snap/
SIFT	FASTA	Sequence	https://sift.bii.a-star.edu.sg/www/SIFT_seq_submit2.html

Prediction methods are classified as using sequence, structural or combined sequence and structural analysis.

sp|P10301|RRAS_HUMAN Ras-related protein R-Ras OS=Homo sapiens OX=9606 GN=RRAS PE=1 SV=1

MSSGAASGTGRGRPRGGGPGPGDPPPSETHKLVVVGGGGVGKSALTIQFIQSYFVSDYD
PTIEDSYTKICSVDGIPARLDILDTAGQEEFGAMREQYMRAGHGFLLVFAINDRQSFNEVGK
LFTQILRVKDRDDFPVVLVGNKADLESQRQVPRSEASAFGASHHVAYFEASAKLRLNVDEA
FEQLVRAVRKYQEQELPPSPPSAPRKKGGGCPCVLL

Figure 2.1. FASTA format of the human R-Ras protein. (NCBI Reference Sequence: NC_000019.10, Bethesda (MD): National Library of Medicine (US), National Center for Biotechnology Information; [1988] – [cited 2022 Jul 06]. Available from: https://www.ncbi.nlm.nih.gov/).

2.1.2.1. ConSurf

The ConSurf server analyses the evolutionary conservation of amino acids in a protein based on phylogeneity between homologous sequences. ConSurf extracts homologous sequences from the protein databases and performs multiple sequence alignment to construct a phylogenetic tree. Conservation scores are calculated using empirical Bayesian algorithms and provided as a percentage. The amino acid sequence was inputted, and homologous sequences were extracted from the PSI-BLAST database. The R-Ras FASTA sequence (Figure 2.1) was inputted into the ConSurf server (https://consurf.tau.ac.il/overview.php, [Accessed 25 May 2022]).

2.1.2.2. SNAP2

SNAP2 is a trained classifier that uses neural network machine learning to determine whether a non-synonymous SNV has an effect or is neutral [283]. SNAP2 produces a score of -100 to +100 (neutral to strong effect) which is (in part) correlated to the severity of the effect. The R-Ras FASTA sequence (Figure 2.1) including the amino acid substitution was inputted into SNAP2 (https://www.rostlab.org/services/snap/ [Accessed 25 May 2022]), with a separate query for each mutant (D133N, D133P, D133K).

2.1.2.3. SIFT

The Sorting Intolerant from Tolerant (SIFT) algorithm uses sequence homology of the input sequence to compute the probability that the amino acid substitution will adversely impact protein function by assuming substitutions in evolutionary conserved regions are more likely to impact function [284,285]. A SIFT score ranging from 0 to 1 is calculated, which is the normalised probability of observing the new amino acid at that position. It outputs whether a substitution is deleterious or tolerated; normalised probabilities less than the threshold are predicted deleterious and those greater or equal to are tolerant. The R-Ras FASTA sequence was the protein query sequence and was inputted into SIFT Sequence (https://sift.bii.a-star.edu.sg/www/SIFT_seq_submit2.html [Accessed 25 May 2022]) with the substitutions of interest D133N, D133P, and D133K. The database used to search was UniProt-SwissProt 2010_09. The median conservation of sequences was set at 3.00 and sequences with more than 90% homology with the query sequence were removed to avoid including SNVs in the database.

2.1.2.4. PROVEAN

Protein Variation Effect Analyzer (PROVEAN) Protein v1.1 [286] predicts the impact of variants of protein function by calculating the delta alignment score of the query and variant sequence. A threshold of -2.5 for the PROVEAN score was determined based on the maximum separation of deleterious and neutral variants for single amino acid substitutions, deletions, insertions and replacements [286]. The R-Ras FASTA query sequence (Figure 2.1) was inputted into PROVEAN Protein (http://provean.jcvi.org [Accessed 25 May 2022). Variants were inputted using Human Genome Variation Society notation (D133N, D133P, D133K). The calculated PROVEAN score was provided, and each variant predicted "deleterious" or "neutral". An amino acid substitution is predicted damaging if the PROVEAN score is below -2.5.

2.1.2.5. PolyPhen-2

Polymorphism Phenotyping v2 (PolyPhen-2) predicts the functional impact of a nonsynonymous SNV on a protein by using machine-learning trained models to predict changes in sequence-based (e.g. disulphide bonds, binding sites) and structural based features (e.g. electrostatic interactions, ligand interactions) [287]. The R-Ras FASTA sequence (Figure 2.1) was inputted into PolyPhen-2 v2.2.3 (http://genetics.bwh.harvard.edu/pph2/, [Accessed 25 May 2022]) using a HumDiv-trained model, and the variant position and substitution selected. An individual query was submitted for each variant (D133N, D133P, D133K). Data is a false positive rate (FPR); mutations are classified based on a 5% / 10% FPR threshold. A variant is "probably damaging" if the FPR is ≤ 5%, "possibly damaging" if ≤ 10%, and "benign" if above 10%.

2.1.2.6. MutPred2

MutPred2 [288] uses machine learning to quantify the pathogenicity of the amino acid substitution but also provides more detailed information on how the structure and function is changed and the key sites or amino acid residues affected. It provides 2 outputs: the predicted pathogenicity (general score), and a list of potential functional and structural alterations resulting from the variant (property score). MutPred2 predicts a general score and a property score, both ranging between 0 to 1. A general score closer to 1 is more pathogenic. A property score is given to each functional or structural property, with a score closer to 1 denoting that

the pathogenesis of the disease involves a change in the property of the protein [288]. The R-Ras FASTA sequence was inputed into MutPred2.0 web server (http://mutpred.mutdb.org/ [Accessed 25 May 2022], followed by the list of amino acid substitutions (D133N, D133K, D133P). A p value threshold of 0.05 was set and the substitution predicted pathogenic if the general score was above 0.5.

2.1.2.7. MUpro

MUpro: Prediction of Protein Stability Changes for Single Site Mutations from Sequences [289] directly imputes the sequence into a Support Vector Machine and provides an output of the relative stability change (ΔΔG). This is predicted based on structure and sequence. ΔΔG output provides a magnitude and a sign, the sign being more important as it is indicative of the direction of the effect of the amino acid substitution. If ΔΔG is negative it increases stability, if positive it is destabilising. The R-Ras FASTA sequence (Figure 2.1) was inputted into MUpro web server (http://mupro.proteomics.ics.uci.edu/ [Accessed 25 May 2022]) and the amino acid substitutions specified. A separate query was run for each mutant.

2.1.2.8. Missense3D-DB

Missense3D-DB predicts the structural impact of an amino acid substitution based on pre-computed atom-based calculations [290]. Missense3D-DB output is “damaging” or “neutral” based on 16 structural features: breakage of a disulphide bond, hydrogen bond or salt bridge, introduction of a proline or a hydrophilic residue or a charge in buried amino acid, steric clash, charge switch or loss of charge in a buried residue, introduction of a residue with disallowed phi/psi angles, and change in secondary structure. The UniProt ID for R-Ras (A0A024QZF2_HUMAN, Uniprot, 2021) was inputed into Missense3D-DB (http://missense3d.bc.ic.ac.uk/missense3d/, [Accessed 25 May 2022]) and the variants inputed (D133N, D133K, D133P). The results were provided as the Missense3D prediction i.e. Damaging or Neutral, and the structural feature predicted.

2.1.3. RRAS variant association analysis in UK Biobank

Association analyses of the rs61760904 SNV with SBP were carried out in the UKB cohort by Dr. Helen Warren (WHRI, QMUL) (Figure 2.2). The UKB includes genetic data from ~500,000

individuals aged 40 – 69 years (y) recruited between 2006 – 2020 [291]. At assessment, all individuals provided electronic signed consent, completed a standardised questionnaire and interview focused on health, lifestyle and family history, and blood, urine and saliva samples were collected. Phenotypic tests were performed, including two automated measurements of BP taken seated after two minutes rest, one measurement apart, using an appropriate cuff and an Omron HEM-7015ITdigital BP monitor. Individuals undergo longitudinal follow-up over their life course through linkage to routinely available national datasets. Genotyping was performed using two arrays –the Affymetrix UK BiLEVE Axiom Array for ~50,000 individuals from the UK BiLEVE study [292], and the UKB Axion Array for ~450,000 individuals, together including ~850,000 variants directly measured and >90 million variants inputed using the Haplotype Reference Consortium and UK10K + 1000 Genomes reference panels [293].

Briefly, further quality control (QC) of the genetic data, including clustering all individuals by ancestry was performed and only individuals of European ancestry were included in this analysis for homogeneity. For the simple linear regression analyses, 1st and 2nd degree relatives were removed, leaving a total of n = 423,655 individuals for analysis. Mean SBP values were calculated from two measurements available and adjusted for BP-lowering medication use by adding 15 mmHg. For age-stratified analyses, individuals were grouped into two subgroups: 'younger' (< 50 y) vs 'older' (≥ 50 y).

The rs61760904 SNV encodes a T>C nucleotide substitution, where T is the minor allele. The SNV was directly genotyped and extracted from UKB genetic data using PLINK software (http://pngu.mgh.harvard.edu/purcell/plink/ [294]). For the association analyses, genotype groups were as follows: CC, homozygotes with no minor alleles; CT, heterozygotes with 1 minor allele; TT, homozygotes with 2 minor alleles.

Simple linear regression association testing was performed using two different genetic models in R statistical software (Version 4.2.1; R Foundation for Statistical Computing, Austria). For analysis of all individuals a per-allelic association model was used. The per-allelic model treated the CC, CT, TT genotype groups as a continuous variable according to the SNV risk allele score 0, 1, 2, respectively CC vs. CT vs. TT. Analyses were adjusted for covariates: sex, age, age^2, BMI, genotyping chip, and top 10 principal components for ancestry. For subsequent age-stratified analyses, a genotype model was used. The genotype model compared each risk allele carrier genotype groups CT and TT vs. the non-carrier homozygous group CC as a reference. An age-interaction analysis was also performed, including an interaction term SNV*age-subgroup, to test for statistically significant differences in the effect of the SNV in younger vs. older individuals (Figure 2.2).

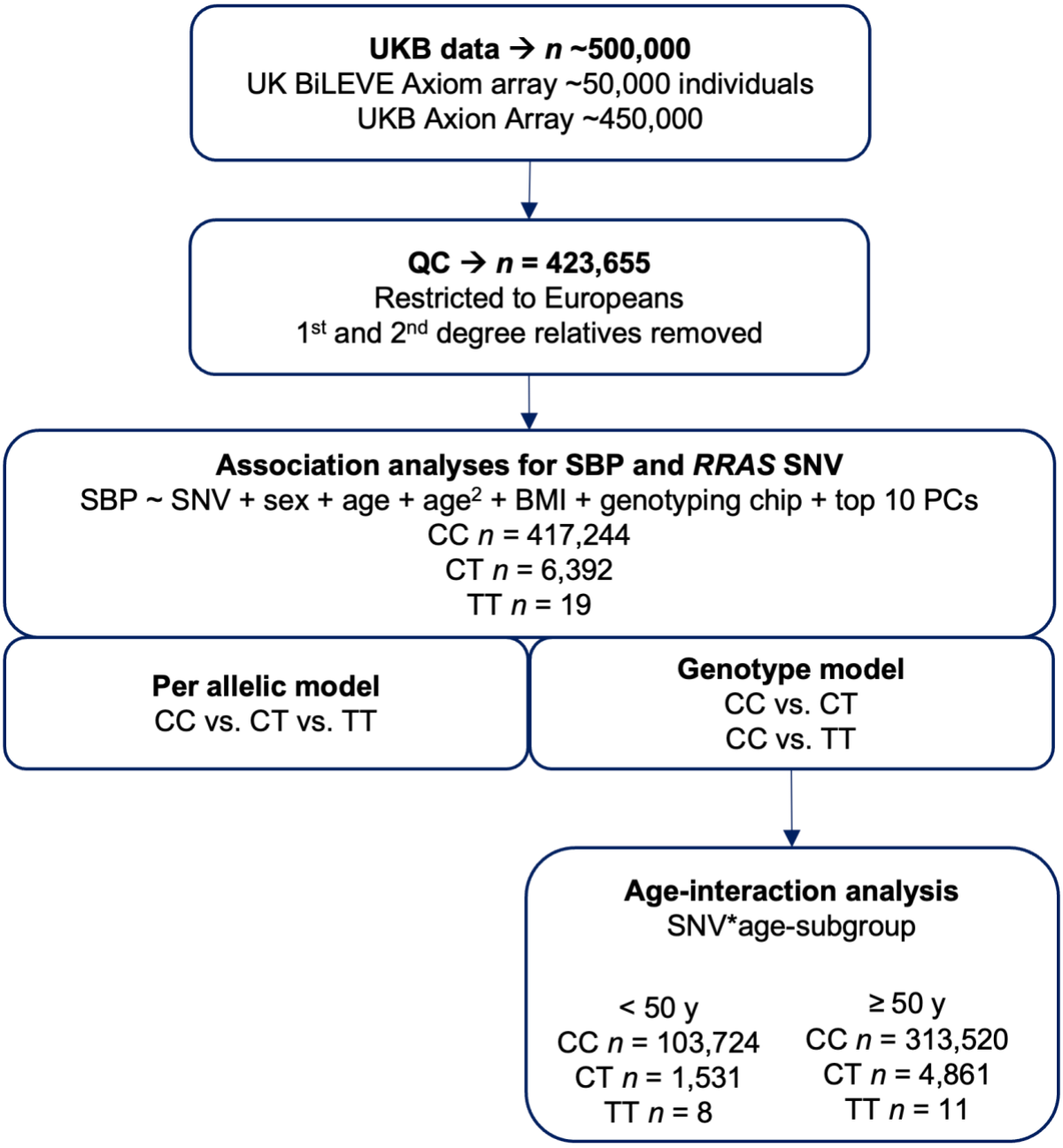

Figure 2.2. Study design schematic for *RRAS* variant association analysis.

2.2. Laboratory materials

2.2.1. Compounds

Compounds (Table 2.2) were dissolved in Milli-Q water (mQH_2O), dimethyl sulfoxide (DMSO) (Sigma-Aldrich, UK), Phosphate Buffered Saline (PBS) (Sigma-Aldrich, UK), 100% ethanol (Thermo Fisher Scientific, US) or Nuclease-Free Water (QIAGEN, Germany). The remaining compounds, once in solution, were stored at -20°C for up to 6 months. Sodium dodecyl sulfate (SDS) was purchased from Riedel-de Haen (Germany).

Table 2.2. List of compounds, preparation, mechanism, and supplier.

Compound	Dissolvent	Mechanism of action	Supplier
9,11-dideoxy-9α,11α-methanoepoxy-prosta-5Z,13E-dien-1-oic acid (U46619)	100% ethanol	Thromboxane A2 receptor agonist	Cayman Chemical, USA
Acetylcholine chloride (ACh)	mQH_2O	Muscarinic acetylcholine receptor agonist	Sigma-Aldrich, UK
Angiotensin II acetate salt (ANGII)	PBS	Angiotensin receptor AT_1 and AT_2 agonist	Bachem, Switzerland
Recombinant Murine $VEGF_{165}$	Nuclease-Free Water	Vascular endothelial growth factor (VEGF) receptor agonist	PeproTech, USA

2.3. Cell lines, culture, and passage

Two cell lines were used for the cellular experiments: primary HUVECs and immortalised CHO-K1 cells. Cells were grown in a humidified atmosphere of 95% air and 5% CO_2 at a temperature of 37°C and procedures carried out in sterile conditions in a Class II laminar flow biological safety cabinet.

Primary HUVECs were provided by Dr Fu Liang Ng (Clinical Pharmacology, WHRI, QMUL). The HUVEC cells were derived from human umbilical veins following a protocol adapted from

Jaffe *et al.,* 1973 [295]. Briefly, the umbilical vein was cannulated and washed with Hanks' Balanced Salt Solution (HBSS) prior to injection of 0.2% type I collagenase to distend the vein. The cord was subsequently clamped upon vein distention and incubated in collagenase for 10 min at 37°C with gentle massaging. The cord was unclamped and the vein flushed, and the fluid collected and centrifuged at 1000 x g for 10 min to isolate HUVECs.

HUVECs were grown in Endothelial Cell Growth Medium (EGM) (Promocell, Germany) supplemented with 0.4% Endothelial Cell Growth Supplement, 0.1 ng/mL Epidermal Growth Factor, 1 ng/mL Basic Fibroblast Growth Factor, 0.09% Heparin, 0.0001% Hydrocortisone (Promocell, Germany) and 2% penicillin-streptomycin (Thermo Fisher Scientific, US), in 0.2% gelatin-coated flasks, and media replaced every 2 days. CHO-K1 cells (ATCC CCL-61^{TM}) were maintained in Ham's F-12 Nutrient Mixture (Sigma, UK) supplemented with 10% foetal bovine serum (FBS) (Thermo Fisher Scientific, US) and 2% penicillin-streptomycin. Cell growth and morphology was monitored using light microscopy.

HUVECs and CHO-K1 cells were passaged upon reaching a confluency of 80 – 100%. Media was removed and cells washed with 3 mL PBS (Sigma-Aldrich, UK). For cell detachment, cells were incubated in 3 mL 10% Trypsin-PBS (Thermo Fisher Scientific, US) if in T75 flasks, and 1 mL 10% Trypsin-PBS if in T25 flasks, at 37°C for at least 3 min. After detachment of at least 90% of total cells, trypsin was neutralised with equal volumes of appropriate cell media and the cells transferred to a 15 mL falcon tube. Cells were then centrifuged for 4 min x 90 g and cell supernatant removed. The remaining cell pellet was resuspended in appropriate media and split into T75 flasks at 25% confluency (Sarstedt, Germany) for passage, or T25 flasks or 6 well plates (Sarstedt, Germany) at 70% confluency in preparation for transfection or drug treatment.

2.4. cDNA constructs

The WT *RRAS* construct was developed by Nicola Burgess, and purchased from Addgene (US) (Addgene plasmid # 38815; http://n2t.net/addgene:38815; RRID:Addgene_38815). WT R-Ras and R-Ras mutant constructs, R-Ras D133N, R-Ras D133P and R-Ras D133K, were generated by Dr Kate Witkowska (Clinical Pharmacology, WHRI). The R-Ras38V construct was developed by Adrienne Cox, and also purchased from Addgene (US) (R-Ras38V: Addgene plasmid #14728; http://n2t.net/addgene:14728; RRID:Addgene_14728).

2.5. Plasmid DNA replication

Bacterial transformation was used to clone and maintain plasmid DNA stocks. DNA is introduced into bacterial cells possessing the ability to uptake exogenous material, termed competent cells. Bacterial cells produce multiple copies of plasmid DNA which can be extracted to make up a stock of DNA ready for use in transfection procedures.

2.5.1. Bacterial transformation

One tablet of Luria-Bertani (LB) broth (10 g/L Tryptone, 5 g/L Yeast Extract, 5 g/L NaCl, 2.2 g/L inert binding agents, Sigma-Aldrich, UK) was added to 50 mL of mQH_2O and autoclaved. To prepare agar plates, one tablet of LB broth with agar (Sigma-Aldrich, UK) was added per 50 mL mQH_2O, autoclaved, and mixed with the antibiotic carbenicillin at 100 ng/mL. Once cooled, the LB-agar mixture was poured into sterile petri dishes and stored at 4°C. For bacterial transformation, competent cells (NEB® 5-alpha Competent *E. coli* High Efficiency; New England Biolabs, US) were thawed on ice. 100 ng of DNA was mixed with 50 µL of competent cells and incubated on ice for 30 min, prior to heat-shock at 42°C for 30 s and a further 5 min incubation on ice. Cells were transferred to 950 µL of LB broth and transferred to a shaker heated at 37°C for 60 min, vigorously shaking at 250 rpm. Cells were thoroughly mixed and spread on a pre-warmed agar plate and incubated overnight in a dry incubator at 37°C.

2.5.2. Bacterial growth

The following day, a single bacterial colony was gathered using a sterile pipette and added to 2 mL LB broth with 100 ng/mL carbenicillin in a falcon tube. The bacterial culture was incubated at 37°C shaking at 250 rpm for 12 h. The culture was then either mixed with 50% glycerol-mQH_2O to create a glycerol stock and stored at -80°C, or the plasmid DNA was isolated for short-term storage, as described below.

2.5.3. Plasmid DNA isolation

Plasmid DNA isolation was carried out using the QIAGEN Plasmid Midi Kit (QIAGEN, Germany), according to the manufacturer's instructions. The overnight bacterial culture was centrifuged at 3000 *g* for 15 min at 4°C, and the resultant pellet resuspended in 4 mL of

resuspension buffer supplemented with RNase A. Following resuspension, lysis buffer was added and the solution inverted 6 times prior to 5 min incubation at room temperature. Lysis was halted with chilled neutralization buffer and the solution mixed vigorously prior to a further 5 min incubation at room temperature. The resultant precipitant, composed of genomic DNA, proteins, and cell debris, was filtered from the solution using 150 mm Whatman filter paper, and the clear solution containing plasmid DNA collected. The solution was passed through a calibrated QIAGEN-tip and washed 2 times with wash buffer before elution of DNA with elution buffer. DNA was precipitated with 3.5 mL isopropanol at room temperature and the resultant solution was centrifuged at 3000 *g* for 90 min at 4°C. The supernatant was discarded and the DNA pellet washed with 1 mL of 70% ethanol prior to centrifugation at 20,000 *g* for 10 min. The supernatant was discarded and the ethanol wash repeated. Again, the supernatant was discarded and the pellet air-dried for 10 min. Finally, the DNA pellet was dissolved in 1 mL nuclease-free water and the DNA concentration was measured using a NanoDrop 2000 Spectrophotometer (Thermo Fisher Scientific, US), according to the manufacturer's protocol. Plasmid DNA was sequenced by the Genome Centre, and sequence alignment carried out using the BLAST programme (National Centre for Biotechnology Information, US) to confirm DNA identity.

2.6. Cell transfection

2.6.1. Lipofectamine

Transfections were performed in CHO-K1 cells using Lipofectamine 2000 reagent (Thermo Fisher Scientific, US) with R-Ras variants D133N, D133P, and D133K, to study the impact of *RRAS* gene mutation on protein expression in a cell system. The day before transfection, CHO-K1 cells were seeded into a 6 well plate at a density of 1 – 2 x 10^6 cells per well and grown overnight to a reach a confluency of 80%. Media was aspirated and cells were washed with PBS prior to addition of 2 mL reduced-serum medium Opti-MEM (ThermoFisher, US). DNA and Lipofectamine reagent were diluted separately in 150 µL Opti-MEM before transfer of the Lipofectamine solution to the DNA. The mixture was incubated for 5 min at room temperature to allow DNA-lipid complexes to form, and subsequently added dropwise to cells, reaching a final amount of 500 ng of DNA and 9 µL of Lipofectamine reagent per well. Opti-MEM was changed for fresh Ham's F12 Nutrient Mixture supplemented with 10% FBS and 2% penicillin-streptomycin after a 5 h incubation. Cells were lysed 48 h post transfection in preparation for analysis of protein levels with Western blotting.

2.6.2. Nucleofection

HUVECs, primary cell lines, were transfected with the constitutively active form of R-Ras, R-Ras38V. HUVECs of passage numbers 2 to 9 were split and grown in 75 cm^2 flasks for 2 days prior to Nucleofection and were ready for Nucleofection at a cell confluency of 80%. The P5 Primary Cell 4D-Nucleofector X Kit (Lonza, Switzerland) was used, and Nucleofection carried out according to the optimised Amaxa 4D-Nucleofector Protocol for HUVEC Transfection in Suspension (Lonza, Switzerland). Mastermixes of 100 µL Nucleofector Solution with a final volume of 2 µg GFP and 2 µg of R-Ras38V was prepared at room temperature. Cells were detached with 10% trypsin-PBS, as described in section 2.3. Cells were resuspended in trypan blue and cell number determined using a haemocytometer under an optical microscope. The appropriate volume of cell suspension to achieve a final cell number of 5 x 10^4 to 1 x10^6 cells per transfection condition was centrifuged for 10 min x 90 g. The supernatant was aspirated, and the remaining cell pellet resuspended in the appropriate mastermix before transfer into a 100 µL Nucleocuvette (Lonza, Switzerland). Nucleocuvettes were immediately placed into the 4D-Nucleofector™ X Unit (Lonza, Switzerland) and the CA-167 programme initiated. After run completion, cells were transferred into 35 mm dishes with 14 mm glass diameter coverslips (MatTek, US) containing 2 mL pre-warmed media for imaging, or 25 cm^2 flasks containing 3 mL pre-warmed media for Griess and Western blot analysis, and grown for 2 days prior to analysis.

2.7. Immunofluorescence microscopy

HUVECs were co-transfected with 2 µg GFP and R-Ras38V, as described in Chapter 2.6.2, to allow validation of transfection efficiency with epifluorescence imaging. Immediately after Nucleofection, HUVECs were seeded into 35 mm glass bottom microwell dishes with a 14 mm glass diameter pre-coated with 0.2% gelatin. 48 h post transfection, cells were washed with PBS and 2 mL colourless media was added (Opti-MEM, Thermo Fisher Scientific, US) for immunofluorescent and confocal imaging. Cells were imaged with a Nikon Eclipse TE200 Inverted microscope (Nikon, Japan) with a 20x microscopic lens. Cells were excited with a 488 nm wavelength laser to detect GFP fluorescence. Confocal imaging was performed on the same cells to allow estimation of transfection efficiency. Images were processed with Fiji (ImageJ).

2.8. Cell Lysis

Cell lysis was performed 2 days post transfection, in preparation of protein lysates for analysis with Western blotting. Media was aspirated and cells washed with ice cold PBS before addition of lysis buffer (50 mM Tris-HCl pH 6.8 (BioRad, UK), 10% glycerol (VWR International, US), 2% SDS (Riedel-de Haen, Germany) and mQH_2O) supplemented with Halt Protease Inhibitor Cocktail (ThermoFisher Scientific, US) at a 1:1,000 dilution. 100 µL of lysis buffer was required for each well in a 6 well plate, 300 µL for 25 cm^2 flasks and 850 µL for 75 cm^2 flasks. Cells were incubated on ice for 2 min and a cell scraper used to gather the cell lysate before transfer to Eppendorf tubes. The cell lysate was homogenised, before heating at 95°C for 3 min and subsequent centrifugation at 20,000 *g* for 10 min at 4°C. The supernatant containing the protein lysate was collected and the remaining cell pellet discarded. Protein concentration was analysed using a NanoDrop 2000 Spectrophotometer (Thermo Fisher Scientific, US), according to the manufacturer's protocol.

2.9. Western blotting

2.9.1. Sample preparation

HUVEC and CHO cell lysates were prepared at a 1:4 ratio with 6 x loading buffer (4% SDS, 20% glycerol, 0.004% bromophenol blue) (Sigma-Aldrich, UK) and 100 mM β-mercaptoethanol (Sigma-Aldrich, UK) and diluted in SDS lysis buffer to reach a final protein volume of 20 – 30 µg per well. Protein samples were heated at 95°C for 5 min prior to centrifugation at 20,000 *g* for 3 min at room temperature. Polyacrylamide gels were cast on the day of the experiment, and composed of mQH_2O, 30% Acrylamide/Bis (BioRad, UK), 1.5 M Tris-HCl (pH 6.8 for stacking gel, pH 8.8 for resolving gel), 10% SDS, 10% Ammonium Persulfate (APS) (Sigma-Aldrich, UK) and *N,N,N',N'*-Tetramethylethylenediamine (TEMED) (Sigma-Aldrich, UK). A resolving gel was made at a gel percentage of 8 – 12%, depending on the protein of interest, and stacking gel was made at a gel percentage of 4%. The PageRuler Plus Prestained Protein Ladder (Thermo Fisher Scientific, US) was used as an indicator of molecular weight (in kilodaltons (kDa)). 10 µL of protein ladder was loaded into the first lane, and 20 – 30 µg of protein sample into the subsequent wells.

2.9.2. Gel electrophoresis and sample transfer to membrane

Loaded gels were placed into tanks containing running buffer (25 mM Tris-Base, 190 mM glycine and 0.1% SDS) and run at 100 mV for 20 min until samples reached the resolving gel, before running at 120 mV until completion. PVDF membranes (Amersham Hybond Western blotting membranes, GE Healthcare, US) were cut to the gel size and pre-soaked in 100% methanol. Gels were extracted from the cast and placed on the PVDF membranes. For membrane transfer, the gel and membrane were sandwiched in between four sheets of 0.03 cm thick blotting paper (Amersam Hybond blotting paper, GE Healthcare, US) and sponges, and placed in a transfer tank filled with transfer buffer (25 mM Tris base, 190 mM glycine, 20% methanol), and a 75 mV was applied for 90 min.

2.9.3. Protein detection

Membranes were removed from transfer apparatus and blocked in 10 mL 5% non-fat milk for detection of non-phosphorylated proteins, or 5% Bovine Albumin Serum (BSA) (Sigma-Aldrich, UK) for detection of phosphorylated proteins, in TBS-T (20 mM Tris-HCl pH 7.5, 150 mM NaCl, 0.1% Tween 20 (Sigma-Aldrich, UK). After blocking, membranes were incubated with a primary antibody (see Table 2.3) overnight at 4°C. Membranes were subsequently washed with T-BST 3 times for 15 min, and incubated with the appropriate HRP-conjugated secondary antibody (Amersham ECL Anti-Mouse IgG HRP-Linked Whole Antibody (from Sheep) or Amersham ECL Anti-Rabbit IgG HRP-Linked Whole Antibody (from Goat) (GE Healthcare, US) at a 1:5,000 dilution for 1 h at room temperature. The membrane was washed again and incubated with Luminata Classico Western HRP Substrate (Sigma-Aldrich, UK) for 2 min, before protein band visualisation with the chemiluminscent imaging system GeneGnome XRG and GeneSys software (Syngene, India). For reprobing, the membrane was stripped with stripping buffer (2% SDS, 0.05 M Tris-HCl 6.8, 1% β-mercaptoethanol) for 7 min prior to washing for 15 min 3 times. The membrane was then ready to be blocked and re-probed for detection of an alternative protein. The blot was stripped and re-probed a maximum of 3 times. Signal intensity of protein bands was analysed with ImageJ software (NIH, US) and normalized to the loading control signal (GAPDH) using the following equations:

$$lane\ normalization\ factor = \frac{observed\ signal\ of\ housekeeping\ protein\ for\ each\ lane}{highest\ observed\ signal\ of\ houskeeping\ protein\ on\ the\ blot}$$

$$normalized\ experimental\ signal = \frac{observed\ experimental\ signal}{lane\ normalization\ factor}$$

Table 2.3. Primary antibodies used in Western blotting assays.

Primary Antibody	Origin	Clonality	Dilution	Supplier	Cat no.
Anti- RRAS	Rabbit	Polyclonal	1:1000	CST, UK	#8446
Anti-NOS3	Mouse	Monoclonal	1:1000	Santa Cruz, USA	sc-376751
Anti-Phospho-eNOS (Ser1177)	Rabbit	Polyclonal	1:1000	BD Biosciences, USA	612393
Anti-GAPDH	Mouse	Monoclonal	1:2000	Santa Cruz, USA	sc-32233

2.10. Animals

Global R-Ras knockout (KO) mice (Rras-DEL415-EM1-B6N) were generated using CRISPR-Cas9 technology by MRC Harwell (UK) in conjunction with the International Mouse Phenotyping Consortium (IMPC). These mice have a C57BL/6N genetic background. Inactivation of *Rras* in these mice is caused by deletion of 415 nucleotide bases, including exon 3 and exon 4, to create a KO allele (Rras-DEL415) (Figure 2.3). All experiments were conducted in accordance with the Guide for the Care and Use of Laboratory Animals published by the British Home Office regulations and by the National Institutes of Health (NIH), under the Project Licence PPL PE9055EAD.

WT *Rras* allele
5′-TGTCTGACTATGATCCCACCATTGAAGATTCCTACACAAAGATCTGCACTGTGGACG GCATCCCTGCACGGCTGGACAGTGAGGATGGGATGGCTGGGCTTGGAAGGGAGGCA GGGGGCAAGACTCAGAGGATTTGTGAACATGCCCAGGACAACCTGGGGGGACCCACA CGTTTCTCTCTCTGTCTCCACAGTCCTGGACACTGCGGGGCAAGAGGAATTTGGTGCC ATGCGGGAGCAGTACATGCGTGCTGGCAACGGCTTCCTGCTGGTGTTTGCCATTAAC GACAGGCAGAGGTGAGGGGGATGCTGGTGGGCCTGGCTGAGCACGGGGCAGGTTCC TGCTAAGGTGGTGCCTCATGCTACTGACTTCTCTTGCAGTTTCAATGAGGTGGGCAAG CTCTTCACACAGATCCTCAGAGTCAAGGACCGGGATGATTTCCCCATTGTGTTGGTTG GGAACAAGGCAGATCTGGAGAACCAGCGCCAGGTTTGAGATGCCCCCTCCCCTGGTC

ACCCCCATTTGGACCTAGGAAGCTCTCTCAGGTGACCATCTCCTACTCTGGATCCCTG GTCCCTCTATTGTCACAACTTTCACTTAAGAGATGACCCCCCAAGAGGAATCGCCCATC ACTGAGCCACACCCCTGGCCATCACTGAGGGATTCTAACCAGGACCCCTAGCACTGA GCCACGGTCCTGGCCCTTATACTAATCCGTTGATACTGGTTCCCCTGTCCTGAA-3′

KO *Rras* allele: 415 nt deletion (Rras-DEL415-EM1-B6N)
5′-TGTCTGACTATGATCCCACCATTGAAGATTCCTACACAAAGATCTGCACTGTGGACG GCATCCCTGCACGGCTGGACAGTGAGGATGGGATGGCTGGGCTTGGAAGGGAGGCA GGGGGCAAGACTCAGAGGATTTGTGAACATG**[415 nt deletion]**CTCTGGATCCCTGGT CCCTCTATTGTCACAACTTTCACTTAAGAGATGACCCCCCAAGAGGAATCGCCCATCAC TGAGCCACACCCCTGGCCATCACTGAGGGATTCTAACCAGGACCCCTAGCACTGAGC CACGGTCCTGGCCCTTATACTAATCCGTTGATACTGGTTCCCCTGTCCTGAA-3′

Figure 2.3. Nucleotide sequence of WT *Rras* allele and KO *Rras* alleles generated by deletion of 415 nucleotide bases spanning the critical exons 3 and 4 (MRC Harwell, UK in conjunction with IMPC). Red lettering indicates the deleted nucleotide bases. Genotyping primer sequences are highlighted (pink: forward 1, green: forward 2, grey: reverse, see table 2.4). Sequences are in the 5′ – 3′ direction.

Male and female mice were used in experiments. Mice were homed in standard Perspex cages at room temperature and a 12 h dark light cycle, with wood chip bedding, paper nesting and enrichment tubes, and access to hard diet and water at all times. All mice were bred in house and caged with at least one other, except for post-surgery where they were individually caged. Young adult mice were used for experiments between 8 and 15 weeks of age, and aged mice between 10 to 12 months.

2.10.1. Genotyping

2.10.1.1. DNA extraction

Genomic DNA was isolated from mouse ears for genotyping. Ear clips were lysed in 75 µL of 25 mM NaOH/0.2 mM EDTA at 95°C for 30 min with intermittent vortexing. The resultant lysate

was neutralised with 75 µL of 40 mM Tris-HCl (pH 5.5), and the DNA product stored at -20°C until ready for use.

2.10.1.2. Polymerase chain reaction

Two PCR reactions were run in parallel with two sets of custom primers (Table 2.4, Integrated DNA Technologies, UK). Reaction 1 (R1) includes a forward primer (F1) located before the excised exon, and a reverse primer located after the excised exon 4 (R) (Figure 2.3). Reaction 2 (R2) includes a forward primer (F2) located within the excised exon and the same reverse primer (R) as R1 (Figure 2.3). 2 µL of template DNA, or nuclease-free water for the negative control, was mixed with 12.5 µL BioMix™ Red containing *Taq* DNA polymerase (Bioline, Ireland), 5 µL of forward and reverse primers (Table 2.4) and 5.5 µL nuclease free water in PCR tubes. PCR tubes were placed in a thermal cycler (VWR International, US) and the appropriate cycling programme initiated (Table 2.5). Samples were stored at -20°c or analysed using gel electrophoresis.

Table 2.4. Primer sequences for Rras-DEL415 mouse genotyping.

Primer	Nucleotide sequence 5′ – 3′
F1	5′-TGTCTGACTATGATCCCACCATTG-3′
F2	5′-GCTGGTGTTTGCCATTAACG-3′
R	5′-TTCAGGACAGGGGAACCAGTA-3′

Primers are listed in the 5′ – 3′ nucleotide sequence direction. Custom primers were produced by Integrated DNA Technologies, UK.

Table 2.5. Thermal cycling conditions for Rras-DEL415 mouse genotyping.

Step		Temperature	Time
Denaturation		94 °C	5 min
Cycle x 34	Denaturation	94 °C	30 s
	Annealing	61 °C	30 s
	Extension	72 °C	1 min
Close cycle		72 °C	5 min

2.10.1.3. Gel electrophoresis

A 1% agarose gel was prepared by dissolving 1 g of agarose powder (Sigma-Aldrich, UK) in 100 mL 1x Tris Acetate-EDTA (TAE) buffer (Thermo Fisher Scientific, US), and 5 µL of Midori Green dye was added (Nippon Genetics, Europe, Germany). The liquid gel was poured into a casting tray and combs inserted to create wells, before setting at room temperature for 20 min. Once set, the gel was placed in an electrophoresis tank containing enough TAE buffer to cover the surface of the gel, and the combs were removed. 25 µL of PCR product was loaded into the resultant wells, parallel to 5 µL of 100 bp DNA ladder (Thermo Fisher Scientific, US), and a voltage of 110 mV applied for 45 min. After run completion, DNA fragments were visualised using GeneGnome XRG and GeneSys software (Syngene, India).

2.11. RNA isolation

Ribonucleic acid (RNA) was extracted from tissues using the RNeasy Fibrous Tissue Mini Kit (QIAGEN, Germany), for real-time quantitative polymerase chain reaction (qPCR) or RNA sequencing. The integrity of RNA must be maintained for accurate analysis. However, RNA is relatively unstable and is sensitive to oxidation and degradation by RNAses [296]. Therefore, RNA samples must be stored quickly at minus temperatures or in reagents that have been developed to stabilise RNA, such as RNAlater (ThermoFisher Scientific, US). It is also

important to perform RNA isolation quickly and using RNAse-free equipment to maintain the integrity of RNA for accurate analysis.

For qPCR, organs were excised from mice and snap frozen in liquid nitrogen. For RNA sequencing, whole aortas were excised from mice and transferred to ice-cold PBS (Sigma-Aldrich, UK). Aortas were quickly cleaned of connective tissue and fat and flushed with ice-cold PBS (Sigma-Aldrich, UK) to remove blood, and stored in RNAlater (Thermo Fisher Scientific, US) at -20°C for up to a month, or -80°C for longer term storage, until ready for processing.

On the day of RNA extraction, surfaces and tools were wiped down with RNaseZap (Thermo Fisher Scientific, US) to avoid RNA degradation by RNases. If extracting RNA from snap frozen tissues, tissues were broken down using a pestle and mortar chilled with liquid nitrogen and <30 mg of tissue transferred to a 2 mL Tissue grinding CKMix Precellys tube (Bertin Instruments, France) with 300 µL buffer RLT (QIAGEN, Germany) supplemented with 10 µL β-mercaptoethanol (Sigma-Aldrich, UK). For RNA sequencing, aortas stored in RNAlater (ThermoFisher Scientific, US) were thawed on ice and transferred to a 2 mL Tissue grinding CKMix Precellys tube (Bertin Instruments, France) containing 50 µL buffer RLT (QIAGEN, Germany). Tissues were homogenised using the Precellys Evolution (Bertin Instruments, France) with a programme of 6 x 20 s pulses with 30 s pause, at 6000 rpm and 0°C. Lysed samples were transferred to RNase-free 1.5 mL tubes (QIAGEN, Germany) and quickly centrifuged to remove bubbles. 590 µL RNase-free water (QIAGEN, Germany) and 10 µL or Proteinase K solution (QIAGEN, Germany) was added and the sample was thoroughly mixed by pipetting, prior to 10 min incubation at 55°C. The sample was then centrifuged at 20,000 *g* for 3 min and 800 µL of the supernatant was transferred to a new RNase-free 1.5 mL tube (QIAGEN, Germany). 400 µL of 100% ethanol was added to the sample and mixed thoroughly by pipetting. 700 µL of the sample was transferred to a RNeasy Mini spin column (QIAGEN, Germany) placed in a 2 mL collection tube (QIAGEN, Germany). The sample was centrifuged at room temperature for 15 s at 20,000 *g* and the flow-through discarded. This was repeated with the remainder of the sample. On column DNase digestion was performed on samples for RNA sequencing. 350 µL Buffer RW1 (QIAGEN, Germany) was added directly to the RNeasy Mini spin column, prior to centrifugation at room temperature for 15 s at 20,000 *g* to wash the membrane. 10 µL DNase I stock solution (QIAGEN, Germany) was added to 70 µL Buffer RDD (QIAGEN, Germany) and mixed by gentle inversion. 80 µL of the DNase I incubation mix was added directly to the RNeasy Mini spin column (QIAGEN, Germany) membrane to ensure complete DNAse digestion, and placed on the benchtop at room temperature for 15 min. The membrane was washed again by addition of 350 µL Buffer RW1 (QIAGEN, Germany) and

centrifugation for 15 s at 20,000 *g*. For qPCR, DNase digestion was omitted, and the membrane washed with addition of 700 µL of Buffer RW1 and centrifugation for 15 s at 20,000 *g*. 500 µL Buffer RPE was added to the RNeasy Mini spin column (QIAGEN, Germany) and centrifuged at room temperature for 15 s at 20,000 *g*. The flow-through was discarded and 500 µL Buffer RPE (QIAGEN, Germany) added and centrifuged at room temperature for 2 min at 20,000 *g*. The RNeasy Mini spin column was placed in a new 2 mL collection tube (QIAGEN, Germany) and centrifuged for 1 min at 20,000 *g* to ensure no Buffer RPE or ethanol carryover. The RNeasy Mini spin column (QIAGEN, Germany) was placed in a new 1.5 mL collection tube (QIAGEN, Germany) and 30 µL RNase-free water (QIAGEN, Germany) added directly to the membrane. RNA was eluted by centrifugation for 1 min at 20,000 *g* at room temperature. Elution was repeated with an additional 30 µL RNase free water (QIAGEN, Germany). RNA concentration was determined using a NanoDrop 2000 Spectrophotometer (Thermo Fisher Scientific, US).

2.12. Real-time quantitative polymerase chain reaction

2.12.1. Reverse transcription

cDNA was produced from extracted RNA using the Applied Biosystems™ High-Capacity cDNA Reverse Transcription Kit with RNase inhibitor (Thermo Fisher Scientific, US). 10 µL of the 2x reverse transcription (RT) mastermix was prepared with RNase inhibitor per reaction by mixing 2 µL 10 x RT buffer, 0.8 µL 25 x dNTP mix (100 nM), 2.0 µL RT Random Primers, 1 µL MultiScribe™ Reverse Transcriptase, 1 µL RNase Inhibitor, and 3.2 µL Nuclease-free water on ice. 10 µL of 2 x RT master mix was pipetted into a 0.2 ml Flat Cap PCR Tube (Starlab, UK). Extracted RNA was diluted to reach a volume of 2 µg in 10 µL of Nuclease-free water for each reaction, and added to the 2 x RT master mix, before mixing by pipetting up and down and brief centrifugation to remove air bubbles. Samples were placed in a thermal cycler with the conditions in Table 2.6. and a reaction volume set to 20 µL. cDNA was quantified immediately with qPCR or stored at -20°c.

Table 2.6. Thermal cycling conditions for the High-Capacity cDNA Reverse Transcription Kit (Thermo Fisher Scientific, US).

	Temperature	Time
Step 1	25 °C	10 min
Step 2	37 °C	120 min
Step 3	85 °C	5 min
Step 4	4 °C	Infinite hold

2.12.2. TaqMan Gene Expression assay

Gene expression was measured using the Applied Biosystems™ TaqMan™ Gene Expression assay (Thermo Fisher Scientific, US). The *Rras* probe Mm00485861_g1 (Table 2.7, Thermo Fisher Scientific, US) crosses the junction between exon 3 and 4, within the region of nucleotide deletion in the Rras-DEL415 mouse model. Probes were FAM labelled.

Table 2.7. ID, sequence, and exon junctions spanned by *Rras* and *Gapdh* TaqMan probes (Thermo Fisher Scientific, US) used for gene expression quantification with real-time qPCR.

Gene	Sequence	Cat. No.	Exon junction
Rras	5′-TCTCTTGCAGTTTCAATGAGGTGGGC-3′	Mm00485861_g1	3 – 4
Gapdh	5′-GAACGGATTTGGCCGTATTGGGCGC-3′	Mm99999915_g1	2 – 3

cDNA was diluted in Nuclease-free water to a concentration of 10 ng/µL. Each sample was assayed in triplicate. *Gapdh* (Table 2.7, Mm99999915_g1, Thermo Fisher Scientific, US) was used as the reference gene, and a no template control (NTC) was carried out with no DNA for both *Rras* and *Gapdh*. A mastermix was made up of 10 µL 2× TaqMan® Gene Expression Master Mix (Thermo Fisher Scientific, US) and 1 µL probe. 11 µL of the mastermix was pipetted into a 96 well non-skirted PCR plate (Thermo Fisher Scientific, US) and 9 µL of sample DNA added, resulting in a total reaction volume of 20 µL. The plate was briefly centrifuged, loaded into the qPCR thermal cycler (CFX96 Touch Real-Time PCR Detection System, BioRad, UK), and the appropriate cycling conditions initiated (Table 2.8).

Table 2.8. Thermal cycling conditions for real-time qPCR.

Step	Temperature	Time
Hold	50 °C	2 min
Hold	95 °C	10 min
Cycle (40 Cycles)	95 °C	15 s
	60 °C	1 min

2.13. Organ bath pharmacology

In this study, the organ bath was used to compare the ability of thoracic aortas isolated from WT and R-Ras KO mice to contract and dilate in response to U46619 and acetylcholine (ACh), respectively. Thoracic aortas were mounted on two parallel wires in an organ bath, and changes in tension in response to drug addition were recorded (Figure 2.4). Concentration response curves (CRCs) of U46619-induced contraction and subsequent ACh-induced relaxation were carried out to assess vascular smooth muscle and endothelial function of the vessel (Figure 2.4).

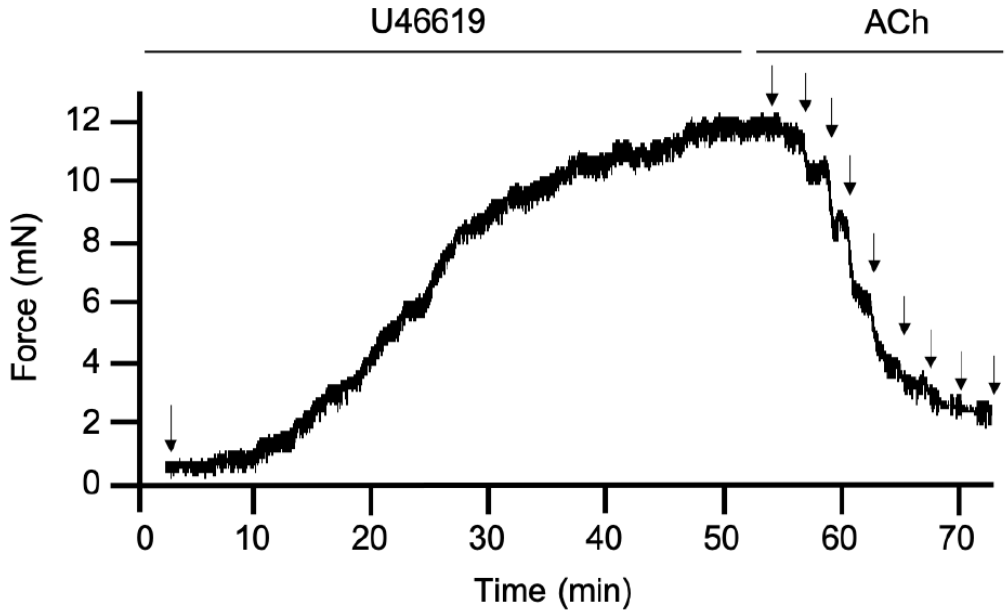

Figure 2.4. Example trace of ACh-induced vasodilation of a thoracic aorta segment pre-contracted with U46619, using the organ bath technique. The arrows indicate addition of U46619 and cumulative addition of ACh.

2.13.1. Isolated vessel preparation

The thoracic aorta from mice aged 12 – 16 weeks was isolated and cleaned of connective tissue and blood in Krebs-bicarbonate buffer composed of (mmol/L): NaCl 118, KCl 4.7, $CaCl_2$ 2.5, $NaHCO_3$ 25, KH_2PO_4 1.2, $MgSO_4$ 1.2, glucose 10. 2 mm aortic rings were mounted onto two parallel tungsten wires 25 µm in diameter in 10 mL organ baths of a Mulvany-Halpern myograph (620 M Multi Wire Myograph System, Danish Myo Technology, Denmark) filled with 6 mL Krebs-bicarbonate bubbled with 5% CO_2 and 95% oxygen, at 37°C. Changes in tension were recorded via an isotonic transducer connected to the wires using PowerLab hardware (AD Instruments, UK) and LabChart 8 software (AD Instruments, UK). Upon mounting, a pre-tension of 5 mN was applied and the aortic rings were equilibrated for 60 min with washing every 15 min. The tension was re-adjusted if it dropped below 5 mN.

2.13.2. Assessment of vascular function

After equilibration, the tension was zeroed, and the aortic rings were stimulated with 48 mM potassium chloride to assess their functional integrity. The aortas were washed for 15 min until the tension returned to 0 mN, and this step repeated. The aortic segments were treated with 1 µM U46619 (Cayman Chemical, US) for 5 min or until the maximum response could be estimated, then washed with Krebs-bicarbonate every 15 min for at least 60 min, until the tension returned to 0 mN. To measure endothelial function of the aortas, segments were stimulated with U46619 to reach 50 – 80% contraction and a cumulative concentration-response curve to ACh (Sigma-Aldrich, UK) (1 nM – 10 µM) was performed. A maximum ACh-induced relaxation of over 75% indicated an intact endothelium. The aortic rings were washed 3 times for 15 min and a cumulative concentration response curve using U46619 (1 nM – 10 µM) was carried out to assess smooth muscle function.

2.14. Aortic sprouting assay

The pro-angiogenic role of R-Ras has been demonstrated in *in vivo* and *ex vivo* angiogenic assays [268,297]. In this thesis, the aortic sprouting assay performed by Komatsu and Ruoslahti was replicated in the Rras-DEL415 mouse model to confirm the cardiovascular phenotype. The preparation of the aortic rings and coating the wells with the collagen matrix is primarily performed outside of the sterile hood, however sterility is paramount to ensure the preparation does not become infected as this will impact vessel growth. Tools were autoclaved and surfaces continuously wiped with 70% ethanol to maintain sterility.

Mice aged 8 – 10 weeks were euthanised and briefly submerged in 70% ethanol. The thoracic aortas were removed and transferred to a petri dish containing ice-cold Opti-MEM™ Reduced Serum media with GlutaMAX™ supplement (Gibco, ThermoFisher Scientific, US). Aortas were cleaned of fat and connective tissue, and gently flushed with ice cold media to remove blood. This was done carefully to avoid damaging the endothelium as this impacts sprouting ability. Aortic rings of ~0.5 mm were cut (~15 from each aorta) and embedded in 1 mg/mL collagen matrix (type 1 rat tail, Millipore, US) in a Corning™ Costar™ 96-well cell culture-treated clear flat-bottom microplate (Thermo Fisher Scientific, US) at 4°C to prevent depolymerisation. The plate was covered and left at room temperature for 15 min prior to incubation for 1 h 37°C in to allow for matrix polymerisation and embedding of aortic rings. The remaining steps were performed in a Class II laminar flow biological safety cabinet. Following incubation, 150 µL Opti-MEM™ + GlutaMAX™ media supplemented with 2.5% FBS (Thermo Fisher Scientific,

US), 2% penicillin-streptomycin (Thermo Fisher Scientific, US) and with 30 ng/mL recombinant murine $VEGF_{165}$ (ProteinTech, US) to induce angiogenesis, or without as a control, was added to each well. Plates were incubated in a humidified atmosphere of 95% air and 5% CO_2 at 37°C. Media was changed on day 3 and 5, and aortic rings were imaged on day 7 using a Nikon Eclipse Ts100 microscope connected to a DS-L3 camera control unit (Nikon, Japan). The number of aortic sprouts was counted using the Cell Counter plugin in ImageJ (Fiji). Conditions were masked, and the mean number of aortic sprouts of all rings was taken for each mouse.

2.15. Surgical procedures

All surgical procedures were performed under aseptic conditions. Mice were anaesthetised with isoflurane (5% induction, 1.5% maintenance). Buprenorphine (0.1 mg/kg) was administered via subcutaneous injection pre-operatively as a pre-emptive analgesic, 8 – 12 h after surgery for 48 h, and thereafter if showing visible signs of pain. Post-surgery, mice were singly housed in sterile standard Perspex cages and provided soft diet. The mice were weighed pre-operatively to calculate the dose of analgesia, and weight was monitored post-operatively for 7 days. Mice were humanely culled if weight dropped by 20% of pre-operative weight, or if showing symptoms of ongoing pain or infection.

2.15.1. Implantation of radiotelemetry probes

PA-C10 probe (DSI, US) catheters were implanted in the carotid artery of mice aged 8 weeks, and the transmitter implanted subcutaneously in the right flank (Figure 2.5). Post-surgery, mice were singly housed in cages located on PhysioTel Receivers (DSI, US) connected to a computer and Dataquest ART acquisition system (DSI, US). Mice were allowed to recover for 10 days prior to baseline recordings taken every 15 min for 120 s for 2 days, diurnally (Figure 2.6). Post-surgery mortality rate was at around 10%.

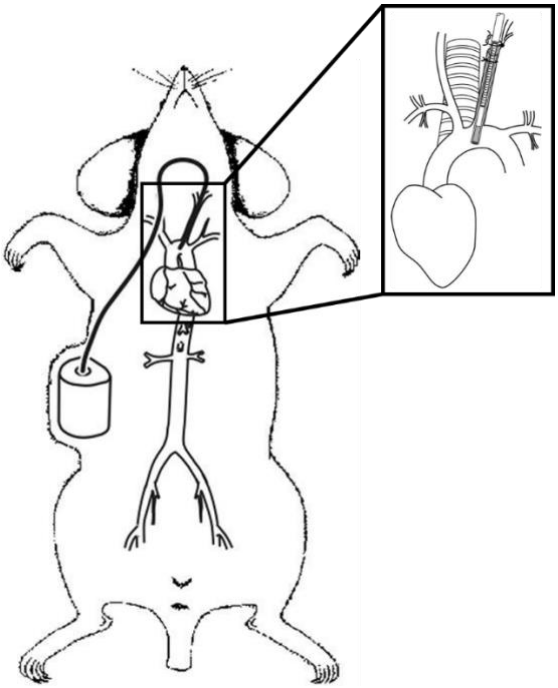

Figure 2.5. Implantation of radiotelemetry probes to measure mouse blood pressure. The catheter is inserted into the left carotid artery of the mouse, with the tip at least 2 mm from the wall of the aortic arch to prevent signal disruption. The probe body is inserted into a subcutaneous pocket on the right flank of the animal. Diagram adapted from Huetteman D.A., Bogie H (2009) [298].

2.15.2. ANGII hypertension model

Mice implanted with radiotelemetry probes were chronically infused with ANGII at a dose of 1.1 mg/kg/min for a period of 14 days to induce hypertension (Figure 2.6). 10 days after implantation of radiotelemetry probes, and 24 h prior to implantation of osmotic pumps, mice were weighed to calculate the appropriate volume of ANGII (Bachem, Switzerland) required to pump 1.1 mg/kg/min. Under sterile conditions, micro-osmotic pumps (Alzet 1004; Alzet, US) with an infusion rate of 0.11 µL/h and a reservoir volume of 28 days were loaded with ANGII (Bachem, Switzerland) dissolved in D-PBS (Sigma-Aldrich, UK) and primed in PBS (Sigma-Aldrich, UK) at 37°C.

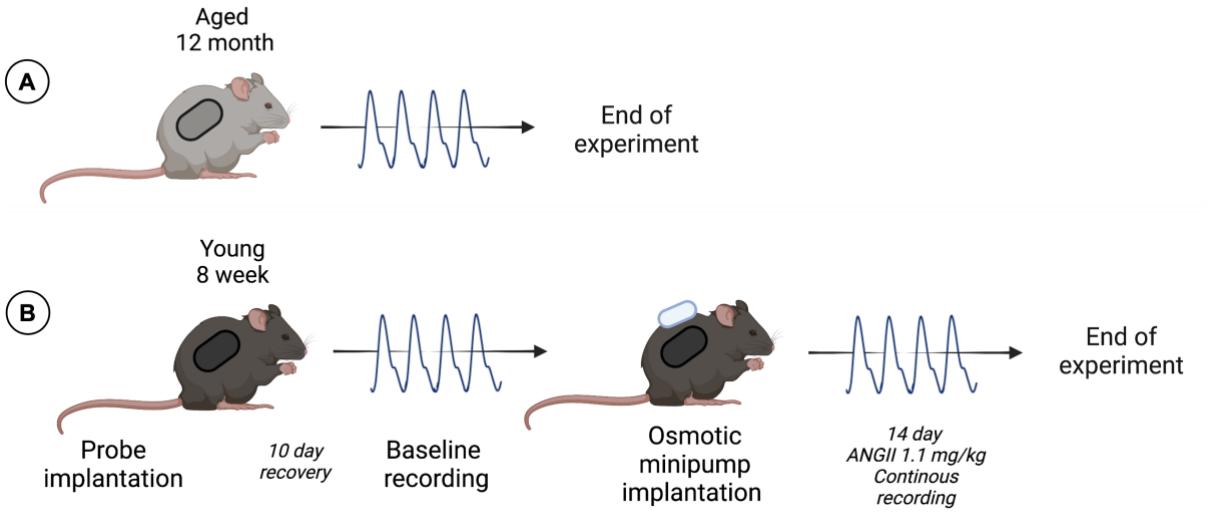

Figure 2.6. Blood pressure radiotelemetry timeline. Mice were implanted with PA-C10 radiotelemetry probes (DSI, US). After 10 days recovery, baseline recordings were taken. (A) Aged mice were culled and organs harvested for phenotyping. (B) Young mice were challenged with ANGII via osmotic minipump implantation for 14 days with recordings taken at day 3, 5, 7, and 10 to 14. Mice were culled, organs harvesting for phenotyping, and the vascular reactivity of aortas assessed with organ bath pharmacology. Diagram created with Biorender.com.

2.16. Mouse phenotyping

Mice were culled by cervical dislocation, and body weight measured. If implanted, the radiotelemetry probe and micro-osmotic pumps were removed, and their weights subtracted from the total body weight to calculate true body weight. The heart, aorta, spleen, and kidneys were harvested, weighed, and either fixed in 10% formalin solution (Sigma-Aldrich, UK) for histology or snap frozen in liquid nitrogen and stored at -80°C for further analysis. The lungs were harvested and wet lung weight noted before dehydration at 60°C overnight and weighing the next day for dry lung weight. The wet lung to dry lung weight ratio was used as a measure of lung fluid retention, an indicator of pulmonary oedema. The tibial length was used to normalise organ weights [299].

2.17. Mouse histology

2.17.1. Masson's Trichrome staining

To analyse aortic wall thickness sectioned mouse thoracic aortas were stained with Masson's Trichrome Stain using the Trichrome Stain Kit (Connective Tissue Stain) (Abcam, UK). Mouse aortas fixed in 10% formalin (Sigma-Aldrich, UK) were embedded in paraffin and sectioned to 5 µm horizontal sections mounted onto slides. Slides were deparaffinised in xylene prior to rehydration in 100%, 95% and 70% ethanol sequentially and incubation in Bouin's solution (Sigma-Aldrich, UK) overnight. The next day slides were washed under running tap water for 5 – 10 min, until the water ran clear. Sections were stained with Weigert's iron haematoxylin solution (parts A and B mixed in equal parts) for 10 min to stain the cell nuclei black, then washed under running tap water for 10 min and rinsed once in mQH_2O. Sections were stained with Beibrich-Scarlet Acid Fuschin solution for 10 min to stain the cytoplasm red, before rinsing once in mQH_2O. Phosphomolybdic-phosphotungstic acid was applied for at least 15 min to differentiate the red stain from the collagen. Without rinsing, sections were stained with aniline blue solution for 10 min to stain the collagen blue. The slides were rinsed once in mQH_2O and differentiated with 1% acetic acid for 3 to 5 min to remove residual colour. Finally, slides were washed in mQH_2O and dehydrated in 95% ethanol, prior to clearing in xylene and remounting. Sections were imaged using the Pannorammic 250 Flash III scanner (3DHISTECH Ltd., Hungary) the next day to ensure the mounting medium was set. Aortic wall thickness was measured using CaseViewer software (3DHISTECH Ltd., Hungary), taking an average of 10 measurements from each aortic section.

2.17.2. Picrosirius red

Picrosirius red staining of murine heart samples was used to assess fibrosis, as a biomarker of successful ANGII challenging. Collagen is stained red on a pale yellow background, nuclei are stained black. Hearts were sectioned and stained by the BCI Pathology Services (Barts Cancer Institute, QMUL) using published methods [300,301]. Briefly, hearts fixed in 10% formalin (Sigma-Aldrich, UK) were embedded in paraffin and sectioned to 5 µm longitudinal sections mounted onto slides. Slides were deparaffinised (2 min in 3 changes of xylene) and rehydrated (2 min in 2 changes of 100% ethanol, 1 min in 90% ethanol, 1 min in 70% ethanol) and rinsed in tap water. Nuclei were stained by immersing slides in working Weigert's Iron Haematoxylin solution (Atom Scientific, UK) for 5 min, prior to washing in running tap water for 2 min. The slide was carefully blotted and placed into Picrosirius red solution (0.5 g Sirius Red F3B (C.I.35782) mixed with 500 mL saturated aqueous solution of picric acid) for 1 h.

Slides were washed in 2 changes of 0.5% acetic acid and water removed by vigorous shaking or blotting with paper. Slides were dehydrated in 3 changes of 100% ethanol and mounted. Sections were imaged using the Pannorammic 250 Flash III scanner (3DHISTECH Ltd., Hungary) and fibrosis quantified as area of red stain (collagen) using ImageJ (Fiji).

2.17.3. Immunofluorescent staining

Immunofluorescent staining of mouse aortas was carried out to visualise Yes-associated protein 1 (YAP1) cytoplasmic and nuclear localisation. Paraffin mounted sectioned mouse aortas were dewaxed followed by antigen retrieval with Citrate buffer pH 6.0 (Vector laboratories, UK) for 10 min in the microwave. Slides were washed in PBS and permeabilised with 0.25% Triton in PBS for 15 min. Slides were then washed 3 times in PBS, prior to blocking for 1 h in 5% goat serum in PBS at room temperature, and overnight incubation in 1% goat serum in PBS at 4°C with primary antibodies for YAP1 and elastin (Table 2.9). The next day, slides were washed in PBS and incubated for 1 h at room temperature with 2 μg/mL of 488 goat anti-mouse (for anti-YAP1) and 555 donkey anti-rabbit (for anti-Elastin) (Invitrogen, UK). Samples were washed with PBS and counterstained with DAPI for 5 min prior to mounting with a 22 mm x 50 mm coverslip with Immunomount (Shandon, UK). The slides were kept in the dark and imaged with confocal microscopy (Zeiss LSM 880, Carl Zeiss, UK). Images were processed using ZEN Blue 3.6 Microscopy software (Carl Zeiss, UK).

Table 2.9. Primary antibodies used in immunofluorescent staining.

Primary Antibody	Origin	Clonality	Dilution	Supplier	Cat. no.
Anti-YAP1	Mouse	Monoclonal	1:50	Santa Cruz, USA	sc-101199
Anti-Elastin	Rabbit	Polyclonal	1:1000	Proteintech, USA	bs-1756R

2.18. RNA sequencing

RNA sequencing (RNA-seq) was carried out on WT and R-Ras KO mouse aortas to identify changes in gene expression resulting from *Rras* gene deletion. RNA was isolated and DNAse treated as described in section 2.11. RNA-seq was carried out by the Genome Centre, QMUL. Briefly, quality control of RNA samples was carried out by measuring RNA quantity using a

NanoDrop 2000 Spectrophotometer (Thermo Fisher Scientific, US), and RNA integrity using the Agilent 100 Bioanalyser (Agilent, US) to generate an RNA integrity number (RIN). Only samples with an RIN of >7 were used, indicating low RNA degradation. mRNA libraries were prepared using the NEBNext Ultra II RNA Library Prep Kit for Illumina (New England Biolabs, US). RNA-seq was performed with Illumina NextSeq500 (Illumina, US) with >25 million short reads generated per sample. RNA-Seq data was aligned and analysed by Dr. Charles Mein using Partek Flow software (Partek, US).

2.19. Phosphoproteomics

The phosphosignalling profiles of WT and R-Ras KO mouse aortas were compared using phosphoproteomics (Figure 2.7). Protein extraction from the mouse aorta was performed by me. Phosphoproteomics was performed by Dr. Vinothini Rajeeve and Ms. Ruth Otunsola, (Cutillas group, Cancer Research UK Barts Centre Mass Spectrometry Facility, QMUL). Published methods were used [302–304], with some modifications. Raw data and quantified phosphopeptide data were supplied in excel format for analysis.

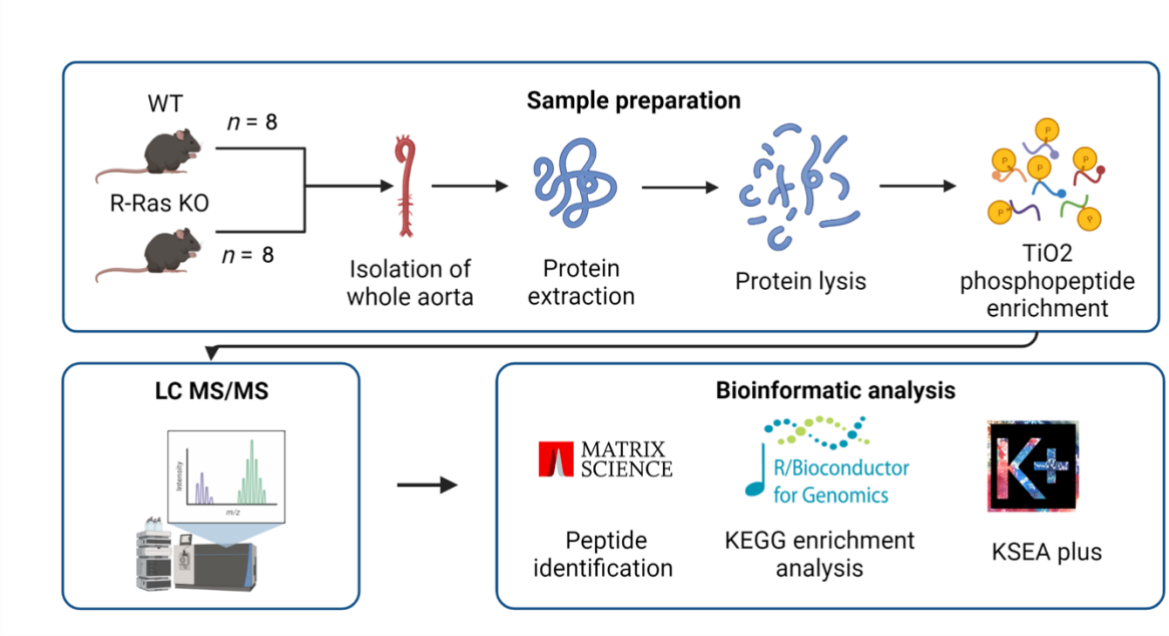

Figure 2.7. **Phosphoproteomics workflow.** Whole aortas were excised from 8 WT and 8 R-Ras KO mice, and 2 aortas pooled per sample. Diagram created with Biorender.com.

2.19.1. Protein extraction from whole mouse aorta

Whole aortas were from mice aged 8 weeks excised and transferred to a dish with ice cold PBS, cleaned and flushed as described previously (Sigma-Aldrich, UK). Aortas were flash frozen in liquid nitrogen until ready for protein extraction. 2 aortas were pooled to achieve sufficient protein. The pulveriser (BioPulverizer, BioSpec, US) was pre-chilled overnight at -80°C prior to protein extraction. On the day of protein extraction, urea buffer was supplemented with phosphatase inhibitors (8 M urea in 20 mM 4-(2-hydroxyethyl)-1-piperazineethanesulfonic acid (HEPES), pH 8.0 supplemented with 1 mM sodium orthovanadate, 1 mM sodium fluoride, 1 mM disodium pyrophosphate and 1 mM β-glycerophosphate) and kept on ice. Aortas were ground to a fine powder using the pre-cooled pulveriser. Liquid nitrogen was carefully poured over the pulveriser during this process to maintain low temperature. The ground aortas (2 per sample) were transferred to a 2mL Lo-bind Eppendorf tube (Thermo Fisher Scientific, US) containing 250 µL urea buffer supplemented with phosphatase inhibitors with a pre-chilled spatula, and placed on ice. The sample was vortexed for 2 min, replacing the sample on ice every 20 s to maintain low temperatures. The sample was homogenised on ice using the Sonifier® Cell Disrupter Model SLPe (Branson Ultrasonics, US) with 6 x 15 s pulses, 15 s rest at 50% intensity. The sample was then centrifuged at 20,000 *g* for 20 min at 4°C and the supernatant collected. Protein concentration was measured using the Pierce™ BCA Protein Assay Kit (Thermo Fisher Scientific, US) as described in section 2.19.2, and samples stored at -80°C until ready for analysis.

2.19.2. BCA Protein Assay

The protein concentration of mouse aorta homogenates was measured using the Pierce™ BCA Protein Assay Kit (Thermo Fisher Scientific, US). The BCA protein assay uses bicinchoninic acid (BCA) to allow colourimetric detection and quantification of total protein concentrations ranging from 20 to 2000 µg/mL. The biuret reaction (the reduction of Cu^{2+} to Cu^{+} ions by protein in an alkaline medium) results in the formation of a purple-coloured reaction product due to chelation of two BCA molecules with one Cu^{+} ion. The purple reaction product exhibits a strong absorbance at 562 nm nearly linear with increasing protein concentrations. A standard curve is plotted using a series of dilutions with albumin standard (BSA) protein and unknown concentrations are extrapolated.

A series of BSA protein standards ranging from 0 (blank) to 2000 µg/mL were prepared by dilution of 2 mg/mL BSA with lysis buffer used for protein extraction (Chapter 2.19.1). The BCA working reagent (WR) was prepared by mixing 50 parts of BCA reagent A to 1 part of BCA Reagent B (50:1, Reagent A:B). The total volume of WR required was calculated as:

Total volume of WR = (# standards + # unknowns) x (# replicates) x (volume of WR per sample)

10 µL of each standard or unknown sample was added into a microplate well in a Corning Costar 96-well clear flat-bottom microplate (Thermo Fisher Scientific, US), in replicates of 3, and 200 µL WR added to each well. Samples were mixed by gentle shaking and incubated for 30 min at 37°C in the dark. After incubation, the absorbance was measured at 562 nm using the Victor^2 Multilabel Counter (PerkinElmer, US). The mean 562 nm absorbance measurement of the blank standard replicates was subtracted from the 562 nm measurements of BSA protein standard and unknown sample replicates to eliminate background signal. A standard curve was constructed, and the protein concentration of each unknown sample extrapolated using y = mx+c.

2.20. Statistical analysis

Quantitative data was plotted as mean with standard error of mean (SEM) bars and analysed using GraphPad Prism 8 Software (GraphPad, US). Normality tests were carried out to assess normality to inform the appropriate post-hoc test choice. Significant differences between quantitative values were analysed using a paired or unpaired Student's two-tailed t-test, a two-way Analysis of Variance (ANOVA) with Sidak's multiple comparisons, or one-way ANOVA with Tukey's multiple comparisons as a *post hoc* test if normal assumptions were met, and Kruskal-Wallis if the data failed to meet assumptions, with P values below 0.05 considered as significant.

2.20.1. Organ bath data analysis

For analysis of organ bath data standard reference curves were fitted with linear regression using the equation shown below, with unconstrained Y intercept and slope values.

$$Y = Y\ Intercept + (X \times\ slope)$$

Prism 8 software was used to interpolate X values from the linear standard reference line from each experiment to calculate IC_{50} and R_{Max} values.

2.20.2. Radiotelemetry mixed model linear regression analysis

Mixed model linear regression analysis was performed on radiotelemetry data using R software (Version 1.4.1103; R Foundation for Statistical Computing, Austria) and visualised using the ggplot2 package [305]. QQplots were plotted to determine normality of data, and data points with a standard deviation (SD) of ± 3 were deemed outliers and excluded from analysis. The lme4 package [306] was used to perform mixed model linear regression analysis and graphs plotted using ggeffects [307].

2.20.3. Real-time qPCR quantification

For real-time qPCR quantification of DNA, relative gene expression was calculated using the comparative cycle threshold (C_t) method [308]. C_t values of the gene of interest are normalised to the housekeeping gene (*Gadph*) to calculate ΔC_t for each sample. The difference in ΔC_t between experimental and control samples ($\Delta\Delta C_t$) is calculated for each. Finally, the fold change in gene expression between experimental and control samples is calculated and expressed as relative units based on $2^{-\Delta\Delta Ct}$. Data is presented as relative change compared to control, and analysed using a one-way ANOVA with Tukey's multiple comparisons.

2.20.4. RNA-Seq data analysis

RNA-Seq data was analysed by Dr. Charles Mein (Genome Centre, QMUL) using Partek Flow software (Partek, US). Significant differential gene expression was assessed using a student's two-tailed t-test with equal variances assumed, with Bonferonni correction and stated as fold change.

2.20.5. Phosphoproteomics data analysis

Phosphoproteomic data was transferred from raw files to Excel and the Log2 (Fold Change) (Log2FC) calculated. Statistical significance of Log2FC was calculated using a student's two-tailed t-test with equal variances assumed ($p < 0.05$, $Log2FC \geq \pm 2$). Bioinformatic analysis of phosphoproteomic data was performed using R (Version 4.2.0; R Foundation for Statistical Computing, Austria) and the packages ggplot2 [305], ggnewscale [309], and cowplot [310] used to visualise data. Bioconductor version 3.15 was used for bioinformatic analysis with the following packages; org.Mm.eg.db (v3.15.0, Carlson, 2019), clusterProfiler (v4.4.4, Yu *et al.*, 2012), DOSE (v3.22.0, Yu G et al., 2015), enrichplot (v1.16.1,[313]), and pathview (v1.36.0, [314]). Gene set enrichment analysis (GSEA) was performed using the KEGG database (release 101.0, Mouse Genome Sequencing Consortium) and Gene Ontology database (release 2022-03-22, [315]).

Chapter 3. Exploring the impact of the rare exonic variant on R-Ras structure and function

3.1. Introduction

Nonsynonymous SNVs are changes in the DNA sequence where a nucleotide substitution results in a different amino acid, and can alter protein function by disrupting structural stability and expression, enzymatic activity, protein-protein interactions, among other physiological properties [11]. The SBP-associated SNV mapped to the *RRAS* gene, encoding a missense mutation from a cytosine (C) to thymine (T) allele (T>C), with a predicted change of an aspartate (D) to an asparagine (N) residue at position 133 (R-Ras D133N). The rs61760904 variant is in strong linkage disequilibrium with two variants both mapping to intronic regions of the *SCAF1* gene: rs189349094 (r^2 = 0.98) and rs139064177 (r^2 = 0.97), encoding the SR-Related CTD Associated Factor 1 gene associated with RNA splicing [316]. The *SCAF1* gene has not been previously linked to BP, and both the corresponding SNVs are intronic. These data indicated rs61760904 as the likely causal variant.

The predicted effect of the rs61760904 SNV on protein structure and function was reported as damaging using the Ensembl VEP tool by Surendran *et al* [11]. However, the importance of the D133 amino acid to R-Ras structure and function has not yet been elucidated, and so the impact of the R-RasD133N missense mutation remains unclear. This chapter explores the possible effect of the D133N variant on R-Ras protein structure and function. Further, the importance of D133 residue is investigated by introducing two additional mutants: an alpha helix breaker (D133P, proline), and a charge reversal mutant (D133K, lysine).

There are two main approaches:

1) *In silico* protein structure prediction, conservation analysis, and damage prediction of the R-Ras variants, and
2) *In vitro* assessment of the impact of the R-Ras variants on protein expression and function using western blotting.

3.2. Results

3.2.1. The D133N variant may not alter R-Ras protein structure in silico

The protein structure prediction service Robetta [282] was used to predict the protein structure of R-Ras, and R-RasD133N, to evaluate changes in protein structure induced by the mutation. Protein structure modelling in PyMOL 2.5 [317] shows the D133 residue is located on a loop (Figure 3.1). Structural alignment of R-Ras and R-RasD133N computed a RMSD value of 2.24, suggesting no stark differences in protein structure.

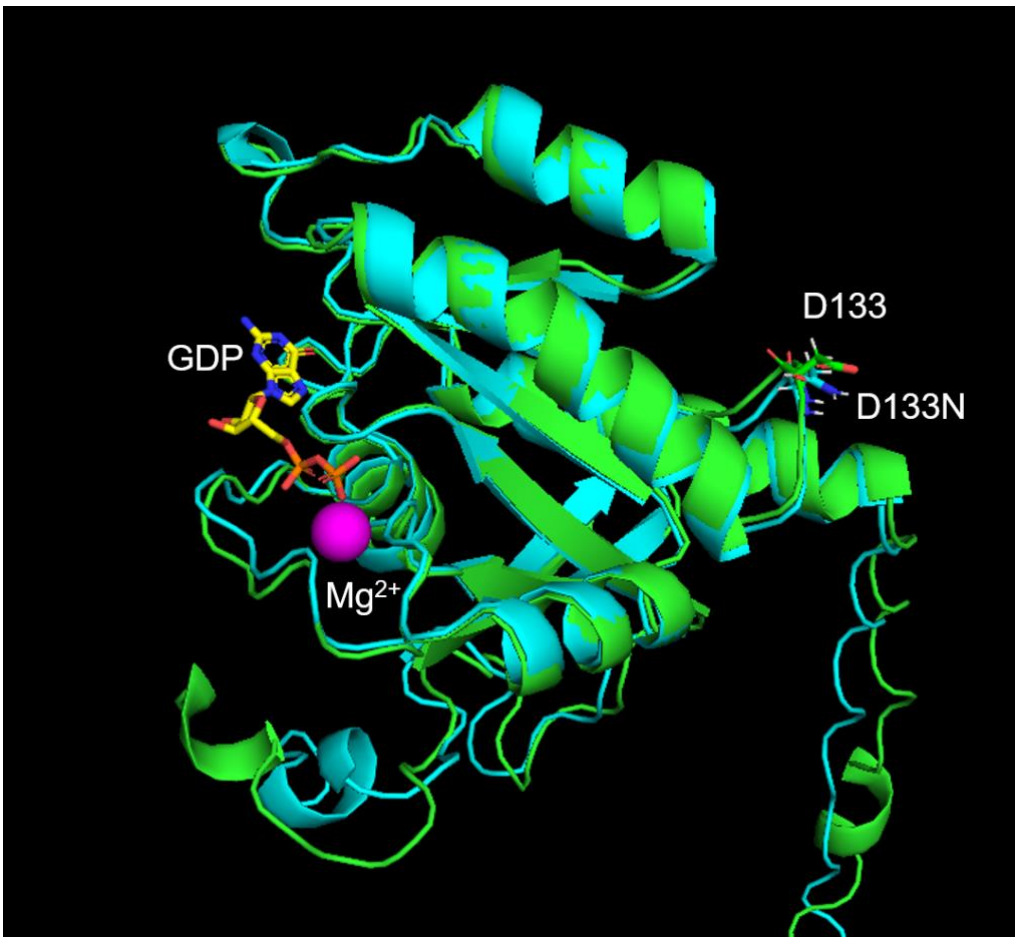

Figure 3.1. Structural alignment R-Ras and R-RasD133N. R-Ras and R-RasD133N protein structures were predicted using Robetta [282] and aligned using PyMOL 2.5 (The PyMOL Molecular Graphics System, Version 2.0 Schrödinger, LLC).

3.2.2. The R-RasD133N variant is predicted damaging in silico

Conservation analysis performed with the ConSurf server [318] showed weak conservation of D133 (normalised conservation score = 1.474, 95% CI [0.766, 2.285]), and predicted D133 to be an exposed residue. In 150 aligned sequences chosen by ConSurf based on amino acid homology to R-Ras, D is the most common amino acid at position 133 (29.252% of 150 sequences). N, P and K are also located in this position with percentage varieties of N = 2.041%, P = 8.844% and K = 5.442 %.

In silico bioinformatics tools were used for damage prediction of the *RRAS* variants D133N based on information on sequence homology, structure, or a combination (Table 3.1). Basic tools (PROVEAN and SIFT) rely on sequence alignment to assess the evolutionary conservation of the residue of interest and provide a general output of whether an amino acid substitution has an effect or is neutral. More complex tools take a structural approach and utilise machine learning methods to combine information on protein structure, sequence, phylogeny, interaction networks and the physicochemical properties of amino acids. Two additional variants were also introduced to investigate the functional importance of the residue; D133P and D133K. D133P introduces an alpha helix break, to assess whether the residue is important for protein structure. D133K is a charge reversal mutant, to assess whether the residue is important for protein-protein interactions.

Detailed methods of variant damage prediction tools are provided in section 2.1.2. Tools rely on sequence homology, structural information, or both (combined) to predict the impact of a mutation on protein structure, providing a score and relative outcome (Table 3.1).

Table 3.1. Variant damage prediction tools used to predict the impact of D133N, D133K and D133P amino acid substitutions, their scores, thresholds and outcomes, and prediction methods.

Tool	Score	Threshold	Outcome	Prediction method
PolyPhen-2	FPR	> 10%	Probably damaging	Combined
		≤ 10%	Possibly damaging	
		≤ 5%	Benign	
Missense3D	Categorical	Damaging or neutral		Structural
MUpro	ΔΔG	+	Decrease stability	Structural
		-	Increase stability	
MutPred2	Continuous 0 to 1	Less to more pathogenic		Combined
PROVEAN	Continuous	< -2.5	Damaging	Sequence
		≤ 2.5	Tolerated	
SIFT	Continuous 0 to 1	≤ 0.05	Damaging	Sequence
		> 0.5	Tolerated	
SNAP2	Continuous -100 to + 100	Neutral to strong effect		Combined

Prediction methods are classified as using sequence, structural or combined sequence and structural analysis. See Chapter 2.1.2. for more details. FPR: false positive rate, ΔΔG: relative stability change.

PolyPhen-2, PROVEAN, Mupro, MutPred2, and SIFT predicted all the variants damaging (Table 3.2). MutPred2 predicted D133P and D133K pathogenic (score threshold > 0.5 without FPR correction), and D133N pathogenic without FPR adjustment (score = 0.526, Table 3.2). The MutPred2 creators suggest a threshold of 0.68 yields a FPR of 10% [288]. With 10% FPR correction, the R-RasD133N score is < 0.68 and is predicted as benign (Table 3.2). MutPred2 also calculates a posterior probability of structural changes resulting from amino acid substitutions. For all variants, MutPred2 predicted a gain of allosteric site at R128 (probability = 0.19 for D133N). However, the probability is low and the importance of this residue has not been elucidated [274]. SNAP2 predicted an effect with the D133N and D133K variant, but not with the D133P variant (Table 3.2). Missense3D is the only tool to predict no effect of any variant. Ensembl VEP was used to predict the impact of the rs61760904 SNV by Surendran *et al.,* [11]; this tool integrates PolyPhen-2 and SIFT. Prediction scores calculated by PolyPhen-2 and SIFT independently of VEP differ slightly to scores obtained in VEP (R-RasD133N, PolyPhen-2 alone = 0.981, PolyPhen-2 in VEP = 0.797, SIFT alone = 0.00, SIFT in VEP = 0.02, Table 3.2).

Table 3.2. In *silico* damage prediction of the impact of R-Ras variants D133N, D133P and D133K.

	D133N		D133P		D133K	
Tool	**Score**	**Outcome**	**Score**	**Outcome**	**Score**	**Outcome**
PolyPhen-2	0.981	Probably damaging	0.999	Probably damaging	0.976	Probably damaging
Missense3D	-	No change	-	No change	-	No change
Mupro	-0.968	Decrease stability	-1.324	Decrease stability	-1.361	Decrease stability
MutPred2	0.526	Maybe pathogenic	0.767	Probably pathogenic	0.7	Probably pathogenic
PROVEAN	-3.926	Deleterious	-5.665	Deleterious	-5.518	Deleterious
SIFT	0	Intolerant substitution	0	Intolerant substitution	0	Intolerant substitution
SNAP2	2	Effect	-8	Neutral	Effect	34

Tools report a score and relative outcome to predict the impact of a variant based on information on sequence, structure, or both, as described in Table 3.1.

3.2.3. The exonic RRAS BP-associated variant does not impact protein expression in vitro

To investigate the effect of the exonic variant of *RRAS* (D133N) on R-Ras protein expression *in vitro*, western blotting was used to quantify R-Ras protein levels in transfected CHO-K1 cells (Figure 3.2). CHO-K1 cells were transfected with WT R-Ras, the exonic variant, D133N, and

two individual variants of interest, D133K and D133P, to investigate the functional importance of this residue. Untransfected (UT) CHO-K1 cells were incubated with Lipofectamine in the absence of DNA and used as a negative control. Protein bands of the same size were detected at 24 kDa with the anti-RRAS primary antibody in all transfected CHO-K1 samples, and no protein band was detected in UT cells (Figure 3.2.A). The normalized signals quantified for WT- (29.82 AU ± 2.44) compared to D133N- (35.45 AU ± 5.23), D133P- (25.10 AU ± 1.67) and D133K-transfected cells (34.26 AU ± 3.67) did not differ significantly with a repeated measures one-way ANOVA and Tukey's multiple comparison testing (Figure 3.2.B).

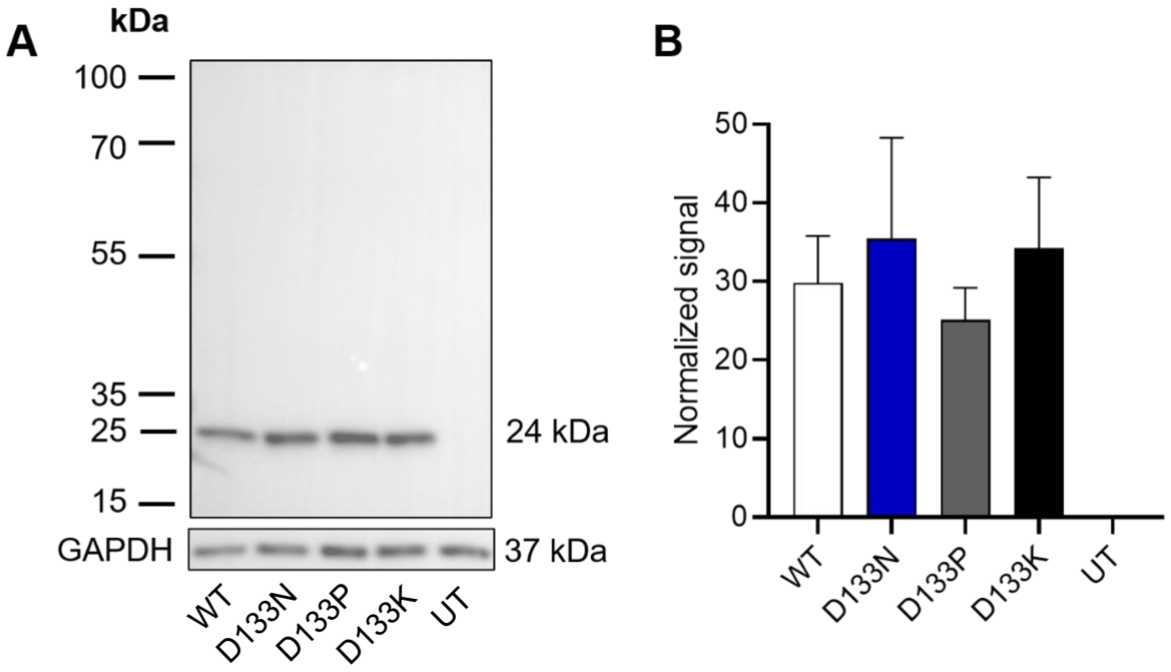

Figure 3.2. Western blot analysis of R-Ras expression in transfected CHO cells. CHO cells were transfected with 500 ng of wild-type (WT) or mutant *RRAS* DNA, or left untransfected (UT), prior to lysis and preparation of protein samples. 20 µg of protein/sample was run on a 12% gel and probed with anti-RRAS (1:1000) or anti-GAPDH (1:1000) as the loading control. A) Representative protein bands obtained with chemiluminescent imaging. B) Mean normalized signal, quantified as described in methods. Significant differences between normalized signal were determined using a repeated measures one-way ANOVA with Tukey's multiple comparison post-hoc test to detect significant differences. Data is presented as mean ± SEM. *N* = 6.

3.3. Discussion

The BP associated SNV encodes a nucleotide change from T>C, and a predicted amino acid change of arginine (D) to asparagine (N) residue at position 133. In *silico* damage prediction is beneficial in prioritising nonsynonymous SNVs in genetic studies for further evaluation, but does not truly reflect the impact of the variant *in vivo*. Here, I have used a combination of *in silico* and *in vitro* methods in an attempt to further investigate the impact of the R-RasD133N mutation, and additionally explore the structural importance of the D133 residue through two additional variants; D133P, an alpha helix breaker (to assess impact on protein structure), and D133K, a charge reversal mutant (to assess importance in protein-protein interactions). In *silico* bioinformatics tools overall predicted the D133N variant as likely damaging. Structural alignment and conservation analysis suggest the D133N variant may not impact protein structure; this observation is supported by no change in protein expression *in vitro*. However, these findings remain inconclusive and further experiments are required to determine the exact impact on protein structure and function of the R-RasD133N variant, and the importance of the D133 residue.

Basic bioinformatics tools (PROVEAN, SIFT Sequence) rely on sequence alignment to assess the evolutionary conservation of the residue of interest, and predict whether a mutation is likely to be benign or pathogenic. More complex tools utilise machine learning methods to combine information on protein structure, sequence, phylogeny, interaction networks and the physicochemical properties of amino acids (PolyPhen-2, Missense3D-DB, SNAP2, MutPred2, Mupro) to predict changes in tertiary structures. I used a combination of these tools to predict the impact of the R-RasD133N variant on R-Ras protein structure and function *in silico*, and to corroborate the Ensembl VEP prediction of rs61760904 as a damaging variant, reported in the GWAS discovery [11]. All bioinformatics tools, except Missense3D, predicted the D133N variant as damaging. When independently run, SIFT and PolyPhen-2 computed scores slightly lower to the scores obtained using Ensembl VEP, the prediction software used by Surendran *et al.,* [11]. This may be explained by different inputs; the SNV identifier is inputted into VEP, whereas the amino acid sequence is inputted into SIFT and PolyPhen-2. Furthermore, the overall outcome of D133N as a predicted damaging mutation is consistent. However, ConSurf reported weak conservation of the D133 residue, in contrast to the damage predictions of SIFT and PROVEAN, which rely on sequence homology to predict the impact of a variant. ConSurf uses 150 supporting sequences, compared to 419 supporting sequences used by PROVEAN, suggesting PROVEAN may have higher powered analysis.

Unlike the other bioinformatics tools used, Missense3D solely relies on structural information. Here, Missense3D reported no change in structure with the D133N, D133K or D133P mutations. This is concurrent with structural alignment of WT R-Ras and R-RasD133N using PyMOL, and a reported RSMD value comparable to that observed with homologous structures [319]. Together, these *in silico* analyses suggest the rs61760904 SNV encoding the R-RasD133N missense mutation could be damaging. I also aimed to assess the impact of the variant *in vitro* in CHO-K1 cells transfected with the WT R-Ras, and the R-Ras variants. R-Ras protein expression detected with western blotting was the same with WT and mutant *RRAS* transfection. This suggests the D133N variant does not change the protein confirmation, and the protein is not degraded. Nonetheless, these *in silico* and *in vitro* analyses do not provide conclusive evidence to support whether the variant impacts structure and/or function.

Future *in vitro* experiments can explore the impact of the D133N variant on R-Ras function. For example;

1) Pull-down assays to assess changes in GTP-loading via measurement of the physical interaction between GTP or GDP and the R-Ras mutant,
2) Assessment of R-Ras interaction with GEFs (e.g. RasGRF1) and GAPs (e.g. p130a) via Ras protein binding assays,
3) Immunofluorescence imaging of transfected cells to determine cellular localisation,
4) Western blotting to explore the impact of the D133N variant on R-Ras on known signalling pathways, such as the PI3K/Akt signalling axis, and
5) Cellular assays to assess the impact of the variant of R-Ras function in more complex processes, including cell motility and proliferation.

Altogether, these *in silico* and *in vitro* data suggest the R-RasD133N variant may impact R-Ras protein structure and/or function, although the exact mechanism is yet to be uncovered.

Chapter 4. Characterising the blood pressure phenotype of the young R-Ras KO mouse model

4.1. Introduction

The SBP-associated variant is mapped to the *RRAS* gene, a promising candidate due to its high expression in the aorta, VSM and endothelial cells, and association with cardiac processes including angiogenesis. These observations suggest R-Ras may physiologically function to regulate BP. This study is the first to explore R-Ras in the context of BP control.

I hypothesised that R-Ras KO mice would have an elevated BP phenotype. Furthermore, the expression of R-Ras in the aorta [323], and endothelial and VSM cells [324] led us to hypothesise that R-Ras may be involved in vascular control of BP. R-Ras is known to potentiate the Akt/PI3K signalling axis [321,325–333]. In endothelial cells, the Akt/PI3K pathway activates eNOS, to generate NO ultimately promoting vasodilation by stimulating contraction of the VSMC layer [27–29]. I propose R-Ras may promote vasodilation by potentiating this pathway in endothelial cells and expect R-Ras KO mice to have altered vascular reactivity. In this chapter, I set out characterise the Rras-DEL415 global KO mouse model and investigate R-Ras signalling *in vitro*. The main aims were to:

1) Establish the BP phenotype of young mice at baseline and with ANGII-induced hypertension,
2) Investigate the potential of R-Ras to promote vasodilation in young mice, specifically via NO signalling,
3) Characterise gross organ morphology of young mice and assess hypertension-related fibrosis, and
4) Determine whether the anti-angiogenic function of R-Ras reported in other *in vivo* models was replicated.

4.2. Results

4.2.1. Confirmation of Rras deletion in the Rras-DEL415 knockout mouse model

The Rras-DEL415 global KO mouse model was generated by MRC Harwell in conjunction with the IMPC specifically for this project, by CRISPR-Cas9 excision of critical exons 3 and 4. as detailed in section 1.4. *Rras* gene expression was quantified using RT-qPCR on RNA extracted from mouse kidneys (Figure 4.1). Relative *Rras* expression normalised to *Gapdh* confirmed *Rras* was completely deleted in R-Ras KO mouse kidneys, and *Rras* expression was approximately half that in R-Ras HET mice compared to WT (R-Ras HET = 0.63 ± 0.09, WT = 0.10 ± 0.11), as expected.

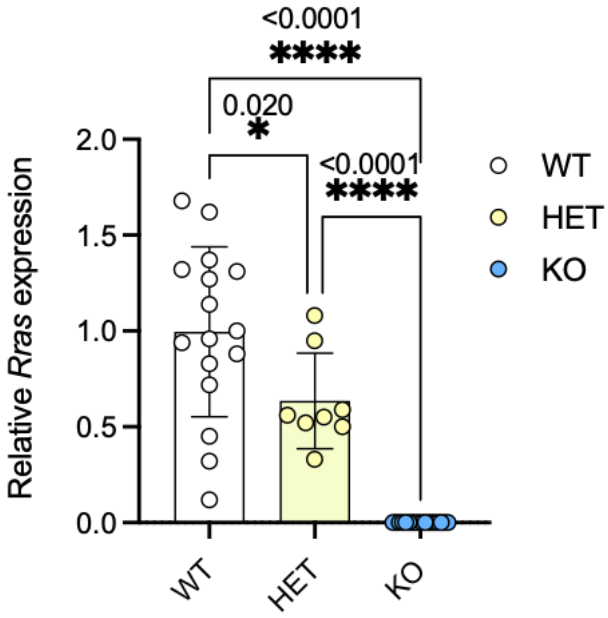

Figure 4.1. Relative *Rras* gene expression in WT, R-Ras HET, and R-Ras KO mouse kidneys quantified using RT-qPCR. Relative *Rras* gene expression was calculated using the comparative C_t method and normalised to *Gapdh*. Mice were aged 12 – 16 weeks. Data is expressed as mean ± SEM and analysed using a one-way ANOVA with Tukey's multiple comparisons. WT *n* = 16, HET *n* = 8, KO *n* = 18. * $p < 0.05$, **** $p < 0.0001$.

4.2.2. BP radiotelemetry in the young adult R-Ras KO mouse

To investigate the impact of R-Ras KO on BP, radiotelemetry probes were implanted into young adult 8-week-old R-Ras KO mice and their WT littermates, and SBP, DBP, MAP, HR

and activity recorded after 10 days recovery. All parameters were higher at night when the mouse was active than at day, as expected (Table 4.1, Figure 4.2). SBP, DBP, MAP and HR were not statistically different at baseline at day or night when analysed with a two-way ANOVA with Sidak's post-hoc testing (Table 4.1, Figure 4.2). The activity of WT mice at night was significantly higher than R-Ras KO (Table 4.1, Figure 4.2.E, $p = 0.032$). Night SBP, DBP, MAP and HR values were therefore activity-corrected by only including readings concurrent to activity readings ranging between 5 – 15 arbitrary units (AU). Differences remained non-significant between WT and R-Ras KO mice across all parameters at night with activity-correction when analysed using a Student's paired two-tailed t-test (Table 4.2, Figure 4.3).

Table 4.1. Baseline SBP, DBP, MAP, HR and activity values in young adult WT and R-Ras KO mice.

	SBP (mmHg)		DBP (mmHg)		MAP (mmHg)		HR (bpm)		Activity (AU)	
	Day	**Night**	**Day**	**Night**	**Day**	**Night**	**Day**	**Night**	**Day**	**Night**
WT	111.4 ± 1.76	123.5 ± 1.69	87.02 ± 9.71	93.75 ± 2.68	96.21 ± 1.88	106.1 ± 2.56	526.6 ± 16.4	590.6 ± 12.3	2.775 ± 0.81	9.935 ± 3.28
KO	110.4 ± 2.52	120.6 ± 2.41	82.4 ± 6.80	91.34 ± 1.91	97.72 ± 1.87	106.7 ± 1.73	533.4 ± 8.10	587.4 ± 8.18	3.126 ± 0.78	6.847 ± 1.33

Data is expressed as mean ± SEM and analysed with a two-way ANOVA with Sidak's post-hoc testing. WT $n = 6$, R-Ras KO $n = 5$.

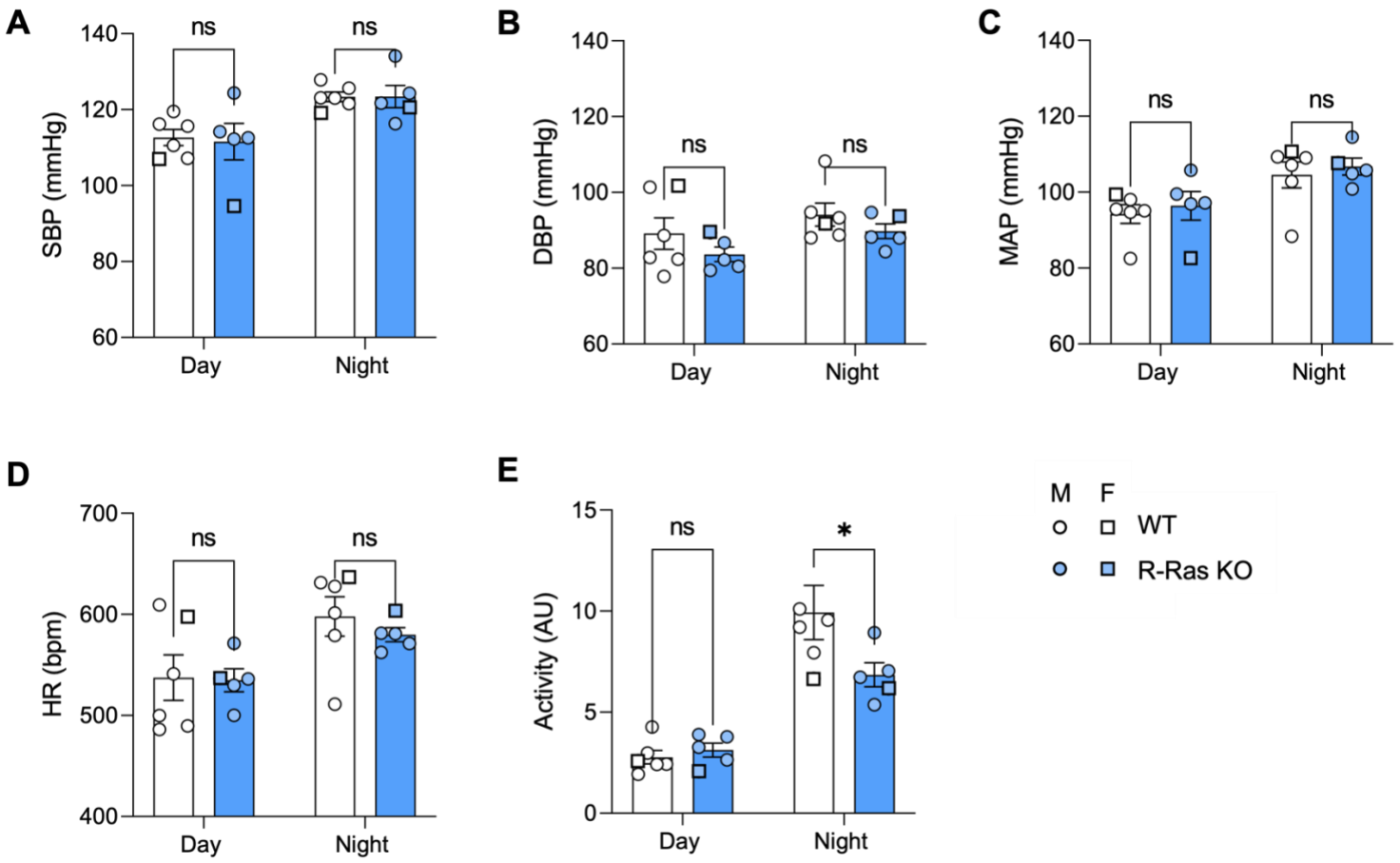

Figure 4.2. Baseline SBP (A), DBP (B), MAP (C), HR (D) and activity (E) values in young adult WT and R-Ras KO mice. Data is expressed as mean ± SEM and analysed with a two-way ANOVA with Sidak's post-hoc testing. * = $p < 0.05$, ns = non-significant. WT $n = 6$, R-Ras KO $n = 5$.

Table 4.2. Activity-corrected baseline SBP, DBP, MAP and HR at night in young adult WT and R-Ras KO mice.

	SBP (mmHg)	DBP (mmHg)	MAP (mmHg)	HR (bpm)
WT	110.4 ± 2.52	93.75 ± 2.68	106.1 ± 2.56	590.6 ± 12.3
KO	120.6 ± 2.41	91.34 ± 1.91	106.7 ± 1.73	587.4 ± 8.18

Data is expressed as mean ± SEM. WT *n* = 6, R-Ras KO *n* = 5.

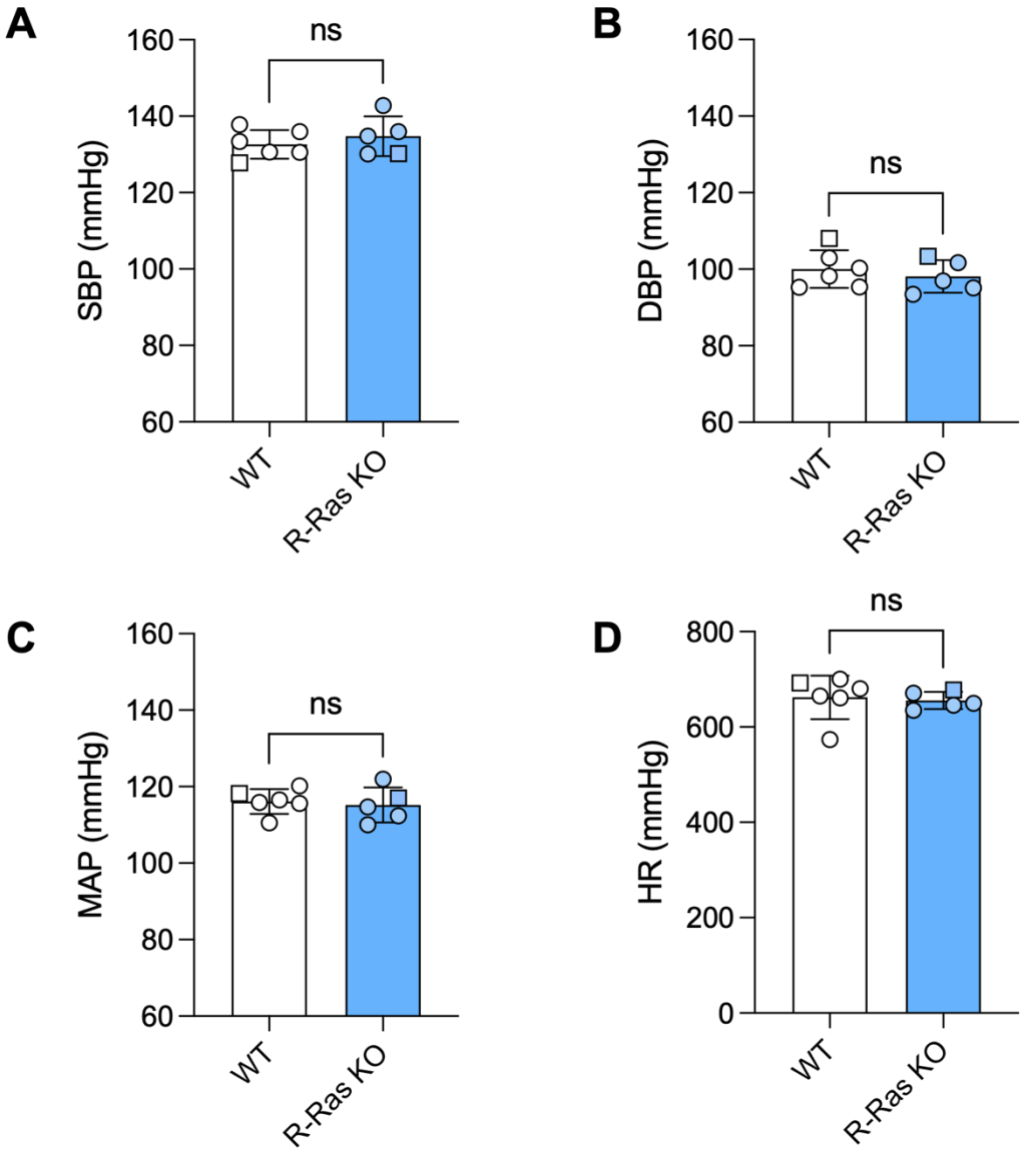

Figure 4.3. Activity-corrected baseline SBP (A), DBP (B), MAP (C) and HR (D) at night in young adult WT and R-Ras KO mice. Data is expressed as mean ± SEM and analysed using a Student's paired two-tailed t-test. Circles represent females, and squares represent males. WT *n* = 6, R-Ras KO *n* = 5.

4.2.3. ANGII challenge increases blood pressure in WT and R-Ras KO mice to the same extent

With no differences observed between WT and R-Ras KO mice for BP and HR, I hypothesised the potential impact of R-Ras deletion on BP may become apparent in a hypertensive phenotype. To investigate this, young adult mice aged 10 weeks implanted with radiotelemetry probes were chronically infused with ANGII (1.1 mg/kg/day) to induce hypertension. SBP, DBP and MAP significantly increased over 14 days of ANGII challenge (Figures 4.4 – 4.6) and HR and activity remained the same, as expected (Figures 4.7 and 4.8). Analysis with multiple unpaired t-tests with Welch's Correction found no significant difference between WT and R-Ras KO SBP, DBP, MAP, HR, or activity at any time point before and during ANGII challenge (Table 4.3, Figures 4.4 – 4.8).

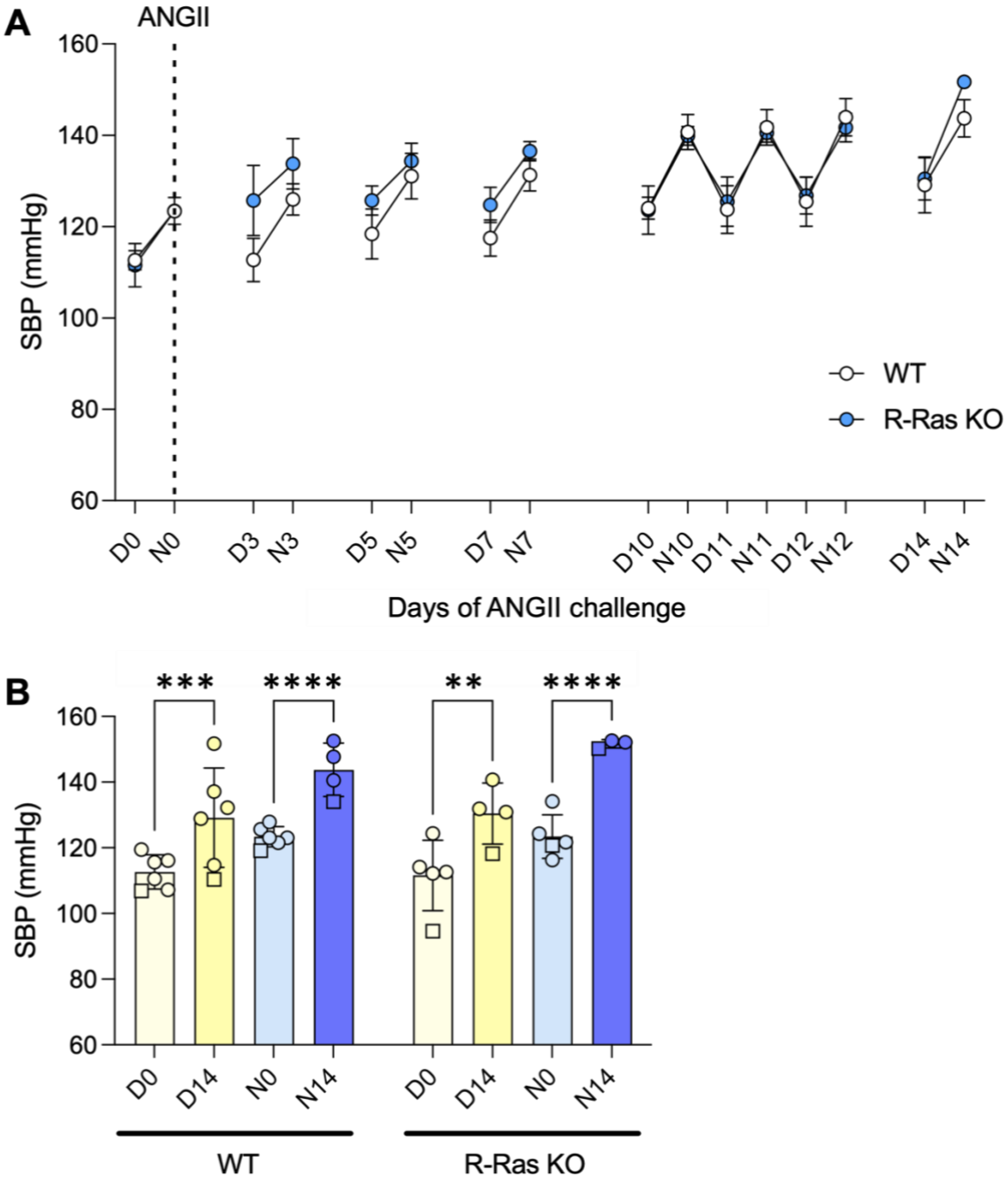

Figure 4.4. SBP of WT and R-Ras KO mice with ANGII challenge. A) Diurnal SBP of WT and R-Ras KO mice over 14 days of ANGII challenge, analysed using multiple unpaired t-tests with Welch's correction. The dotted line indicates ANGII minipump implantation. B) SBP at day/night 0 and day/night 14 for WT and R-Ras KO mice, analysed using a two-way ANOVA with Sidak's post-hoc test. Circles represent males, squares represent females. $N = 3 – 6$, see Table 4.4. **p < 0.01, ***p < 0.001, ****p < 0.0001.

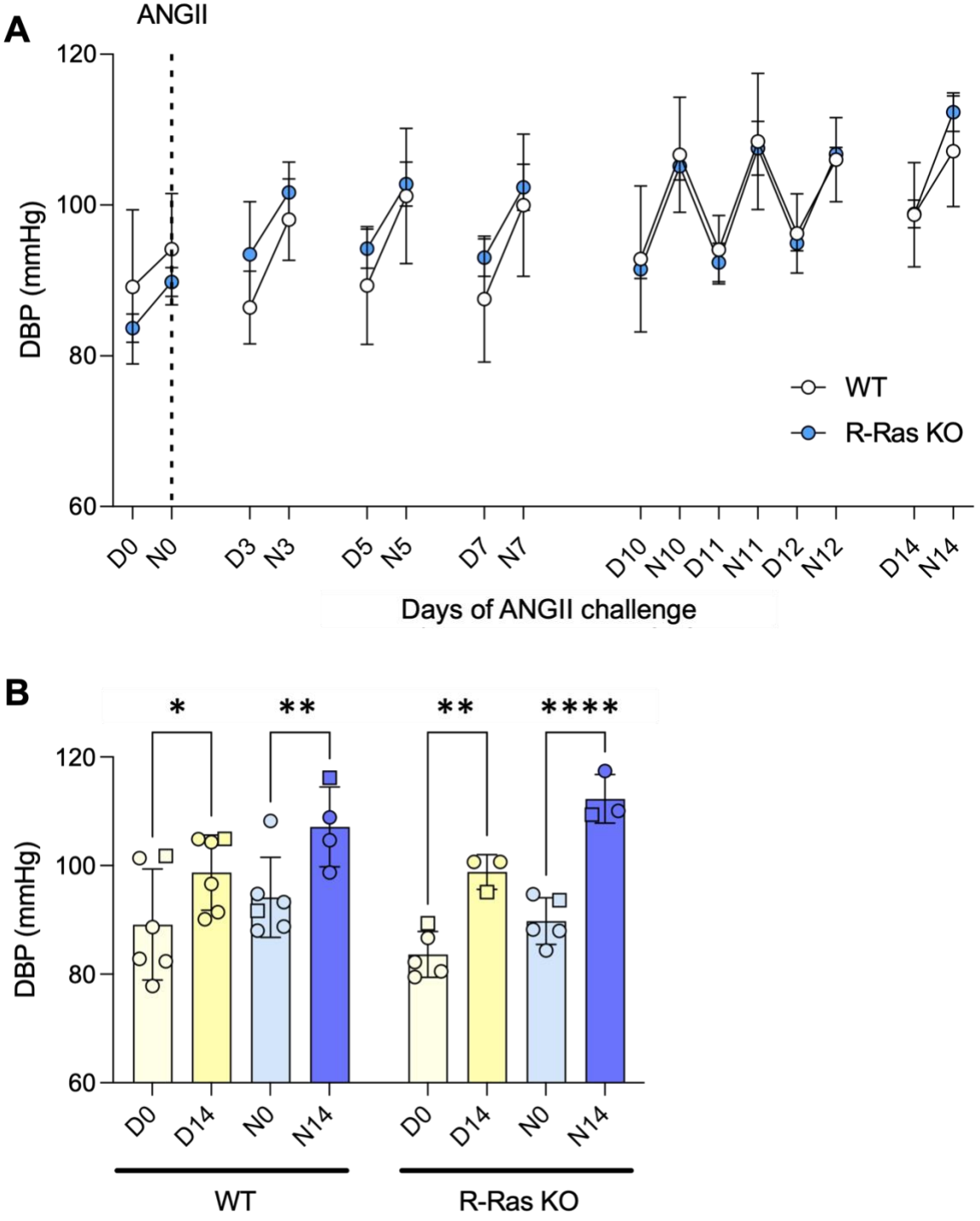

Figure 4.5. DBP of WT and R-Ras KO mice with ANGII challenge. A) Diurnal DBP of WT and R-Ras KO mice over 14 days of ANGII challenge, analysed using multiple unpaired t-tests with Welch's correction. The dotted line indicates ANGII minipump implantation. B) DBP at day/night 0 and day/night 14 for WT and R-Ras KO mice, analysed using a two-way ANOVA with Sidak's post-hoc test. Circles represent males, squares represent females. $N = 3 – 6$, see Table 4.4. *$p < 0.05$, **$p < 0.001$, ****$p < 0.0001$.

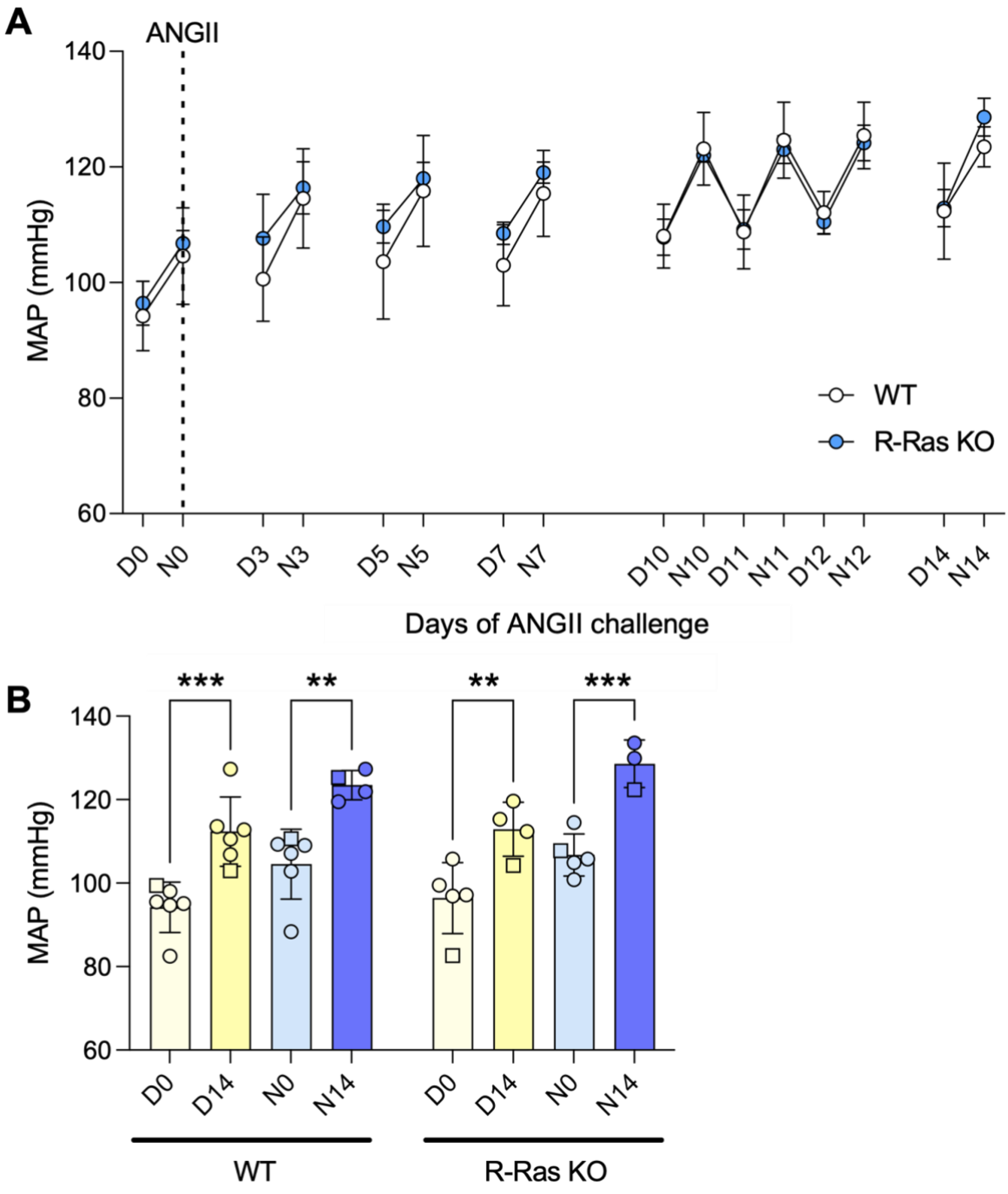

Figure 4.6. MAP of WT and R-Ras KO mice with ANGII challenge. A) Diurnal MAP of WT and R-Ras KO mice over 14 days of ANGII challenge, analysed using multiple unpaired t-tests with Welch's correction. The dotted line indicates ANGII minipump implantation. B) MAP at day/night 0 and day/night 14 for WT and R-Ras KO mice, analysed using a two-way ANOVA with Sidak's multiple post-hoc. Circles represent males, squares represent females. *N* = 3 – 6, see Table 4.4. **p < 0.01, ***p < 0.001.

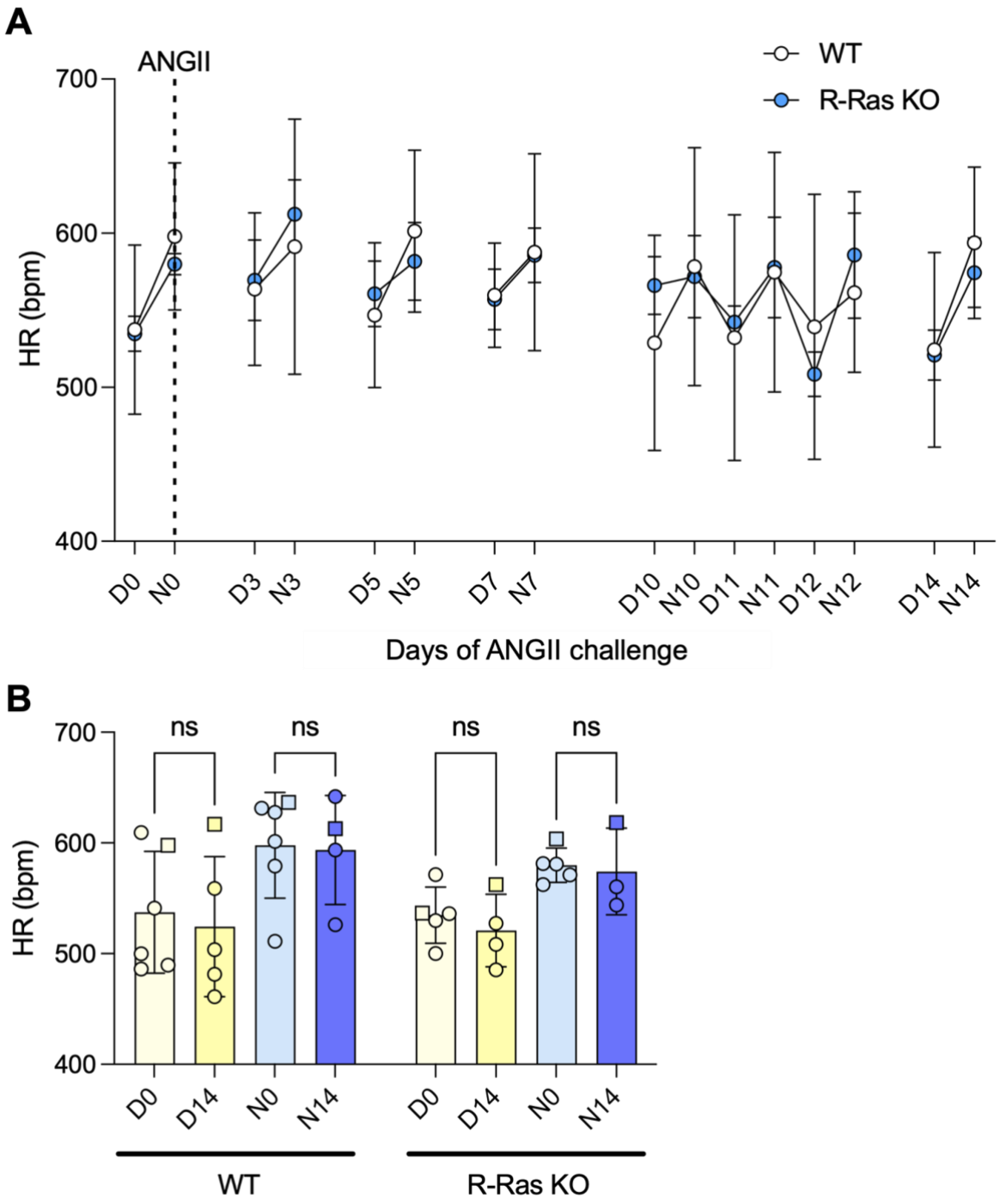

Figure 4.7. HR of WT and R-Ras KO mice with ANGII challenge. A) Diurnal HR of WT and R-Ras KO mice over 14 days of ANGII challenge, analysed using multiple unpaired t-tests with Welch's correction. The dotted line indicates ANGII minipump implantation. B) HR at day/night 0 and day/night 14 for WT and R-Ras KO mice, analysed using a two-way ANOVA with Sidak's post-hoc test. Circles represent males, squares represent females. *N* = 3 – 6, see Table 4.4.

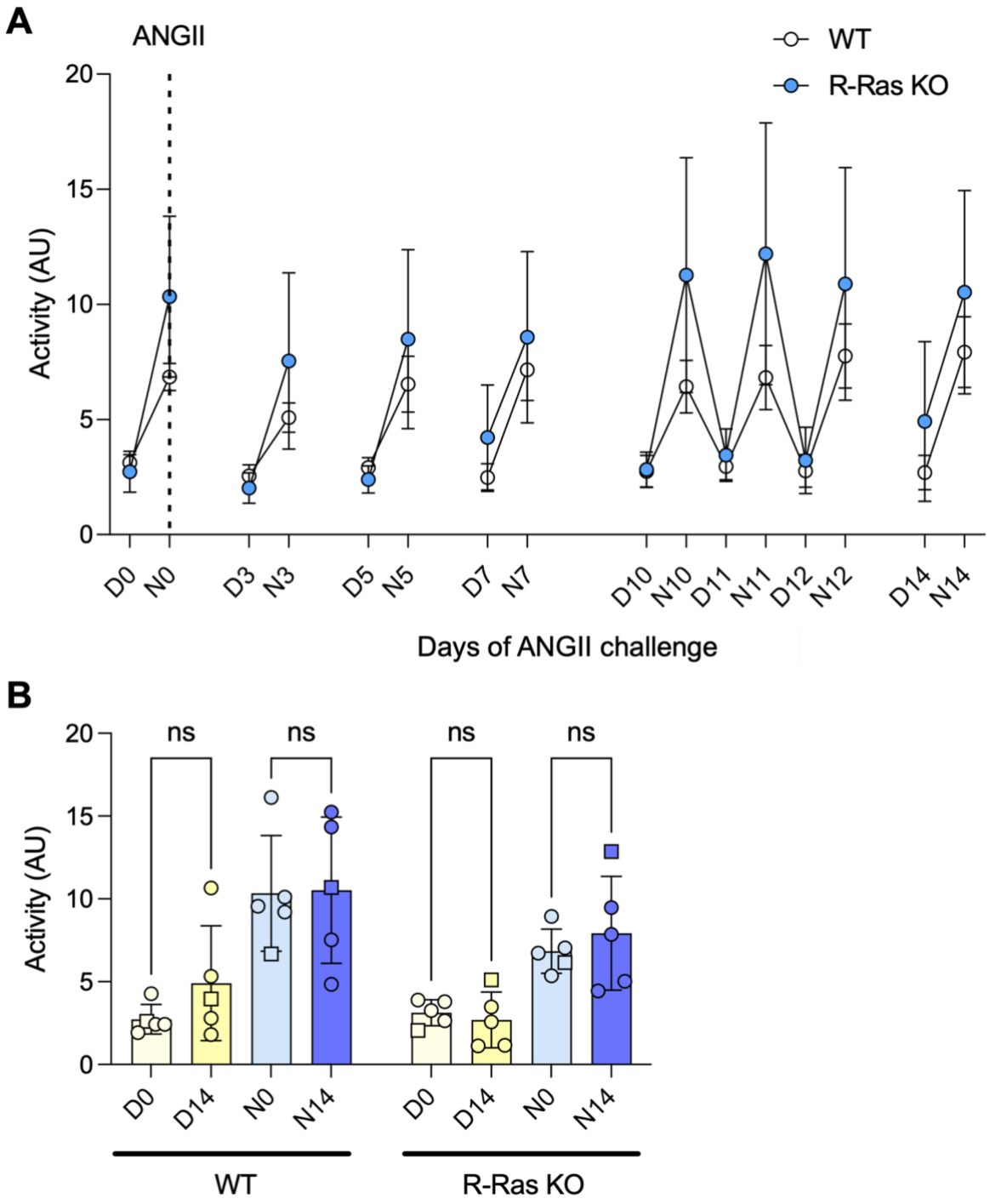

Figure 4.8. Activity of WT and R-Ras KO mice with ANGII challenge. A) Diurnal SBP of WT and R-Ras KO mice over 14 days of ANGII challenge, analysed using multiple unpaired t-tests with Welch's correction. The dotted line indicates ANGII minipump implantation. B) SBP at day/night 0 and day/night 14 for WT and R-Ras KO mice, analysed using a two-way ANOVA with Sidak's post-hoc test. Circles represent males, squares represent females. *N* = 5 – 6.

Table 4.3. Mean SBP, DBP and MAP of WT and R-Ras KO mice challenged with ANGII.

	SBP (mmHg)		DBP (mmHg)		MAP (mmHg)	
	WT	**R-Ras KO**	**WT**	**R-Ras KO**	**WT**	**R-Ras KO**
D0	112.65 ± 2.13	111.59 ± 4.79	89.14 ± 4.18	83.65 ± 1.89	94.21 ± 2.46	96.40 ± 3.79
N0	123.37 ± 1.25	123.43 ± 2.96	94.13 ± 3.01	89.79 ± 1.93	104.54 ± 3.42	106.75 ± 2.25
D3	112.73 ± 4.75	125.72 ± 7.70	86.42 ± 2.17	93.47 ± 7.01	100.57 ± 3.26	107.62 ± 7.67
N3	125.95 ± 3.43	133.78 ± 5.56	98.05 ± 2.41	101.67 ± 4.06	114.55 ± 3.51	116.34 ± 4.55
D5	118.40 ± 5.45	125.69 ± 3.22	89.33 ± 3.20	94.22 ± 2.60	103.62 ± 4.07	109.65 ± 2.82
N5	131.07 ± 4.97	134.34 ± 3.91	101.19 ± 3.66	102.78 ± 2.90	115.84 ± 2.93	117.99 ± 2.78
D7	117.52 ± 3.97	124.78 ± 3.86	87.51 ± 3.41	93.01 ± 2.50	102.97 ± 2.87	108.49 ± 1.94
N7	131.27 ± 3.53	136.50 ± 2.11	99.98 ± 3.85	102.33 ± 3.07	115.42 ± 3.04	119.00 ± 1.85
D10	124.02 ± 2.40	123.61 ± 5.31	92.85 ± 3.95	91.47 ± 1.22	108.01 ± 2.26	107.84 ± 3.13

N10	140.72 ± 3.86	139.87 ± 2.07	106.65 ± 3.13	105.15 ± 1.82	123.14 ± 2.57	122.01 ± 1.22
D11	123.74 ± 5.24	125.46 ± 5.41	94.06 ± 2.04	92.38 ± 2.56	108.74 ± 2.86	109.15 ± 3.42
N11	141.74 ± 3.88	140.53 ± 2.01	108.44 ± 4.05	107.53 ± 3.57	124.62 ± 2.95	122.97 ± 2.39
D12	125.46 ± 5.43	126.77 ± 4.06	96.24 ± 2.15	94.94 ± 1.01	112.11 ± 1.50	110.47 ± 2.11
N12	143.94 ± 4.07	141.68 ± 3.12	106.01 ± 2.50	106.74 ± 0.91	125.41 ± 2.58	124.14 ± 3.10
D14	129.16 ± 6.17	130.44 ± 4.64	98.72 ± 2.83	98.83 ± 1.84	112.34 ± 3.40	112.88 ± 3.24
N14	143.72 ± 4.06	151.67 ± 0.74	107.12 ± 3.67	112.30 ± 2.58	123.49 ± 1.75	128.59 ± 3.29

Data is expressed as mean ± SEM. *N* = 3 – 6, see Table 4.4.

The actual number of mice from which recordings were included per day of ANGII challenge varied due to complications including loss of signal, dislodgement of the telemetry catheter, or mortality (Table 4.4). This resulted in a reduction in power in the analysis of the study however, mean SBP, DBP, and MAP values were consistently higher in R-Ras KO mice than WT mice (Tables 4.2 and 4.3, Figures 4.2 and 4.4 – 4.8). I therefore tested for a trend in elevated BP using linear mixed model (LMM), to account for inter-individual variance of mice within genoty–e - the random effect. Fixed effects were genotype (WT or KO), days of ANGII challenge and diurnal differences (day vs. night).

Table 4.4. Number of WT and R-Ras KO mice across days of ANGII challenge.

		Day of ANGII challenge							
Genotype	**D/N**	**0**	**3**	**5**	**7**	**10**	**11**	**12**	**14**
WT	**D**	6	5	6	6	6	5	6	6
	N	6	5	6	6	6	5	6	4
KO	**D**	5	5	5	4	4	4	4	4
	N	5	5	5	4	4	4	4	3

LMM detected a diurnal difference, with higher SBP, DBP and MAP in the night than day, when mice are active (Figure 4.9, Table 4.5). The 95% confidence intervals (CIs) did not overlap and the effect of night vs. day appeared strong, evidencing a diurnal difference in SBP, MAP, DBP and HR (Figure 4.10). This was observed across baseline and all durations of ANGII treatment. Furthermore, in line with the previous analysis (Figures 4.4 – 4.6, Table 4.3), ANGII challenge over 14 days increased SBP, DBP, and MAP over time (Figures 4.9.A – C and 4.10.A – C). Interestingly, LMM visualisation shows a decline in HR with ANGII challenge (Figures 4.9.D and 4.10.D), which was not as apparent in previous analysis (Figure 4.7).

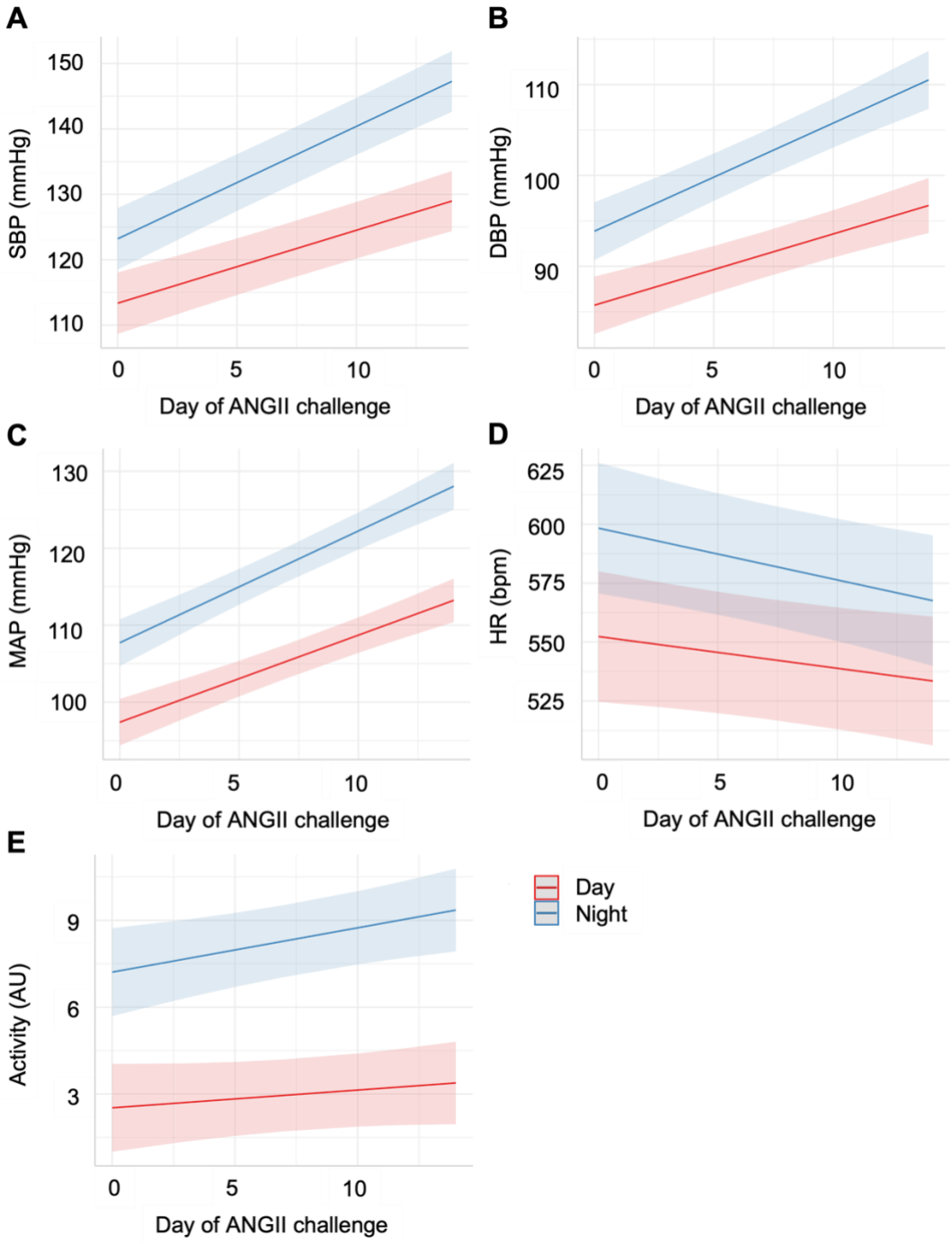

Figure 4.9. Linear mixed model regression plots of A) SBP, B) DBP, C) MAP, D) HR and E) Activity from all mice (WT and R-Ras KO) during the day (red) and night (blue) over days of ANGII challenge. LMM was carried out in R using lme4 package, and plots were plotted using the ggeffects package with an unfixed slope. Shaded areas indicate 95% confidence intervals. *N* = 5 – 6.

Fixed effects estimate values from LMM analysis suggested overall R-Ras KO mice had higher SBP and MAP values compared to WT mice, after ANGII challenge. However, DBP and HR were higher in WT than KO mice (Table 4.5). Plotting the trends with 95% CIs indicated a weak genotype effect, varying over days of ANGII challenge. Furthermore, 95% CIs were large and overlapping and therefore it cannot concluded that there is an effect of genotype on SBP, DBP, MAP or HR (Figure 4.10).

Table 4.5. Fixed effects estimate values from linear mixed model regression performed on SBP, DBP, MAP and HR diurnal data from radiotelemetry experiments on R-Ras WT and KO mice, with ANGII treatment.

	SBP (mmHg)	DBP (mmHg)	MAP (mmHg)	HR (bpm)	Activity (AU)
WT vs. KO	-3.01 ± 5.09	0.73 ± 3.23	-2.23 ± 3.18	10.23 ± 28.96	0.96 ± 1.49
Day of ANGII challenge	1.28 ± 0.26	0.98 ± 0.23	1.08 ± 0.24	-1.12 ± 1.03	0.05 ± 0.09
Night vs. Day	9.85 ± 1.63	8.15 ± 1.62	10.32 ± 1.75	45.98 ± 9.14	4.69 ± 0.73

Fixed effect estimate values correspond to graphs in Figures 4.9 and 4.10. Data is expressed as fixed effect estimate ± SEM. $N = 3 – 6$.

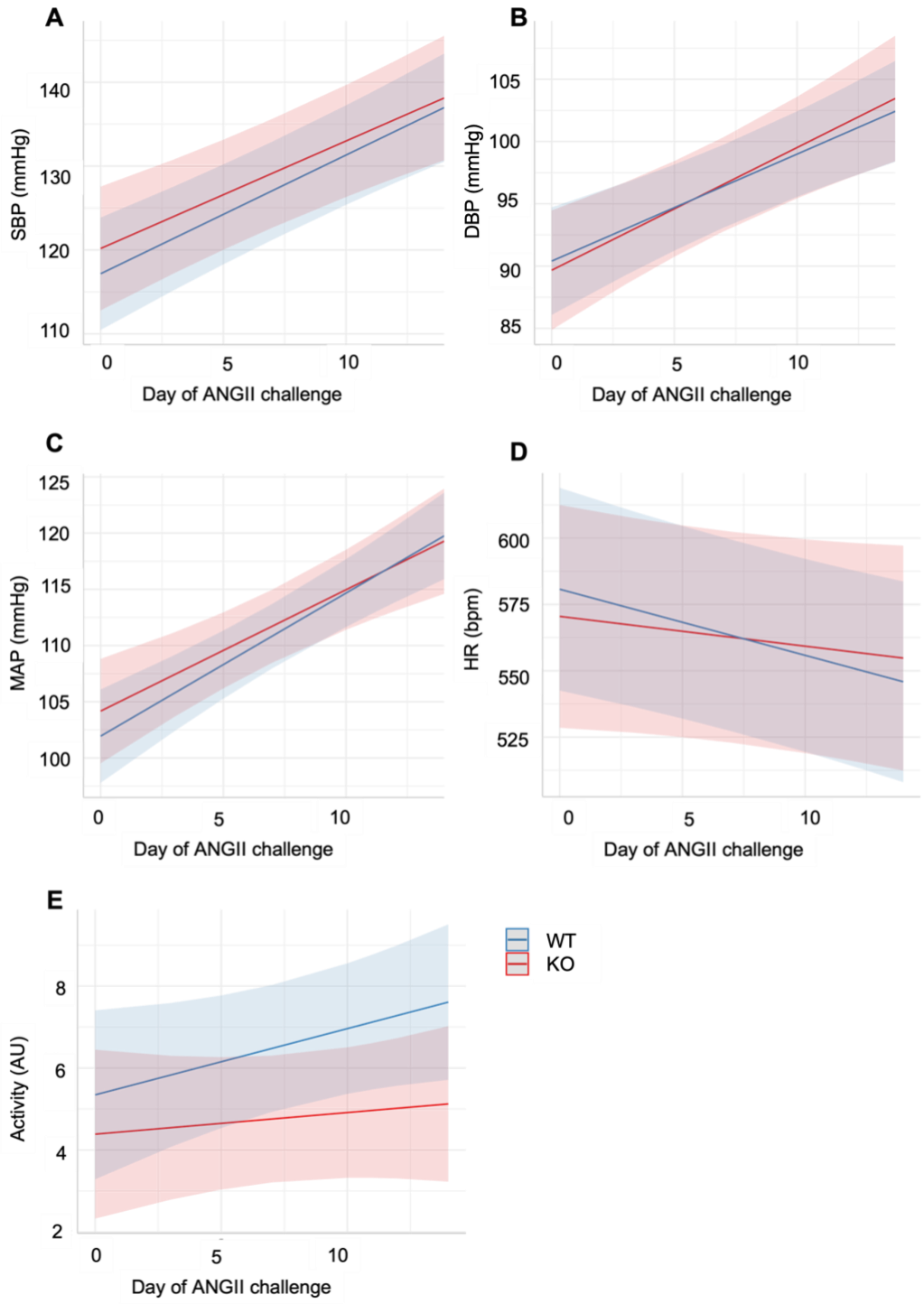

Figure 4.10. Linear mixed model regression plots of A) SBP, B) DBP, C) MAP, D) HR and E) activity from WT (blue) and R-Ras KO (red) mice over days of ANGII challenge. LMM was carried out in R using lme4 package, and plots were plotted using the ggeffects package with an unfixed slope. Shaded areas indicate 95% confidence intervals. *N* = 5 – 6.

4.2.4. The ANGII-induced hypertension model was successful

Aortic wall thickening, cardiac fibrosis and loss of vascular reactivity are hallmark features of the ANGII-induced hypertensive mouse model [334,335]. To establish whether ANGII-challenge successfully induced aortic wall thickening, and to explore potential differences between WT and R-Ras KO mice, histology was performed on mouse aortas and hearts and organ bath studies were carried out to assess vasodilatory and vasocontractile properties of the mouse aorta.

Aortas were stained with Masson's trichrome staining to visualise collagen (blue), cytoplasm (red) and nuclei (black), and aortic wall thickness measured (Figure 4.11). ANGII treatment increased aortic wall thickness, in both WT and KO mice (WT = 54.22 µm ± 0.89 v WT + ANGII: 64.38 µm ± 0.72, KO = 50.84 µm ± 2.12, KO + ANGII = 66.22 µm ± 4.04). One-way ANOVA with Tukey's post-hoc test found this increase with ANGII challenge was only significant in R-Ras KO mice ($p = 0.0019$, $n = 3 – 5$), however, in WT mice, the p value is close to significance ($p = 0.0558$, $n = 4 – 5$). There was no significant difference between WT and R-Ras KO mouse aortic wall thickness without ANGII challenge ($p = 0.6928$, $n = 5$), or with ANGII challenge ($p = 0.9582$, $n = 3 – 4$) (Figure 4.11.B).

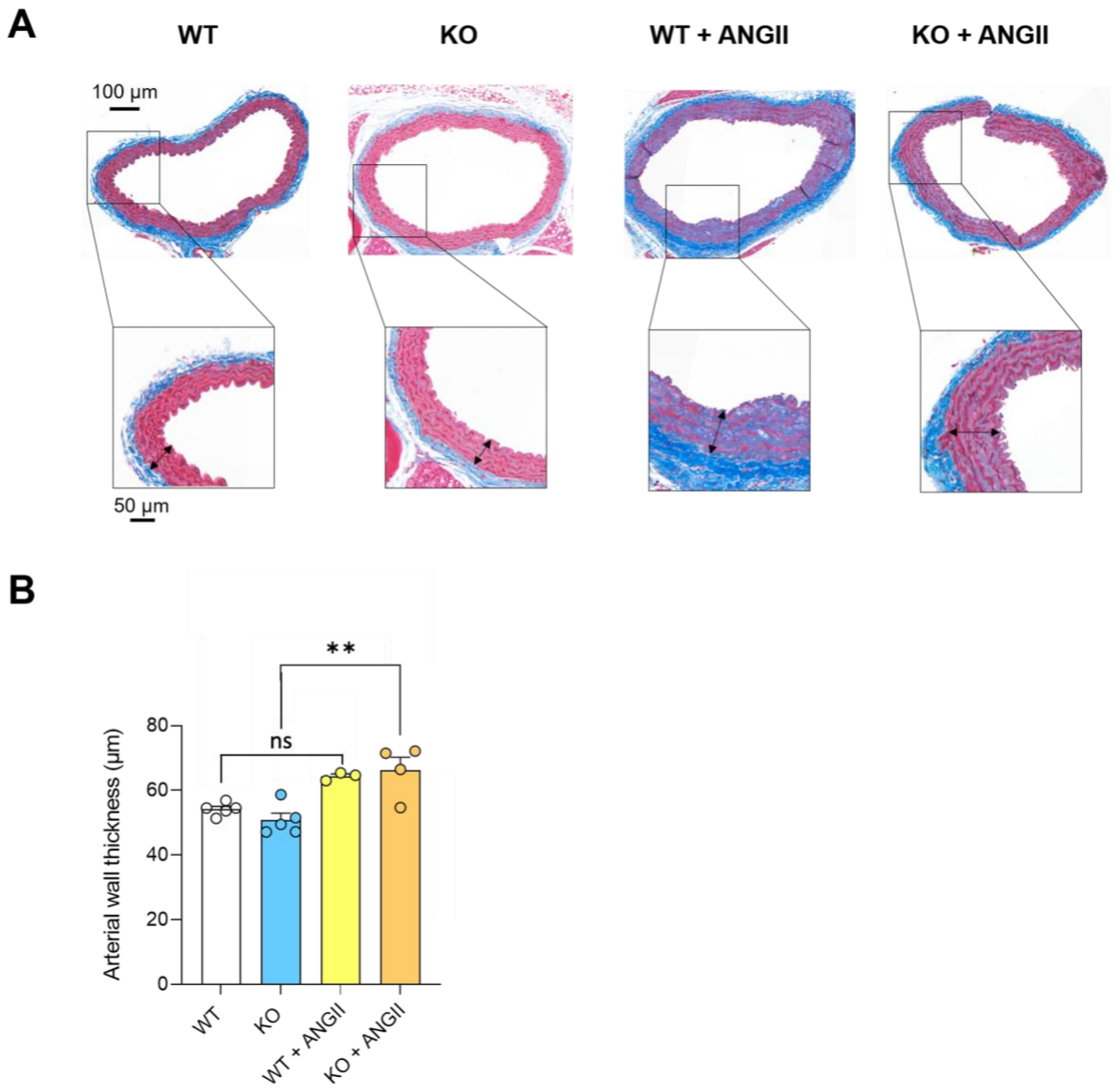

Figure 4.11. Aortic wall thickness. Aortas were sectioned and stained with Masson's trichrome. A) Images were acquired using the Pannoramic 250 scanner, and viewed using CaseViewer software. The whole cross-sectional image was taken at 8x magnification, and the enlarged image at 30x magnification. Arrows indicate measurement of the aortic wall. B) Aortic wall thickness was measured 10 times per sample and averaged. Significant differences between mean aortic wall thickness were calculated using a one-way ANOVA with Tukey's post hoc test. * = $p < 0.05$, ** = $p < 0.01$. *N* =–3 - 5.

Hearts were sectioned longitudinally and stained with Picrosirius Red to visualise collagen fibres as an indication of fibrosis (Figure 4.12.A). % fibrosis was calculated as the percentage of red stained area compared to the whole tissue area (Figure 4.12.B). ANGII challenge increased % fibrosis in WT and R-Ras KO mouse hearts (WT = 2.33% ± 0.64, WT + ANGII = 14.71% ± 2.46, KO = 1.71% ± 0.62, KO + ANGII = 14.28% ± 1.71). This increase was significant as analysed with ANOVA with Tukey's post-hoc testing (WT vs. WT + ANGII p = 0.0002, KO vs. KO + ANGII = 0.0002, *n* = 5). There was no significant difference in % fibrosis between WT and R-Ras KO mouse hearts with and without ANGII challenge (WT vs. KO p = 0.9919, WT + ANGII vs. KO + ANGII p = 0.9973, *n* = 5).

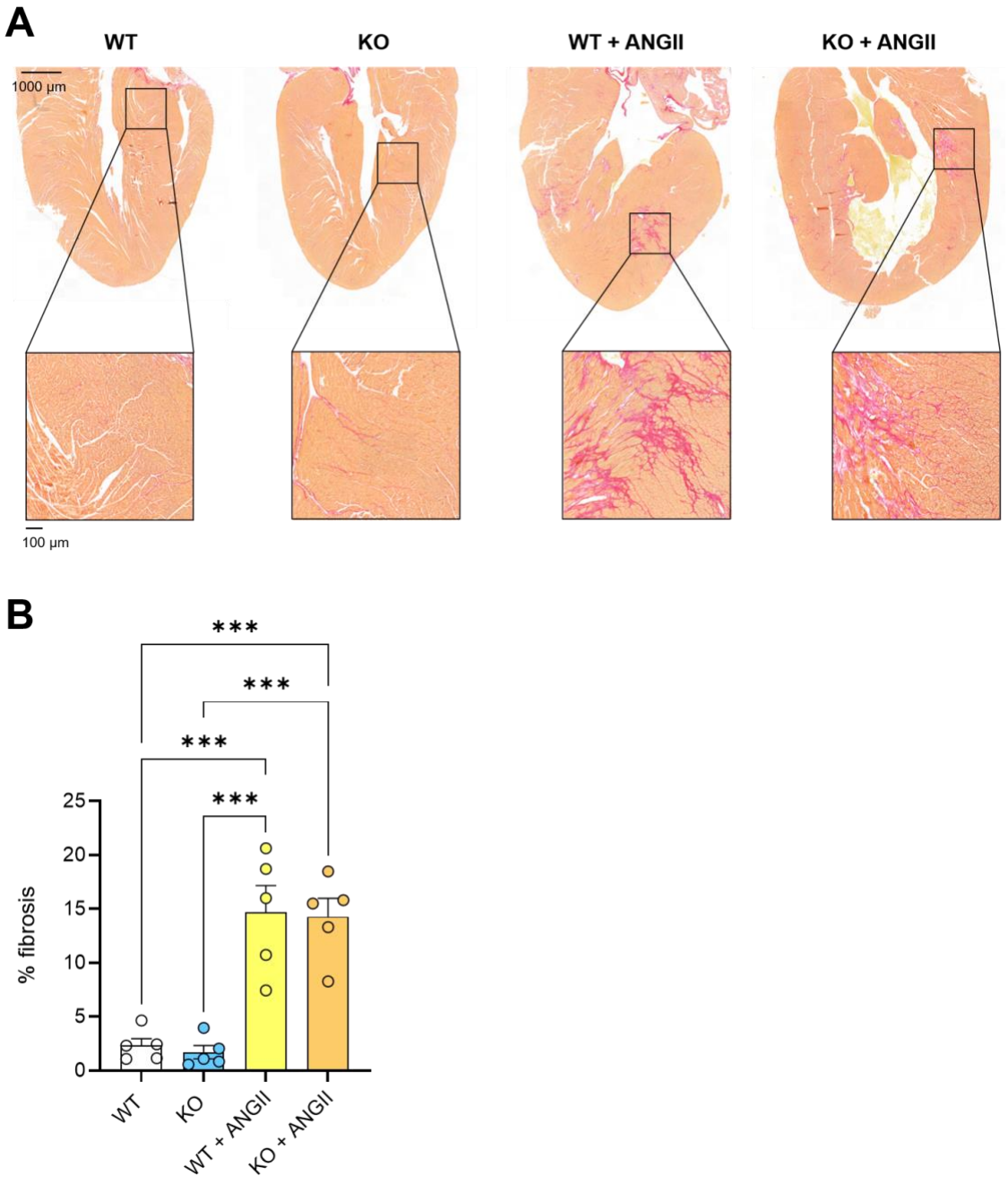

Figure 4.12. Picrosirius Red staining of WT and R-Ras KO mouse hearts with and without ANGII challenge to measure cardiac fibrosis. Hearts were sectioned longitudinally and stained with Picrosirius Red to visualise collagen. A) Images were acquired using the Pannoramic 250 scanner and viewed using CaseViewer software. The whole cross-sectional image was taken at 1x magnification, and the enlarged image at 20x magnification. B) Mean % fibrosis was quantified by comparing to the total amount of tissue using colour thresholding in ImageJ software. Data is expressed as mean ± SEM and analysed with one-way ANOVA with Tukey's post hoc test. *** = $p < 0.001$. *N* = 5.

4.2.5. Active R-Ras upregulates eNOS phosphorylation in endothelial cells

The original hypothesis of this study states that R-Ras promotes vasodilation via activation of the PI3K/Akt signalling pathway in ECs, resulting in phosphorylation and activation of eNOS, and subsequent NO production. Prior to investigating this hypothesis in the R-Ras KO mouse model (Chapter 4.2.6), I studied the impact of R-Ras on NO signalling *in vitro*.

HUVECs were transfected with the constitutively active (R-Ras38V) mutant of R-Ras using the Nucleofection Amaxa system (Lonza, Switzerland). HUVECs were co-transfected with green fluorescent protein (GFP) to allow confirmation of protein expression in cells with immunofluorescence microscopy (Figure 4.13). Fluorescent imaging detected GFP expression throughout the cell, indicating successful transfection. Furthermore, a transfection efficiency of around 60% was estimated by comparison with brightfield imaging (Figure 4.13).

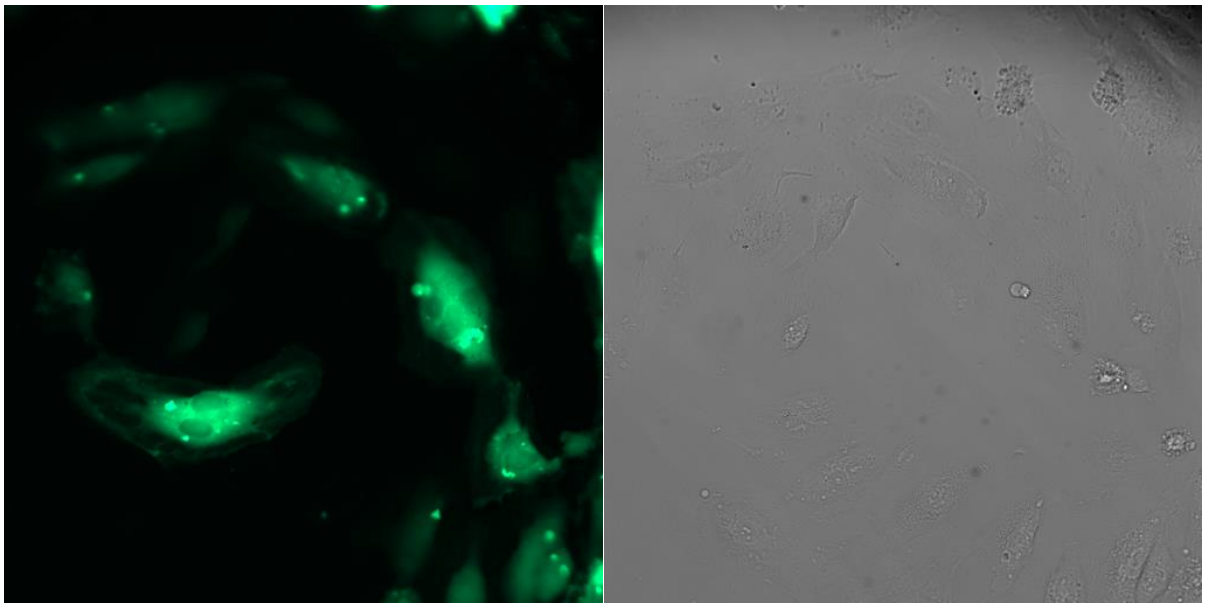

Figure 4.13. Fluorescent and brightfield confocal microscopy images of GFP-transfected HUVECs. HUVECs co-transfected with GFP and R-Ras38V were plated onto glass bottom microwell dishes and imaged using a Nikon Eclipse TE200 inverted microscope 48 h post-transfection. Cells were imaged using a wide-field fluorescent microscope with a GFP filter cube to detect GFP fluorescence (left), and with brightfield illumination (right). Images were processed with Fiji (ImageJ).

The formation of NO from L-arginine in endothelial cells is catalysed by eNOS, which is activated by phosphorylation. eNOS is activated by phosphorylation at Ser1177 via Akt [336], a downstream signalling molecule of R-Ras. Western blotting was used to detect phosphorylation of eNOS at Ser1177 (phospho-eNOS, Ser1177) in HUVEC lysates transfected with R-Ras38V to explore the effect of R-Ras activity on NO signalling. HUVECs were stimulated with VEGF, known to result in phosphorylation of eNOS at Ser1177 via PI3K/Akt signalling, as a positive control.

HUVECs were serum starved for 24 h before treatment with VEGF (100 ng/mL) or 10% DMSO for 30 min as a positive and negative control, respectively, or transfected with 5 μg GFP or R-Ras38V. Blots were probed with anti-GAPDH to control for loading differences. Incubation with phospho-eNOS (Ser1177) (BD Sciences) resulted in bands at 140 kDa in VEGF-treated, and GFP- and R-Ras38V transfected cells upon chemiluminescent imaging (Figure 4.14.A). A band was not detected for phospho-eNOS (Ser1177) in untransfected control cells treated with DMSO, but a band was detected in GFP-transfected cells, suggesting transfection caused baseline phosphorylation of eNOS (Figure 4.14.A). Blots were probed with anti-eNOS (BD Sciences) to measure total eNOS levels, and a band was present in all cell lysates (Figure 4.14.A). Phospho-eNOS bands were normalised against eNOS bands to ensure changes in phospho-eNOS levels were the result of differences in phosphorylation and not abundance of eNOS in the lysate. The mean normalised signal was greater in R-Ras38V transfected HUVEC (2.02 AU) compared to the GFP control (0.927 AU) (Figure 4.14.B). Probing with anti-RRAS (CST) confirmed transfection with R-Ras38V (Figure 4.14.A).

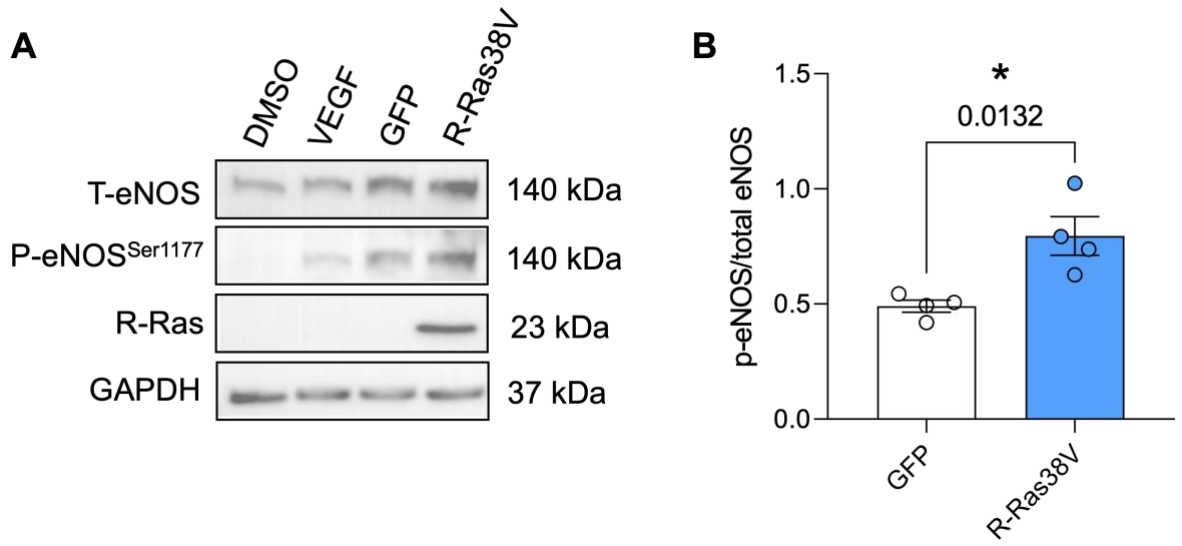

Figure 4.14. Western blot analysis of expression of phospho-eNOS (Ser1177) in HUVECs. HUVECs were treated with DMSO (10%) or VEGF (100 µM) after serum starvation for 24 h or transfected with GFP (control) or R-Ras38V. Protein samples of cell lysates were prepared and 30 µg of protein/sample run on 8% gels. Blots were probed with anti-phospho-eNOS (Ser1177) (1:200, BD Sciences), anti-RRAS (1:1000, CST, UK), anti-eNOS (1:1000, BD Sciences) and GAPDH as a loading control (1:1000, CST, UK). A) Protein bands obtained with chemiluminescent imaging. B) Normalised signal quantified as described in methods. *N* = 3.

4.2.6. Normal vasodilatory and contractile responses of R-Ras KO mouse aortas

Following the observation that R-Ras potentiates eNOS activity *in vitro* (section 4.2.5), and the high expression of R-Ras in the aorta [203], and ECs and VSMCs [204], I hypothesised the vasodilatory response would be attenuated in mouse aorta with R-Ras KO. The vasodilation and vasocontraction response of mouse aortas from mice aged 12 – 16 weeks was assessed using the organ bath. WT and KO mouse aortas were pre-contracted with U46619, and cumulative concentration response curves (CRCs) carried out with acetylcholine (ACh) to assess vasodilation (Figure 4.15.A). U46619 is a thromboxane A2 (TxA2) receptor agonist that stimulates VSM contraction via a G_q-coupled pathway leading to an increase in intracellular calcium, and via a $G_{12/13}$-coupled pathway inhibiting myosin light chain phosphatase via Rho Kinase activation [337]. ACh acts on endothelial G_q-coupled m3AChRs to stimulate activation of the PI3k-Akt pathway leading to phosphorylation of eNOS and subsequent NO formation and release. The ACh CRCs for WT and R-Ras KO aortas were the

same, and mean IC_{50} and R_{Max} values did not differ (Figure 4.15.A – C, Table 4.6). U46619 CRCs were also carried out to assess vasocontraction (Figure 4.4.D). These were the same for WT and R-Ras KO mouse aortas and EC_{50} values were not significant different (Figure 4.15.D and E, Table 4.6).

Chronic ANGII infusion induces endothelial dysfunction, thereby attenuating endothelium-mediated vasodilation [75]. In WT and R-Ras KO mice challenged with ANGII, CRCs were significantly shifted to the right (Figure 4.15.A). The IC_{50} values were higher with ANGII challenge, and the maximum inhibition of U46619-precontraction was significantly reduced (Figure 14.15.B and C, Table 4.6). The vasocontractile response of WT and R-Ras KO aortas to U46619 did not change with ANGII challenge (Figure 14.15.D and E, Table 4.6).

Table 4.6. Mean IC_{50}, R_{Max} and EC_{50} values calculated from acetylcholine and U46619 concentration response curves in WT and R-Ras KO mouse aortas with ANGII challenge.

Drug	Parameter	WT	KO	WT + ANGII	KO + ANGII
ACh	**IC_{50} (μM)**	0.03 ± 0.01	0.05 ± 0.01	0.89 ± 0.3	1.35 ± 0.6
	R_{Max} (%)	24.2 ± 2.9	25.3 ± 0.6	55.7 ± 11.1	57.9 ± 6.8
U46619	**EC_{50} (nM)**	8.25 ± 1.2	8.92 ± 1.3	6.33 ± 1.1	6.87 ± 3.1

IC_{50} was calculated as the concentration of acetylcholine needed for 50% of the maximum relaxation of aortic rings pre-contracted with U46619. R_{Max} is the maximum % inhibition of the U46619 pre-contraction by ACh. EC_{50} is the U46619 concentration required for 50% of the maximum U46619 contraction. Data is expressed as mean ± SEM. *N* = 5 – 10.

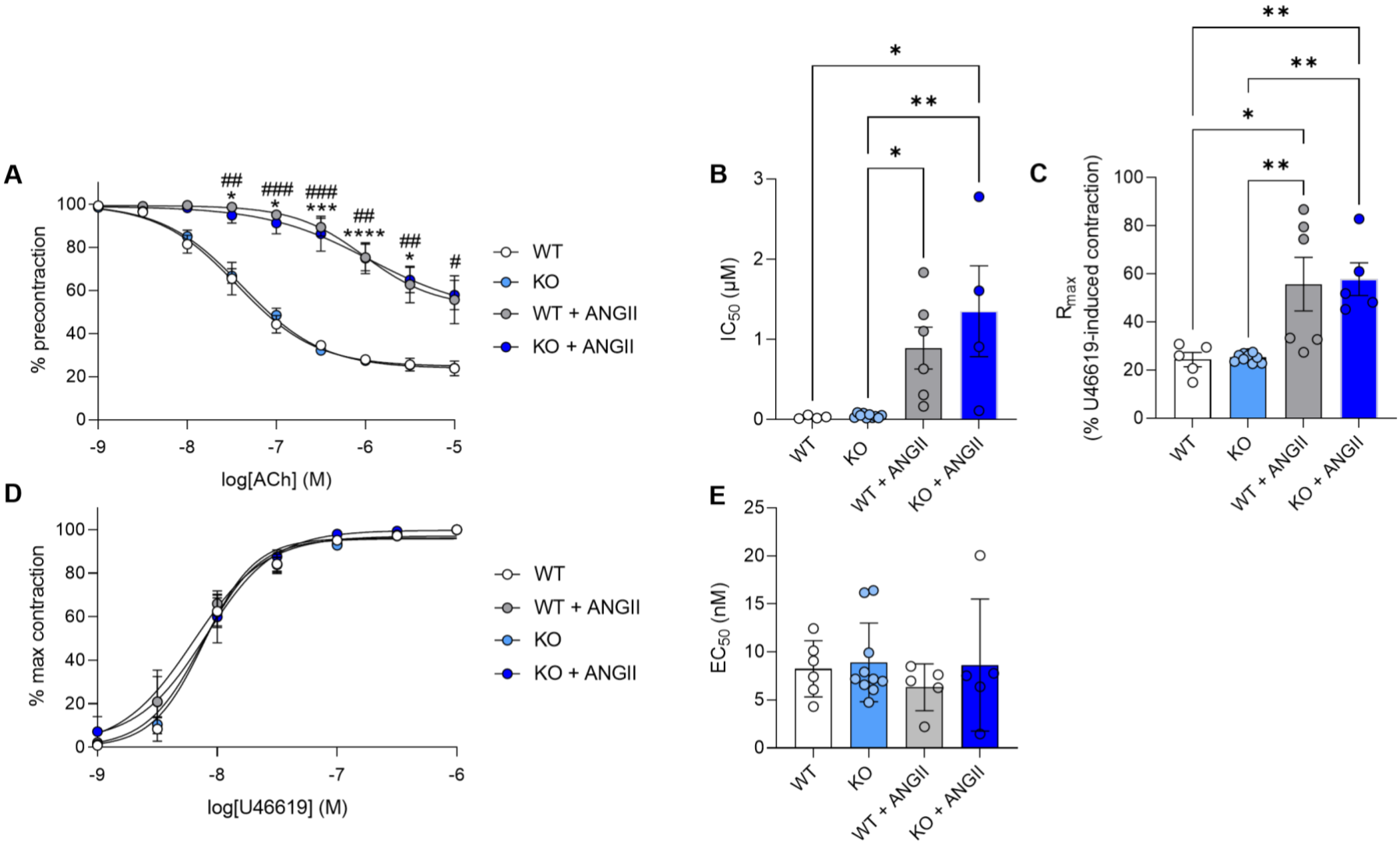
A
% precontraction
log[ACh] (M)
WT
KO
WT + ANGII
KO + ANGII
B
IC50 (μM)
C
Rmax
(% U46619-induced contraction)
D
% max contraction
log[U46619] (M)
E
EC50 (nM)

Figure 4.15. Vascular reactivity of WT and R-Ras KO aortas with and without ANGII challenge. Aortas from 10 to 12-week-old WT and R-Ras KO mice, and mice challenged with ANGII (1.1 mg/kg/day) for 14 days, were mounted in an organ bath. A) A cumulative acetylcholine (ACh) concentration response curve (CRC) was performed in aortic rings pre-contracted with U46619 to measure the relaxation response of the aorta (1 nM – 10 µM). Mean IC_{50} (B) and R_{Max} (C) were calculated from individual ACh CRCs. % precontraction was calculated as the % of U46619-precontraction. D) Cumulative U46619 CRCs (1 nM – 1 µM). E) Mean EC_{50} values calculated from individual U46619 CRCs in (D). % contraction for U44196 CRCs was calculated as % maximum U46619 contraction. Data is expressed as mean ± SEM. CRCs were analysed using a two-way ANOVA with Sidak's post-hoc test. WT vs. WT + ANGII * = $p < 0.05$, *** = $p < 0.001$, **** = $p < 0.0001$, KO vs. KO + ANGII # = $p < 0.05$, ## = $p < 0.01$, ### = $p < 0.001$. Mean EC_{50} and R_{Max} values were compared using a one-way ANOVA with Tukey's post-hoc testing. * = $p < 0.05$, ** = $p < 0.01$. *N* = 5 – 10.

4.2.7. R-Ras KO promotes aortic sprouting

To confirm the pro-angiogenic effect of R-Ras KO observed in previous mouse models [269,297,320–322], the aortic ring angiogenesis assay was performed on aortas from WT and R-Ras KO mice aged 8 weeks (Figure 4.16). In the absence of VEGF (control), R-Ras KO mouse aortas had significantly more aortic sprouts after 7 days than WT, as analysed using a one-way ANOVA with Tukey's post-hoc test (Figure 4.16, WT = 8.1 ± 0.7, KO = 20.4 ± 1.6, $p = 0.02$). VEGF-treatment significantly increased aortic sprouting in both WT and R-Ras KO aortas (Figure 4.16, WT control vs. WT + VEGF, $p = 0.0007$, KO control vs. KO + VEGF, $p < 0.0001$). R-Ras KO aortas had more aortic sprouts at day 7 of VEGF (30 ng/µL) treatment than WT (Figure 4.16, WT = 27.2 ± 3.6, KO = 52.8 ± 2.8, $p < 0.0001$). Moreover, untreated R-Ras KO mouse aortas and WT aortas treated with VEGF had comparable levels of aortic sprouting (Figure 4.16, $p = 0.26$).

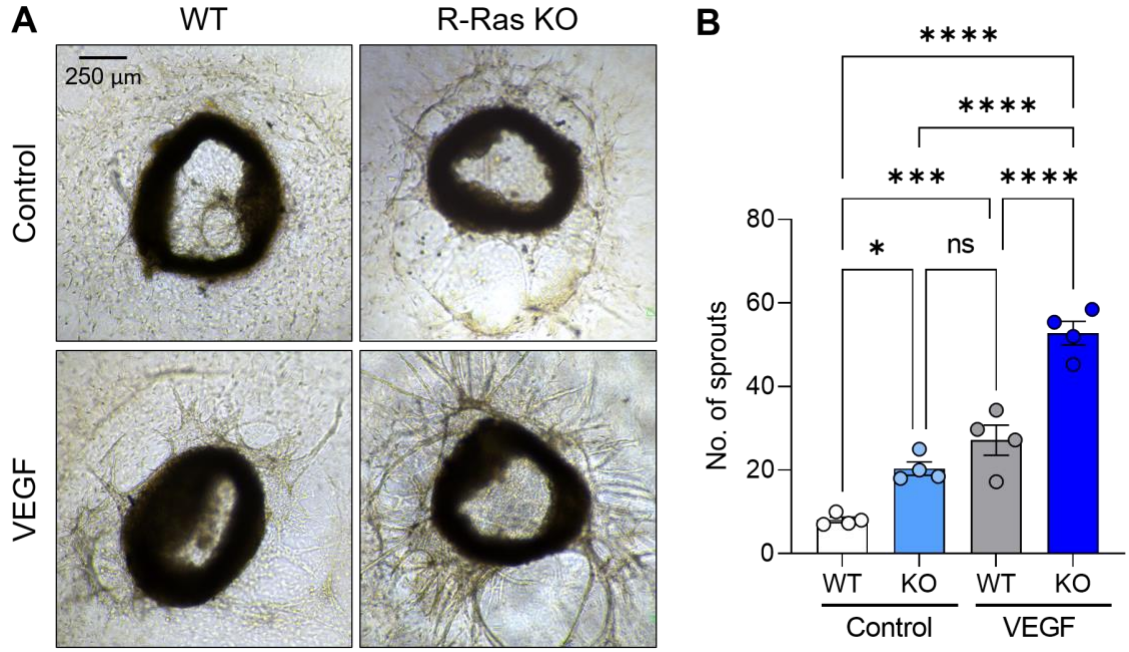

Figure 4.16. **R-Ras KO increases novel sprout formation in the aortic ring assay.** Aortic rings from 8-week-old WT and R-Ras KO mice were embedded in Matrigel and incubated with Opti-MEM supplemented with PBS (control) or VEGF (30 ng/µL) for 7 days. Mouse n = 4, aortic rings ~15/mouse. A) Images were taken at day 7 using a Nikon Eclipse Ts100 microscope at 4 x magnification. B) The mean number of aortic sprouts was compared using a one-way ANOVA with Tukey's post-hoc test. * = $p < 0.05$, *** = $p < 0.001$, **** = $p < 0.0001$.

4.2.8. R-Ras KO mice have normal organ morphology

As this is the first study to use the Rras-DEL415 mouse model to look at blood pressure, I characterised the gross organ morphology of the R-Ras KO mouse. The hearts, kidneys, spleens, and lungs from mice aged 12 – 15 weeks were weighed and normalised to tibia length (Figure 4.17). There was no significant difference in body weight, normalised heart, kidney, or spleen weight between WT and R-Ras KO mice (Figure 4.17.A – D). Wet to dry lung weight ratio was calculated and used as a measure of lung fluid retention, an indicator of pulmonary oedema. This was the same between WT and R-Ras KO mice (Figure 4.17.E).

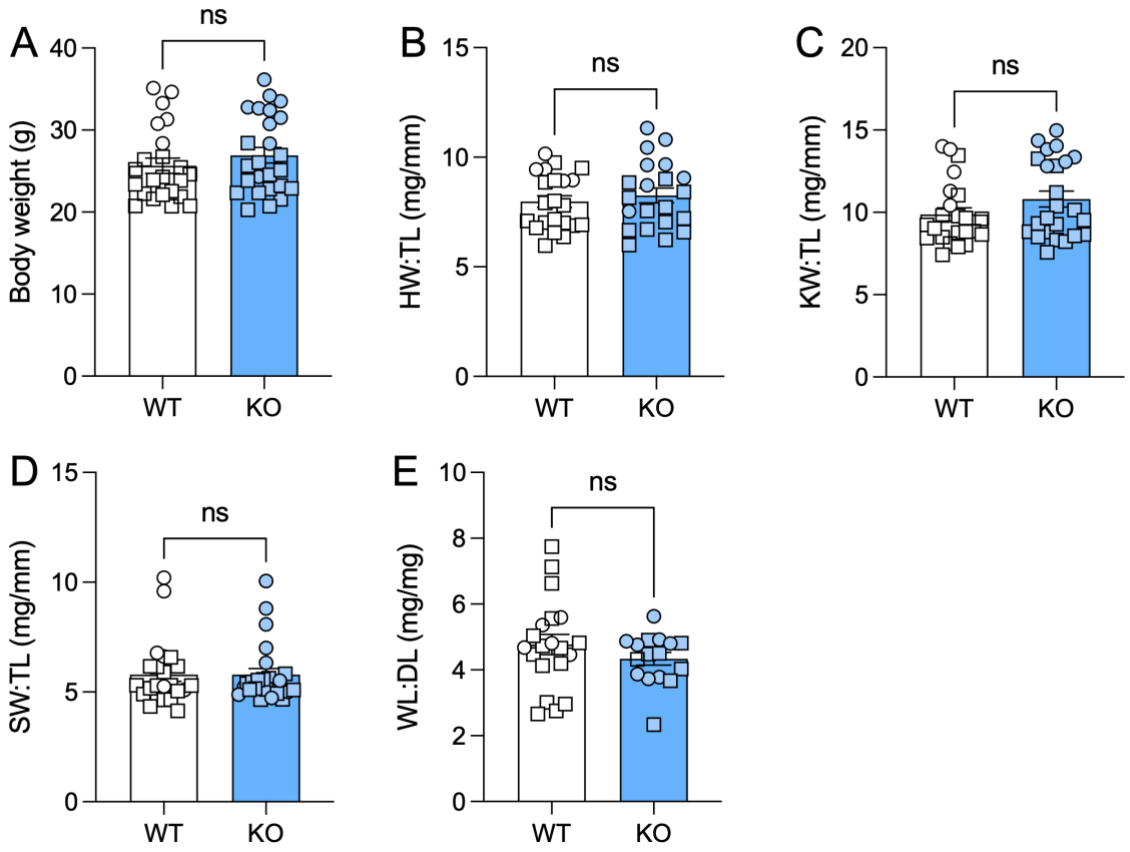

Figure 4.17. Body weight (A), normalised heart (B), kidney (C) and spleen (D) weight, and wet lung : dry lung weight ratio (E) in WT and KO R-Ras mice. Circles are male mice, and squares are female mice. Data is presented as mean ± SEM. Statistical differences between means were calculated using unpaired Student's t-test. *N* = 16 – 25.

4.3. Discussion

The R-Ras KO mouse model has been a valuable tool in R-Ras research *in vivo* [253,269,297,320–322]. This is the first study to investigate R-Ras in the context of blood pressure regulation and hypertension, and the first to use the Rras-DEL415 mouse (MRC Harwell).

To supplement the IMPC WT loss of allele assay to validate *Rras* WT allele deletion, I measured *Rras* expression using qPCR in the mouse kidneys. Using radiotelemetry I determined the young R-Ras KO mouse had a normal BP phenotype, in normotensive conditions and when challenged with ANGII to induce hypertension. Further, the aortas of young R-Ras KO mice exhibited normal vasodilatory and vasocontractile responses. I measured gross organ weight and morphology of the mouse to complement the IMPC phenotyping data [338], but found no change in the hearts, kidneys, spleen or the aorta of R-Ras KO mice. Finally, I replicated the pro-angiogenic effect of R-Ras KO seen in previous KO mouse models with the aortic ring assay. Overall, the results indicate the young R-Ras KO mouse exhibits a normal BP phenotype, contrary to our original hypothesis.

4.3.1. R-Ras is not essential for BP control in the young mouse or in ANGII-induced hypertension

Given the *RRAS* missense variant is associated with an increase in SBP in humans, I hypothesised R-Ras KO in the mouse would exhibit elevated BP. To investigate this, I implanted radiotelemetry probes in young adult (10 to 12 week) WT and R-Ras KO mice to allow continuous diurnal BP measurement. Young adult mice were investigated to explore whether R-Ras was essential for blood pressure control, even in non-hypertensive conditions. Contrary to the hypothesis, I observed normal SBP, DBP, MAP, and HR, in R-Ras KO. As expected, activity was higher in the night than day when mice are most active, and this correlated with increased BP and HR. Interestingly, young WT mice had significantly higher activity levels at night than R-Ras KO. To investigate whether mean BP or HR values were not confounded by increased levels of activity, the baseline data was corrected for activity. There remained no difference between young WT and R-Ras KO BP and HR phenotypes. However, it must be noted the method used to correct for activity was not a standardized, peer-reviewed method. Furthermore, the hypoactive phenotype of the young adult R-Ras KO mouse was not investigated further; repeated activity measurements are warranted to determine the reproducibility of this hypoactive phenotype, and establish this is not a result of

study conditions. Together, this data suggests that R-Ras is not essential for BP control in the young adult mouse.

I therefore considered whether the impact of R-Ras deletion on BP may become apparent in hypertensive conditions. Here the ANGII-induced hypertension model was used, an established rodent model of hypertension often used in conjunction with radiotelemetry [339]. It can be concluded that ANGII challenge was a successful model of hypertension; there was a clear upward trend with increasing days of ANGII challenge and BP parameters, as observed previously [334]. Furthermore, cardiac fibrosis, arterial wall thickening and attenuated aortic vasodilation was observed with ANGII challenge, as expected. A decline in HR with ANGII challenge was observed in the LMM visualisation, which was not as apparent in prior analyses, likely reflecting the baroreceptor reflex [335]. Comparable to normotensive conditions, there was no statistically significant difference in BP elevation between WT and R-Ras KO young mice treated with ANGII. However, there was a trend for R-Ras KO mice to have numerically increased values across SBP, DBP and MAP. I therefore hypothesised the complexity of the experimental design of the radiotelemetry studies with ANGII treatment required more sophisticated statistical analysis for full data interpretation. Interindividual variance between each mouse even within the same genotype will introduce a random effect that must be distinguished from fixed effects (ANGII treatment, day v night, genotype). Furthermore, repeated measures are taken from the same mouse over cumulative days of ANGII treatment, introducing non-independent data. To overcome this, LMM regression was applied which uses both random and fixed effects as predictor variables to account for non-independence. Visualisation of LMM suggests a trend of higher SBP in R-Ras KO mice, but inconsistent trends in MAP, DBP and HR. Despite WT mice initially appearing to have a higher DBP, at 5 days of treatment this trend is reversed. R-Ras KO mice initially appear to have higher MAP, until day 10 where the trend is reversed. MAP equals DBP + 1/3(SBP – DBP), and so it is interesting the trend is reversed at this point, inverse to the trend seen with DBP and SBP at 10 days. Moreover, HR appears to be decrease over days of ANGII infusion, with higher HR observed in WT than R-Ras KO mice initially, and reversal of this trend at day 7. Ultimately, large and overlapping 95% CIs do not allow a confident conclusion of an effect of R-Ras deletion on these parameters, suggesting R-Ras is unlikely to be involved in ANGII-related hypertension.

ANGII challenge is the gold-standard method to induce hypertension in mouse models [334,340], hence this model was chosen for this study. Acute systemic infusion of ANGII results in peripheral vasoconstriction via activation of AT1R in the vasculature, however the effects of chronic ANGII are mainly mediated by its central effects via stimulation of the RAAS

pathway, activation of the SNS [335,341], blunting of the baroreceptor flex [335], and oxidative stress [342], and the myogenic effect of ANGII loses significance [335]. Perhaps a BP phenotype is not observed with R-Ras KO as the impact of R-Ras on BP is mainly regulated in the vasculature. Other hypertensive models with a more dominant vascular mechanism, such as L-NAME infusion inhibiting NOS [343], may reveal differences between WT and R-Ras KO mouse BP phenotype in younger mice not apparent with ANGII challenge.

This radiotelemetric study has some limitations. Firstly, this study is limited by small *n* numbers, both at baseline and across days of ANGII challenge. Radiotelemetry is a gold-standard technique for long-term continuous recording of BP *in vivo* and is often implemented to compare BP phenotype in KO mouse models. Genetic variation in the *UMOD* gene encoding uromodulin (UMOD) was identified as associated with hypertension [344]. Telemetric BP recordings in adult 12 week UMOD KO mice detected a change in SBP of + 20 mmHg with an *n* of 6 [345]. Similarly, in telemetric studies of H-Ras KO mice, the "opposing sibling" of R-Ras, an *n* of 7 was required to detect a decrease of 13 mmHg in H-Ras KO mice, although the authors do not indicate the age at which these mice are studied [346]. The radiotelemetric BP data from WT and R-Ras KO mice failed at baseline to detect a difference in BP phenotype, with comparable *n* numbers to studies with UMOD and H-Ras KO mice. This could suggest that the magnitude of effect of R-Ras KO on BP in young mice is too small, and the study requires more *n* to reach sufficient power for detection. This limitation is also seen in the ANGII challenged model; *n* numbers fluctuate across days of ANGII challenge, decreasing toward the end of experiment due to complications with catheter dislodgement, signal loss, and mortality. Repeat experiments are required to establish whether a phenotype in young adult R-Ras KO mice, and with ANGII-induced hypertension, is actually present.

Secondly, there is substantial evidence for sex differences in blood pressure and hypertension, in humans and animals [347]. A telemetric study in FVN/B and C57BL/6 mice observed an average 5 ± 4 mmHg increase in MAP males vs. females aged 3 months [340]. Moreover, ANGII challenge increases BP to a greater extent in male mice than females; in C57BL/6J mice aged 12-16 week challenge with ANGII at 800 ng/kg/min over 7 days, elevations in MAP were substantially greater in males than females [335]. In the radiotelemetry study, an uneven number of female and male mice were included, potentially confounding results and masking differences in BP seen with R-Ras deletion. The current dataset is underpowered to perform separate analyses on each sex and repeat radiotelemetry experiments in each sex are essential to uncover any potential differences in BP between WT and R-Ras KO mice. Recent national guidelines introduced by the MRC (2021) outline the need for both sexes to be included in experimental research. However, given the human and

animal data supporting sex differences in BP, additional analyses stratified by sex (if sufficient power is reached) may still reveal a sex difference in relation to R-Ras.

4.3.2. R-Ras promotes NO signalling in vitro but is not essential for NO-mediated vasodilation in vivo

I hypothesised that, due to its expression in the aorta [323] and endothelial and VSM cell lines [324], R-Ras will have a role in vascular control of blood pressure. More specifically, R-Ras activates the PI3K/Akt axis [321,325–333] which potentiates vasodilation by NO signalling [27–29]. I therefore proposed R-Ras could potentiate NO production via activation of the PI3K/Akt signalling pathway in endothelial cells, promoting vasodilation. In *vitro* analysis of R-Ras signalling showed the potential of R-Ras to upregulate eNOS phosphorylation in endothelial cells. In *vivo,* acetylcholine stimulates NO production in endothelial cells via activation of M3AChR [348]. I therefore expected to see ablated vasodilatory responses of the R-Ras KO mouse aorta to acetylcholine addition. This was not observed in *ex vivo* organ bath studies, suggesting R-Ras is not essential for NO signalling in endothelial cells *ex vivo.* R-Ras is also expressed at high levels in VSMCs [204] and has been shown to modulate VSMC proliferation and angiogenesis [208,217,250,251], and so I proposed R-Ras may play a role in contraction of the VSM layer independent of the endothelial monolayer. However, there was no difference between contraction induced by U46619 in WT and R-Ras KO mouse endothelium denuded aortas. Finally, ANGII challenge inhibited the maximum ACh-induced vasodilation as expected, due to its known impact on endothelial dysfunction [73,74,349]. However, this was to the same extent in WT and R-Ras KO aortas. This is complementary to the radiotelemetry data, which saw no BP phenotype in the young adult R-Ras KO mouse. This could suggest that the impact of R-Ras KO on vascular BP control mechanisms may be masked by compensatory mechanisms in the young adult Rras-DEL415 mouse model.

In vivo BP is predominantly regulated by small resistance arterioles, while large arteries like the aorta are responsible for distribution of blood around the body [14]. In hypertension, persistent elevated BP is largely due to increased total peripheral resistance which is predominantly determined by the small resistance vessels [14]. Pathophysiological changes in small resistance vessels contribute to this, including arterial wall thickening and lumen narrowing [350], and endothelial dysfunction and oxidative stress [64,351]. In this study, aortas were used to assess endothelial dysfunction. Perhaps the vascular reactivity of smaller resistance vessels is altered in R-Ras KO mice; small vessel myography using mesenteric arteries from mice could explore this. Finally, elevated BP was observed in the aged R-Ras

KO mouse. It would be interesting to see whether the vascular reactivity of the aged mouse aorta is impacted by R-Ras KO, in line with the elevations in BP.

4.3.3. BP-related phenotypes in the Rras-DEL415 mouse

The anti-angiogenic role of R-Ras is well established *in vivo* [208,217,251,320]. I sought to confirm this phenotype in the Rras-DEL415 KO mouse using the *ex vivo* aortic ring assay. In line with previous data, R-Ras KO increased aortic sprouting, without an angiogenic stimulus, and in VEGF-induced angiogenesis. This is not a novel finding but instils confidence in the mouse model and further supports a role of R-Ras in signalling related to CV processes.

Normal body weight, and normalised heart and spleen weights observed in the Rras-DEL415 model are in line with IMPC reported phenotypes [338]. I additionally assessed kidney weights, and wet to dry lung ratio as an indication of pulmonary oedema (a symptom of pulmonary hypertension) but found no difference between age-matched WT and R-Ras KO mice. In hypertensive patients [352] and animal models [334,335,353], chronic elevations in BP lead to arterial wall thickening and cardiac fibrosis. This was observed in WT and R-Ras KO mice challenged with ANGII, corroborating previous literature [334,335,353]. However, no difference in arterial wall thickness or cardiac fibrosis was observed between genotype, in normotensive or hypertensive conditions. This is perhaps not surprising, as the telemetry studies found the BP of young adult R-Ras KO mice was the same as WT.

4.3.4. Conclusions and limitations

This study has not identified significant differences in the phenotype of the young adult Rras-DEL415 mouse with strong relations to BP. Furthermore, R-Ras KO does not appear to have a large effect on the vasodilatory or vasocontractile properties of the young adult mouse aorta. A BP phenotype in young adult R-Ras KO mice was not observed, in both normotensive and ANGII-induced hypertensive conditions; this is perhaps not too surprising, as cell signalling in the vasculature and globally is complex *in vivo*. It may be the lack of phenotype in these young adult mice can be explained by compensatory mechanisms at play.

There are limitations to this work in the young adult Rras-DEL415 mouse. Firstly, although *Rras* gene deletion was previously validated using a WT loss of allele assay, and in this thesis using qPCR in mouse kidneys, R-Ras protein levels have not been directly measured. Therefore, it cannot be concluded that there is a complete lack of R-Ras protein in this mouse

model. Western blotting experiments on Rras-DEL415 mouse tissue should be performed to confirm R-Ras protein KO, most importantly in the aorta in the context of this thesis.

Furthermore, the vasodilation and vasocontraction properties of mouse vasculature were explored using the organ bath in the mouse aorta. However, *in vivo* the aorta is not responsible for changes in BP but mainly functions to carry blood around the body. Smaller resistance vessels, including the mesenteric artery, are responsible for subtle changes in BP. Therefore, small vessel myography should be performed to investigate differences in vascular reactivity with R-Ras KO, which may not obvious in the aorta.

Chapter 5. The role of R-Ras in age-related hypertension in mice and humans

5.1. Introduction

Pilot radiotelemetry data in the aged mouse showed increased SBP and MAP with R-Ras KO (Figure 1.14). Converse to this data, in this PhD results showed young adult R-Ras KO mice had a normal BP phenotype at baseline and with ANGII-induced hypertension. This led to the hypothesis that R-Ras may contribute to age-dependent changes in the vasculature responsible for elevated BP attributed to old age, in humans and mice.

In this chapter, I performed experiments to confirm the age-related SBP phenotype in the R-Ras KO mouse model by supplementing the pilot radiotelemetry data. I also sought to relate findings in the mouse model back to humans. Thus, an exploratory age-stratified association analysis looking at the effect of the *RRAS* SNV on SBP was performed, using UKB data from over 400,000 individuals of European ancestry (see methods section 2.1.4).

5.2. Results

5.2.1. Aged R-Ras KO mice exhibit elevated SBP

Pilot radiotelemetry data in the aged 10 – 12-month R-Ras KO mouse model was supplemented to confirm the phenotype observed (Table 5.1, Figure 5.1). Aged R-Ras KO mice had significantly higher SBP than WT mice at day and night, as analysed using a two-way ANOVA with Sidak's post-hoc test (Day $p = 0.027$, Night $p = 0.028$, Table 5.1, Figure 5.1.A). DBP and MAP were higher in aged R-Ras KO mice compared to WT at day and night, but not significantly different (DBP Day $p = 0.401$ Night $p = 0.557$, MAP Day $p = 0.855$ Night $p = 0.853$, Table 5.1, Figure 5.1.B and C). HR was the same in aged WT and R-Ras KO mice (Table 5.1, Figure 5.1.D).

Table 5.1. SBP, DBP, MAP, and HR in aged WT and R-Ras KO mice.

	SBP (mmHg)		DBP (mmHg)		MAP (mmHg)		HR (bpm)	
	Day	Night	Day	Night	Day	Night	Day	Night
WT	117.8 ± 2.46	129.6 ± 2.50	96.9 ± 2.35	101.1 ± 5.09	106.2 ± 1.81	112.0 ± 3.32	563.2 ± 15.7	597.0 ± 21.6
KO	127.5± 2.93	139.2 ± 2.28	109.0 ± 2.94	112.4 ± 4.25	116.4 ± 1.94	121.8 ± 2.22	554.9 ± 17.1	596.1 ± 12.2

Data is expressed as mean ± SEM. WT *n* = 7, KO *n* = 9.

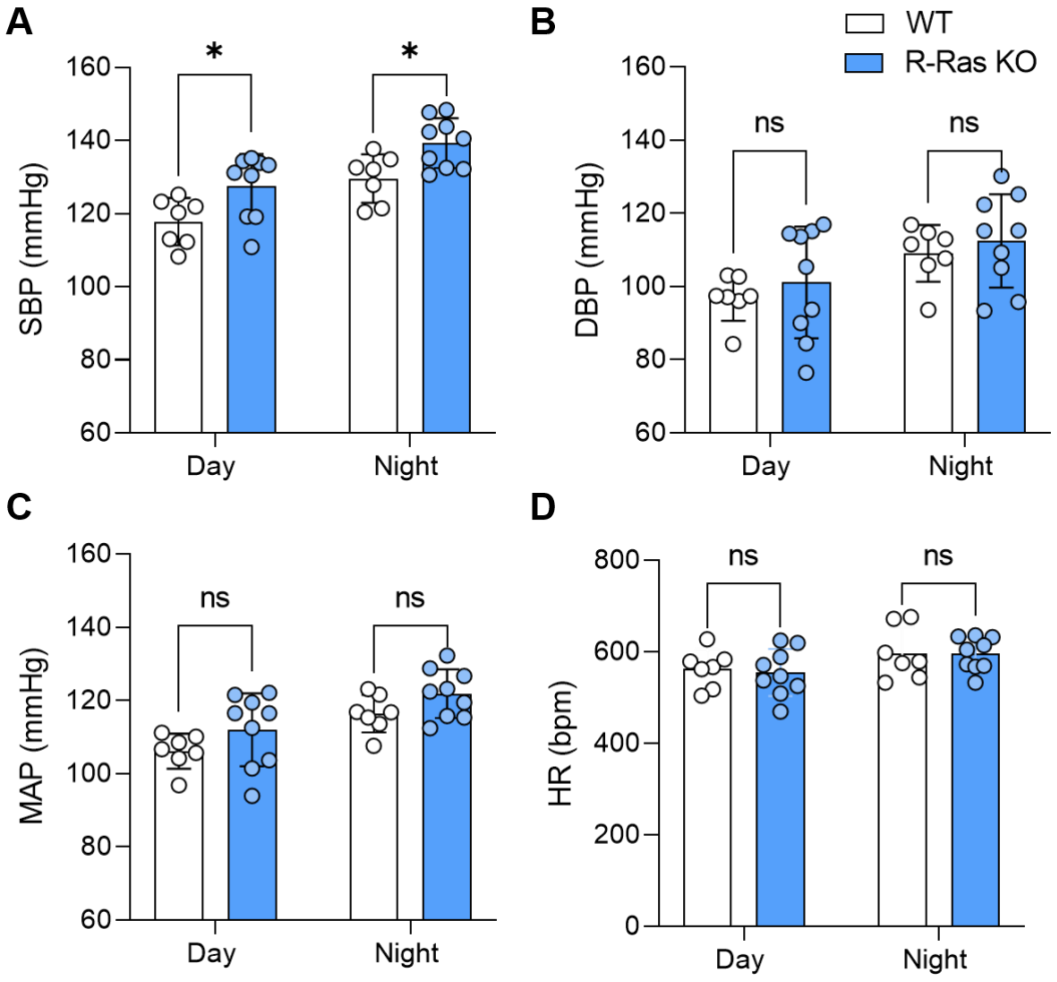

Figure 5.1. SBP (A), DBP (B), MAP (C) and HR (D) in aged WT and R-Ras KO mice. Data is expressed as mean ± SEM and analysed with a two-way ANOVA with Sidak's post-hoc test. * = $p < 0.05$, ns = non-significant. WT *n* = 7, R-Ras KO *n* = 9.

Both WT and R-Ras KO mice exhibited significantly elevated diurnal DBP and MAP in the aged vs. young adult group, as analysed using a mixed effects analysis with Sidak's post-hoc testing (Figure 5.2.B and C, Table 5.2). Diurnal SBP was not significantly increased in aged WT mice vs. young adult WT mice but was significantly increased in R-Ras KO mice with age (Figure 5.2.A, Table 5.2). Diurnal HR was the same in young and aged R-Ras KO mice (Figure 5.2.D, Table 5.2).

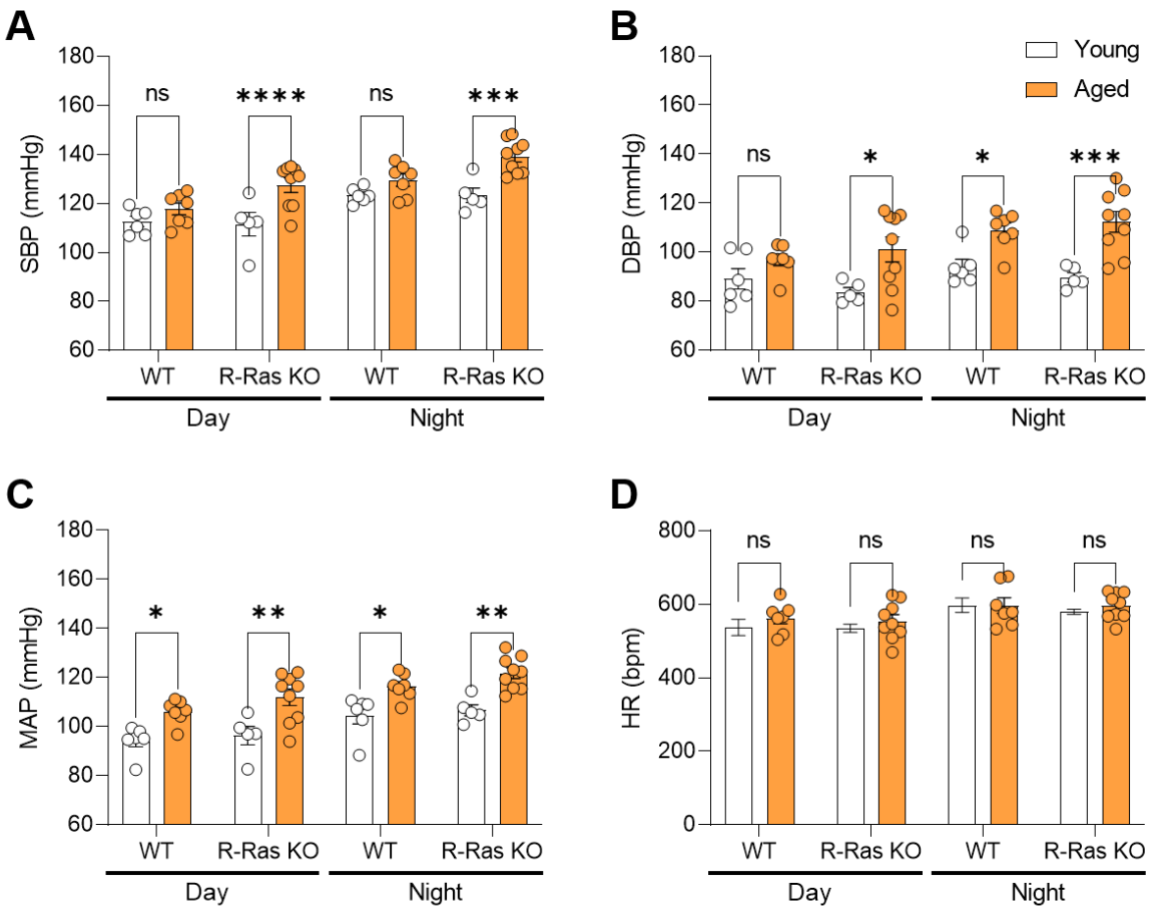

Figure 5.2. SBP (A), DBP (B), MAP (C) and HR (D) in young and aged WT and R-Ras KO mice. Radiotelemetry probes were surgically implanted in young (8 week) and aged (10 – 12 month) WT and R-Ras KO mice. Data is expressed as mean ± SEM and analysed using a mixed model with Sidak's post-hoc test. * = $p < 0.05$, ** = $p < 0.01$, *** = $p < 0.001$, **** $p < 0.0001$. ns = non-significant. WT $n = 7$, R-Ras KO $n = 9$.

Table 5.2. Comparison of young and aged WT and R-Ras KO mouse SBP, DBP, MAP and HR.

		Day		Night	
		WT	**KO**	**WT**	**KO**
SBP	**Mean difference [95% CI]**	-0.33 mmHg [-7.87 – 8.54]	10.19 mmHg [3.204 – 16.98]	0.54 mmHg [-7.66 – 8.75]	9.52 mmHg [2.63 – 16.41]
	P value (sig)	>0.999 (ns)	<0.0001 (****)	0.999 (ns)	0.0002 (***)
DBP	**Mean difference [95% CI]**	7.72 mmHg [-6.86 - 22.29]	17.48 mmHg [2.87 – 32.10]	14.90 mmHg [0.32 – 29.48]	22.65 mmHg [8.04 – 37.26]
	P value (sig)	0.540 (ns)	0.013 (*)	0.043 (*)	0.001 (***)
MAP	**Mean difference [95% CI]**	12.22 mmHg [1.98 – 22.47]	16.14 mmHg [5.71 – 26.57]	12.11 mmHg [1.86 – 22.36]	15.20 mmHg [4.77 – 25.63]
	P value (sig)	0.016 (*)	0.002 (**)	0.017 (*)	0.003 (**)
HR	**Mean difference [95% CI]**	25.88 bpm [-38.53 - 90.29]	20.16 bpm [-44.42 - 84.73]	-0.82 bpm [-65.42 - 63.59]	16.19 bpm [-48.38 - 80.77]
	P value (sig)	0.764 (ns)	0.889 (ns)	>0.999 (ns)	0.946 (ns)

The mean difference between aged (10 – 12-months) vs. young (8 weeks) mice is calculated using a mixed effects analysis with Sidak's post-hoc test, and the 95% CI, p value and significance stated. * = $p < 0.05$, ** = $p < 0.01$, *** = $p < 0.001$, **** = $p < 0.0001$, ns = non-significant. Young WT $n = 6$, aged WT $n = 7$, young R-Ras KO $n = 5$, aged R-Ras KO $n = 9$.

5.2.2. Exploring the age-related effect of the SBP-associated RRAS variant in humans

In vivo radiotelemetry studies in the R-Ras KO mouse revealed an elevated SBP phenotype in the aged mouse, absent in the young adult mouse (Figure 5.2.A). This suggested R-Ras contributes to age-related increases in BP. To explore whether this age-related effect was apparent in human data, an age-stratified association analysis of the rare *RRAS* variant rs61760904 was performed in the UKB cohort by Dr. Helen Warren. The UKB includes genetic data from ~500,000 individuals aged 40-69 years. Only individuals of European ancestry were included in this analysis for homogeneity (*n* = 423,655). The descriptive summary statistics are presented in Supplementary Table S1. For age-stratified analyses, individuals were grouped into two subgroups: 'younger' (<50 y) vs. 'older' (≥ 50 y). The variant rs61760904 encodes a T>C nucleotide substitution, where T is the minor allele. Genotype groups were therefore as follows; CC, homozygotes with no minor alleles; CT, heterozygotes with 1 minor allele; TT, homozygotes with 2 minor alleles (Table 5.3). The minor allele frequency (MAF) of the SNP in the UKB cohort was 0.008.

Table 5.3. Number of individuals from the UK Biobank cohort used in the age-stratified association analysis of the *RRAS* variant rs61760904 on systolic blood pressure, grouped by genotype and age.

Age group	CC (*n*)	CT (*n*)	TT (*n*)	Total (*n*)
All	417,244	6,392	19	423,655
< 50 y	103,724	1,531	8	105,263
≥ 50 y	313,520	4,861	11	318,392

Individuals with the T minor allele had numerically increased mean SBP compared to the homozygote CC group in all individuals and both age groups. The increase in mean SBP was greater in the homozygote TT groups vs the heterozygote CT group (Table 5.4, Figure 5.3). Furthermore, the mean SBP of the TT group in ≥ 50 y individuals is numerically larger than the CC group in < 50 y, highlighting a strong effect of the variant on SBP.

Table 5.4. Mean systolic blood pressure (SBP) of individuals below and above 50 years of age carrying the rs61760904 variant in the UK Biobank cohort.

Age group	Genotype	Mean SBP (mmHg)	SEM	*N*
All	CC	137.6	0.04	417,244
	CT	139.1	0.36	6,392
	TT	154.6	9.26	19
< 50 y	CC	130.7	0.05	103,724
	CT	132.1	0.42	1,531
	TT	147.1	6.79	8
≥ 50 y	CC	144.6	0.04	313,520
	CT	146.1	0.30	4,861
	TT	162.1	11.7	11

Mean SBP was calculated for homozygotes with no minor allele (CC), heterozygotes with one minor allele (CT), and homozygotes with two risk alleles (TT).

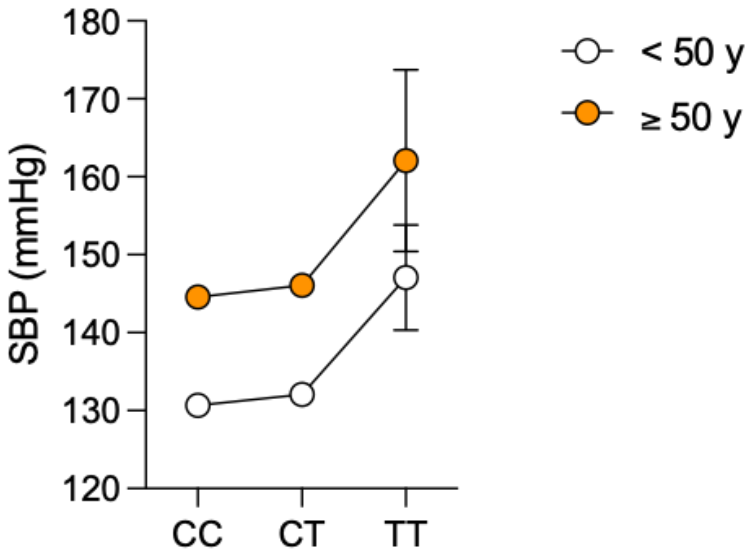

Figure 5.3. Graph of mean systolic blood pressure (SBP) of individuals below and above 50 years of age carrying the rs61760904 variant in the UK Biobank cohort. Data is expressed as mean SBP ± SEM.

5.2.2.1. Per-allelic additive association of the exonic variant on SBP in all individuals in UKB

Firstly, an association of the exonic variant was explored using a per-allelic additive model in all individuals treating genotype groups as a continuous variable. This model was used by Surendran *et al.,* in the discovery analysis of *RRAS* [11]. The calculated effect size of the exonic variant on SBP in the total dataset (all individuals) was +1.53 mmHg/T allele. This association was highly significant ($p = 3.5x10^{-11}$), confirming the previous result that the rare variant at *RRAS* has a large effect size on SBP.

5.2.2.2. Genotype association of the exonic variant on SBP in all individuals

Next, an association analysis using the genotype model was performed on all individuals, comparing each minor risk allele carrier genotype group (CT and TT) to the non-carrier homozygous group (CC). Across all individuals, the genotype effect size was greater in the CC vs. TT comparison (+12.6 mmHg ± 4.22, $p = 2.3x10^{-10}$), than the CC vs. CT comparison (+1.47 mmHg ± 0.23, p = 0.003) (Table 5.5). The CC vs. CT effect size is similar to the per allelic additive association model (+1.53 mmHg/T allele), as these two genotype groups constitute the majority of individuals. Despite the lack of statistical power for analysis of the

rare variant due to a low *n* number in the TT group (*n* = 19), the large effect size of the CC vs. TT comparison is significant (p = 0.003). Individuals homozygous for both T risk alleles have a mean SBP +12.6 mmHg higher than CC homozygotes, demonstrating a dominant effect of the T risk allele that was not identified in the previous per allelic association model. The genotype model was therefore used for the subsequent age-stratified analysis.

5.2.2.3. Age-stratified genotype association of the exonic variant on SBP

In the age-stratified analysis, the effect size estimates for both the CC vs. CT comparison and the CC vs. TT comparison were greater in 'older' individuals ≥ 50 y than 'younger' individuals < 50 y (Table 5.5). Notably, in individuals ≥ 50 y the effect size estimate in the CC vs. TT comparison of +14.6 mmHg is ~50% greater than for < 50 y individuals (+9.68 mmHg). The effect size estimate of CC vs. CT was highly significant in all age groups (Table 5.5). CC vs. TT was statistically significant in the ≥ 50 y age group (p = 0.012, Table 5.5), but it did not reach statistical significance in the < 50 y age group (p = 0.073, Table 5.5). Furthermore, an age-interaction result was non-significant (effect = +0.29 mmHg ± 0.54, p = 0.059, see methods section 2.1.4). The lack of significance in the < 50 y CC vs. TT comparison and in the age-interaction result are likely due to low statistical power due to the small *n* number of the TT cohort (TT all *n* = 19, < 50 y *n* = 8, ≥ 50 y *n* = 11).

Table 5.5. Effect of the rs61760904 variant on systolic blood pressure calculated using a genotype association model.

Age group	Genotype comparison	Effect (mmHg)	SE	95% CI	P value
All	CC vs. CT	1.47	0.23	1.02 to 1.92	$2.3x10^{-10}$
	CC vs. TT	12.6	4.22	4.34 to 20.9	0.003
< 50 y	CC vs. CT	1.24	0.39	0.47 to 2.01	0.002
	CC vs. TT	9.68	5.40	-0.90 to 20.3	0.073
≥ 50 y	CC vs. CT	1.56	0.28	1.01 to 2.10	$2.6x10^{-8}$
	CC vs. TT	14.6	5.82	3.21 to 26.0	0.012

An association analysis was carried out using a genotype model in individuals of white European ancestry from the UK Biobank, for all individuals, and stratified by age (< 50 y v ≥ 50 y).

5.3. Discussion

In this chapter, the age-related phenotype of elevated SBP in the R-Ras KO mouse was confirmed by supplementing pilot radiotelemetry data (see Chapter 1.4). Secondly, an age-related phenotype was demonstrated in humans, via an age-stratified association analysis of the SNV with SBP in ~500,000 individuals from UKB.

Despite a lack of a BP phenotype observed with global R-Ras KO in young adult mice, and with ANGII-induced hypertension, the aged mice (10 – 12 months) did exhibit significantly elevated SBP in the supplemented pilot data set. This supports that R-Ras contributes to age-related increases in BP. Interestingly, when the pilot data was supplemented, the significant difference observed with increased MAP between WT and R-Ras KO mice was lost. This

observation may be explained by the addition of female mice in the dataset. A previous study found no significant difference in MAP in female mice with a C57BL/6J genetic background between 3 and 14 months of age, contrary to male littermates, despite a robust increase in SBP [340]. It should be noted that these mice have a different genetic background to the Rras-DEL415 mice used in this study, which have a C57BL/6N background, and therefore these findings may not be true for the Rras-DEL415 mice. Nevertheless, the radiotelemetry data evidenced that aged WT and R-Ras KO mice had an increased BP phenotype compared to young adult mice of the same genotype – this is concurrent with previous literature [340,354]. This increase appears to be emphasised in the R-Ras KO mice. Considering the young adult R-Ras KO mouse is normotensive, this increase in BP exaggerated compared to WT mice may be related to changes in BP control mechanisms occurring with age, as explored using phosphoproteomics in the mouse aorta in Chapter 6. Overall, the radiotelemetry data provides a strong indication that R-Ras is involved in age-dependent development of hypertension.

An exploratory association analysis was performed to investigate the effect of the SNV on SBP, using UKB data from ~500,000 individuals of European ancestry. A per-allelic additive model analysing all individuals indicated the effect size of the SNV on SBP of +1.53 mmHg/T allele was comparable to that previously reported by the original discovery analysis (+1.51 mmHg/T allele [11]) and more recently in a larger meta-analysis using Million Veteran Program data for discovery and 140,886 white individuals from UKB, and individuals from ICBP for replication (+1.16 mmHg/T allele [13]). The MAFs are also comparable (here, 0.008, discovery, 0.007 [11]). These data corroborate the large effect of the rs61760904 variant on SBP.

For the age-stratified association analysis a genotype model was used because it is more appropriate for rare variants where there is less statistical power indicated in all individuals. The calculated effect size in the CC vs. TT comparison was +12.6 mmHg; this is much larger than the effect size calculated in the CC vs. CT comparison (+1.47 mmHg), These results demonstrate a strong dominant effect of the T risk allele. This large effect has not been previously reported and the effect size is comparable to all common variants combined (+12.9 mmHg, [195]). This dominant effect was hidden in the per allelic association analysis. Following these results, the genotype model was used for the subsequent age-stratified analyses.

A sub-analysis stratified by age where individuals were divided into ‘younger’ (≥ 50 y) or ‘older’ (≥ 50 y) groups found a similar trend of a small increase in mean SBP between CC and CT groups, and a big jump between CC and TT groups. This was observed in both age groups, as with the combined analysis. Most notably, the effect size of the TT group was larger in older

individuals (+14.9 mmHg) than younger individuals (+9.68 mmHg). These data strongly suggest older individuals carrying both alleles have a much greater risk of developing hypertension. This is a novel observation, and in tandem with the age-related association, provides support from humans of a similar age-related association to what was observed in mice.

There are some limitations to this SNV association analysis. Notably, rs61760904 is a rare variant, and therefore the *n* number in the TT groups is low. Validation of this result in larger cohorts is thus warranted. Furthermore, validation across other ancestries is important as the *RRAS* variant was discovered in a multi-ancestry analysis. Low power may explain the lack of significance of the age-interaction observed with the genotype model. Nonetheless, the mean SBP values and significant effect estimates in the per allelic and genotype analyses, and in the age-stratified analysis, describe a major effect of the SNV on SBP, and suggest an age-dependency. The human data from the UKB analyses supports the experimental findings in the R-Ras KO mice, and together indicate an age-related effect of R-Ras on the pathogenesis of hypertension.

Chapter 6. Multi-omic analyses of the young R-Ras KO mouse aorta

6.1. Introduction

The original hypothesis stated that R-Ras regulates BP via cell signalling mechanisms in the vasculature, namely NO-mediated vasodilation. I therefore proposed the R-Ras KO mouse model would have an elevated BP phenotype and abnormal vascular reactivity. However, radiotelemetric recordings found a normal BP phenotype in young adult R-Ras KO mice, and with ANGII-induced hypertension (Chapter 4). Moreover, the vasodilatory and vasocontractile response of the R-Ras KO mouse aorta was the same as WT, as assessed using the organ bath (Chapter 4). Yet, aged R-Ras KO mice exhibited elevated SBP (Chapter 5). BP is a complex phenotype, governed by multiple signalling mechanisms across several organ systems. At the level of the vasculature numerous signalling pathways work concomitantly to regulate vasodilation and vasocontraction, including the NO pathway. Therefore, I considered whether the impact of R-Ras KO on BP in young adult mice may be masked by compensatory mechanisms at play, becoming dysregulated in the aged mouse to reveal the elevated SBP phenotype. To explore this, I adopted a hypothesis-free multi-omic approach (Figure 6.1). Using aortas from young adult male and female WT and R-Ras KO mice, I first analysed the transcriptome using RNA sequencing (RNA-seq) to measure changes in gene expression (methods section 2.18, Figure 6.1). Secondly, I assessed changes in phosphorylation status of proteins using phosphoproteomic analysis, and contextualised changes observed into cell signalling mechanisms (methods section 2.19, Figure 6.1).

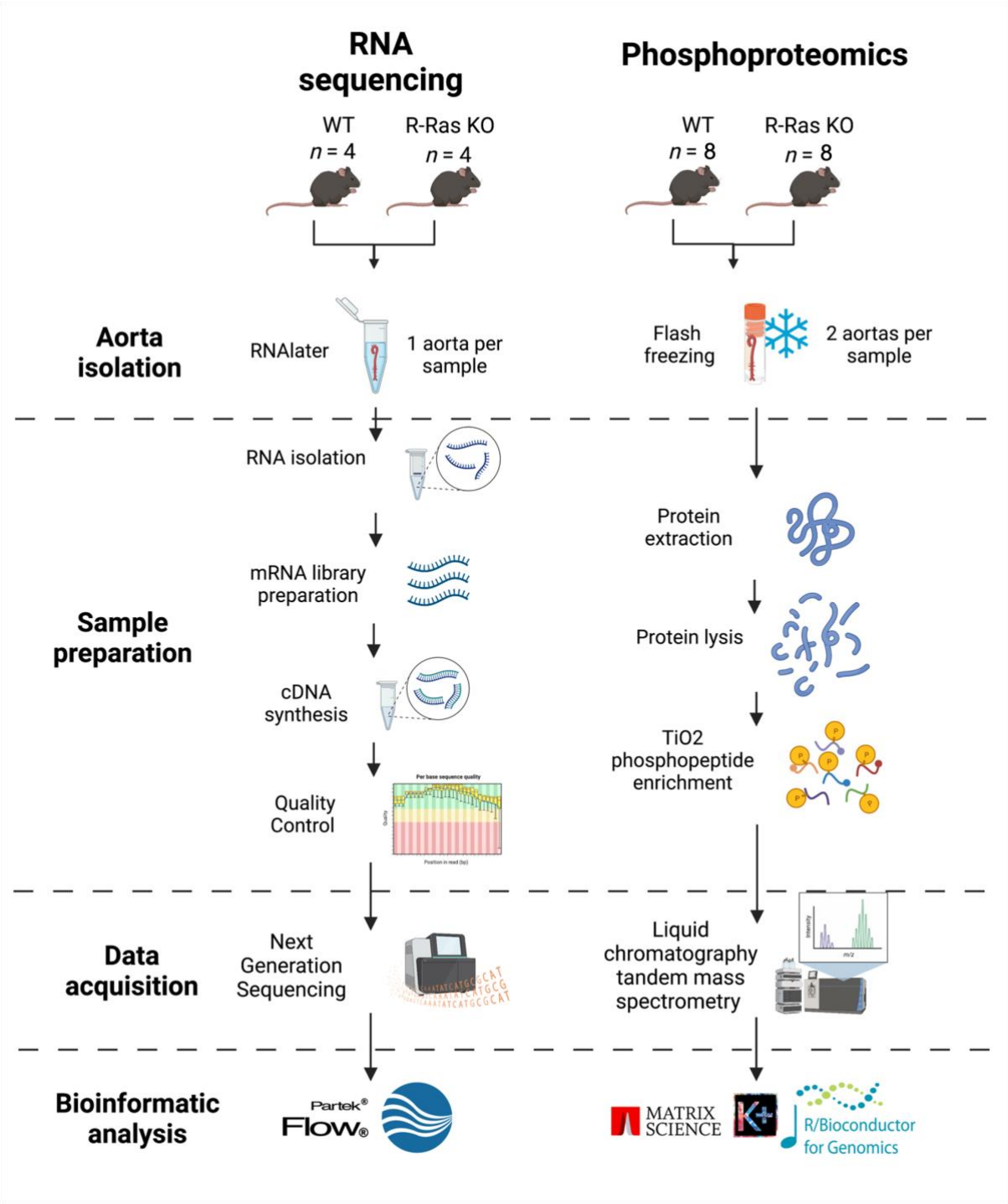

Figure 6.1. Outline of RNA sequencing and phosphoproteomic analyses of the R-Ras KO mouse aorta. RNA or protein was isolated from 8-week-old mouse aortas from WT and R-Ras KO mice. For phosphoproteomics, 2 aortas were pooled per sample.

6.2. Results

6.2.1. RNA sequencing

6.2.1.1. Quality control reveals variation between samples within genotype

All aortic RNA samples had an acceptable RNA integrity number (RIN) of >7, indicating low levels of RNA degradation. Samples were processed in two batches, with final *n* numbers of 5 for WT, 3 for HET, and 4 for R-Ras KO. All samples, except two, were DNase treated during RNA extraction. Two samples were treated with DNase after RNA extraction to remove residual DNA detected in quality control (Figure 6.2). Principal component analysis (PCA) failed to demonstrate clustering within the groups, or with DNase treatment (Figure 6.2). This indicates a high level of variation between samples within genotype and DNAse treated groups.

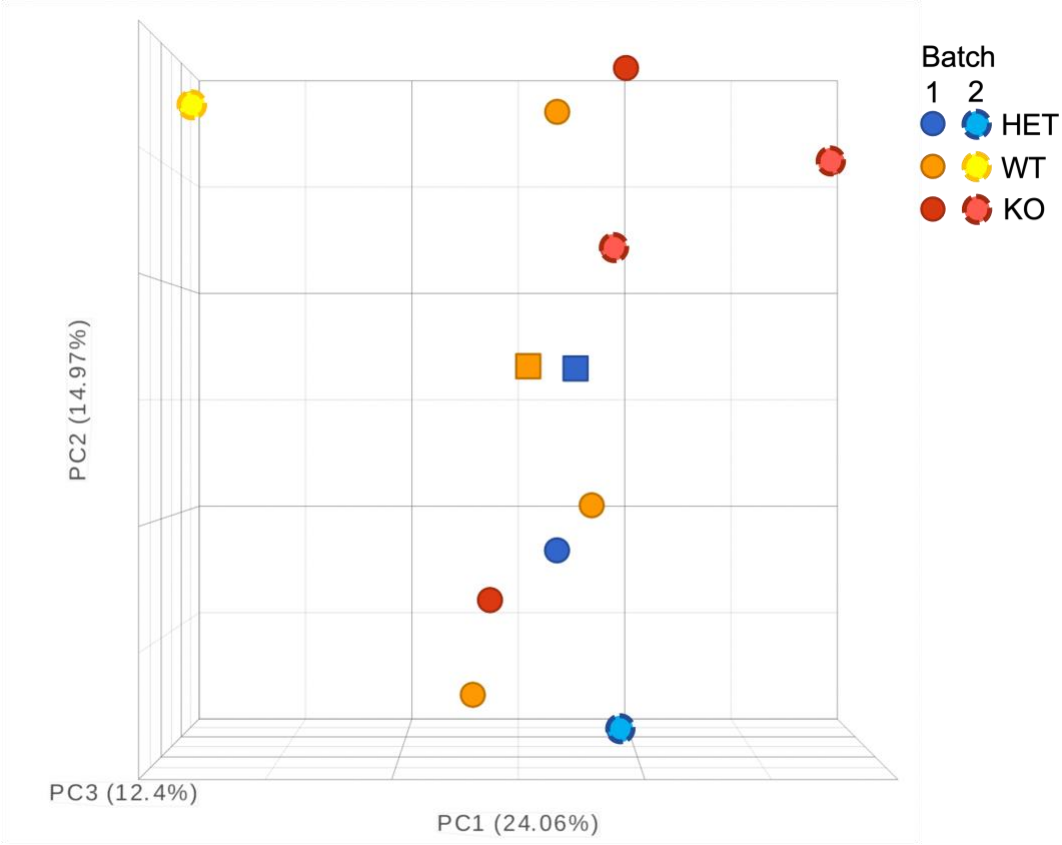

Figure 6.2. Principal Component Analysis (PCA) showing variation within and between genotypes. RNA was isolated from 8-week-old mouse aortas from WT, HET, and R-Ras KO mice for RNA-seq (WT *n* = 5, HET *n* = 3, KO *n* = 4). Samples were processed in two batches, and treated with DNase during RNA extraction (circles), or after (squares). PCA was carried out by Dr. Charles Mein (Genome Centre, QMUL) using Partek Flow software.

6.2.1.2. Gene set analysis does not identify changes in gene expression between WT and R-Ras KO mouse aortas

Analysis carried out using the Partek Flow Gene Set Analysis (GSA) tool identified 428 genes that were differentially expressed (DE) between WT and R-Ras KO mouse aortas. HET data was excluded. 53 of these genes passed the p value threshold of $p < 0.05$ after a t-test with unequal variances and a Log2FC ≥ ± 2, of which 19 were upregulated and 34 were downregulated (Figure 6.3, Supplementary Table S2). The heat map visualising DE using normalised gene counts by z-scores shows a lack of consistent pattern with gene expression (Figure 6.4). Results from a separate GSA of WT vs. HET samples are presented in Supplementary Table S2.

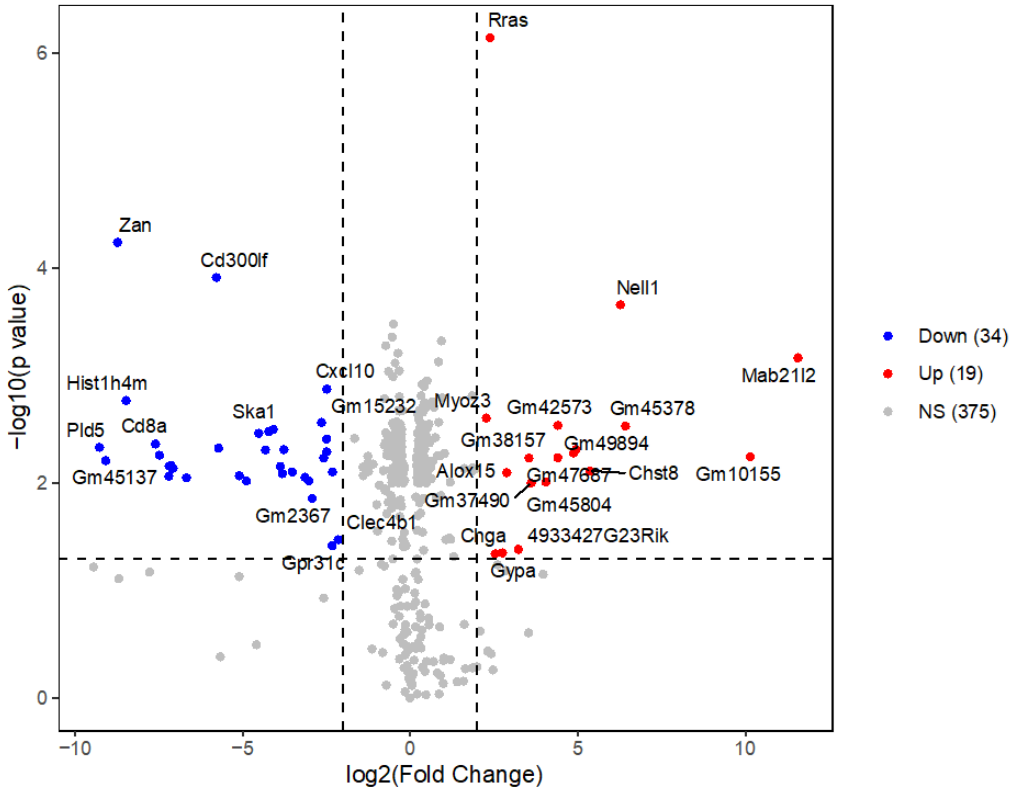

Figure 6.3. Volcano plot of differentially expressed genes in WT vs. R-Ras KO mouse aortas identified with RNA-seq. Differential expression was analysed using a t-test with unequal variances. P values presented are before Bonferonni correction. Significant thresholds: $p < 0.05$, log2(Fold Change) ≥ ±2. Analysis was carried out using Partek Flow software.

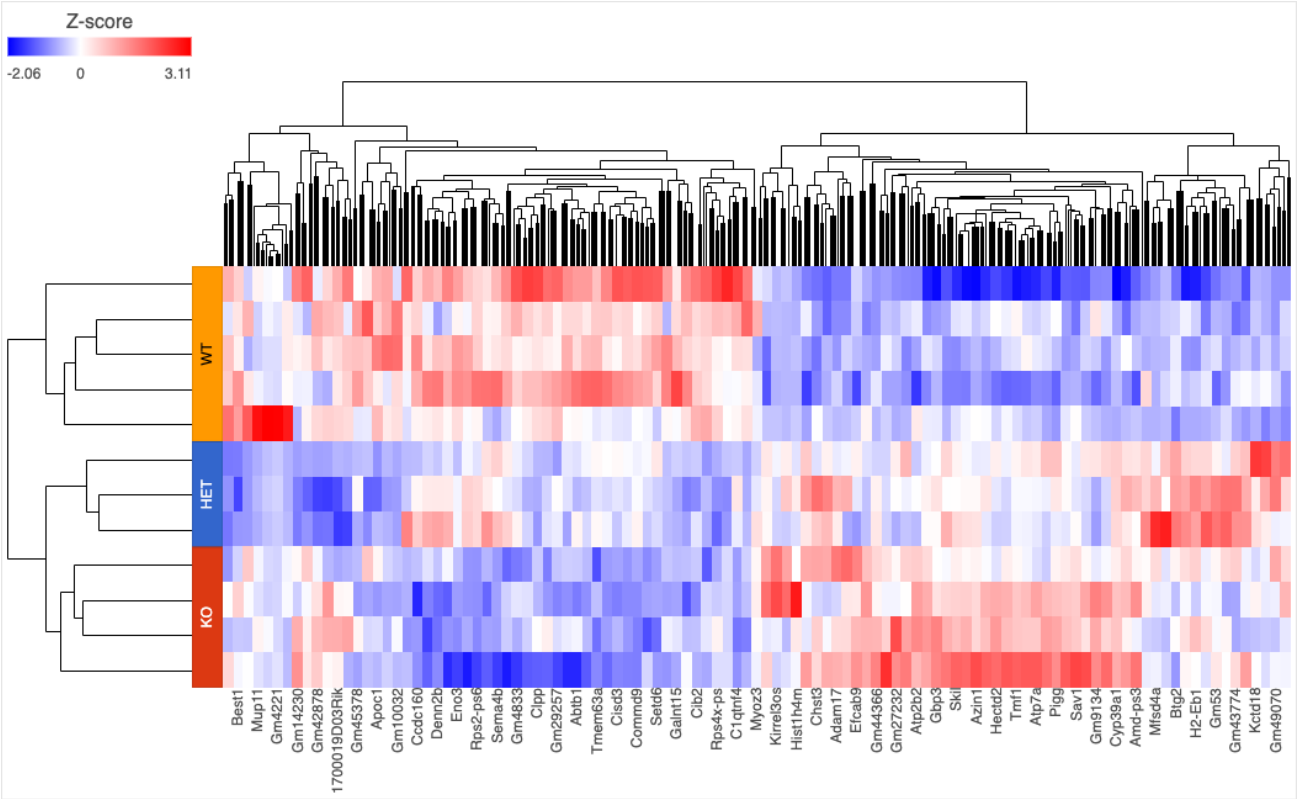

Figure 6.4. Heatmap of RNA-seq expression data showing differential expression of genes in R-Ras KO, heterozygous (HET) and WT mouse aortas. Gene expression is shown as z-scores, calculated as the expression count minus the mean and divided by the standard deviation (SD). Hierarchical clusters are identified with dendograms. Gene names are on the X axis. Samples are grouped depending on genotype. WT *n* = 5, HET *n* = 3, KO *n* = 4. The diagram was generated by Dr. Charles Mein (Genome Centre, QMUL) using Partek Flow software.

After Bonferonni correction with a false discovery rate (FDR) threshold of ≤ 5%, only 1 gene, *Rras,* passed the p value threshold in the GSA of WT vs. R-Ras KO samples (Figure 6.5, Supplementary Table S2).

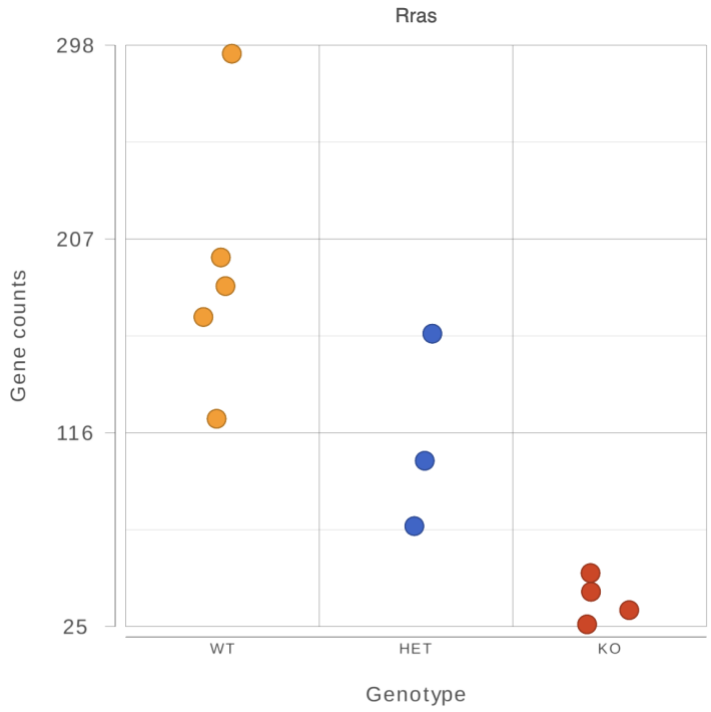

Figure 6.5. Dot plot of *Rras* gene expression in WT, R-Ras HET and R-Ras KO mouse aorta analysed with RNA-seq. Data was plotted using Partek Flow software. WT *n* = 5, HET *n* = 3, KO *n* = 4.

6.2.1.3. Exploratory KEGG geneset enrichment analysis of RNA-seq data yields no significantly enriched pathways

Prior to Bonferonni correction, GSA found 53 statistically DE genes in WT vs. KO mouse aortas. KEGG gene set enrichment analysis was therefore performed as an exploratory analysis using this dataset, to investigate whether the culmination of these genes may translate to significantly DE pathways. KEGG geneset enrichment analysis (GSEA) imputes the directional Log2FC and p value associated with DE genes to calculate an enrichment score in a given condition. GSEA can only be performed between two groups, therefore HET data was excluded from this analysis. However, no KEGG pathway was significantly enriched.

6.2.2. Phosphoproteomics

6.2.2.1. R-Ras KO results in changes in phosphorylation status of proteins in the young mouse aorta

Phosphoproteomic analysis was carried out to investigate changes in cell signalling pathways in the mouse aorta, resulting from R-Ras KO. Phosphoproteins and phosphosites were identified using the PhosphoSitePlus database. The PhosphoSitePlus database includes additional post-translational modifications (PTMs) to phosphorylation. PTMs are categorised as phosphorylation of serine (S), threonine (T) and tyrosine (Y), methylation of arginine (R), and acetylation and ubiquitination on lysine (K), oxidation of methionine (M), or no modification (no_mod). The term phosphosite used in this thesis covers any of these PTMs reported by PhosphoSitePlus.

Using cut-off values of $p < 0.05$ and Log2FC $\geq \pm 2$, 702 differentially expressed phosphosites in 498 proteins were identified (Figure 6.6). A negative Log2FC value indicates a larger phosphosite signal in the WT aorta (indicating downregulation by R-Ras) and a positive Log2FC indicates a larger phosphosite signal in the R-Ras KO aorta (indicating upregulation y R-Ras). 302 phosphosites were significantly downregulated in 274 proteins, and 400 phosphosites significantly upregulated in 224 proteins, in the R-Ras KO mouse aorta compared to WT (Figure 6.6). The top 10 upregulated (Table 6.1) and downregulated (Table 6.2) phosphosites and the phosphoprotein functions are listed below, the remaining significant phosphosites are presented in Supplementary Tables S3 and S4.

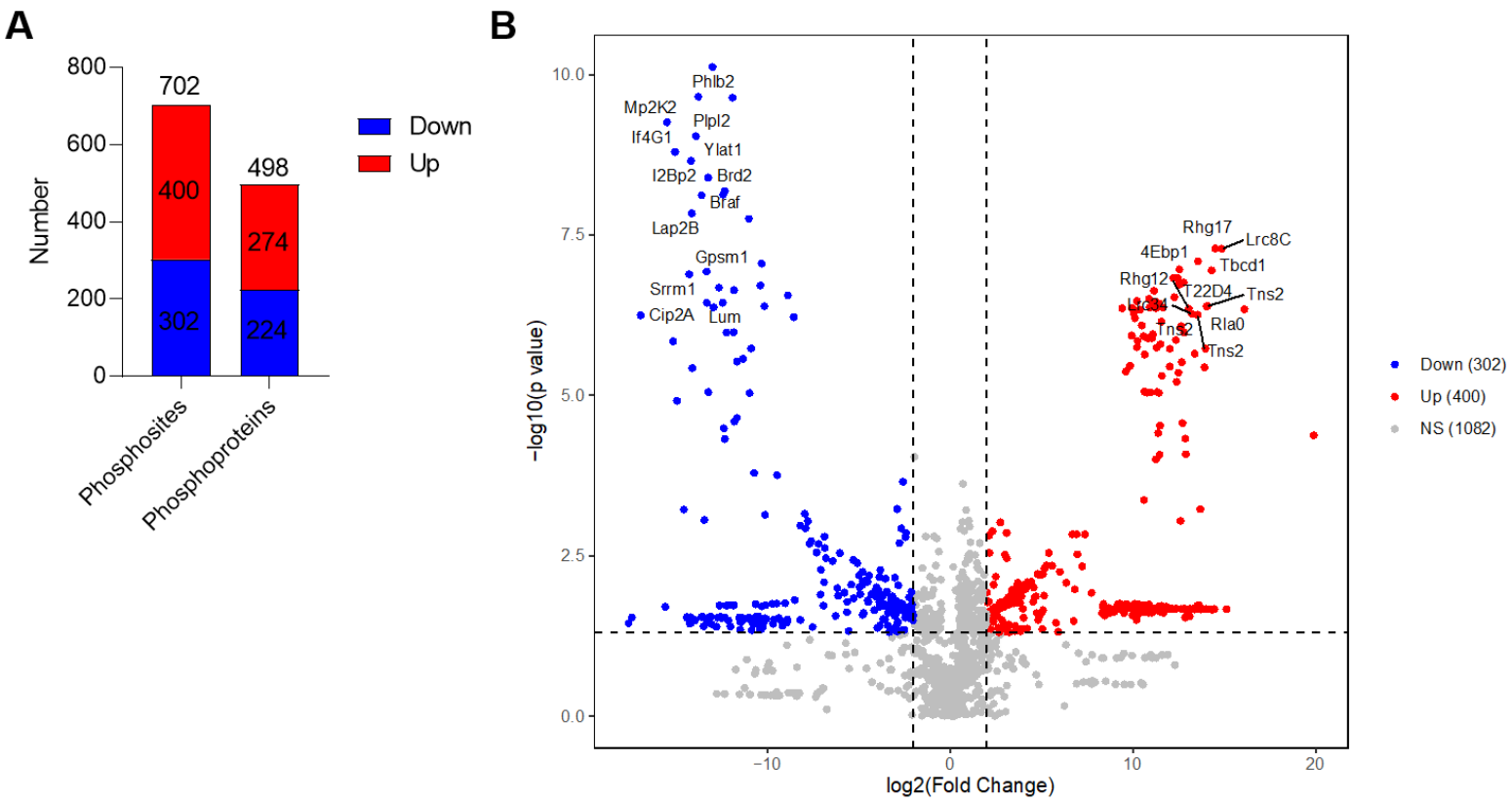

Figure 6.6. Upregulated and downregulated phosphosites in the R-Ras KO mouse aorta. Phosphoproteomic analysis was carried out on WT and R-Ras KO mouse aortas (*n* = 8) and phosphosite/protein abundance calculated and normalised as the log2(Fold Change) of R-Ras KO vs. WT. A) Bar plot of the number of significantly up- and downregulated phosphosites and phosphoproteins in the R-Ras KO mouse aorta. Plotted using Prism 8 software. B) Volcano plot of significantly up- and downregulated phosphosites in the R-Ras KO mouse aorta. Top significant proteins are labelled with their gene names. Dotted lines indicate significance thresholds. Plotted using the ggplot2 package in R. Significance thresholds are $p < 0.05$ and log2(Fold Change) ≥ ±2.

Table 6.1. Top 10 phosphosites significantly upregulated in R-Ras KO mouse aortas

Uniprot ID	Name	Phosphosite	Log2FC	P value	Function
Tns2	Tensin-2	Y483; S481	19.89	$4.2x10^{-5}$	Focal adhesion molecule that binds actin filamin. Role in cell migration.
Rla0	60S acidic ribosomal protein P0	M311; S304; S307	16.10	$4.6x10^{-7}$	Ribosomal protein important for RNA binding.
Hnrpk	Heterogeneous nuclear ribonucleoprotein K	Y280	15.12	0.022	Pre-mRNA-binding protein. Related to hypertension and kidney injury in diabetes via renal *AGT* transcription.
Lrc8c	Volume-regulated anion channel subunit LRRC8C	T660	14.85	$5.2x10^{-8}$	Component of volume-regulated anion channel which regulates cellular volume homeostasis. Implicated in vascular remodelling in hypertension. Expressed in SMCs.
Rhg17	Rho GTPase-activating protein 17	S698	14.50	$5.1x10^{-8}$	GTPase activator of CDC42, Rho, RAC1. Role in maintenance of tight junction, cell polarity, Ca^{2+} dependent exocytosis.
H4	Histone H4	S48	14.44	0.021	Core component of nucleosome. Role in transcription regulation, DNA repair, DNA replication and chromosomal stability.
Cdkl5	Cyclin-dependent kinase-like 5	S341	14.36	0.022	Phosphorylation of methyl CpG binding protein 2. May regulate ciliogenesis. Related to glomelular filtration rate.

Nub1	Negative Regulator of Ubiquitin Like Proteins 1	S100	14.31	0.022	Promotes degradation of NEDD8 (cell-cycle regulator).
Tbcd1	TBC1 domain family member 1	S697	14.31	$1.1x10^{-7}$	Glucose transport mediator. May act as a GTPase-activating protein for Rab family protein. Plays role in cell differentiation, and insulin-stimulated glucose uptake into cells.
Necp2	Adaptin ear-binding coat-associated protein 2	S186	14.28	0.021	Involved in endocytosis.

Phosphosite abundance was normalised as log2(Fold Change) KO vs. WT, and p value determined using a t-test with unequal variance. Phosphosites are labelled as phosphorylation of Y (tyrosine), T (threonine), or S (serine), or oxidation of M (methionine). Sites with no modification (no_mod) are excluded. Information on function is extracted from GeneCards – the human gene database, www.genecard.org [355].

Table 6.2. Top 10 phosphosites significantly downregulated in R-Ras KO mouse aortas.

Uniprot ID	Name	Phosphosite	Log2FC	P value	Function
Myo9b	Unconventional myosin-IXb	S1175	-17.41	0.029	Binds actin to regulate intracellular movement. RhoA GTPase activator.
Cip2a	Protein CIP2A	M680	-16.92	$5.6x10^{-7}$	Oncogenic protein.
Srrm2	Serine/arginine repetitive matrix protein 2	S1628; S1631	-15.58	0.020	Involved in mRNA splicing in the spliceosome. A biomarker of Parkinson's disease.
Mp2k2	Dual specificity mitogen-activated protein kinase kinase 2	T397	-15.48	$5.5x10^{-10}$	Activates MAPK/ERK/BRAF. Critical in mitogen growth factor signal transduction.
Lorf2	LINE-1 retrotransposable element ORF2 protein	S1072	-15.15	$1.44x10^{-6}$	Reverse transcriptase.
If4g1	Eukaryotic translation initiation factor 4 gamma 1	T1213	-15.04	$1.6x10^{-09}$	Regulates mRNA translation of *ATF4*.
Septin7	Septin-7	S422	-14.40	0.028	Filament-forming cytoskeletal GTPase required for normal organisation of actin cytoskeleton.

Srrm1	Serine/arginine repetitive matrix protein 1	S702; S704	-14.27	$1.3x10^{-7}$	Involved in numerous pre-mRNA processing events.
Map1b	Microtubule-associated protein 1B	M827; S825; T834	-14.25	0.036	Involved in microtubule assembly and neurite extension.
I2bp2	Interferon regulatory factor 2-binding protein 2	T73	-14.18	$2.2x10^{-9}$	Acts as a coactivator of VEGFA expression in cardiac and skeletal muscles. Plays a role in immature B-cell differentiation.

The phosphoproteomic analysis revealed novel and known phosphoproteins to interact with R-Ras. Notably, the upregulated phosphosite with the highest Log2FC was located in the Tensin-2 protein (Tns2(Y483;S481), Log2FC = 19.89, p = 4.2×10^{-5}, Table 6.1). Tensin-2 has not been previously associated with R-Ras. In total, there were 5 significantly upregulated phosphosites in Tns2 (Y483; S481; S466; Y456; S455), Figure 6.7, Supplementary Table S3).

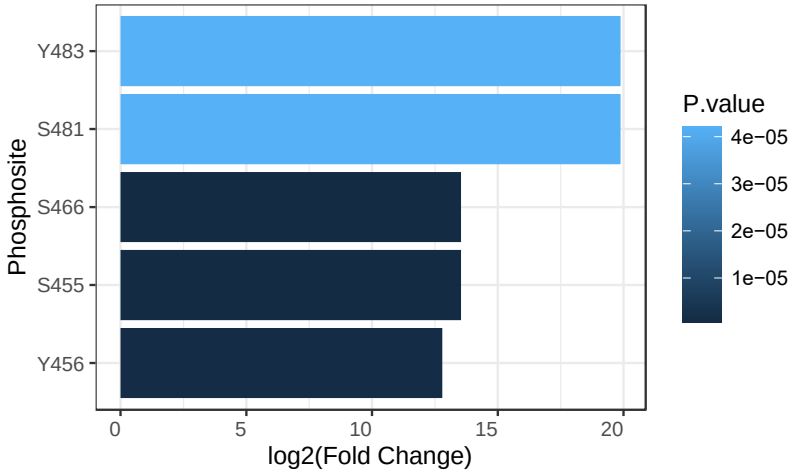

Figure 6.7. Differential phosphorylation of tensin-2 phosphosites in R-Ras KO mouse aortas. Plotted using the ggplot2 package in R.

In filamin-A (Flna), a known effector of R-Ras [215,356], 4 phosphosites are upregulated and 1 downregulated in the R-Ras KO mouse aorta (Figure 6.8, Supplementary Tables S3 and S4).

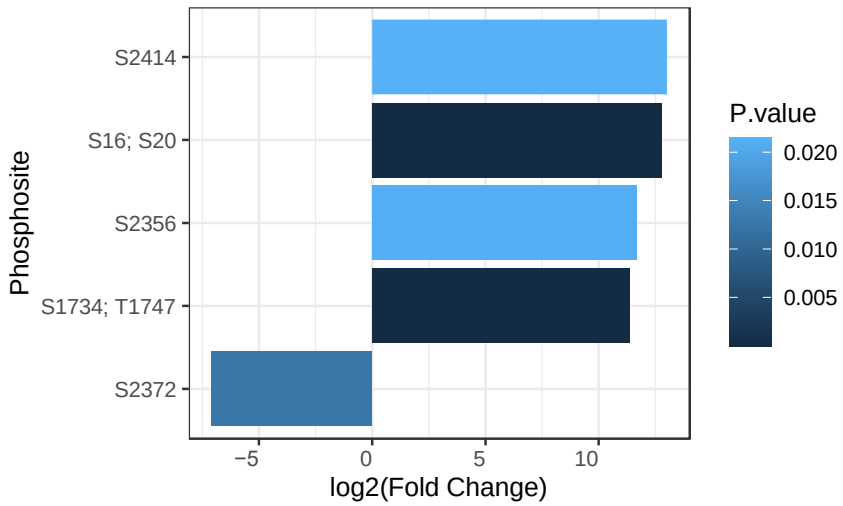

Figure 6.8. Differential phosphorylation of filamin-A phosphosites in R-Ras KO mouse aortas. Plotted using the ggplot2 package in R.

There were also significant changes in phosphorylation status of proteins involved in the PI3K/Akt signalling; inositol 1,4,5-Triphosphate Receptor Associated 1 (Irag1), and Akt Serine/Threonine Kinase 1 (Akt1) (Figure 6.9.A, Supplementary Table S3). Phosphorylation of Rho-associated protein kinase-1 (Rock1) at S1100 and S1102 was downregulated in R-Ras KO mouse aortas (Figure 6.9.B, Supplementary Table S4, mean Log2FC WT = 0.31 ± 2.7, KO = -7.35 ± 0.1, $p = 0.03$); R-Ras is known to activate Rock1 by phosphorylation *in vitro* [279]. Adenylate cyclase type 6 (Adcy6), an activator of R-Ras [240], is less phosphorylated in R-Ras KO mouse aortas (Figure 6.9.C, Supplementary Table S4, mean Log2FC WT = 5.67 ± 0.03, KO = -7.35 ± 0.1, $p < 0.0001$). Phosphorylation of eNOS, Nos3(S632) was also downregulated, although this was not statistically significant (Figure 6.9.D, Supplementary Table S4, mean Log2FC WT = -2.45 ± 3.3, KO = -7.35 ± 0.1, p = 0.20). However, phosphorylation of the inducible form Nos2(S118) was upregulated and significant (Figure 6.9.D, Supplementary Table S3, mean Log2FC WT = 7.44 ± 1.7, KO = -2.69 ± 3.5, p = 0.03). Finally, multiple phosphosites on the R-Ras GAP, Rasa3, were differentially phosphorylated (Figure 6.9.D, Supplementary Tables S3 and S4).

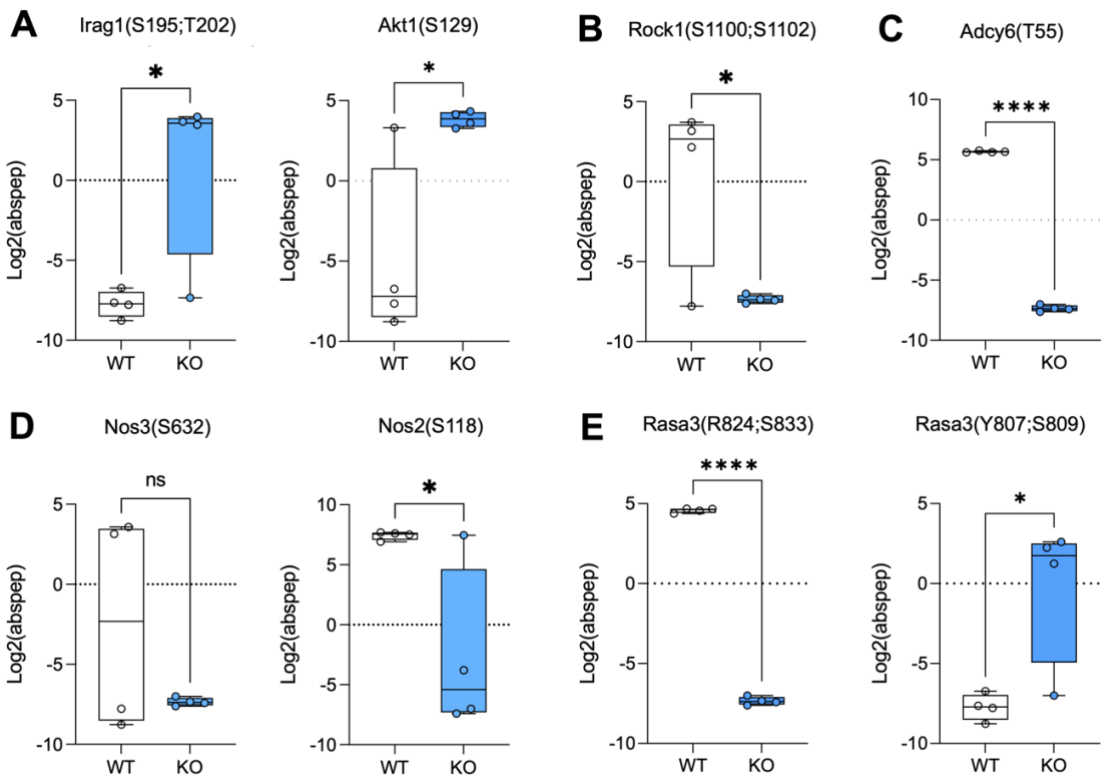

Figure 6.9. Boxplots of differential expression of phosphosites in the R-Ras KO mouse aorta. A) Proteins involved in PI3K/Akt signalling. B) Rock1. C) Adcy6. D) NOS isoforms. E) Rasa3. Significant differences between normalised absolute peptide abundance (Log2(abspep)) were compared using a 2-tailed t-test with unequal variance. *$p < 0.05$, ****$p < 0.0001$. Boxplots were plotted using Prism 8 software.

6.2.2.2. Kinase substrate enrichment analysis shows changes in kinase activity with R-Ras KO in the mouse aorta

Phosphorylation of protein phosphosites is dependent on kinases. Kinase substrate enrichment analysis (KSEA) combines phosphoproteomic data with PhosphoSitePlus and Phospho.ELM databases to infer kinase activity based on the abundance of phosphosites and known kinase-substrate relationships [357]. KSEA analysis found Mek1 activity was significantly upregulated in R-Ras KO mouse aortas (Log2FC = 1.25, p = 0.001, Figure 6.10). Mtor (mechanistic target of rapamycin) activity was also upregulated but failed to reach statistical significance. Pkaca (cAMP-dependent protein kinase catalytic subunit alpha), Akt1, Pkca (Protein kinase C alpha), Erk2 and Erk1 activity were downregulated in R-Ras KO mouse aortas, but again were not statistically significant (Figure 6.10).

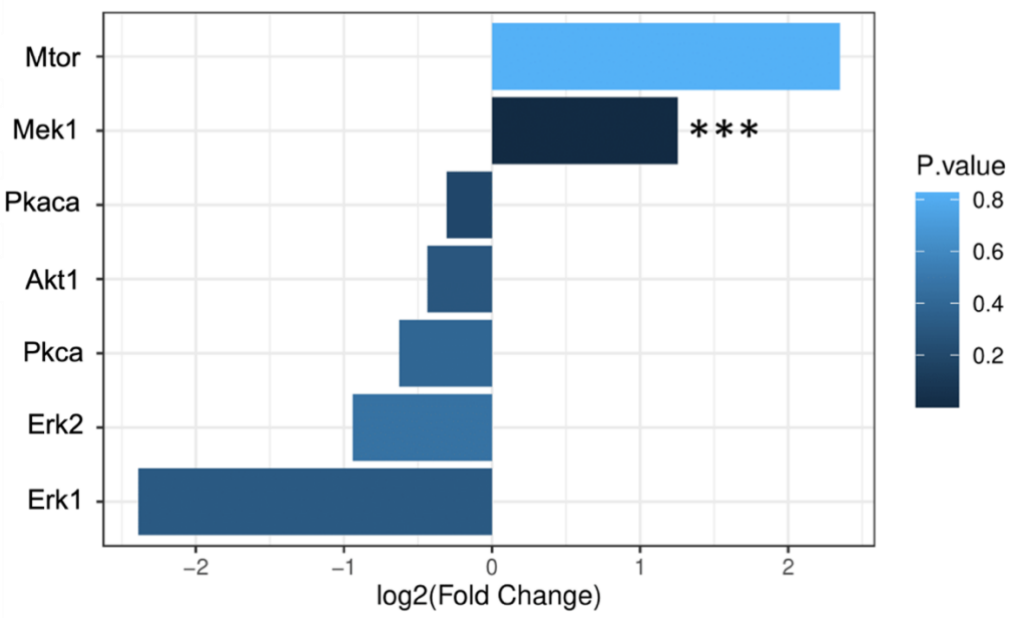

Figure 6.10. Kinase substrate enrichment analysis (KSEA) of changes in kinase activity in R-Ras KO v WT mouse aorta. Mean log2(Fold Change) in phosphosite abundance in KO vs. WT samples were calculated for each sample, and used for KSEA analysis [357]. Changes in kinase activity are expressed as log2(Fold Change) in KO vs. WT samples. Bars are coloured dependent on p values obtained using an unpaired t-test with unequal variance. ***p < 0.001. Plotted using ggplot2 in R.

6.2.2.3. KEGG geneset enrichment analysis reveals pathways related to BP

KEGG geneset enrichment analysis (GSEA) was performed on the phosphoproteomic dataset using the gseKEGG function in R/ClusterProfiler to explore changes in signalling pathways in mouse aortas resulting from R-Ras KO. Some phosphoproteins have multiple phosphosites. KEGG GSEA does not consider the specific phosphosite, and therefore an individual phosphoprotein may appear in the analysis multiple times, potentially introducing bias. To assess whether this potential bias impacts GSEA output, three separate analyses were performed, as follows:

A1 Analysis 1

Multiplicate genes removed and the highest Log2FC value for that protein included, with the corresponding p value (Supplementary Table S5).

A2 Analysis 2

Multiplicate genes removed and the most significant p value for that protein included, with the corresponding Log2FC value (Supplementary Table S6).

A3 Analysis 3

All multiplicate genes included (Supplementary Table S7).

The results were largely consistent between all 3 analyses, A1, A2, and A3 (Figure 6.11, Supplementary Tables S5 to S7). All significantly enriched pathways in A1 and A2 were downregulated. A1 shared every significantly enriched pathway with A2, with minor discrepancies in p value or normalised enrichment score (NES) (Figure 6.12, Supplementary Tables S5 and S6). A1 however reports ‘Thermogenesis’ as significantly downregulated – this was not significant in A2.

The results from A3 included all the pathways significantly enriched in A1 and A2. The ‘cAMP signaling’ pathway had the highest NES and p value for all three GSEAs (Supplementary Tables S5 to S7). There were also some other significant pathways only in A3. These included the ‘Adrenergic signaling in cardiomyocytes’ pathway which was significantly downregulated; this downregulation was mirrored in A1 and A2 but did not reach significance (Figure 6.11, Supplementary Tables S5 to S7). There was also a significantly upregulated pathway - ‘Hippo signaling pathway – multiple species’ (NES = 1.48, p = 0.047) (Supplementary Table S7). The A3 analysis included all multiplicate genes and this may reflect some bias on these results.

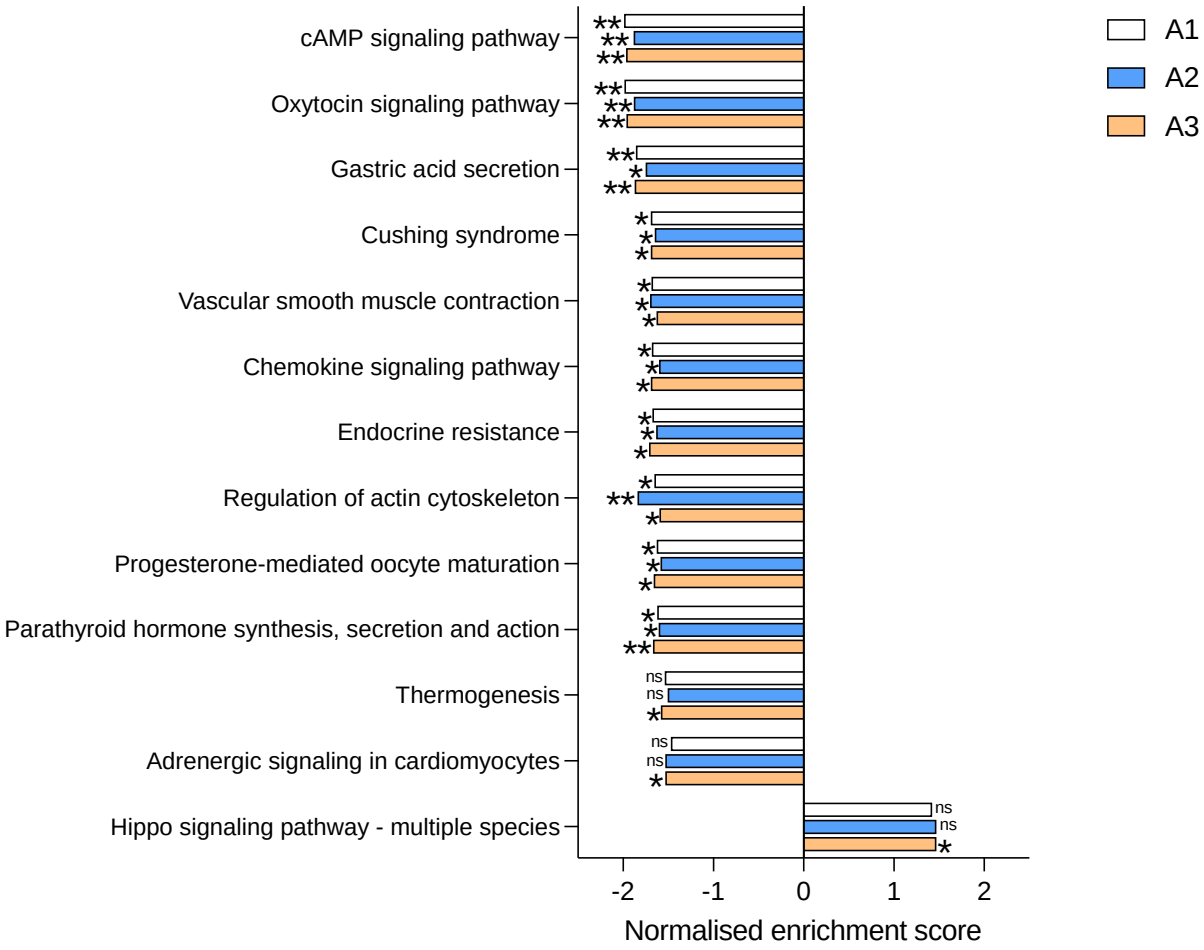

Figure 6.11. Comparative barplot of enriched KEGG pathways in the R-Ras KO mouse aorta from KEGG geneset enrichment analyses (GSEA) A1, A2 and A3. Three GSEA analyses were run to assess bias imparted by multiplicate phosphoproteins. A1 included only phosphoproteins with highest Log2FC value (white). A2 included only phosphoproteins with highest p value (blue). A3 included all multiplicate phosphoproteins (orange). KEGG GSEA was performed using the gseKEGG function in the R/Bioconductor package. Significant enrichment was calculated with permutation testing. * = $p < 0.05$, ** = $p < 0.01$, ns = non-significant.

Following the large overlap observed between GSEA A1, A2, and A3, only results from A1 are reported here (phosphoproteins with highest Log2FC values). A1 identified 28 upregulated and 75 downregulated KEGG genesets/pathways in the R-Ras KO mouse aorta (Table 6.3, Supplementary Table S5). 11 downregulated pathways were statistically significantly enriched with permutation testing ($p < 0.05$, Figure 6.12, Table 6.3). The ‘cAMP signaling’ pathway had the highest NES, and was most significant (NES = 1.99, $p = 0.002$, Figure 6.12 and Table 6.3).

There were no upregulated pathways which reached statistical significance with permutation testing in A1. Table 6.3 lists the enriched genes in the significant pathways, which appear in the ranked list before the maximum running score is reached in the GSEA. There is a lot of overlap in these enriched genes between significantly downregulated pathways, suggesting these pathways are related (Table 6.3).

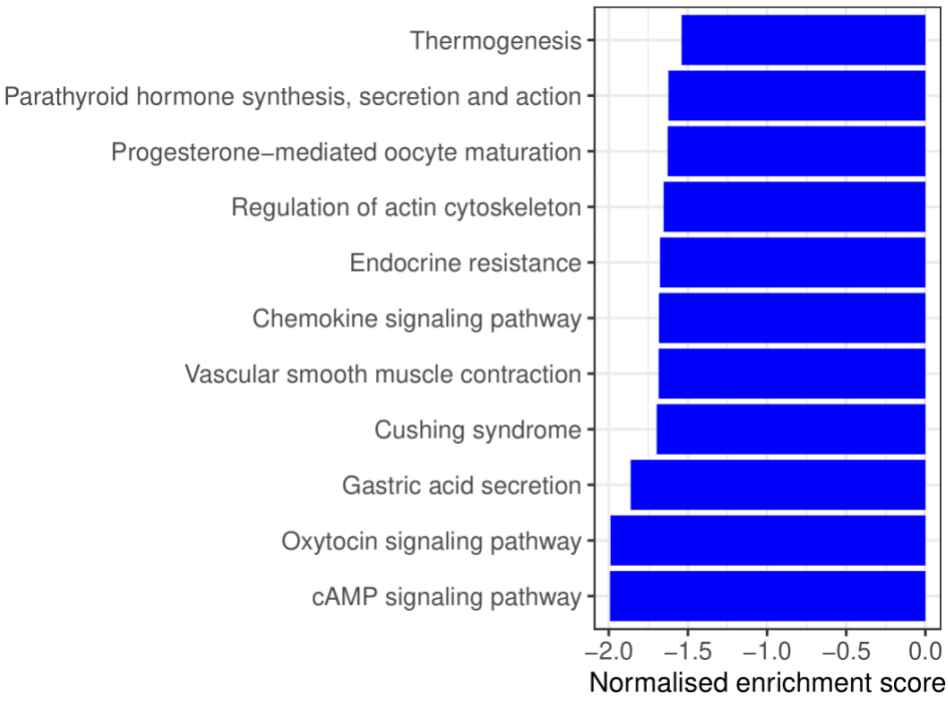

Figure 6.12. Barplot of significantly enriched pathways in the R-Ras KO mouse aorta - results from analysis A1. The phosphoproteomic dataset was filtered by removing multiplicate phosphosites and including phosphoproteins with the highest Log2FC (Analysis A1, Supplementary Table S5). KEGG gene set enrichment analysis was performed using the gseKEGG function in the R/Bioconductor package. The normalised enrichment score is calculated from the running score of a random walk of the phosphoproteomics gene list against the KEGG geneset, normalised against the number of genes in the geneset.

Table 6.3. Significantly enriched KEGG pathways in R-Ras KO mouse aortas - GSEA results from analysis A1.

Pathway	NES	P value	Enriched genes
cAMP signaling pathway	-1.99	0.002	*Adcy6/Braf/Cnga3/Myl9*
Oxytocin signaling pathway	-1.99	0.002	*Actb/Adcy6/Myl9/Mylk/Mylk2*
Gastric acid secretion	-1.86	0.005	*Actb/Adcy6/Adcy9/Mylk/Mylk2*
Cushing syndrome	-1.70	0.013	*Adcy6/Adcy9/Braf*
Endocrine resistance	-1.68	0.017	*Adcy6/Adcy9/Braf/Ncor1*
Parathyroid hormone synthesis, secretion and action	-1.62	0.017	*Adcy6/Braf*
Chemokine signaling pathway	-1.68	0.019	*Adcy6/Adcy9/Braf*
Progesterone-mediated oocyte maturation	-1.63	0.024	*Adcy6/Adcy9/Braf*
Vascular smooth muscle contraction	-1.68	0.031	*Adcy6/Braf/Myl9/Mylk2*
Thermogenesis	-1.54	0.037	*Actb/Adcy6*
Regulation of actin cytoskeleton	-1.65	0.038	*Actb/Braf/Enah/Myl9/Mylk/Mylk2*

KEGG GSEA was performed using the R/Bioconductor package, with multiplicate genes filtered based on highest Log2FC values (Analysis 1). Enrichment scores are normalised against the number of genes in the KEGG geneset and presented as normalised enrichment scores (NES). A negative NES indicates downregulation in the R-Ras KO vs. WT mouse aorta. Enriched genes appear in the ranked list at or before the point at which the running sum reaches its maximum enrichment score.

The overarching aim of this PhD study was to investigate the contribution of R-Ras to BP control. Therefore, the downregulation of pathways directly related to BP control in the R-Ras KO mouse aorta were assessed ('cAMP signaling', 'Oxytocin signaling', 'Vascular smooth muscle contraction', 'Regulation of actin cytoskeleton'). These KEGG pathways share the cAMP and RhoA/ROCK signalling cascades. R-Ras is activated by cAMP [248], and potentiates RhoA/ROCK signalling [279,358]. Genes common between the significantly downregulated pathways are actin beta (*Actb*), adenylate cyclase isoforms 6 (*Adcy6*) and 9 (*Adcy9*), the oncogene v-raf murine sarcoma viral oncogene, B-raf (*Braf*), and MLCK isoforms (*Mylk, Mylk2*) and myosin light chain 9 (*Myl9*) (Table 6.3, Figure 6.13). These genes are also common in the pathways listed in Table 6.3 (Figure 6.13). Together, this data suggests a role of R-Ras in vascular BP control signalling.

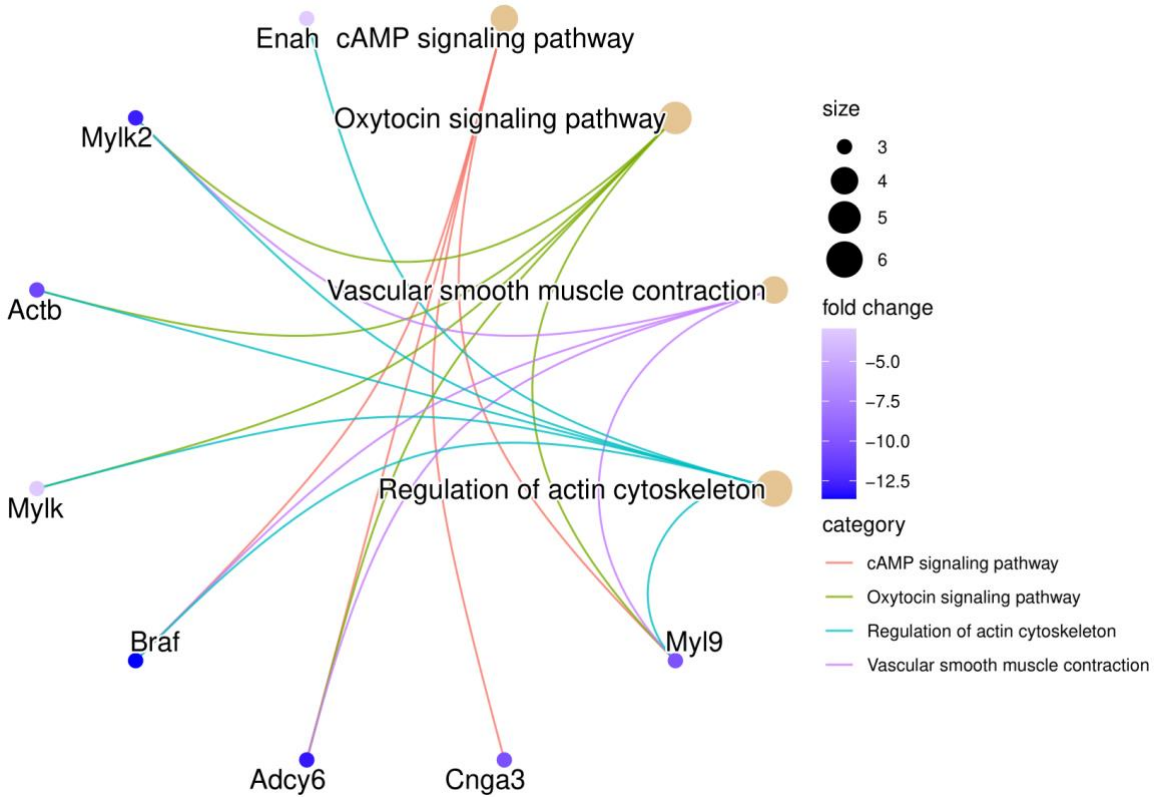

Figure 6.13. Circle plot illustrating crossover of genes in significantly upregulated pathways directly related to blood pressure control in the R-Ras KO mouse aorta. The genes shown are present in the phosphoproteomics gene list. The dot size corresponds to the number of genes in the KEGG gene set that are present in the other gene sets. The fold change illustrates the Log2FC value in the R-Ras KO mouse aorta compared to WT. Plotted with R/ggplot2.

6.2.2.4. Evaluating a role of R-Ras in Hippo signalling

The 'Hippo signalling pathway – multiple species' KEGG geneset was the only pathway upregulated in the R-Ras KO mouse aorta (Figure 6.11, Supplementary Tables S5 to S7). This enrichment had nominal significance in the KEGG enrichment analyses A1 and A2 (multiplicate genes removed) and reached significance when multiplicate genes were included (analysis A3). This pathway further was chosen for further follow-up as it is evidenced to promote VSM contraction [359], and is implicated in other cardiovascular processes also linked to R-Ras, including angiogenesis and smooth muscle cell restenosis [360–362]. The gold-standard method to confirm changes in phosphorylation status of proteins is western blotting. However, this technique is time-consuming, and antibodies are expensive, and this method was not achievable in the remaining time frame of this PhD. Therefore, an immunofluorescence staining protocol of mouse aortas using YAP/TAZ antibodies previously optimised by our research group was performed as preliminary validation experiments to explore the impact of R-Ras KO on YAP/TAZ signalling.

The YAP (Yes-associated protein 1) and TAZ (Transcriptional co-activator with PDZ binding motif) are the primary sensors of the Hippo signalling pathway. YAP/TAZ binds TEAD (Transcriptional enhanced associate domain) in the nucleus and influences gene expression to regulate cell proliferation, differentiation, and apoptosis (Figure 6.14). YAP/TAZ signalling contributes to adaptation of the VSM to mechanical forces, both acutely and chronically [359,363]. This is in line with the downregulation of VSM contraction KEGG pathway observed in the R-Ras KO mouse aorta.

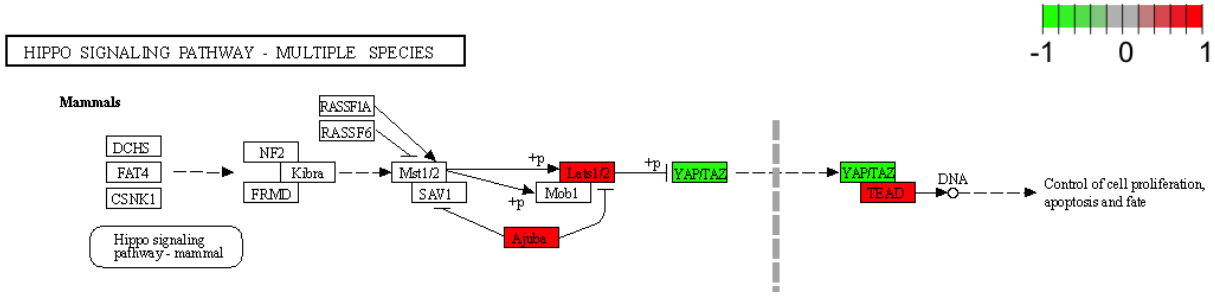

Figure 6.14. Changes in phosphorylation of proteins in the 'Hippo signalling pathway – multiple species' KEGG pathway with R-Ras KO. Changes in phosphorylation of proteins resulting from R-Ras KO were visualised using Pathview (R/Bioconductor). Red indicates upregulated phosphorylation, and green downregulated phosphorylation.

Lats1 and TEAD phosphorylation were upregulated in the R-Ras KO mouse aorta (Lats1(S461); Log2FC = 13.3, p = 0.02, Tead3(S145); Log2FC = 11.5, p < 0.0001, Supplementary Table S2). YAP phosphorylation was downregulated (Yap1(S148); Log2FC = -2.24, p = 0.02, Supplementary Table S3, Figure 6.14). The hypothesis was that R-Ras will promote YAP/TAZ localisation to the nucleus in VSMCs where it is active, thus regulating VSM contraction. To explore this, immunofluorescence staining was performed to monitor nuclear translocation of YAP/TAZ in WT and R-Ras KO mouse aortas with the hypothesis that YAP/TAZ will be retained in the cytoplasm in KO. However, this yielded inconclusive results as cytoplasmic and nuclear localisation was not discernible (Figure 6.15).

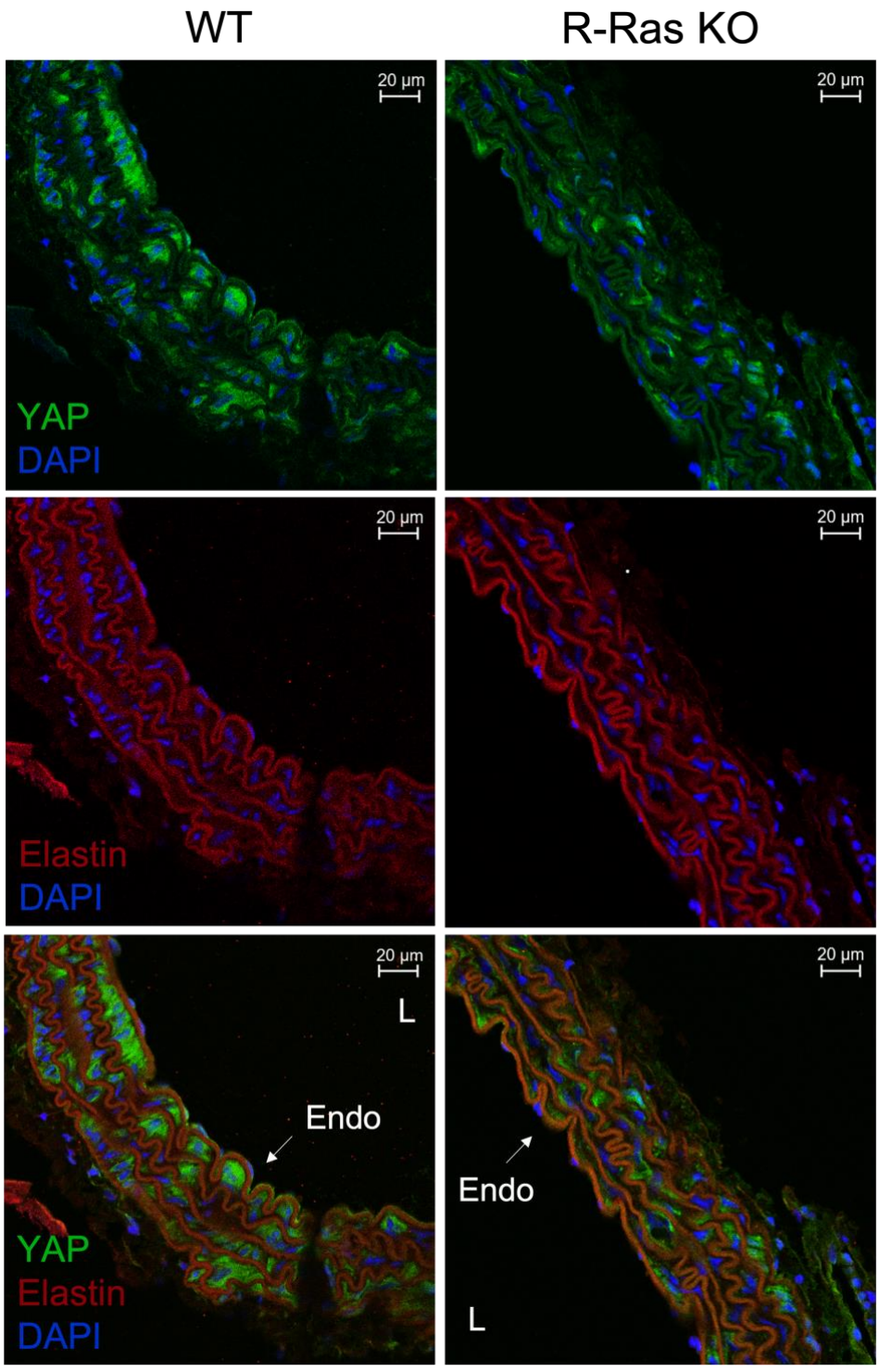

Figure 6.15. Confocal immunofluorescence images of YAP localisation in the WT and R-Ras KO mouse aorta. Aortas were sectioned horizontally and incubated with anti-YAP (green), anti-elastin (red), and DAPI (blue, nuclei). Images were acquired using the Zeiss LSM 710 Confocal Microscope at x40 magnification. The endothelium (Endo) and the lumen (L) are indicated.

6.3. Discussion

A hypothesis-free multi-omic approach was adopted to ascertain if there were changes in gene expression (RNA-seq) and cell signalling pathways (phosphoproteomics) between R-Ras KO and WT mice aorta, in a bid to elucidate whether R-Ras KO had an impact on BP related pathways in the young mouse, and to identify mechanisms which may be contributing to the age-related BP phenotype. Transcriptomic analysis with RNA-seq failed to detect changes in gene expression, which may be due to issues with sample heterogeneity and study design. Phosphoproteomics was more fruitful; analysis revealed hundreds of significantly up- and down-regulated phosphosites. When contextualised as changes in cell signalling pathways, pathways related to BP control were enriched. These findings warrant follow up studies to confirm these observations and delineate how R-Ras contributes to signalling mechanisms acting to regulate BP.

6.3.1. Transcriptomics of the young R-Ras KO mouse aorta

RNA-seq analysis was used to measure changes in gene expression resulting from *Rras* gene deletion in the young adult mouse aorta. PCA demonstrated a lack of clustering between samples within genotype. This is likely explained by limitations in study design. Samples were processed in two batches, and two samples required additional DNase treatment to improve quality after RNA isolation, introducing differing processing conditions. Thus, the results from the RNA-seq must be interpreted with caution.

I considered whether the lack of clustering of groups in PCA may be explained by the heterogeneous genetic architecture of the aorta. Embryological [364] and single-cell RNA-seq (scRNA-seq) studies [365] have highlighted the spatial diversity in the SMC and EC types along the aorta. In this RNA-seq study, RNA was extracted from the whole aorta, but it is not certain that the whole aorta was harvested for each sample, and flushing of the aorta to remove blood during sample preparation may have accidentally removed endothelial cells. This limitation is likewise acknowledged in an RNA-seq comparative study of the young and aged whole mouse aorta [366]. Gao and colleagues performed RNA-seq on 5 replicates of male whole aortas from young and aged mice, reporting over 2,000 DE genes. However, the PCA showed distinct clustering of samples in young and aged groups [366]. The lack of clustering observed in this study is therefore more likely to be due to processing conditions. ScRNA-seq on individual EC and SMCs may provide more informative data in this study, by reducing noise from studying multiple cell types at once. Notably, Zhang and colleagues have

used scRNA-seq to demonstrate changes in transcriptome of subpopulations of ECs and SMCs extracted from the mouse aorta after salt-induced hypertension, including in expression of genes related to contractility [367]. Repeating this scRNA-seq on ECs and SMCs isolated from the R-Ras KO mouse aorta may facilitate identification of more subtle changes resulting from *Rras* gene deletion .

Rras was the only significantly DE gene in the young adult R-Ras KO mouse aorta after Bonferonni correction. Prior to Bonferonni correction, 53 genes were significantly DE in the R-Ras KO mouse aorta using an unpaired t-test with unequal variances assumed, and a threshold of Log2FC ± ≥ 2. of these genes, many were pseudogenes, or appear to be unrelated to R-Ras or BP and hypertension. I performed an exploratory KEGG enrichment analysis on the dataset of genes significantly DE prior to Bonferonni correction to identify whether these genes were related and involved in BP-relevant pathways. However, this yielded no significantly enriched KEGG pathways in R-Ras KO in the mouse aorta. Overall, RNA-seq of the young R-Ras KO mouse aorta failed to produce any interesting results. This is potentially due to issues with study design and underpowering, which may be overcome with scRNA-seq, including higher *n* numbers, and more stringent sample preparation to minimise heterogeneity between samples. Alternatively, there may simply be no major transcriptomic changes induced by *Rras* KO in the mouse aorta.

6.3.2. Phosphoproteomics analysis of the young R-Ras KO mouse aorta

Phosphoproteomics detects changes in PTMs of proteins as an indicator of change in protein activity. A phosphoproteomic approach was chosen over proteomics (which provides information on the proteins present in a sample) in the hope to delve deeper into changes in protein signalling pathways resulting from R-Ras KO in the mouse aorta, as well as the proteomic makeup. Over 700 differentially phosphorylated phosphosites were identified in the R-Ras KO mouse aorta, corresponding to nearly 500 phosphoproteins. These included novel phosphoproteins not previously associated with R-Ras (e.g. tensin-2, myosin light chain kinases), and previously associated phosphoproteins (e.g. filamin-A, adenylyl cyclase). These changes were then contextualised into cell signalling pathways using geneset enrichment analysis (GSEA) and the KEGG database. Three analyses were performed with multiplicate phosphoproteins removed (A1, A2) or included (A3). All three GSEA analyses revealed the ‘cAMP signaling pathway’ as the most significant and enriched downregulated pathway in the R-Ras KO mouse aorta compared to WT. A role of R-Ras in vascular BP control was supported by downregulation of ‘Vascular smooth muscle contraction’ and ‘Regulation of the

actin cytoskeleton' pathways in all 3 analyses. These discoveries warrant confirmation and further investigation to delineate the mechanisms by which R-Ras may contribute to vascular BP control.

When interpreting this data, it must be stressed that phosphoproteomics is an exploratory analysis. An individual phosphoprotein has multiple phosphosites and can be simultaneously up- or downregulated. Therefore, the change in phosphorylation status of proteins observed can sometimes be contradictory to that reported in the literature, depending on the phosphosite. This data can be interpreted as an indication of changes in potential pathways, however *in vitro* confirmation of changes in phosphorylation status of proteins, and observations in cell signalling pathways, are essential to draw any concrete conclusions. Phosphoproteomics is therefore a useful tool to generate new hypotheses.

6.3.2.1. Downregulation of eNOS phosphorylation with R-Ras KO is not significant

One of the preliminary hypotheses was that R-Ras would potentiate NO signalling via PI3K/Akt/eNOS signalling in endothelial cells. Western blotting assays in human umbilical vein endothelial cells demonstrated transfection with constitutively active R-Ras results in upregulated eNOS (Nos3) phosphorylation, indicating eNOS activation (section 4.2.5). Here, the phosphoproteomic data suggest that eNOS phosphorylation is downregulated with R-Ras KO at S632, although not significantly. In the western blotting experiments, the antibody specifically targeted the S1177 phosphosite on eNOS, however eNOS activity is mediated by phosphorylation at multiple sites. Phosphorylation of Nos3(S633), located in the flavin mononucleotide binding domain of eNOS, also increases eNOS activity and appears particularly important for the maintenance of NO synthesis after initial activation by Ca^{2+} flux and S1177 phosphorylation [368]. Could R-Ras modulate S1177 phosphorylation indirectly via S633 phosphorylation? It is important to consider the lack of significance observed with this finding. This may be explained by the endothelial localisation of eNOS, and the delicate nature of the endothelium monolayer meaning it could have been accidentally removed during sample preparation, explaining the lack of phosphosite present in 2 out of 4 WT samples. However, it is not certain that this didn't happen in the KO samples, in which case the lack of Nos3(S633) phosphosite will be due to lack of endothelial cells in the preparation rather than downregulated phosphorylation. Furthermore, why was downregulated phosphorylation at Nos3(S1177) not observed in the phosphoproteomics dataset? The *in vitro* observations

suggest R-Ras potentiates eNOS activity, yet this was not validated in the *in vivo* phosphoproteomic data.

6.3.2.2. R-Ras KO alters the phosphorylation status of novel and known proteins in the mouse aorta

The most differentially phosphorylated phosphosites in the R-Ras KO mouse aorta were in the tensin-2 protein. Five phosphosites in tensin-2 were significantly upregulated in the R-Ras KO. Tensin-2 is a ubiquitously expressed focal adhesion molecule, with a prominent role in maintaining structural integrity of the glomerular basement membrane in kidneys [369]. Studies in *Tns2* deficient mice reveal development of glomerular and nephrotic kidney disease, depending on the genetic background [369,370]. Numerous homozygous recessive mutations in the *TNS2* gene are associated with nephrotic syndrome (NS) in humans, as revealed with whole exome sequencing in affected families [371]. Hypertension is a common comorbidity of NS, in part due to RAAS activation, glomerular fibrosis and reduced glomerular filtration rate [372]. A direct link between tensin-2 and BP has not been established *in vivo*, although numerous genome and exome wide studies have associated *TNS2* gene variants with SBP [373–377], DBP, and MAP [376]. Tensin-2 downregulates Akt activity [378], in contrast to the stimulatory effect of Akt by R-Ras [208,217,224,230,231,234–239,379,380]. In R-Ras KO mouse aortas, tensin-2 phosphorylation is upregulated i.e. activated. A possible interaction between R-Ras and tensin-2 could be related to the RAAS. However, in the KO mice challenged with ANGII to induce hypertension differences to WT were not observed in BP, or associated cardiac fibrosis and arterial wall thickening (Chapter 4), suggesting the link between tensin-2 and R-Ras is distinct from renal BP control. However, R-Ras does have medium expression levels in the glomeruli [203]; possible colocalization and interaction of tensin-2 and R-Ras in the kidneys may warrant investigation. Tensin-2 is highly expressed in the aorta [203], however literature predominantly reports on the renal function of tensin-2, and there is a lack of research into the vasculature. Tensin-2 is an focal adhesion molecule, and R-Ras promotes focal adhesion formation [212,262]. Focal adhesions are integral in actin cytoskeleton reorganisation in vascular smooth muscle contraction, and in vascular remodelling. Could an interaction of tensin-2 and R-Ras in the aorta be a novel pathway for actin cytoskeleton regulation in the vasculature?

Another gene that appears in the phosphoproteomics dataset is *Flna*, encoding filamin-A. Filamin-A is a large-actin binding cytoskeletal protein, highly expressed in vascular tissues [381]. Smooth muscle specific deletion of *Flna* in mice results in attenuated caudal and renal

myogenic tone [382]. Mice with impaired RNA-editing of *Flna*, important for optimal function of the protein, exhibit diminished aortic contraction to U46619, and elevated DBP at rest measured with radiotelemetry [383]. MLC phosphorylation is increased in these mice; dephosphorylation of MLC premediates smooth muscle relaxation [383]. With R-Ras KO in the mouse aorta, 4 phosphosites on filamin-A are upregulated, and 1 downregulated. Notably, phosphorylation of S16, S20 and T1747 is upregulated with R-Ras KO. These sites are in the actin binding region, and Hinge 1 region (responsible for maintaining viscoelastic properties of actin networks [384]), respectively (UniProt ID: Q8BTM8), suggesting R-Ras may impact filamin-A function. This is supported by literature evidencing an interaction of filamin-A and R-Ras in maintenance of vascular permeability in human coronary artery endothelial cells [356] and in a mouse model of hindlimb ischaemia [217]. Together, this data suggests R-Ras and filamin-A may also interact to regulate vascular tone.

It is well established that R-Ras activation initiates PI3K/Akt signalling [208,217,224,230,231,234–239,379,380]. The phosphoproteomics data indicate members of the PI3K/Akt signalling axis have upregulated phosphorylation in the R-Ras KO mouse aorta; this is contrary to what would be expected as R-Ras potentiates PI3K/Akt signalling. This includes Irag1 (inositol 1,4,5-triphosphate receptor associated 1) which is involved in NO-mediated relaxation of gastric smooth muscle [385], although a link with VSM has not yet been established. R-Ras KO mice also have upregulated phosphorylation at Akt1(S129). Akt1 is the predominant isoform of Akt in endothelial cells, and is implicated in the pathogenesis of hypertension via its roles in eNOS phosphorylation [386], endothelial dysfunction [387], and in angiogenesis [388]. Akt1 activity is largely mediated by phosphorylation at S473 and T308 [379]. The Akt1(S129) phosphosite on the other hand has been demonstrated to facilitate anti-apoptopic activity of Akt by preventing dephosphorylation at T308, facilitated by the CK2 kinase and association with the Hsp90 chaperone [53]. R-Ras also contributes to the anti-apoptopic role of PI3K/Akt signalling axis, as demonstrated in HUVECs where active R-Ras inhibits Bax-induced apoptosis in the context of angiogenesis, particularly at phosphosites S473 and T308 [379]. Therefore, R-Ras KO would be expected to result in downregulated phosphorylation at Akt1(S129), contrary to what is observed in the phosphoproteomics data. Furthermore, results from the KSEA analysis, which provides a measure of kinase activity based on changes in phosphorylation status of downstream effectors of kinases, suggest Akt1 phosphorylation is downregulated with R-Ras KO, although this failed to reach significance. The significance of Akt1(S129) upregulated phosphorylation with R-Ras KO therefore remains unclear, but does affirm interaction of R-Ras with the protein. Whether R-Ras contributes to the NO-mediated vasorelaxation and anti-hypertensive roles of Akt remains unknown.

Rasa3 is an R-Ras GAP which has been shown to inactivate R-Ras in neuronal [390] and breast cancer cell lines, and *in vivo* in the zebrafish xenograft model [391]. Specifically, Rasa3 functions to oppose R-Ras action, leading to destabilisation of focal adhesions and promoting metastasis of cancer cells [391], or preventing the development of stable embryonic blood vessels by limiting endothelial cell migration [390]. Phosphoproteomic analysis indicated R-Ras KO in the mouse aorta results in upregulated phosphorylation of Rasa3 at phosphosites Y807 and S809, and downregulated phosphorylation at S833. The functional relevance of these sites is not known. This is an interesting observation nonetheless as Rasa3 has only been implicated to work upstream of R-Ras in previous literature.

6.3.2.3. MEK1 activity could be upregulated with R-Ras KO in the mouse aorta

The impact of phosphorylation at phosphosites on proteins do not always have a functional impact, evidenced by the poor conservation of phosphorylation sites across species [392]. Throughout the phosphoproteomics dataset, phosphorylation at different phosphosites of the same protein are differentially up- and downregulated with R-Ras KO, despite being located on the same protein. Kinase-Substrate Enrichment Analysis (KSEA) instead combines information on known kinase-substrate relationships available in databases with phosphoproteomic datasets to estimate the kinase activity of known kinases [357,393]. Mek1 (MAPK/ERK kinase) was the only kinase to reach significance with KSEA, and was upregulated in R-Ras KO, suggesting R-Ras normally inhibits its activity. There is contradictory literature on R-Ras and MEK1. Notably, constitutively active R-Ras does not stimulate MEK or its downstream activator ERK in transfected COS-7 cells [224], or human carcinoma cell lines [394]. Yet, a more recent study in glioma cells proposes R-Ras to inhibit MEK via Eph receptor tyrosine kinase signalling, attenuating proliferation [395]. This is concurrent with the KSEA data, indicating MEK activity is upregulated in R-Ras KO mouse aortas. In contrast, Erk1 and Erk2 activity appears to be downregulated as analysed with KSEA, although this does not reach significance. This KSEA has limitations. Firstly, the databases used are biased towards well-known kinases and pathways, so the size of the substrate sets differs, and other less-studied kinases could be missed. Secondly, KSEA was specifically designed for applications in human data, and does not include the phosphosite when analysing mouse datasets.

MEK/ERK signalling is associated with VEGF-induced angiogenesis [396,397], contrary to the anti-angiogenic role of R-Ras [208], also exemplified by the aortic ring assay in this study (Chapter 4.2.7). More relevant in the context of this thesis however is the role of MEK/ERK in

VSM contraction. MEK/ERK activates MLCK, leading to increased MLC phosphorylation and contraction [398]. This is further evidenced in spontaneously hypertensive rats, which exhibit elevated ERK levels [399], and increased ANGII-mediated contraction of VSMCs from SHRs compared to normotensive controls is normalised by ERK inhibition [400]. Upregulation of Mek1 activity with R-Ras KO may propose a role for R-Ras in VSM contraction mediated by MEK/ERK.

6.3.2.4. A potential role of R-Ras in regulation of vascular tone

KEGG GSEA contextualises changes in phosphorylation status of proteins to measure the up- and downregulation of pathways between different conditions – in this study, between WT and R-Ras KO. The KEGG pathway database is a continuously updated database of molecular pathways based on genomic, chemical and systemic functional information [401]. As described, three GSEA analyses were performed with multiplicate phoshoproteins excluded (A1, A2) or included (A3). The results from analyses A1 and A2 were largely consistent, with all pathways downregulated. Analysis A3 with multiplicate phosphoproteins included reported one significantly upregulated pathway – 'Hippo signaling – multiple species'.

When multiplicate phosphoproteins were excluded, KEGG GSEA resulted in 11 significantly enriched pathways, all of them downregulated. These included pathways directly associated with vascular blood pressure control, namely 'Vascular smooth muscle contraction', the 'cAMP signaling pathway', the 'Oxytocin signaling pathway', and 'Regulation of actin cytoskeleton'.

cAMP signalling in endothelial and vascular smooth muscle cells promotes vasodilation [49,240]. Here, downregulation of cAMP signalling in the R-Ras KO mouse aorta is reported, and more specifically downregulated phosphorylation of the adenylyl cyclase isoforms 6 (Adcy6) and 9 (Adcy9) in the mouse aorta. AC is activated by Gαs-coupled GPCRs and catalyses the formation of cAMP. While the Adcy9 isoform is highly expressed in skeletal muscle [402], the predominantly VSM expressed Adcy6 isoform is key in regulating vasoreactivity via cAMP/PKA-mediated cytoskeletal reorganisation of VSM [403–405]. cAMP/PKA signalling also promotes vasodilation via direct phosphorylation and activation of K_{ATP} channels to induce hyperpolarisation, subsequently attenuating VGCC activity in VSMCs [50]. Likewise, Epac has been demonstrated to promote vasodilation via inhibition of RhoA and via K_{ATP} channel activation [49,398], however cAMP/PKA signalling is primarily responsible for K_{ATP} channel activity (Figure 6.16). In ECs, cAMP-mediated activation of PKA and Epac promotes NO formation to induce vasodilation [243] (Figure 6.16). R-Ras is

activated by AC downstream of Gαs-coupled receptors, including M3AChRs and β2-adrenoreceptors; this was shown as dependent on Epac, and independent of PKA [240]. This cAMP/Epac/R-Ras signalling mechanism has been explored in the context of endothelial integrity. Epac enhances endothelial barrier integrity by stimulating cAMP activity and stabilising actin [248]. This is determined by the interaction between filamin-A and R-Ras *in vitro* [356], and the observation that Flna is differentially phosphorylated with R-Ras KO may support this.

VSM contraction relies on the phosphorylation status of MLC, governed by MLCK and MLCP activity which phosphorylate and dephosphorylate MLC, respectively [406]. RhoA/ROCK signalling downstream of G12/13 coupled receptors promotes VSM contraction by increasing Ca^{2+} sensitization via ROCK-mediated phosphorylation of Mypt1, a subunit of MLCP, leading to its inhibition [406] (Figure 6.16). The phosphoproteomics data shows R-Ras KO results in differential phosphorylation of Rock1, Mypt1, and MLC (Figure 6.16). Specifically, R-Ras KO results in downregulated phosphorylation of Rock1 at S1100;S1102. This observation is concurrent with *in vitro* studies showing R-Ras activates ROCK [279], via RhoA [358]. The same study found R-Ras promotes phosphorylation of Mypt1 [279], but this is contrary to the upregulation observed with the R-Ras KO in the mouse aorta in this study. The Rock1(S1100;S1102) phosphosite is located in the RhoA binding region (Uniprot ID: P70335). Rock1 is downstream of RhoA. Downregulation of this phosphosite via R-Ras may attenuate Rock1 binding to RhoA, thus inhibiting VSM contraction as observed with GSEA. However, R-Ras KO also results in the upregulation of phosphorylation of Rock1 at S1108; the function of this phosphosite has not been elucidated. R-Ras KO also results in downregulated phosphorylation of MLCK (Mylk(S1781;S1782)), and MLC isoform 9 (Myl9(45-63,no_mod)), although at a 'no modification' site. Previous literature shows R-Ras38V transfection in breast epithelial cells results in accumulation of MLC and MLC-P S19 at edges, promoting changes in cell morphology and cell motility [407], but there are no reported experiments directly linking MLCK and MLC activity with R-Ras in the context of VSM contraction.

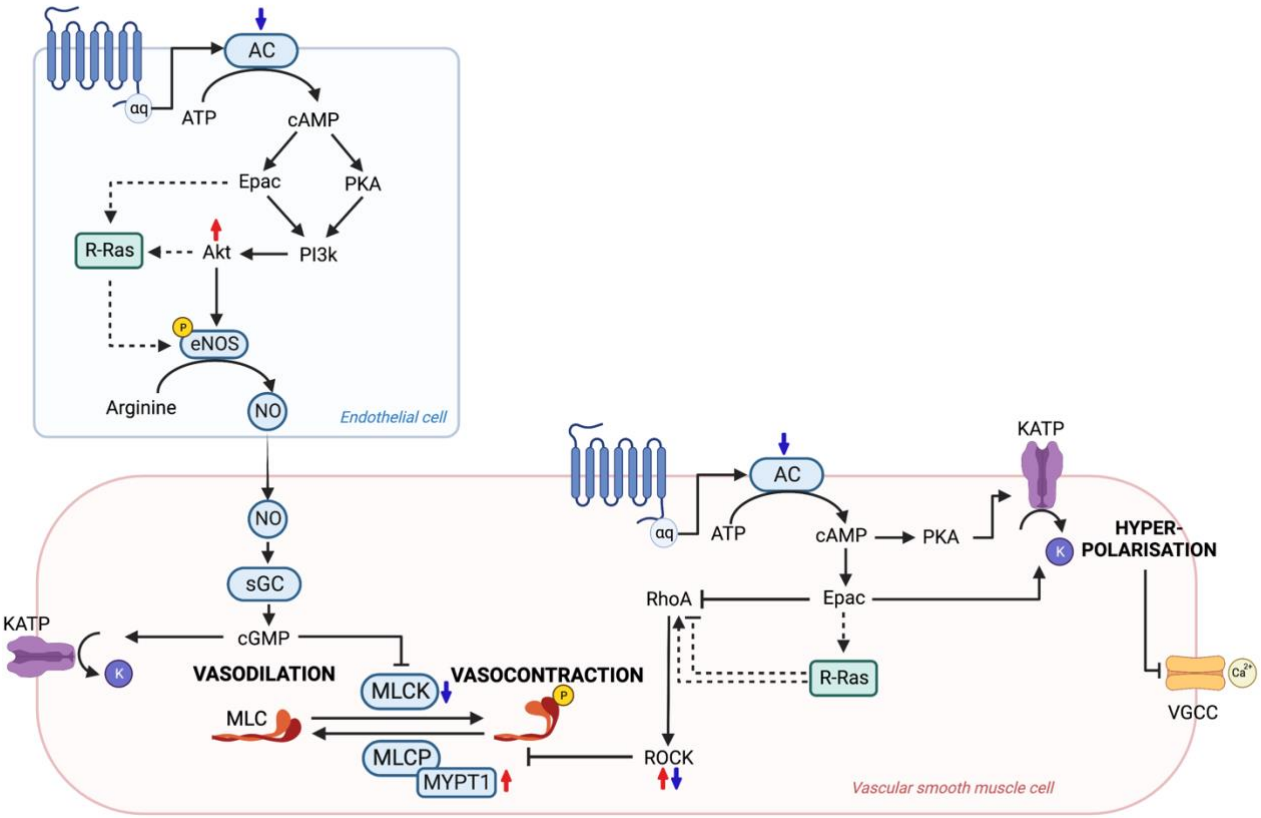

Figure 6.16. Proposed role of R-Ras in cAMP signalling to mediate vascular tone in endothelial and smooth muscle cells. Solid black arrows indicate known mechanisms of vasodilation and vasoconstriction. Dotted black arrows indicate proposed mechanisms of R-Ras to mediate vascular tone. Red (upregulation) and blue (downregulation) arrows indicate phosphorylation status of phosphosites in the young R-Ras KO mouse aorta identified with phosphoproteomics.

In vitro studies have showed R-Ras is activated by Epac, but not PKA [240], and by PI3K/Akt. In ECs, PI3k/Akt signalling stimulates NO production which induces vasodilation by sGC signalling in VSMCs. R-Ras could potentially be activated by cAMP/Epac/PI3k/Akt signalling in ECs to mediate NO formation (Figure 6.16), evidenced by the *in vitro* western blotting assays (section 4.2.5). In VSMCs, cAMP signalling activates Epac, which inhibits RhoA/ROCK signalling disinhibiting MLCP and resulting in vasodilation. Epac also activates K_{ATP} channels resulting in hyperpolarisation and closing of VGCCs, preventing Ca^{2+} influx and thus Ca^{2+}/CaM/MLCK-mediated vasocontraction. Could R-Ras regulate vasodilation downstream of cAMP/Epac? (Figure 6.16). There is also evidence in the literature that R-Ras activates Rho/ROCK, and the 'Vascular smooth muscle contraction' pathway is

downregulated in the R-Ras KO mouse aorta. This could be another potential pathway R-Ras regulates vascular tone, via Rho/ROCK inhibition of MLCP to promote vasoconstriction, albeit opposing the cAMP/Epac-mediated vasodilation (Figure 6.16). This is in line with the concurrent downregulation of both 'cAMP signaling', and 'Vascular smooth muscle contraction' pathways in the phosphoproteomics dataset. These observations reflect how phosphoproteomics analysis can provide multiple potential mechanisms for further interrogation. It is imperative these reported changes in cell signalling are confirmed *in vitro*.

The oxytocin signalling pathway is also implicated in VSM contraction and vasorelaxation; low doses stimulate PI3K/eNOS signalling to cause vasorelaxation, and high doses increase phospho-ERK1/2 expression to induce vasoconstriction in rat aortic ring organ bath [408]. Altogether, the exact position of R-Ras in all of this remains unclear, yet the data does evidence R-Ras involvement in pathways regulating vascular contractility.

The 'Regulation of actin cytoskeleton' pathway is also downregulated in R-Ras KO mouse aortas. This supports the literature evidencing R-Ras-regulation of the actin cytoskeleton to enable formation of protrusions and facilitate cell spreading, migration, adhesion, and proliferation, and more complex processes such as angiogenesis [208,216,217,251,267–269]. Reorganisation of the actin cytoskeleton in VSMCs is further implicated in vascular remodelling and aortic stiffness associated with hypertension, in tandem with focal adhesion signalling [409]. R-Ras also promotes the formation of focal adhesions [212,262]. These changes may contribute to the age-related BP phenotype observed in R-Ras KO mice. This is discussed in more detail in Chapter 7.3.

The 'Chemokine signalling' KEGG pathway is downregulated in the R-Ras KO mouse aorta. This is in line with the literature indicating R-Ras is activated by chemokines to stimulate T cell trafficking in the adaptive immune response [253]. Inflammation and the immune system contribute to the pathogenesis of hypertension, and with age-related hypertension. Perhaps R-Ras also interacts with the immune system with age to regulate these changes leading to hypertension. An investigation into inflammatory profiles of young and aged R-Ras KO mouse aortas may further support this finding. For example, performing flow cytometry using specific cell markers (such as CD4 for T cells) on digested mouse aortas may reveal differences in leukocyte cell populations. Furthermore, as discussed above, scRNA-seq can provide a more detailed analysis of changes in expression of inflammatory genes in individual cells.

Other enriched pathways are related to endocrine disorders, namely 'Cushing syndrome', 'Endocrine resistance', and 'Parathyroid hormone synthesis, secretion and action', which often have hypertension as a co-morbidity [410]. Hypertension results from endocrine orders via a

multitude of pathways, including endothelial dysfunction, enhanced vasoconstriction to pressor hormones including ANGII and norepinephrine, and effects on the RAAS system [411,412]. The involvement of R-Ras in this pathway is unclear, but the dysregulation of KEGG pathways in the GSEA may support a role for R-Ras in endocrine BP control. Further, the 'Gastric acid secretion' pathway is downregulated pathway with R-Ras KO in the mouse aorta. R-Ras has recently been shown to regulate gastric acid production downstream of plexin-semaphorin signalling and regulated by the RasGAP Rasal1 *in vivo* and in human organoids [413]. It is important to note this study was carried out in mouse aortas, so the findings are not confidently translatable to other organ systems.

6.3.2.5. R-Ras and Hippo signalling

The phosphoproteomics analysis suggested Hippo signalling pathway is upregulated in the R-Ras KO mouse aorta. However, this only reached in GSEA with multiplicate phosphoproteins included, and significance was lost when multiplicated proteins were excluded. Nonetheless, given the time frame and the resources at hand, I chose to follow up the potential role of R-Ras in this pathway to regulate myogenic tone.

The Hippo pathway is a highly conserved pathway associated with organ development and tumorigenesis [362], and cardiovascular processes including angiogenesis and smooth muscle restenosis [360–362]; pathways R-Ras also plays a role in. YAP (Yes-associated protein 1) and TAZ (Transcriptional coactivator with PDZ-binding motif) are the key members of the Hippo pathway, and in the vasculature act as mechanosensitive transcriptional coactivators that respond to stiffness, cell density and shear stress [362]. YAP/TAZ binds TEAD (Transcriptional enhanced associate domain) in the nucleus and influences gene expression to regulate cell proliferation, differentiation, and apoptosis. When the inhibitor kinases LATS1/2 of the Hippo pathway are activated, YAP/TAZ is phosphorylated and sequesters in the cytoplasm, and cannot enter the nucleus [414]. YAP/TAZ can also be activated by Rho GTPases and actin polymerisation [415]. YAP/TAZ is additionally implicated in vascular control of BP. YAP/TAZ KO mice exhibit attenuated acute and chronic adaption of the VSM to mechanical forces, an inhibited contractile response of tail arteries, including to the TxA2 receptor agonist U46619 [359]. Interestingly, these mice exhibit normal MAP, at baseline and with ANGII-challenging, like the R-Ras KO mice. The authors suggest this is due to ANGII-induced hypertension primarily resulting from mechanisms distinct from VSM, including renal fluid retention; as discussed in section 4.3.1 [359]. In R-Ras KO mouse aortas, the phosphoproteomics data indicates upregulation of this LATS1/2 phosphorylation of

YAP/TAZ, suggesting entry of YAP/TAZ into the nucleus in inhibited. This is concurrent with the downregulation of 'Vascular smooth muscle contraction' pathway in the KEGG GSEA analyses. RhoA-ROCK also regulates YAP/TAZ activity to promote endothelial cell sprouting, VSMC migration and proliferation; Rho/ROCK suppresses LATS1/2 induced phosphorylation of YAP/TAZ pathway, and stimulates YAP/TAZ activity independent of LATS/2 by stabilising F-actin and myosin [361]. Previous research demonstrates R-Ras activates Rho-ROCK signalling [279], further evidenced by the phosphoproteomic data. This suggests R-Ras/ROCK/YAP signalling could be involved in VSM remodelling, extending to regulation of VSM contraction. I hypothesised R-Ras will promote YAP/TAZ localisation to the nuclear in VSMCs, thus regulating VSM contraction. However, immunofluorescence staining of young adult mouse aortas yielded inconclusive results. Quantifying cytoplasmic and nuclear YAP with fractionation and subsequent western blotting of the aorta will provide a more accurate measure of R-Ras KO impact on YAP activity. Furthermore, repeating immunofluorescence staining *in vitro* in a VSMC line will provide a clearer picture of events.

6.3.2.6. Limitations of phosphoproteomics

There are limitations to the phosphoproteomics analysis that must be considered. Firstly, as aforementioned, multiple post translational modifications can occur at different phosphosites on the same protein, with opposing directional fold change. In GSEA, the phosphosite information is disregarded and only the corresponding gene name and Log2FC and p values are inputted. Therefore, to prevent bias resulting from one protein entered multiple times in GSEA, multiplicate genes were filtered from the phosphoproteomics gene list, and only the gene with the highest Log2FC included in the main body of text. This could lead to uneven weighting, therefore the GSEA was repeated with the phosphoproteomics gene list filtered based on p value, and with the unfiltered phosphoproteomics gene list. Results were comparable, indicating the results were reliable. This filtered analysis can be interpreted for overall changes in KEGG genesets/pathways with R-Ras KO in the mouse aorta, but to understand the exact down- and upregulation of individual phosphosites and proteins it is essential to refer to the unfiltered raw phosphoproteomics dataset. Notably, R-Ras is a known activator of ROCK and therefore phosphorylation of ROCK would be expected to be downregulated in the R-Ras KO mouse aorta. Yet in the raw phosphoproteomics dataset R-Ras KO results in both up- and downregulation of Rock1 phosphorylation at different phosphosites. This result illustrates the importance of interpreting the raw phosphoproteomics dataset and the KEGG GSEA in tandem to gain an understanding of changes in protein

phosphorylation status with R-Ras KO. Nonetheless, this does not explain the unexpected upregulation of Akt1 phosphorylation with R-Ras KO, discussed in section 6.3.2.2. Secondly, the database used for phosphosite identification, PhosphoSitePlus, includes PTMs beyond phosphorylation of serine (S), threonine (T) and tyrosine (Y), namely methylation of arginine (R), and acetylation and ubiquitination on lysine (K), oxidation of methionine (M), or no modification (no_mod). The functional relevance of a majority of the PTMs identified in the phosphoproteomics dataset are unclear, and therefore interpretation of these data as an indication of a relationship between R-Ras and the indicated protein must be carried out with caution, rather than concluding that R-Ras activity results in PTMs at those residues. This was overcome to an extent with KSEA and KEGG GSEA. Yet it is imperative to confirm observations from these analyses *in vitro* using phosphosite-specific western blotting of endothelial and smooth muscle cells lines, and protein extracted from aortas. Finally, R-Ras is an established cell signalling molecule and has been shown to regulate phosphorylation of various kinases and proteins, some of which did not appear in this dataset at all, most notably PI3K. This may reflect the difficult nature of working with phosphosites. Proteins are easily denatured and phosphorylation status can change in sample preparation. Measures to maintain cold temperatures and inclusion of protease inhibitor cocktails prevents this only somewhat. Increasing sample number may also improve this.

Overall, this hypothesis-free multi-omic approach to investigating the role of R-Ras in the vasculature has suggested a role of R-Ras in vascular mechanisms of blood pressure control, and in the pathogenesis of hypertension. In the R-Ras KO mouse aorta, there was no detectable change in gene expression measured with RNA-seq, however phosphoproteomic analysis suggested changes in phosphosignalling, notably in regulation of VSM contraction, via mediation of Rho/ROCK signalling, cAMP/Epac-induced vasodilation, and/or YAP/TAZ signalling. However, this rich phosphoprotoeomic dataset generates more questions than answers. Finally, as discussed in chapter 4, BP is largely controlled by smaller resistance arteries, whilst the aorta is responsible for transport of blood. These multi-omic analyses were performed in the aorta as it is very difficult to extract appropriate volumes of genetic material and protein from resistance arteries, such as the mesenteric artery, and large numbers of mice would be required. Therefore, these findings are not directly translatable to BP control mechanisms. Further work is necessary to confirm these observations, create more succinct hypotheses, and contextualise these changes in *in vitro* and *in vivo,* beyond pathway analysis.

Chapter 7. Conclusions and Future Work

7.1. Motivation

Primary hypertension is a complex polygenic disorder with an estimated heritability of 30 – 50%. Researchers have employed genetic studies to identify gene variants associated with BP in a bid to better understand the pathophysiology of hypertension, discover new drug targets, and facilitate personalised treatment.

Since the sequencing of the human genome in 2003, genome- and exome-wide association analyses have identified over 1,200 variants associated with BP traits, explaining an estimated 6% heritability. Despite these genetic advances, unexpectedly few novel mechanisms have been uncovered. Partly, because most variants identified are common with small effect sizes reflecting the polygenic nature of hypertension. Identification of rare variants with large effect sizes is favoured as these genes are more likely to have a greater impact on BP. Candidate genes must be validated *in vivo* to understand their contribution to BP control and hypertension. One such rare variant with a large effect size is the rs61760904 variant, functionally mapped to the *RRAS* gene and encoding the small GTPase R-Ras. This SBP-associated variant provided the motivation behind this project; to functionally validate and investigate the potential role of R-Ras in BP control.

7.2. Summary of key findings

The SBP-associated variant was predicted damaging *in silico* in the original discovery meta-analysis [11]. This missense variant encodes a cytosine to thymine (T>C) nucleotide substitution, translating to an aspartate (D) to asparagine (N) amino acid change (D133N) in the R-Ras protein. Using a combination of *in silico* tools and *in vitro* western blotting of the R-Ras mutant, the work in my thesis suggested the impact of the missense variant may be on R-Ras function, and not structure or protein expression. However, this remains inconclusive, and future work is necessary to understand whether this variant impacts R-Ras structure and/or function.

The Rras-DEL415 KO mouse was specifically generated for this project via CRISPR-Cas9-mediated deletion of critical exons 3 and 4 with a C57BL/6N genetic background, in conjunction with IMPC (MRC Harwell, UK). As this was the first study to use this mouse model, I aimed to establish the overall phenotype. *Rras* gene KO was validated by IMPC using a WT loss of allele assay, and in this thesis using qPCR in the mouse kidneys. However, it must be noted that R-Ras protein levels have not been measured, and therefore R-Ras protein KO cannot be confirmed. Nevertheless, published research in other R-Ras KO mouse models

report a pro-angiogenic phenotype with *Rras* KO [208]. This phenotype was replicated in the R-Ras KO mouse model using the aortic ring assay, instilling confidence in the mouse model. I observed normal body, heart, kidney, spleen, and lung weight, comparable to in-house phenotyping data reported by the IMPC. Basic histology of the heart and aorta did not identify major morphological differences with R-Ras KO in the young mouse.

R-Ras is highly expressed in endothelial cells, and is reported to potentiate the PI3K/Akt axis in several cell lines [217,224,230,231,234–239]. The PI3K/Akt pathway potentiates NO formation in the EC monolayer lining the lumen of blood vessels to promote vasodilation [27–29]. I hypothesised R-Ras could promote vasodilation via activation of the PI3K/Akt axis, subsequently phosphorylating and activating eNOS to trigger NO formation. In human umbilical vein endothelial cells, I observed upregulation of eNOS phosphorylation as an indication of activity with transfection of the constitutively active form of R-Ras, supporting this hypothesis. I thus hypothesised this *in vitro* observation would translate to inhibited vasodilation in the R-Ras KO mouse vasculature. This was not observed; the aorta from young adult mice had normal vasodilatory and vasocontractile responses in organ bath studies.

This study is the first to explore the BP phenotype resulting from R-Ras KO in the mouse. Given the exonic *RRAS* variant is associated with an elevated systolic BP in humans, I hypothesised the R-Ras KO mouse would have an elevated BP. However, radiotelemetric recordings of diurnal BP in the young adult mouse did not detect differences in BP or heart rate at baseline, contrary to the hypothesis. To explore whether the impact of R-Ras KO may become apparent in hypertensive conditions, I induced hypertension with ANGII challenge – a gold-standard technique. The efficacy of this model was confirmed with observed cardiac fibrosis and aortic wall thickening, inhibited vasodilatory response of the mouse aorta, and progressive increases in BP. Yet again, there was no difference between WT and R-Ras KO mice.

Pilot data in the aged R-Ras KO mouse showed elevations in SBP, and this remained true when the dataset was supplemented in this project. This led us to question why there was no BP phenotype in the young adult mouse. To address this, I employed a hypothesis-free approach using RNA-seq to measure gene expression and phosphoproteomics to investigate cell signalling in the mouse aorta. The RNA-seq of the mouse aorta did not detect changes in gene expression with *Rras* gene deletion; this may be due to study underpowering. Phosphoproteomics provided more robust data. Significant changes in the phosphosignalling profile of the young mouse aorta were observed with R-Ras KO, indicating a role of R-Ras in vascular signalling. Importantly, gene set enrichment analysis revealed alterations in signalling pathways directly related to BP control. These data support a role of R-Ras in BP signalling at

a post-transcriptional level in the mouse aorta. Altogether, the data in the R-Ras KO mouse suggests that R-Ras does play a role in BP control, however its role is masked by compensatory mechanisms in the young mouse which become dysregulated with age to reveal the BP phenotype.

Finally, the age-related association of R-Ras in BP observed in the mouse model was explored in humans. An age-stratified association analysis in UK Biobank data was performed to assess whether the impact of the SBP-associated exonic T>C *RRAS* variant, rs61760904, differed across age groups. This analysis confirmed the association of the *RRAS* variant with SBP in a larger cohort than the discovery analyses [11], and importantly, found an age-related trend with the *RRAS* variant.

7.3. R-Ras and age-related mechanisms of hypertension

Together, the observations in the R-Ras KO mouse model and human genetic data support a role of the R-Ras protein in age-related mechanisms of BP control. Age is a major contributing factor to the pathogenesis of hypertension. In the vasculature, age-related progression of BP is associated with increased arterial stiffness [142–144], vascular dysfunction [143], and inflammation [143,145].

Arterial stiffness is characterised by increased collagen deposition and elastin degradation in the ECM, reorganisation of the actin cytoskeleton in VSMCs, and decreased VSM contractility [142]; these processes are regulated by integrins. Seawright and colleagues demonstrated aged VSMCs from the rat soleus muscle feed arteries present increased α5β1 integrin adhesion to fibronectin and concomitant decreased focal adhesion kinase (FAK) activation, contributing to both arterial stiffness and decreased contractility [416]. α5β1 activation also mediates force generation in VSMCs by increasing myosin II activity via RhoA/ROCK signalling [417]. R-Ras is proposed to modulate both α5β1 activity [259,418], and focal adhesion formation via FAK [262] *in vitro*. In this thesis, phosphoproteomics analysis of the R-Ras KO mouse aorta revealed downregulation of the pathway related to reorganisation of the actin cytoskeleton, specifically in Rho/ROCK signalling. R-Ras signalling mediates actin cytoskeleton organisation in cellular processes including cell shape spreading and adhesion [214,231,232,235,237,247], migration [256,261,262], and proliferation, and is evidenced to influence collagen via integrin signalling [256,261,262]. These findings support a potential role of R-Ras in the progressive stiffening of aged arteries and decreased VSM contractility associated with ageing, warranting further study.

Endothelial dysfunction is also a contributing factor in vascular ageing [145]. In this thesis, *in vitro* western blotting data demonstrated that active R-Ras can potentiate eNOS activation, and thus NO production. Phosphoproteomic analysis in the young adult mouse aorta demonstrated decreased phospho-eNOS expression with R-Ras KO, however this failed to reach significance. NO availability has been shown to be decreased in small arteries of older individuals [143]. Organ bath data in the young R-Ras KO mouse aorta did not show change in vasodilatory response observed with diminished NO signalling. This suggests R-Ras may potentiate NO signalling but is not essential in the young mouse. Further explorations, particularly in mesenteric arteries and in aged arteries, are essential to investigate this potential relationship.

7.4. BP-related phenotypes in the Rras-DEL415 mouse model – insights from IMPC

Beyond this study, the IMPC has reported significant phenotypes in the Rras-DEL415 mouse [338]. First, Rras-DEL415 mice have normal vascular blood vessel morphology. This is concurrent with observations in the global R-Ras KO mouse model generated by Komatsu and colleagues [297]. R-Ras was shown to be essential for retinal angiogenesis in pathological conditions, namely hypoxia, but not in neonatal development of retinal blood vessels [320]. Interestingly, in a pericyte-targeted conditional R-Ras KO model, neonatal mice had abnormal retinal vasculature development and morphology [269]. However, the authors speculate that this difference is explained by other genes compensating for the loss of *Rras* in the global KO, whereas in the conditional model *Rras* KO is induced at a later stage [269]. Second, decreased circulating calcium levels are reported in early adult female Rras-DEL415 mice, although this was not significant in males. Calcium signalling plays important roles in mechanisms of blood pressure control, notably in vasodilation via activation of eNOS and increases in calcium influx in VSMCs promoting contraction [419]. Furthermore, calcium intake is inversely associated with BP in humans [420] and animals [421]. A direct connection between R-Ras and calcium signalling has not been previously established, however R-Ras potentiates calcium signalling pathways, including intracellular PI3K/Akt and PLCϵ/IP_3/DAG signalling axes. Could the potential modulation of calcium signalling by R-Ras contribute to vascular control of blood pressure? This is yet to be explored. Fourth, the Rras-DEL415 mouse model is reported to exhibit elevated triglyceride levels, significant in males only. Elevated triglyceride levels are often co-expressed with CVD, and have been demonstrated as predictors of hypertension in humans [422,423]. Yet, there is a lack of strong supporting evidence for a direct relationship

between triglycerides and BP. Fourth, elevated serum albumin levels in Rras-DEL415 reach significance in male mice. In human studies, serum albumin is positively associated with BP [424,425], but this is contradictory to the cardioprotective effects associated with low serum albumin [424]. Elevated BP is hypothesised to cause vascular leakage of albumin, resulting in increased serum albumin levels [426]. These are observational studies and a causal relationship has not been explored, although authors hypothesise albumin contributes to BP via serotonergic influence [424]. Again, a link between R-Ras and albumin is yet to be explored. Fifth, male mice have low fasting circulating glucose levels. A link between low fasting blood glucose and CVD is again under debate, with research suggesting BP and low fasting circulating glucose levels may be interacting factors leading to CVD, and not causal [427,428]. Finally, male and female young adult and late adult mice have increased 'Grip strength'. Overall, these significant phenotypic differences observed by IMPC in the Rras-DEL415 mouse model suggest some pathways for exploration, including calcium signalling, however more evidence in mouse models is required to establish any confident links.

7.5. Future work

The work presented in this thesis suggests that R-Ras contributes to age-related hypertension, yet the question remains – what are the exact mechanisms behind this? To address this, there are multiple avenues of future study.

1) Confirmation of the absence of R-Ras protein in the Rras-DEL415 model

Firstly, the absence of R-Ras protein in the Rras-DEL415 mouse model must be confirmed. Absence of the *Rras* WT allele was validated by the IMPC using the WT loss of allele assay, and in this thesis using qPCR in mouse kidneys, however, it is possible R-Ras protein was still generated from the CRISPR-Cas9 edited allele. Therefore, confirmation of R-Ras protein KO must be carried out, for example by performing western blotting on multiple tissues, including the mouse aorta in the context of this thesis, before conclusions can be drawn from this study.

2) Validation of phosphoproteomic data

Phosphoproteomics identified hundreds of differentially phosphorylated phosphoproteins in the young mouse aorta. In published literature, it is imperative to confirm observations of relevance *in vitro* using western blotting. In this study, I was particularly interested in changes in Rho/ROCK signalling resulting from R-Ras KO, as this pathway is heavily involved in VSM

contraction. Due to time-constraints, I could not explore ROCK phosphorylation in the young mouse aorta using western blotting. If these observations are confirmed with western blotting, this would support the contribution of R-Ras to VSM contraction via ROCK/Rho signalling I proposed in Chapter 6.

3) Assessment of the aged-mouse vasculature

The main hypothesis generated from this thesis is that R-Ras contributes to progressive BP increase with age via mechanisms of arterial stiffening. Given the age-related phenotype, repeating the phosphoproteomic analysis in the aged R-Ras KO mouse aorta and comparing to the young adult mouse data may highlight changes in BP control mechanisms with age and with R-Ras KO. This hypothesis can further be explored using pressure myography of the age mouse aorta to measure aortic stiffness and compliance. Histological analysis of the aged mouse aorta can visualise changes in ECM composition, notably elevated collagen deposition or elastin degradation, characteristic of aortic ageing. I hypothesise these changes will be pronounced in the R-Ras KO mouse aorta. Finally, organ bath experiments in the aged mouse aorta may also reveal a change in vasodilation and vasocontraction response that were not observed in the young mouse aorta, in line with the progressive BP phenotype.

4) Assessment of small resistance vasculature

This thesis focused on the mouse aorta, however, *in vivo* small resistance vessels are responsible BP control, whereas the primary function of the aorta is to transport blood around the body. Therefore, future experiments should explore the characteristics of the small resistance vessels of these mice, such as small vessel myography of mesenteric arteries, in both young adult and aged mice. Similarly, multi-omic analyses, including RNAseq and phosphoproteomics, were performed on the mouse aorta. While phosphoproteomics of resistance vessels is impractical due to protein volume constraints, scRNA-seq on individual vascular endothelial cells and smooth muscle cells from the small resistance vessels may provide greater insight into genetic changes consequent from R-Ras KO.

5) Understanding the impact of the rs61760904 *RRAS* variant on BP

Finally, the mechanisms responsible for the impact of the rs61760904 variant on SBP in humans remain unknown. The effect of the *RRAS* variant on protein structure, expression, and function was not concretely determined in this thesis. R-Ras activity can be assessed *in vitro* using GTP-loading assays, and interactions with GAPs and GEFs using fluorescence resonance energy transfer and Ras effector binding assays. R-Ras function resulting from its activity, notably cell polarity and migration, can also be assessed visually *in vitro,* by

generating a mutant containing both the exonic variant mutation (D133N) and the constitutively activating mutation, 38V. Most crucially, however, generation of a mouse model carrying the rs61760904 variant, with the D133N missense mutation, may provide translatable insights on the mechanisms behind the impact on SBP *in vivo*.

7.6. Concluding remarks

In this thesis, the potential role of R-Ras in blood pressure control was explored using a combination of *in vitro*, *ex vivo*, and *in vivo* techniques. Radiotelemetry in the R-Ras KO mouse model demonstrated an elevated SBP phenotype in the aged mouse. In contrast, the young R-Ras KO mouse exhibited normal BP and vascular reactivity. Interrogation of the phosphoproteome of the young mouse aorta revealed significant alterations in cell signalling pathways related to BP control, including vascular smooth muscle contraction and reorganisation of the actin cytoskeleton. I therefore propose R-Ras contributes to BP control mechanisms in the young adult mouse, but the impact of R-Ras KO is masked by compensatory mechanisms which become dysregulated with age. Finally, returning to human data, a similar trend of SBP is observed with age in patients homozygous for the exonic *RRAS* variant identified in the original meta-analysis. The work presented here is a step towards validating the genetic discovery of R-Ras association with SBP, and supports a potential role of R-Ras in the age-related pathogenesis of hypertension. Importantly, it has opened several avenues of future work necessary to delineate the exact mechanisms behind this.

8. References

1. Kannel WB, Wolf PA, Verter J, Mcnamara PM. Epidemiologic Assessment of the Role of Blood Pressure in Stroke. The Framingham Study. *JAMA* 1970; **214**: 301–10.

2. Kannel WB, Gordon T, Schwartz MJ. Systolic Versus Diastolic Blood Pressure and Risk of Coronary Heart Disease. The Framingham Study. *Am J Cardiol* 1971; **27**: 335–46.

3. Sprint Research Group, Wright JT, Williamson JD, *Et Al.* A Randomized Trial of Intensive Versus Standard Blood-Pressure Control. *N Engl J Med* 2015; **373**: 2103–16.

4. Ettehad D, Emdin CA, Kiran A, *Et Al.* Blood Pressure Lowering for Prevention of Cardiovascular Disease and Death: A Systematic Review and Meta-Analysis. *Lancet Lond Engl* 2016; **387**: 957–67.

5. GBD 2015 Risk Factors Collaborators. Global, Regional, and National Comparative Risk Assessment of 79 Behavioural, Environmental and Occupational, and Metabolic Risks or Clusters Oo Risks, 1990-2015: A Systematic Analysis for the Global Burden of Disease Study 2015. *Lancet Lond Engl* 2016; **388**: 1659–724.

6. Zhou B, Bentham J, Di Cesare M, *Et Al.* Worldwide Trends in Blood Pressure from 1975 to 2015: A Pooled Analysis of 1479 Population-Based Measurement Studies with 19·1 Million Participants. *The Lancet* 2017; **389**: 37–55.

7. Williams B, Mancia G, Spiering W, *Et Al.* [2018 ESC/ESH Guidelines for the Management of Arterial Hypertension]. *Kardiol Pol* 2019; **77**: 71–159.

8. Kannel WB, Castelli WP, Mcnamara PM, Mckee PA, Feinleib M. Role of Blood Pressure in the Development of Congestive Heart Failure. The Framingham Study. *N Engl J Med* 1972; **287**: 781–7.

9. Kannel WB. Role of Blood Pressure in Cardiovascular Morbidity and Mortality. *Prog Cardiovasc Dis* 1974; **17**: 5–24.

10. Wright JM, Musini VM, Gill R. First-Line Drugs for Hypertension. *Cochrane Database Syst Rev* 2018; **4**: CD001841.

11. Surendran P, Drenos F, Young R, *Et Al.* Trans-Ancestry Meta-Analyses Identify Rare and Common Variants Associated with Blood Pressure and Hypertension. *Nat Genet* 2016; **48**: 1151–61.

12. Surendran P, Feofanova EV, Lahrouchi N, *Et Al.* Discovery of Rare Variants Associated with Blood Pressure Regulation Through Meta-Analysis of 1.3 Million Individuals. *Nat Genet* 2020; **52**: 1314–32.

13. Giri A, Hellwege JN, Keaton JM, *Et Al.* Trans-Ethnic Association Study of Blood Pressure Determinants in Over 750,000 Individuals. *Nat Genet* 2019; **51**: 51–62.

14. Klabunde, RE. (2021) *Cardiovascular physiology concepts.* Philadelphia: Wolters Kluwer

15. Roguin A. Scipione Riva-Rocci and the Men Behind the Mercury Sphygmomanometer. *Int J Clin Pract* 2006; **60**: 73–9.

16. Saklayen MG, Deshpande NV. Timeline of History of Hypertension Treatment. *Front Cardiovasc Med* 2016; **3**: 3.

17. Mahmood SS, Levy D, Vasan RS, Wang TJ. The Framingham Heart Study and the Epidemiology of Cardiovascular Disease: A Historical Perspective. *Lancet Lond Engl* 2014; **383**: 999–1008.

18. Whelton PK, Carey RM, Aronow WS, *Et Al.* 2017 ACC/AHA/AAPA/ABC/ACPM/AGS/Apha/ASH/ASPC/NMA/PCNA Guideline for the Prevention, Detection, Evaluation, and Management of High Blood Pressure in Adults: Executive Summary: A Report of the American College of Cardiology/American Heart Association Task Force On Clinical Practice Guidelines. *Circulation* 2018; **138**: E426–83.

19. ACCORD Study Group, Cushman WC, Evans GW, *Et Al.* Effects of Intensive Blood-Pressure Control in Type 2 Diabetes Mellitus. *N Engl J Med* 2010; **362**: 1575–85.

20. Qaseem A, Wilt TJ, Rich R, *Et Al.* Pharmacologic Treatment of Hypertension in Adults Aged 60 Years or Older to Higher Versus Lower Blood Pressure Targets: A Clinical Practice Guideline from the American College of Physicians and the American Academy of Family Physicians. *Ann Intern Med* 2017; **166**: 430–7.

21. NCD Risk Factor Collaboration (NCD-Risc). Trends in Adult Body-Mass Index in 200 Countries from 1975 to 2014: A Pooled Analysis of 1698 Population-Based Measurement Studies with 19·2 Million Participants. *Lancet Lond Engl* 2016; **387**: 1377–96.

22. Chow CK. Prevalence, Awareness, Treatment, and Control of Hypertension in Rural and Urban Communities in High-, Middle-, and Low-Income Countries. *JAMA* 2013; **310**: 959.

23. Lewington S, Clarke R, Qizilbash N, Peto R, Collins R, Prospective Studies Collaboration. Age-Specific Relevance of Usual Blood Pressure to Vascular Mortality: A Meta-Analysis of Individual Data for One Million Adults in 61 Prospective Studies. *Lancet* 2002; **360**: 1903–13.

24. Rapsomaniki E, Timmis A, George J, *Et Al.* Blood Pressure and Incidence of Twelve Cardiovascular Diseases: Lifetime Risks, Healthy Life-Years Lost, and Age-Specific Associations in 1·25 Million People. *The Lancet* 2014; **383**: 1899–911.

25. Hsu C, Mcculloch CE, Darbinian J, Go AS, Iribarren C. Elevated Blood Pressure and Risk of End-Stage Renal Disease in Subjects without Baseline Kidney Disease. *Arch Intern Med* 2005; **165**: 923.

26. Xie X, Atkins E, Lv J, *Et Al.* Effects of Intensive Blood Pressure Lowering On Cardiovascular and Renal Outcomes: Updated Systematic Review and Meta-Analysis. *The Lancet* 2016; **387**: 435–43.

27. Furchgott RF, Zawadzki JV. The Obligatory Role of Endothelial Cells in the Relaxation of Arterial Smooth Muscle by Acetylcholine. *Nature* 1980; **288**: 373–6.

28. Ignarro LJ, Buga GM, Wood KS, Byrns RE, Chaudhuri G. Endothelium-Derived Relaxing Factor Produced and Released from Artery and Vein is Nitric Oxide. *Proc Natl Acad Sci U A* 1987; **84**: 9265–9.

29. Palmer RM, Ferrige AG, Moncada S. Nitric Oxide Release Accounts for the Biological Activity of Endothelium-Derived Relaxing Factor. *Nature* 1987; **327**: 524–6.

30. Ziche M, Morbidelli L, Choudhuri R, *Et Al.* Nitric Oxide Synthase Lies Downstream from Vascular Endothelial Growth Factor-Induced But Not Basic Fibroblast Growth Factor-Induced Angiogenesis. *J Clin Invest* 1997; **99**: 2625–34.

31. Murohara T, Horowitz JR, Silver M, *Et Al.* Vascular Endothelial Growth Factor/Vascular Permeability Factor Enhances Vascular Permeability Via Nitric Oxide and Prostacyclin. *Circulation* 1998; **97**: 99–107.

32. Landmesser U, Dikalov S, Price SR, *Et Al.* Oxidation of Tetrahydrobiopterin Leads to Uncoupling of Endothelial Cell Nitric Oxide Synthase in Hypertension. *J Clin Invest* 2003; **111**: 1201–9.

33. Huang PL, Huang Z, Mashimo H, *Et Al.* Hypertension in Mice Lacking the Gene for Endothelial Nitric Oxide Synthase. *Nature* 1995; **377**: 239–42.

34. Dimmeler S, Rippmann V, Weiland U, Haendeler J, Zeiher AM. Angiotensin II Induces Apoptosis of Human Endothelial Cells. Protective Effect of Nitric Oxide. *Circ Res* 1997; **81**: 970–6.

35. Fukumura D, Gohongi T, Kadambi A, *Et Al.* Predominant Role of Endothelial Nitric Oxide Synthase in Vascular Endothelial Growth Factor-Induced Angiogenesis and Vascular Permeability. *Proc Natl Acad Sci U A* 2001; **98**: 2604–9.

36. Yoon HJ, Cho SW, Ahn BW, Yang SY. Alterations in the Activity and Expression of Endothelial NO Synthase in Aged Human Endothelial Cells. *Mech Ageing Dev* 2010; **131**: 119–23.

37. Touyz RM, Schiffrin EL. Increased Generation of Superoxide by Angiotensin II in Smooth Muscle Cells from Resistance Arteries of Hypertensive Patients: Role of Phospholipase D-Dependent NAD(P)H Oxidase-Sensitive Pathways. *J Hypertens* 2001; **19**: 1245–54.

38. Somlyo AP, Somlyo AV. Ca2+ Sensitivity of Smooth Muscle and Nonmuscle Myosin II: Modulated by G Proteins, Kinases, and Myosin Phosphatase. *Physiol Rev* 2003; **83**: 1325–58.

39. Ito M, Hartshorne DJ. Phosphorylation of Myosin as A Regulatory Mechanism in Smooth Muscle. *Prog Clin Biol Res* 1990; **327**: 57–72.

40. Touyz RM, Alves-Lopes R, Rios FJ, *Et Al.* Vascular Smooth Muscle Contraction in Hypertension. *Cardiovasc Res* 2018; **114**: 529–39.

41. Xiong Z, Sperelakis N. Regulation of L-Type Calcium Channels of Vascular Smooth Muscle Cells. *J Mol Cell Cardiol* 1995; **27**: 75–91.

42. Somlyo AV, Bond M, Somlyo AP, Scarpa A. Inositol Trisphosphate-Induced Calcium Release and Contraction in Vascular Smooth Muscle. *Proc Natl Acad Sci U S A* 1985; **82**: 5231–5.

43. Lin Q, Zhao G, Fang X, *Et Al.* IP3 Receptors Regulate Vascular Smooth Muscle Contractility and Hypertension. *JCI Insight* 2016; **1**: E89402.

44. Qiao Y-N, He W-Q, Chen C-P, *Et Al.* Myosin Phosphatase Target Subunit 1 (MYPT1) Regulates the Contraction and Relaxation of Vascular Smooth Muscle and Maintains Blood Pressure. *J Biol Chem* 2014; **289**: 22512–23.

45. Moosmang S. Dominant Role of Smooth Muscle L-Type Calcium Channel Cav1.2 for Blood Pressure Regulation. *EMBO J* 2003; **22**: 6027–34.

46. Oloizia B, Paul RJ. Ca2+ Clearance and Contractility in Vascular Smooth Muscle: Evidence from Gene-Altered Murine Models. *J Mol Cell Cardiol* 2008; **45**: 347–62.

47. Kitazawa T, Eto M, Woodsome TP, Brautigan DL. Agonists Trigger G Protein-Mediated Activation of the CPI-17 Inhibitor Phosphoprotein of Myosin Light Chain Phosphatase to Enhance Vascular Smooth Muscle Contractility. *J Biol Chem* 2000; **275**: 9897–900.

48. Hagerty L, Weitzel DH, Chambers J, *Et Al.* ROCK1 Phosphorylates and Activates Zipper-Interacting Protein Kinase. *J Biol Chem* 2007; **282**: 4884–93.

49. Zieba BJ, Artamonov MV, Jin L, *Et Al.* The Camp-Responsive Rap1 Guanine Nucleotide Exchange Factor, Epac, Induces Smooth Muscle Relaxation by Down-Regulation of Rhoa Activity. *J Biol Chem* 2011; **286**: 16681–92.

50. Quinn KV, Giblin JP, Tinker A. Multisite Phosphorylation Mechanism for Protein Kinase A Activation of the Smooth Muscle ATP-Sensitive K^+ Channel. *Circ Res* 2004; **94**: 1359–66.

51. Leonetti G, Cuspidi C, Sampieri L, Terzoli L, Zanchetti A. Comparison of Cardiovascular, Renal, and Humoral Effects of Acute Administration of Two Calcium Channel Blockers in Normotensive and Hypertensive Subjects: *J Cardiovasc Pharmacol* 1982; **4**: S325.

52. Tabet F, Schiffrin EL, Touyz RM. Mitogen-Activated Protein Kinase Activation by Hydrogen Peroxide is Mediated Through Tyrosine Kinase-Dependent, Protein Kinase C-Independent Pathways in Vascular Smooth Muscle Cells: Upregulation in Spontaneously Hypertensive Rats. *J Hypertens* 2005; **23**: 2005–12.

53. Matsuda K, Lozinskaya I, Cox RH. Augmented Contributions of Voltage-Gated Ca2+ Channels to Contractile Responses in Spontaneously Hypertensive Rat Mesenteric Arteries. *Am J Hypertens* 1997; **10**: 1231–9.

54. Cario-Toumaniantz C, Ferland-Mccollough D, Chadeuf G, *Et Al.* Rhoa Guanine Exchange Factor Expression Profile in Arteries: Evidence for A Rho Kinase-Dependent Negative Feedback in Angiotensin II-Dependent Hypertension. *Am J Physiol Cell Physiol* 2012; **302**: C1394-1404.

55. Zhou Q, Wei S-S, Wang H, *Et Al.* Crucial Role of ROCK2-Mediated Phosphorylation and Upregulation of FHOD3 in the Pathogenesis of Angiotensin II-Induced Cardiac Hypertrophy. *Hypertens Dallas Tex 1979* 2017; **69**: 1070–83.

56. Calò LA, Davis PA, Pagnin E, *Et Al.* Increased Level of P63rhogef and Rhoa/Rho Kinase Activity in Hypertensive Patients. *J Hypertens* 2014; **32**: 331–8.

57. Carbone ML, Brégeon J, Devos N, *Et Al.* Angiotensin II Activates the Rhoa Exchange Factor Arhgef1 in Humans. *Hypertens Dallas Tex 1979* 2015; **65**: 1273–8.

58. Cai Z, Gong Z, Li Z, Li L, Kong W. Vascular Extracellular Matrix Remodeling and Hypertension. *Antioxid Redox Signal* 2021; **34**: 765–83.

59. Mitchell GF. Arterial Stiffness and Hypertension: Chicken or Egg? *Hypertension* 2014; **64**: 210–4.

60. Didangelos A, Yin X, Mandal K, Baumert M, Jahangiri M, Mayr M. Proteomics Characterization of Extracellular Space Components in the Human Aorta. *Mol Cell Proteomics* 2010; **9**: 2048–62.

61. Li Q, Muragaki Y, Hatamura I, Ueno H, Ooshima A. Stretch-Induced Collagen Synthesis in Cultured Smooth Muscle Cells from Rabbit Aortic Media and A Possible Involvement of Angiotensin II and Transforming Growth Factor-Beta. *J Vasc Res* 1998; **35**: 93–103.

62. Louis H, Kakou A, Regnault V, *Et Al.* Role of Alpha1beta1-Integrin in Arterial Stiffness and Angiotensin-Induced Arterial Wall Hypertrophy in Mice. *Am J Physiol Heart Circ Physiol* 2007; **293**: H2597-2604.

63. Ergul A, Portikdobos V, Hutchinson J, Franco J, Anstadt M. Downregulation of Vascular Matrix Metalloproteinase Inducer and Activator Proteins in Hypertensive Patients. *Am J Hypertens* 2004; **17**: 775–82.

64. Schulz E, Gori T, Münzel T. Oxidative Stress and Endothelial Dysfunction in Hypertension. *Hypertens Res Off J Jpn Soc Hypertens* 2011; **34**: 665–73.

65. Dinh QN, Drummond GR, Sobey CG, Chrissobolis S. Roles of Inflammation, Oxidative Stress, and Vascular Dysfunction in Hypertension. *Biomed Res Int* 2014; **2014**: 406960.

66. Seshiah PN, Weber DS, Rocic P, Valppu L, Taniyama Y, Griendling KK. Angiotensin II Stimulation of NAD(P)H Oxidase Activity: Upstream Mediators. *Circ Res* 2002; **91**: 406–13.

67. Doughan AK, Harrison DG, Dikalov SI. Molecular Mechanisms of Angiotensin II–Mediated Mitochondrial Dysfunction: Linking Mitochondrial Oxidative Damage and Vascular Endothelial Dysfunction. *Circ Res* 2008; **102**: 488–96.

68. Fountain JH, Lappin SL. Physiology, Renin Angiotensin System. In: *Statpearls*. Treasure Island (FL): Statpearls Publishing, 2021.

69. Matsusaka T, Niimura F, Shimizu A, *Et Al.* Liver Angiotensinogen is the Primary Source of Renal Angiotensin II. *J Am Soc Nephrol JASN* 2012; **23**: 1181–9.

70. Levy BI, Benessiano J, Henrion D, *Et Al.* Chronic Blockade of AT2-Subtype Receptors Prevents the Effect of Angiotensin II On the Rat Vascular Structure. *J Clin Invest* 1996; **98**: 418–25.

71. Muñoz-Durango N, Fuentes CA, Castillo AE, *Et Al.* Role of the Renin-Angiotensin-Aldosterone System Beyond Blood Pressure Regulation: Molecular and Cellular Mechanisms Involved in End-Organ Damage During Arterial Hypertension. *Int J Mol Sci* 2016; **17**: E797.

72. Kushibiki M, Yamada M, Oikawa K, Tomita H, Osanai T, Okumura K. Aldosterone Causes Vasoconstriction in Coronary Arterioles of Rats Via Angiotensin II Type-1 Receptor: Influence of Hypertension. *Eur J Pharmacol* 2007; **572**: 182–8.

73. Henrion D, Benessiano J, Lévy BI. In Vitro Modulation of A Resistance Artery Diameter by the Tissue Renin-Angiotensin System of A Large Donor Artery. *Circ Res* 1997; **80**: 189–95.

74. Soltis EE. Alterations in Vascular Structure and Function After Short-Term Losartan Treatment in Spontaneously Hypertensive Rats. *J Pharmacol Exp Ther* 1993; **266**: 642–6.

75. Ryan MJ, Didion SP, Mathur S, Faraci FM, Sigmund CD. Angiotensin II-Induced Vascular Dysfunction is Mediated by the AT1A Receptor in Mice. *Hypertens Dallas Tex 1979* 2004; **43**: 1074–9.

76. Garner MG, Phippard AF, Fletcher PJ, *Et Al.* Effect of Angiotensin II On Baroreceptor Reflex Control of Heart Rate in Conscious Baboons. *Hypertens Dallas Tex 1979* 1987; **10**: 628–34.

77. Cowley AW, Liard JF, Guyton AC. Role of Baroreceptor Reflex in Daily Control of Arterial Blood Pressure and Other Variables in Dogs. *Circ Res* 1973; **32**: 564–76.

78. Dobbs WA, Prather JW, Guyton AC. Relative Importance of Nervous Control of Cardiac Output and Arterial Pressure. *Am J Cardiol* 1971; **27**: 507–12.

79. Goldstein DS. Plasma Catecholamines and Essential Hypertension. An Analytical Review. *Hypertens Dallas Tex 1979* 1983; **5**: 86–99.

80. Grassi G, Seravalle G, Cattaneo BM, *Et Al.* Sympathetic Activation in Obese Normotensive Subjects. *Hypertens Dallas Tex 1979* 1995; **25**: 560–3.

81. Lohmeier TE, Lohmeier JR, Reckelhoff JF, Hildebrandt DA. Sustained Influence of the Renal Nerves to Attenuate Sodium Retention in Angiotensin Hypertension. *Am J Physiol Regul Integr Comp Physiol* 2001; **281**: R434-443.

82. Macheret F, Heublein D, Costello-Boerrigter LC, *Et Al.* Human Hypertension is Characterized by A Lack of Activation of the Antihypertensive Cardiac Hormones ANP and BNP. *J Am Coll Cardiol* 2012; **60**: 1558–65.

83. Waldman SA, Rapoport RM, Murad F. Atrial Natriuretic Factor Selectively Activates Particulate Guanylate Cyclase and Elevates Cyclic GMP in Rat Tissues. *J Biol Chem* 1984; **259**: 14332–4.

84. Song DL, Kohse KP, Murad F. Brain Natriuretic Factor. Augmentation of Cellular Cyclic GMP, Activation of Particulate Guanylate Cyclase and Receptor Binding. *FEBS Lett* 1988; **232**: 125–9.

85. Holditch SJ, Schreiber CA, Nini R, *Et Al.* B-Type Natriuretic Peptide Deletion Leads to Progressive Hypertension, Associated Organ Damage, and Reduced Survival: Novel Model for Human Hypertension. *Hypertens Dallas Tex 1979* 2015; **66**: 199–210.

86. International Consortium for Blood Pressure Genome-Wide Association S, Ehret GB, Munroe PB, *Et Al.* Genetic Variants in Novel Pathways Influence Blood Pressure and Cardiovascular Disease Risk. *Nature* 2011; **478**: 103–9.

87. Newton-Cheh C, Larson MG, Vasan RS, *Et Al.* Association of Common Variants in NPPA and NPPB with Circulating Natriuretic Peptides and Blood Pressure. *Nat Genet* 2009; **41**: 348–53.

88. Belluardo P, Cataliotti A, Bonaiuto L, *Et Al.* Lack of Activation of Molecular Forms of the BNP System in Human Grade 1 Hypertension and Relationship to Cardiac Hypertrophy. *Am J Physiol Heart Circ Physiol* 2006; **291**: H1529-1535.

89. Geng Q, Yan R, Wang Z, Hou F. Effects of LCZ696 (Sacubitril/Valsartan) On Blood Pressure in Patients with Hypertension: A Meta-Analysis of Randomized Controlled Trials. *Cardiology* 2020; **145**: 589–98.

90. Izzo JL, Zappe DH, Jia Y, Hafeez K, Zhang J. Efficacy and Safety of Crystalline Valsartan/Sacubitril (LCZ696) Compared with Placebo and Combinations of Free Valsartan and Sacubitril in Patients with Systolic Hypertension: the RATIO Study. *J Cardiovasc Pharmacol* 2017; **69**: 374–81.

91. Schmieder RE, Wagner F, Mayr M, *Et Al.* The Effect of Sacubitril/Valsartan Compared to Olmesartan On Cardiovascular Remodelling in Subjects with Essential Hypertension: the Results of a Randomized, Double-Blind, Active-Controlled Study. *Eur Heart J* 2017; **38**: 3308–17.

92. Khder Y, Shi V, Mcmurray JJV, Lefkowitz MP. Sacubitril/Valsartan (LCZ696) in Heart Failure. *Handb Exp Pharmacol* 2017; **243**: 133–65.

93. Moyes AJ, Hobbs AJ. C-Type Natriuretic Peptide: A Multifaceted Paracrine Regulator in the Heart and Vasculature. *Int J Mol Sci* 2019; **20**: E2281.

94. Sudoh T, Minamino N, Kangawa K, Matsuo H. C-Type Natriuretic Peptide (CNP): A New Member of Natriuretic Peptide Family Identified in Porcine Brain. *Biochem Biophys Res Commun* 1990; **168**: 863–70.

95. Stingo AJ, Clavell AL, Heublein DM, Wei CM, Pittelkow MR, Burnett JC. Presence of C-Type Natriuretic Peptide in Cultured Human Endothelial Cells and Plasma. *Am J Physiol* 1992; **263**: H1318-1321.

96. Del Ry S, Cabiati M, Vozzi F, *Et Al.* Expression of C-Type Natriuretic Peptide and Its Receptor NPR-B in Cardiomyocytes. *Peptides* 2011; **32**: 1713–8.

97. Horio T, Tokudome T, Maki T, *Et Al.* Gene Expression, Secretion, and Autocrine Action of C-Type Natriuretic Peptide in Cultured Adult Rat Cardiac Fibroblasts. *Endocrinology* 2003; **144**: 2279–84.

98. Matsukawa N, Grzesik WJ, Takahashi N, *Et Al.* The Natriuretic Peptide Clearance Receptor Locally Modulates the Physiological Effects of the Natriuretic Peptide System. *Proc Natl Acad Sci U S A* 1999; **96**: 7403–8.

99. Andrade FA, Restini CBA, Grando MD, Ramalho LNZ, Bendhack LM. Vascular Relaxation Induced by C-Type Natriuretic Peptide Involves the Ca2+/NO-Synthase/NO Pathway. *Plos One* 2014; **9**: E95446.

100. Nakao K, Kuwahara K, Nishikimi T, *Et Al.* Endothelium-Derived C-Type Natriuretic Peptide Contributes to Blood Pressure Regulation by Maintaining Endothelial Integrity. *Hypertens Dallas Tex 1979* 2017; **69**: 286–96.

101. Ono K, Mannami T, Baba S, Tomoike H, Suga S, Iwai N. A Single-Nucleotide Polymorphism in C-Type Natriuretic Peptide Gene May Be Associated with Hypertension. *Hypertens Res Off J Jpn Soc Hypertens* 2002; **25**: 727–30.

102. Li N, Luo W, Juhong Z, *Et Al.* Associations Between Genetic Variations in the FURIN Gene and Hypertension. *BMC Med Genet* 2010; **11**: 124.

103. Liu C, Kraja AT, Smith JA, *Et Al.* Meta-Analysis Identifies Common and Rare Variants Influencing Blood Pressure and Overlapping with Metabolic Trait Loci. *Nat Genet* 2016; **48**: 1162–70.

104. Giri A, Hellwege JN, Keaton JM, *Et Al.* Trans-Ethnic Association Study of Blood Pressure Determinants in Over 750,000 Individuals. *Nat Genet* 2019; **51**: 51–62.

105. Ehret GB, Ferreira T, Chasman DI, *Et Al.* The Genetics of Blood Pressure Regulation and Its Target Organs from Association Studies in 342,415 Individuals. *Nat Genet* 2016; **48**: 1171–84.

106. Loperena R, Van Beusecum JP, Itani HA, *Et Al.* Hypertension and Increased Endothelial Mechanical Stretch Promote Monocyte Differentiation and Activation: Roles of STAT3, Interleukin 6 and Hydrogen Peroxide. *Cardiovasc Res* 2018; **114**: 1547–63.

107. Wang L, Zhao X-C, Cui W, *Et Al.* Genetic and Pharmacologic Inhibition of the Chemokine Receptor CXCR2 Prevents Experimental Hypertension and Vascular Dysfunction. *Circulation* 2016; **134**: 1353–68.

108. Ishibashi M, Hiasa K, Zhao Q, *Et Al.* Critical Role of Monocyte Chemoattractant Protein-1 Receptor CCR2 On Monocytes in Hypertension-Induced Vascular Inflammation and Remodeling. *Circ Res* 2004; **94**: 1203–10.

109. Chan CT, Moore JP, Budzyn K, *Et Al.* Reversal of Vascular Macrophage Accumulation and Hypertension by a CCR2 Antagonist in Deoxycorticosterone/Salt-Treated Mice. *Hypertension* 2012; **60**: 1207–12.

110. Liao T-D, Yang X-P, Liu Y-H, *Et Al.* Role of Inflammation in the Development of Renal Damage and Dysfunction in Angiotensin II–Induced Hypertension. *Hypertension* 2008; **52**: 256–63.

111. Guzik TJ, Hoch NE, Brown KA, *Et Al.* Role of the T Cell in the Genesis of Angiotensin II–Induced Hypertension and Vascular Dysfunction. *J Exp Med* 2007; **204**: 2449–60.

112. Youn J-C, Yu HT, Lim BJ, *Et Al.* Immunosenescent CD8 $^{+}$ T Cells and C-X-C Chemokine Receptor Type 3 Chemokines Are Increased in Human Hypertension. *Hypertension* 2013; **62**: 126–33.

113. Bautista LE, Vera LM, Arenas IA, Gamarra G. Independent Association Between Inflammatory Markers (C-Reactive Protein, Interleukin-6, and TNF-A) and Essential Hypertension. *J Hum Hypertens* 2005; **19**: 149–54.

114. Devallière J, Charreau B. The Adaptor Lnk (SH2B3): An Emerging Regulator in Vascular Cells and a Link Between Immune and Inflammatory Signaling. *Biochem Pharmacol* 2011; **82**: 1391–402.

115. Intersalt Cooperative Research Group. Intersalt: An International Study of Electrolyte Excretion and Blood Pressure. Results for 24 Hour Urinary Sodium and Potassium Excretion. Intersalt Cooperative Research Group. *BMJ* 1988; **297**: 319–28.

116. Weinberger MH. Salt Sensitivity of Blood Pressure in Humans. *Hypertens Dallas Tex 1979* 1996; **27**: 481–90.

117. Strazzullo P, D'Elia L, Kandala N-B, Cappuccio FP. Salt Intake, Stroke, and Cardiovascular Disease: Meta-Analysis of Prospective Studies. *BMJ* 2009; **339**: B4567.

118. Campese VM, Romoff MS, Levitan D, Saglikes Y, Friedler RM, Massry SG. Abnormal Relationship Between Sodium Intake and Sympathetic Nervous System Activity in Salt-Sensitive Patients with Essential Hypertension. *Kidney Int* 1982; **21**: 371–8.

119. Ahmed SB, Fisher NDL, Stevanovic R, Hollenberg NK. Body Mass Index and Angiotensin-Dependent Control of the Renal Circulation in Healthy Humans. *Hypertens Dallas Tex 1979* 2005; **46**: 1316–20.

120. Zhu J, Mori T, Huang T, Lombard JH. Effect of High-Salt Diet On NO Release and Superoxide Production in Rat Aorta. *Am J Physiol-Heart Circ Physiol* 2004; **286**: H575–83.

121. Wilck N, Matus MG, Kearney SM, *Et Al.* Salt-Responsive Gut Commensal Modulates TH17 Axis and Disease. *Nature* 2017; **551**: 585–9.

122. Saneei P, Salehi-Abargouei A, Esmaillzadeh A, Azadbakht L. Influence of Dietary Approaches to Stop Hypertension (DASH) Diet On Blood Pressure: A Systematic Review and Meta-Analysis On Randomized Controlled Trials. *Nutr Metab Cardiovasc Dis* 2014; **24**: 1253–61.

123. Kannel WB. The Relation of Adiposity to Blood Pressure and Development of Hypertension: The Framingham Study. *Ann Intern Med* 1967; **67**: 48.

124. Landsberg L, Aronne LJ, Beilin LJ, *Et Al.* Obesity-Related Hypertension: Pathogenesis, Cardiovascular Risk, and Treatment-A Position Paper of *The Obesity Society* and the *American Society of Hypertension*: Obesity-Related Hypertension. *Obesity* 2013; **21**: 8–24.

125. Grassi G, Seravalle G, Colombo M, *Et Al.* Body Weight Reduction, Sympathetic Nerve Traffic, and Arterial Baroreflex in Obese Normotensive Humans. *Circulation* 1998; **97**: 2037–42.

126. Whelton PK, Carey RM, Aronow WS, *Et Al.* 2017 ACC/AHA/AAPA/ABC/ACPM/AGS/Apha/ASH/ASPC/NMA/PCNA Guideline for the Prevention, Detection, Evaluation, and Management of High Blood Pressure in Adults: Executive Summary: A Report of the American College of Cardiology/American Heart Association Task Force On Clinical Practice Guidelines. *Circulation* 2018; **138**: E426–83.

127. Zago AS, Park J-Y, Fenty-Stewart N, Silveira LR, Kokubun E, Brown MD. Effects of Aerobic Exercise On the Blood Pressure, Oxidative Stress and Enos Gene Polymorphism in Pre-Hypertensive Older People. *Eur J Appl Physiol* 2010; **110**: 825–32.

128. Roerecke M, Kaczorowski J, Tobe SW, Gmel G, Hasan OSM, Rehm J. The Effect of a Reduction in Alcohol Consumption On Blood Pressure: A Systematic Review and Meta-Analysis. *Lancet Public Health* 2017; **2**: E108–20.

129. Briasoulis A, Agarwal V, Messerli FH. Alcohol Consumption and the Risk of Hypertension in Men and Women: A Systematic Review and Meta-Analysis: Alcohol and Hypertension. *J Clin Hypertens* 2012; **14**: 792–8.

130. Roerecke M, Tobe SW, Kaczorowski J, *Et Al.* Sex-Specific Associations Between Alcohol Consumption and Incidence of Hypertension: A Systematic Review and Meta-Analysis of Cohort Studies. *J Am Heart Assoc* 2018; **7**: E008202.

131. Aladin AI, Chevli PA, Ahmad MI, Rasool SH, Herrington DM. Alcohol Consumption and Systemic Hypertension (From the Third National Health and Nutrition Examination Survey). *Am J Cardiol* 2021; **160**: 60–6.

132. Puddey IB, Mori TA, Barden AE, Beilin LJ. Alcohol and Hypertension—New Insights and Lingering Controversies. *Curr Hypertens Rep* 2019; **21**: 79.

133. Abdel-Rahman AA, Wooles WR. Ethanol-Induced Hypertension Involves Impairment of Baroreceptors. *Hypertens Dallas Tex 1979* 1987; **10**: 67–73.

134. Stewart CW, Kennedy RH. Effects of Chronic Ethanol Consumption On Aortic Constriction in Male and Female Rats. *Eur J Pharmacol* 1999; **366**: 55–60.

135. Abou-Agag LH, Khoo NK, Binsack R, *Et Al.* Evidence of Cardiovascular Protection by Moderate Alcohol: Role of Nitric Oxide. *Free Radic Biol Med* 2005; **39**: 540–8.

136. Tirapelli CR, Leone AFC, Yogi A, *Et Al.* Ethanol Consumption Increases Blood Pressure and Alters the Responsiveness of the Mesenteric Vasculature in Rats. *J Pharm Pharmacol* 2008; **60**: 331–41.

137. Husain K. Vascular Endothelial Oxidative Stress in Alcohol-Induced Hypertension. *Cell Mol Biol Noisy--Gd Fr* 2007; **53**: 70–7.

138. Freitas SRS, Alvim RO. Smoking and Blood Pressure Phenotypes: New Perspective for an Old Problem. *Am J Hypertens* 2017; **30**: 554–5.

139. Grassi G. Assessment of Sympathetic Cardiovascular Drive in Human Hypertension: Achievements and Perspectives. *Hypertension* 2009; **54**: 690–7.

140. Sparrenberger F, Cichelero FT, Ascoli AM, *Et Al.* Does Psychosocial Stress Cause Hypertension? A Systematic Review of Observational Studies. *J Hum Hypertens* 2009; **23**: 12–9.

141. Mozaffarian D, Benjamin EJ, Go AS, *Et Al.* Heart Disease and Stroke Statistics—2015 Update: A Report from the American Heart Association. *Circulation* 2015; **131**.

142. Sun Z. Aging, Arterial Stiffness, and Hypertension. *Hypertens Dallas Tex 1979* 2015; **65**: 252–6.

143. Bruno RM, Duranti E, Ippolito C, *Et Al.* Different Impact of Essential Hypertension On Structural and Functional Age-Related Vascular Changes. *Hypertension* 2017; **69**: 71–8.

144. Alghatrif M, Strait JB, Morrell CH, *Et Al.* Longitudinal Trajectories of Arterial Stiffness and the Role of Blood Pressure: the Baltimore Longitudinal Study of Aging. *Hypertens Dallas Tex 1979* 2013; **62**: 934–41.

145. Guzik TJ, Touyz RM. Oxidative Stress, Inflammation, and Vascular Aging in Hypertension. *Hypertension* 2017; **70**: 660–7.

146. Kaess BM, Rong J, Larson MG, *Et Al.* Aortic Stiffness, Blood Pressure Progression, and Incident Hypertension. *JAMA* 2012; **308**: 875–81.

147. Bavishi C, Goel S, Messerli FH. Isolated Systolic Hypertension: An Update After SPRINT. *Am J Med* 2016; **129**: 1251–8.

148. Wang M, Zhang J, Telljohann R, *Et Al.* Chronic Matrix Metalloproteinase Inhibition Retards Age-Associated Arterial Proinflammation and Increase in Blood Pressure. *Hypertension* 2012; **60**: 459–66.

149. Jiang L, Zhang J, Monticone RE, *Et Al.* Calpain-1 Regulation of Matrix Metalloproteinase 2 Activity in Vascular Smooth Muscle Cells Facilitates Age-Associated Aortic Wall Calcification and Fibrosis. *Hypertens Dallas Tex 1979* 2012; **60**: 1192–9.

150. Björling K, Joseph PD, Egebjerg K, *Et Al.* Role of Age, Rho-Kinase 2 Expression, and G Protein-Mediated Signaling in the Myogenic Response in Mouse Small Mesenteric Arteries. *Physiol Rep* 2018; **6**: E13863.

151. Barnes JN, Hart EC, Curry TB, *Et Al.* Aging Enhances Autonomic Support of Blood Pressure in Women. *Hypertens Dallas Tex 1979* 2014; **63**: 303–8.

152. Page IH. Pathogenesis of Arterial Hypertension. *JAMA J Am Med Assoc* 1949; **140**: 451.

153. Page IH. The Mosaic Theory 32 Years Later. *Hypertens Dallas Tex 1979* 1982; **4**: 177.

154. Havlik RJ, Garrison RJ, Feinleib M, Kannel WB, Castelli WP, Mcnamara PM. BLOOD PRESSURE AGGREGATION IN FAMILIES. *Am J Epidemiol* 1979; **110**: 304–12.

155. Feinleib M, Garrison RJ, Fabsitz R, *Et Al.* The NHLBI Twin Study of Cardiovascular Disease Risk Factors: Methodology and Summary of Results. *Am J Epidemiol* 1977; **106**: 284–5.

156. Fagard R, Brguljan J, Staessen J, *Et Al.* Heritability of Conventional and Ambulatory Blood Pressures. A Study in Twins. *Hypertens Dallas Tex 1979* 1995; **26**: 919–24.

157. Raina R, Krishnappa V, Das A, *Et Al.* Overview of Monogenic or Mendelian Forms of Hypertension. *Front Pediatr* 2019; **7**: 263.

158. Lifton RP, Gharavi AG, Geller DS. Molecular Mechanisms of Human Hypertension. *Cell* 2001; **104**: 545–56.

159. Brown MJ. Platt Versus Pickering: What Molecular Insight to Primary Hyperaldosteronism Tells Us About Hypertension. *JRSM Cardiovasc Dis* 2012; **1**.

160. International Human Genome Sequencing Consortium. Finishing the Euchromatic Sequence of the Human Genome. *Nature* 2004; **431**: 931–45.

161. Cowley AW. The Genetic Dissection of Essential Hypertension. *Nat Rev Genet* 2006; **7**: 829–40.

162. Niu T, Xu X, Rogus J, *Et Al.* Angiotensinogen Gene and Hypertension in Chinese. *J Clin Invest* 1998; **101**: 188–94.

163. Atwood LD, Kammerer CM, Samollow PB, Hixson JE, Shade RE, Maccluer JW. Linkage of Essential Hypertension to the Angiotensinogen Locus in Mexican Americans. *Hypertens Dallas Tex 1979* 1997; **30**: 326–30.

164. Caulfield M, Lavender P, Newell-Price J, *Et Al.* Linkage of the Angiotensinogen Gene Locus to Human Essential Hypertension in African Caribbeans. *J Clin Invest* 1995; **96**: 687–92.

165. Caulfield M, Lavender P, Farrall M, *Et Al.* Linkage of the Angiotensinogen Gene to Essential Hypertension. *N Engl J Med* 1994; **330**: 1629–33.

166. Brand E, Chatelain N, Keavney B, *Et Al.* Evaluation of the Angiotensinogen Locus in Human Essential Hypertension: A European Study. *Hypertension* 1998; **31**: 725–9.

167. Hata A, Namikawa C, Sasaki M, *Et Al.* Angiotensinogen as a Risk Factor for Essential Hypertension in Japan. *J Clin Invest* 1994; **93**: 1285–7.

168. Agarwal A, Williams GH, Fisher NDL. Genetics of Human Hypertension. *Trends Endocrinol Metab TEM* 2005; **16**: 127–33.

169. Gurdasani D, Barroso I, Zeggini E, Sandhu MS. Genomics of Disease Risk in Globally Diverse Populations. *Nat Rev Genet* 2019; **20**: 520–35.

170. Levy D, Destefano AL, Larson MG, *Et Al.* Evidence for a Gene Influencing Blood Pressure On Chromosome 17. Genome Scan Linkage Results for Longitudinal Blood Pressure Phenotypes in Subjects from the Framingham Heart Study. *Hypertens Dallas Tex 1979* 2000; **36**: 477–83.

171. Thiel BA, Chakravarti A, Cooper RS, *Et Al.* A Genome-Wide Linkage Analysis Investigating the Determinants of Blood Pressure in Whites and African Americans. *Am J Hypertens* 2003; **16**: 151–3.

172. Krushkal J, Ferrell R, Mockrin SC, Turner ST, Sing CF, Boerwinkle E. Genome-Wide Linkage Analyses of Systolic Blood Pressure Using Highly Discordant Siblings. *Circulation* 1999; **99**: 1407–10.

173. Caulfield M, Munroe P, Pembroke J, *Et Al.* Genome-Wide Mapping of Human Loci for Essential Hypertension. *Lancet Lond Engl* 2003; **361**: 2118–23.

174. Ehret GB, O'Connor AA, Weder A, Cooper RS, Chakravarti A. Follow-Up of a Major Linkage Peak On Chromosome 1 Reveals Suggestive Qtls Associated with Essential Hypertension: Gennet Study. *Eur J Hum Genet EJHG* 2009; **17**: 1650–7.

175. Munroe PB, Wallace C, Xue M-Z, *Et Al.* Increased Support for Linkage of a Novel Locus On Chromosome 5q13 for Essential Hypertension in the British Genetics of Hypertension Study. *Hypertension* 2006; **48**: 105–11.

176. Chang Y-PC, Liu X, Kim JDO, *Et Al.* Multiple Genes for Essential-Hypertension Susceptibility On Chromosome 1q. *Am J Hum Genet* 2007; **80**: 253–64.

177. Lifton RP, Jeunemaitre X. Finding Genes that Cause Human Hypertension. *J Hypertens* 1993; **11**: 231–6.

178. Wellcome Trust Case Control Consortium. Genome-Wide Association Study of 14,000 Cases of Seven Common Diseases and 3,000 Shared Controls. *Nature* 2007; **447**: 661–78.

179. Newton-Cheh C, Johnson T, Gateva V, *Et Al.* Genome-Wide Association Study Identifies Eight Loci Associated with Blood Pressure. *Nat Genet* 2009; **41**: 666–76.

180. Levy D, Ehret GB, Rice K, *Et Al.* Genome-Wide Association Study of Blood Pressure and Hypertension. *Nat Genet* 2009; **41**: 677–87.

181. Johnson AD, Newton-Cheh C, Chasman DI, *Et Al.* Association of Hypertension Drug Target Genes with Blood Pressure and Hypertension in 86 588 Individuals. *Hypertension* 2011; **57**: 903–10.

182. Wain LV, Verwoert GC, O'Reilly PF, *Et Al.* Genome-Wide Association Study Identifies Six New Loci Influencing Pulse Pressure and Mean Arterial Pressure. *Nat Genet* 2011; **43**: 1005–11.

183. Levy D, Larson MG, Benjamin EJ, *Et Al.* Framingham Heart Study 100K Project: Genome-Wide Associations for Blood Pressure and Arterial Stiffness. *BMC Med Genet* 2007; **8 Suppl 1**: S3.

184. Visscher PM, Wray NR, Zhang Q, *Et Al.* 10 Years of GWAS Discovery: Biology, Function, and Translation. *Am J Hum Genet* 2017; **101**: 5–22.

185. Wellcome Trust Case Control C. Genome-Wide Association Study of 14,000 Cases of Seven Common Diseases and 3,000 Shared Controls. *Nature* 2007; **447**: 661–78.

186. Newton-Cheh C, Johnson T, Gateva V, *Et Al.* Genome-Wide Association Study Identifies Eight Loci Associated with Blood Pressure. *Nat Genet* 2009; **41**: 666–76.

187. 1000 Genomes Project Consortium, Auton A, Brooks LD, *Et Al.* A Global Reference for Human Genetic Variation. *Nature* 2015; **526**: 68–74.

188. Mccarthy S, Das S, Kretzschmar W, *Et Al.* A Reference Panel of 64,976 Haplotypes for Genotype Imputation. *Nat Genet* 2016; **48**: 1279–83.

189. Bycroft C, Freeman C, Petkova D, *Et Al.* The UK Biobank Resource with Deep Phenotyping and Genomic Data. *Nature* 2018; **562**: 203–9.

190. Evangelou E, Warren HR, Mosen-Ansorena D, *Et Al.* Genetic Analysis of Over 1 Million People Identifies 535 New Loci Associated with Blood Pressure Traits. *Nat Genet* 2018; **50**: 1412–25.

191. Tam V, Patel N, Turcotte M, Bossé Y, Paré G, Meyre D. Benefits and Limitations of Genome-Wide Association Studies. *Nat Rev Genet* 2019; **20**: 467–84.

192. Guo Y, He J, Zhao S, *Et Al.* Illumina Human Exome Genotyping Array Clustering and Quality Control. *Nat Protoc* 2014; **9**: 2643–62.

193. Liu C, Kraja AT, Smith JA, *Et Al.* Meta-Analysis Identifies Common and Rare Variants Influencing Blood Pressure and Overlapping with Metabolic Trait Loci. *Nat Genet* 2016; **48**: 1162–70.

194. Evangelou E, Warren HR, Mosen-Ansorena D, *Et Al.* Genetic Analysis of Over 1 Million People Identifies 535 New Loci Associated with Blood Pressure Traits. *Nat Genet* 2018; **50**: 1412–25.

195. Warren H, Edwards T, Vaez A, *Et Al. Genome-Wide Analysis in Over 1 Million Individuals Reveals Over 2,000 Independent Genetic Signals for Blood Pressure*. In Review, 2022.

196. Allen NE, Sudlow C, Peakman T, Collins R, U. K. Biobank. UK Biobank Data: Come and Get It. *Sci Transl Med* 2014; **6**: 224ed4.

197. Kato N, Loh M, Takeuchi F, *Et Al.* Trans-Ancestry Genome-Wide Association Study Identifies 12 Genetic Loci Influencing Blood Pressure and Implicates a Role for DNA Methylation. *Nat Genet* 2015; **47**: 1282–93.

198. Warren HR, Evangelou E, Cabrera CP, *Et Al.* Genome-Wide Association Analysis Identifies Novel Blood Pressure Loci and Offers Biological Insights Into Cardiovascular Risk. *Nat Genet* 2017; **49**: 403–15.

199. Kaiser J, Gibbons A. Biology in the Bank. *Science* 2019; **363**: 18–20.

200. National Institute for Health and Care Excellence (Great Britain), National Guideline Centre (Great Britain). *Hypertension in Adults: Diagnosis and Management*., 2019.

201. Sprint Research Group, Wright JT, Williamson JD, *Et Al.* A Randomized Trial of Intensive Versus Standard Blood-Pressure Control. *N Engl J Med* 2015; **373**: 2103–16.

202. Karczewski KJ, Francioli LC, Tiao G, *Et Al.* The Mutational Constraint Spectrum Quantified from Variation in 141,456 Humans. *Nature* 2020; **581**: 434–43.

203. Uhlen M, Fagerberg L, Hallstrom BM, *Et Al.* Proteomics. Tissue-Based Map of the Human Proteome. *Science* 2015; **347**: 1260419.

204. Thul PJ, Akesson L, Wiking M, *Et Al.* A Subcellular Map of the Human Proteome. *Science* 2017; **356**.

205. Tian X, Feig LA. Basis for Signaling Specificity Difference Between Sos and Ras-GRF Guanine Nucleotide Exchange Factors. *J Biol Chem* 2001; **276**: 47248–56.

206. Wennerberg K, Rossman KL, Der CJ. The Ras Superfamily at a Glance. *J Cell Sci* 2005; **118**: 843–6.

207. Rojas AM, Fuentes G, Rausell A, Valencia A. The Ras Protein Superfamily: Evolutionary Tree and Role of Conserved Amino Acids. *J Cell Biol* 2012; **196**: 189–201.

208. Komatsu M, Ruoslahti E. R-Ras is a Global Regulator of Vascular Regeneration that Suppresses Intimal Hyperplasia and Tumor Angiogenesis. *Nat Med* 2005; **11**: 1346–50.

209. Vigil D, Cherfils J, Rossman KL, Der CJ. Ras Superfamily Gefs and Gaps: Validated and Tractable Targets for Cancer Therapy? *Nat Rev Cancer* 2010; **10**: 842–57.

210. Lowe DG, Goeddel DV. Heterologous Expression and Characterization of the Human R-Ras Gene Product. *Mol Cell Biol* 1987; **7**: 2845–56.

211. Lowe DG, Capon DJ, Delwart E, Sakaguchi AY, Naylor SL, Goeddel DV. Structure of the Human and Murine R-Ras Genes, Novel Genes Closely Related to Ras Proto-Oncogenes. *Cell* 1987; **48**: 137–46.

212. Furuhjelm J, Peranen J. The C-Terminal End of R-Ras Contains a Focal Adhesion Targeting Signal. *J Cell Sci* 2003; **116**: 3729–38.

213. Baumgart F, Corral-Escariz M, Perez-Gil J, Rodriguez-Crespo I. Palmitoylation of R-Ras by Human DHHC19, a Palmitoyl Transferase with a CAAX Box. *Biochim Biophys Acta* 2010; **1798**: 592–604.

214. Conklin MW, Ada-Nguema A, Parsons M, Riching KM, Keely PJ. R-Ras Regulates Beta1-Integrin Trafficking Via Effects On Membrane Ruffling and Endocytosis. *BMC Cell Biol* 2010; **11**: 14.

215. Gawecka JE, Griffiths GS, Ek-Rylander B, Ramos JW, Matter ML. R-Ras Regulates Migration Through an Interaction with Filamin A in Melanoma Cells. *Plos One* 2010; **5**.

216. Vähätupa M, Prince S, Vataja S, *Et Al.* Lack of R-Ras Leads to Increased Vascular Permeability in Ischemic Retinopathy. *Invest Ophthalmol Vis Sci* 2016; **57**: 4898–909.

217. Li F, Sawada J, Komatsu M. R-Ras-Akt Axis Induces Endothelial Lumenogenesis and Regulates the Patency of Regenerating Vasculature. *Nat Commun* 2017; **8**: 1720.

218. Spaargaren M, Martin GA, Mccormick F, Fernandez-Sarabia MJ, Bischoff JR. The Ras-Related Protein R-Ras Interacts Directly with Raf-1 in a GTP-Dependent Manner. *Biochem J* 1994; **300 (Pt 2)**: 303–7.

219. Gotoh T, Niino Y, Tokuda M, *Et Al.* Activation of R-Ras by Ras-Guanine Nucleotide-Releasing Factor. *J Biol Chem* 1997; **272**: 18602–7.

220. Lenzen C, Cool RH, Prinz H, Kuhlmann J, Wittinghofer A. Kinetic Analysis by Fluorescence of the Interaction Between Ras and the Catalytic Domain of the Guanine Nucleotide Exchange Factor Cdc25Mm. *Biochemistry* 1998; **37**: 7420–30.

221. Cerutti C, Ridley AJ. Endothelial Cell-Cell Adhesion and Signaling. *Exp Cell Res* 2017; **358**: 31–8.

222. Rey I, Taylor-Harris P, Van Erp H, Hall A. R-Ras Interacts with Rasgap, Neurofibromin and C-Raf But Does Not Regulate Cell Growth or Differentiation. *Oncogene* 1994; **9**: 685–92.

223. Yamamoto T, Matsui T, Nakafuku M, Iwamatsu A, Kaibuchi K. A Novel Gtpase-Activating Protein for R-Ras. *J Biol Chem* 1995; **270**: 30557–61.

224. Marte BM, Rodriguez-Viciana P, Wennström S, Warne PH, Downward J. R-Ras Can Activate the Phosphoinositide 3-Kinase But Not the MAP Kinase Arm of the Ras Effector Pathways. *Curr Biol* 1997; **7**: 63–70.

225. Ohba Y, Mochizuki N, Yamashita S, *Et Al.* Regulatory Proteins of R-Ras, TC21/R-Ras2, and M-Ras/R-Ras3. *J Biol Chem* 2000; **275**: 20020–6.

226. Zhang Z, Vuori K, Wang H, Reed JC, Ruoslahti E. Integrin Activation by R-Ras. *Cell* 1996; **85**: 61–9.

227. Wang B, Zou JX, Ek-Rylander B, Ruoslahti E. R-Ras Contains a Proline-Rich Site that Binds to SH3 Domains and is Required for Integrin Activation by R-Ras. *J Biol Chem* 2000; **275**: 5222–7.

228. Matsumoto K, Asano T, Endo T. Novel Small Gtpase M-Ras Participates in Reorganization of Actin Cytoskeleton. *Oncogene* 1997; **15**: 2409–17.

229. Iwasawa N, Negishi M, Oinuma I. R-Ras Controls Axon Branching Through Afadin in Cortical Neurons. *Mol Biol Cell* 2012; **23**: 2793–804.

230. Hansen M, Prior IA, Hughes PE, *Et Al.* C-Terminal Sequences in R-Ras Are Involved in Integrin Regulation and in Plasma Membrane Microdomain Distribution. *Biochem Biophys Res Commun* 2003; **311**: 829–38.

231. Self AJ, Caron E, Paterson HF, Hall A. Analysis of R-Ras Signalling Pathways. *J Cell Sci* 2001; **114**: 1357–66.

232. Frémin C, Guégan JP, Plutoni C, *Et Al.* ERK1/2-Induced Phosphorylation of R-Ras Gtpases Stimulates Their Oncogenic Potential. *Oncogene* 2016; **35**: 5692–8.

233. Cox AD, Brtva TR, Lowe DG, Der CJ. R-Ras Induces Malignant, But Not Morphologic, Transformation of NIH3T3 Cells. *Oncogene* 1994; **9**: 3281–8.

234. Rodriguez-Viciana P, Warne PH, Dhand R, *Et Al.* Phosphatidylinositol-3-OH Kinase as a Direct Target of Ras. *Nature* 1994; **370**: 527–32.

235. Berrier AL, Mastrangelo AM, Downward J, Ginsberg M, Laflamme SE. Activated R-Ras, Rac1, PI 3-Kinase and Pkcepsilon Can Each Restore Cell Spreading Inhibited by Isolated Integrin Beta1 Cytoplasmic Domains. *J Cell Biol* 2000; **151**: 1549–60.

236. Holly SP, Larson MK, Parise LV. The Unique N-Terminus of R-Ras is Required for Rac Activation and Precise Regulation of Cell Migration. *Mol Biol Cell* 2005; **16**: 2458–69.

237. Goldfinger LE, Ptak C, Jeffery ED, Shabanowitz J, Hunt DF, Ginsberg MH. RLIP76 (Ralbp1) is an R-Ras Effector that Mediates Adhesion-Dependent Rac Activation and Cell Migration. *J Cell Biol* 2006; **174**: 877–88.

238. Ito Y, Oinuma I, Katoh H, Kaibuchi K, Negishi M. Sema4D/Plexin-B1 Activates GSK-3beta Through R-Ras GAP Activity, Inducing Growth Cone Collapse. *EMBO Rep* 2006; **7**: 704–9.

239. Oinuma I, Katoh H, Negishi M. R-Ras Controls Axon Specification Upstream of Glycogen Synthase Kinase-3beta Through Integrin-Linked Kinase. *J Biol Chem* 2007; **282**: 303–18.

240. López De Jesús M, Stope MB, Oude Weernink PA, *Et Al.* Cyclic AMP-Dependent and Epac-Mediated Activation of R-Ras by G Protein-Coupled Receptors Leads to Phospholipase D Stimulation. *J Biol Chem* 2006; **281**: 21837–47.

241. Nakada M, Niska JA, Tran NL, Mcdonough WS, Berens ME. Ephb2/R-Ras Signaling Regulates Glioma Cell Adhesion, Growth, and Invasion. *Am J Pathol* 2005; **167**: 565–76.

242. Hodkinson PS, Elliott PA, Lad Y, *Et Al.* Mammalian NOTCH-1 Activates Beta1 Integrins Via the Small Gtpase R-Ras. *J Biol Chem* 2007; **282**: 28991–9001.

243. Garcia-Morales V, Luaces-Regueira M, Campos-Toimil M. The Camp Effectors PKA and Epac Activate Endothelial NO Synthase Through PI3K/Akt Pathway in Human Endothelial Cells. *Biochem Pharmacol* 2017; **145**: 94–101.

244. Oertli B, Han J, Marte BM, *Et Al.* The Effector Loop and Prenylation Site of R-Ras Are Involved in the Regulation of Integrin Function. *Oncogene* 2000; **19**: 4961–9.

245. Oinuma I, Ishikawa Y, Katoh H, Negishi M. The Semaphorin 4D Receptor Plexin-B1 is a Gtpase Activating Protein for R-Ras. *Science* 2004; **305**: 862–5.

246. Sethi T, Ginsberg MH, Downward J, Hughes PE. The Small GTP-Binding Protein R-Ras Can Influence Integrin Activation by Antagonizing a Ras/Raf-Initiated Integrin Suppression Pathway. *Mol Biol Cell* 1999; **10**: 1799–809.

247. Ada-Nguema AS, Xenias H, Hofman JM, Wiggins CH, Sheetz MP, Keely PJ. The Small Gtpase R-Ras Regulates Organization of Actin and Drives Membrane Protrusions Through the Activity of Plcepsilon. *J Cell Sci* 2006; **119**: 1307–19.

248. Perrot CY, Sawada J, Komatsu M. Prolonged Activation of Camp Signaling Leads to Endothelial Barrier Disruption Via Transcriptional Repression of RRAS. *FASEB J* 2018: Fj201700818rrr.

249. Griffiths GS, Grundl M, Allen JS, Matter ML. R-Ras Interacts with Filamin A to Maintain Endothelial Barrier Function. *J Cell Physiol* 2011; **226**: 2287–96.

250. May U, Prince S, Vahatupa M, *Et Al.* Resistance of R-Ras Knockout Mice to Skin Tumour Induction. *Sci Rep* 2015; **5**: 11663.

251. Shi X, Luo X, Xu X. Dimethylarginine Dimethylaminohydrolase-1 Contributes to Exercise-Induced Cardiac Angiogenesis in Mice. *Biosci Trends* 2020; **14**: 115–22.

252. Sawada J, Perrot CY, Chen L, *Et Al.* High Endothelial Venules Accelerate Naive T Cell Recruitment by Tumor Necrosis Factor-Mediated R-Ras Upregulation. *Am J Pathol* 2021; **191**: 396–414.

253. Yan X, Yan M, Guo Y, *Et Al.* R-Ras Regulates Murine T Cell Migration and Intercellular Adhesion Molecule-1 Binding. *Plos One* 2015; **10**: E0145218.

254. Singh G, Hashimoto D, Yan X, *Et Al.* R-Ras is Required for Murine Dendritic Cell Maturation and CD4+ T-Cell Priming. *Blood* 2012; **119**: 1693–701.

255. Ray A, Basu S, Miller NM, Chan AM, Dittel BN. An Increase in Tolerogenic Dendritic Cell and Natural Regulatory T Cell Numbers During Experimental Autoimmune Encephalomyelitis in *Rras* $^{-/-}$ Mice Results in Attenuated Disease. *J Immunol* 2014; **192**: 5109–17.

256. Keely PJ, Rusyn EV, Cox AD, Parise LV. R-Ras Signals Through Specific Integrin Alpha Cytoplasmic Domains to Promote Migration and Invasion of Breast Epithelial Cells. *J Cell Biol* 1999; **145**: 1077–88.

257. Vicente-Manzanares M, Webb DJ, Horwitz AR. Cell Migration at a Glance. *J Cell Sci* 2005; **118**: 4917–9.

258. Lilja J, Zacharchenko T, Georgiadou M, *Et Al.* SHANK Proteins Limit Integrin Activation by Directly Interacting with Rap1 and R-Ras. *Nat Cell Biol* 2017; **19**: 292–305.

259. Lehto M, Mayranpaa MI, Pellinen T, *Et Al.* The R-Ras Interaction Partner ORP3 Regulates Cell Adhesion. *J Cell Sci* 2008; **121**: 695–705.

260. Weber-Boyvat M, Kentala H, Lilja J, *Et Al.* OSBP-Related Protein 3 (ORP3) Coupling with VAMP-Associated Protein A Regulates R-Ras Activity. *Exp Cell Res* 2015; **331**: 278–91.

261. Wozniak MA, Kwong L, Chodniewicz D, Klemke RL, Keely PJ. R-Ras Controls Membrane Protrusion and Cell Migration Through the Spatial Regulation of Rac and Rho. *Mol Biol Cell* 2005; **16**: 84–96.

262. Kwong L, Wozniak MA, Collins AS, Wilson SD, Keely PJ. R-Ras Promotes Focal Adhesion Formation Through Focal Adhesion Kinase and P130(Cas) by a Novel Mechanism that Differs from Integrins. *Mol Cell Biol* 2003; **23**: 933–49.

263. Mora N, Rosales R, Rosales C. R-Ras Promotes Metastasis of Cervical Cancer Epithelial Cells. *Cancer Immunol Immunother* 2007; **56**: 535–44.

264. Arora PD, He T, Ng K, Mcculloch CA. The Leucine-Rich Region of Flightless I Interacts with R-Ras to Regulate Cell Extension Formation. *Mol Biol Cell* 2018; **29**: 2481–93.

265. Arora PD, Nakajima K, Nanda A, *Et Al.* Flightless Anchors IQGAP1 and R-Ras to Mediate Cell Extension Formation and Matrix Remodeling. *Mol Biol Cell* 2020; **31**: 1595–610.

266. Fernandez-Sarabia MJ, Bischoff JR. Bcl-2 Associates with the Ras-Related Protein R-Ras P23. *Nature* 1993; **366**: 274–5.

267. Sawada J, Li F, Komatsu M. R-Ras Protein Inhibits Autophosphorylation of Vascular Endothelial Growth Factor Receptor 2 in Endothelial Cells and Suppresses Receptor Activation in Tumor Vasculature. *J Biol Chem* 2015; **290**: 8133–45.

268. Sawada J, Li F, Komatsu M. R-Ras Inhibits VEGF-Induced P38mapk Activation and HSP27 Phosphorylation in Endothelial Cells. *J Vasc Res* 2015; **52**: 347–59.

269. Herrera JL, Komatsu M. R-Ras Deficiency in Pericytes Causes Frequent Microphthalmia and Perturbs Retinal Vascular Development. *J Vasc Res* 2021; **58**: 252–66.

270. Takino J-I, Sato T, Nagamine K, Hori T. The Inhibition of Bax Activation-Induced Apoptosis by Rasgrp2 Via R-Ras-PI3K-Akt Signaling Pathway in the Endothelial Cells. *Sci Rep* 2019; **9**: 16717.

271. Nishigaki M, Aoyagi K, Danjoh I, *Et Al.* Discovery of Aberrant Expression of R-RAS by Cancer-Linked DNA Hypomethylation in Gastric Cancer Using Microarrays. *Cancer Res* 2005; **65**: 2115–24.

272. Ohata S, Uga H, Okamoto H, Katada T. Small Gtpase R-Ras Participates in Neural Tube Formation in Zebrafish Embryonic Spinal Cord. *Biochem Biophys Res Commun* 2018; **501**: 786–90.

273. Sanz-Rodriguez M, Gruart A, Escudero-Ramirez J, *Et Al.* R-Ras1 and R-Ras2 Are Essential for Oligodendrocyte Differentiation and Survival for Correct Myelination in the Central Nervous System. *J Neurosci Off J Soc Neurosci* 2018; **38**: 5096–110.

274. Alcover-Sanchez B, Garcia-Martin G, Wandosell F, Cubelos B. R-Ras Gtpases Signaling Role in Myelin Neurodegenerative Diseases. *Int J Mol Sci* 2020; **21**: E5911.

275. Chaplin DD. Overview of the Immune Response. *J Allergy Clin Immunol* 2010; **125**: S3-23.

276. Cole AL, Subbanagounder G, Mukhopadhyay S, Berliner JA, Vora DK. Oxidized Phospholipid-Induced Endothelial Cell/Monocyte Interaction is Mediated by a Camp-Dependent R-Ras/PI3-Kinase Pathway. *Arter Thromb Vasc Biol* 2003; **23**: 1384–90.

277. Wang HG, Millan JA, Cox AD, *Et Al.* R-Ras Promotes Apoptosis Caused by Growth Factor Deprivation Via a Bcl-2 Suppressible Mechanism. *J Cell Biol* 1995; **129**: 1103–14.

278. Raza A, Pandey MS, Jin Q, Mulder KM. Km23-1/DYNLRB1 Regulation of MEK/ERK Signaling and R-Ras in Invasive Human Colorectal Cancer Cells. *Cell Biol Int* 2020; **44**: 155–65.

279. Weber SM, Brossier NM, Prechtl A, *Et Al.* R-Ras Subfamily Proteins Elicit Distinct Physiologic Effects and Phosphoproteome Alterations in Neurofibromin-Null MPNST Cells. *Cell Commun Signal CCS* 2021; **19**: 95.

280. Flex E, Jaiswal M, Pantaleoni F, *Et Al.* Activating Mutations in RRAS Underlie a Phenotype Within the Rasopathy Spectrum and Contribute to Leukaemogenesis. *Hum Mol Genet* 2014; **23**: 4315–27.

281. Lifelines Cohort Study, EPIC-CVD, EPIC-Interact, *Et Al.* Discovery of Rare Variants Associated with Blood Pressure Regulation Through Meta-Analysis of 1.3 Million Individuals. *Nat Genet* 2020; **52**: 1314–32.

282. Baek M, Dimaio F, Anishchenko I, *Et Al.* Accurate Prediction of Protein Structures and Interactions Using a Three-Track Neural Network. *Science* 2021; **373**: 871–6.

283. Hecht M, Bromberg Y, Rost B. Better Prediction of Functional Effects for Sequence Variants. *BMC Genomics* 2015; **16 Suppl 8**: S1.

284. Ng PC, Henikoff S. SIFT: Predicting Amino Acid Changes that Affect Protein Function. *Nucleic Acids Res* 2003; **31**: 3812–4.

285. Sim N-L, Kumar P, Hu J, Henikoff S, Schneider G, Ng PC. SIFT Web Server: Predicting Effects of Amino Acid Substitutions On Proteins. *Nucleic Acids Res* 2012; **40**: W452-457.

286. Choi Y, Sims GE, Murphy S, Miller JR, Chan AP. Predicting the Functional Effect of Amino Acid Substitutions and Indels. De Brevern AG, Ed. *Plos ONE* 2012; **7**: E46688.

287. Adzhubei IA, Schmidt S, Peshkin L, *Et Al.* A Method and Server for Predicting Damaging Missense Mutations. *Nat Methods* 2010; **7**: 248–9.

288. Pejaver V, Urresti J, Lugo-Martinez J, *Et Al.* Inferring the Molecular and Phenotypic Impact of Amino Acid Variants with Mutpred2. *Nat Commun* 2020; **11**: 5918.

289. Cheng J, Randall A, Baldi P. Prediction of Protein Stability Changes for Single-Site Mutations Using Support Vector Machines. *Proteins* 2006; **62**: 1125–32.

290. Khanna T, Hanna G, Sternberg MJE, David A. Missense3D-DB Web Catalogue: An Atom-Based Analysis and Repository of 4M Human Protein-Coding Genetic Variants. *Hum Genet* 2021; **140**: 805–12.

291. Sudlow C, Gallacher J, Allen N, *Et Al.* UK Biobank: An Open Access Resource for Identifying the Causes of a Wide Range of Complex Diseases of Middle and Old Age. *PLOS Med* 2015; **12**: E1001779.

292. Wain LV, Shrine N, Miller S, *Et Al.* Novel Insights Into the Genetics of Smoking Behaviour, Lung Function, and Chronic Obstructive Pulmonary Disease (UK Bileve): A Genetic Association Study in UK Biobank. *Lancet Respir Med* 2015; **3**: 769–81.

293. Bycroft C, Freeman C, Petkova D, *Et Al.* The UK Biobank Resource with Deep Phenotyping and Genomic Data. *Nature* 2018; **562**: 203–9.

294. Purcell S, Neale B, Todd-Brown K, *Et Al.* PLINK: A Tool Set for Whole-Genome Association and Population-Based Linkage Analyses. *Am J Hum Genet* 2007; **81**: 559–75.

295. Jaffe EA, Nachman RL, Becker CG, Minick CR. Culture of Human Endothelial Cells Derived from Umbilical Veins. Identification by Morphologic and Immunologic Criteria. *J Clin Invest* 1973; **52**: 2745–56.

296. Fabre A-L, Colotte M, Luis A, Tuffet S, Bonnet J. An Efficient Method for Long-Term Room Temperature Storage of RNA. *Eur J Hum Genet* 2014; **22**: 379–85.

297. Komatsu M, Ruoslahti E. R-Ras is a Global Regulator of Vascular Regeneration that Suppresses Intimal Hyperplasia and Tumor Angiogenesis. *Nat Med* 2005; **11**: 1346–50.

298. Huetteman DA, Bogie H. Direct Blood Pressure Monitoring in Laboratory Rodents Via Implantable Radio Telemetry. *Methods Mol Biol* 2009; **573**: 57–73.

299. Yin FC, Spurgeon HA, Rakusan K, Weisfeldt ML, Lakatta EG. Use of Tibial Length to Quantify Cardiac Hypertrophy: Application in the Aging Rat. *Am J Physiol* 1982; **243**: H941-947.

300. Puchtler H, Waldrop FS, Valentine LS. Polarization Microscopic Studies of Connective Tissue Stained with Picro-Sirius Red FBA. *Beitr Zur Pathol* 1973; **150**: 174–87.

301. Junqueira LC, Bignolas G, Brentani RR. Picrosirius Staining Plus Polarization Microscopy, a Specific Method for Collagen Detection in Tissue Sections. *Histochem J* 1979; **11**: 447–55.

302. Gruhler A, Olsen JV, Mohammed S, *Et Al.* Quantitative Phosphoproteomics Applied to the Yeast Pheromone Signaling Pathway. *Mol Cell Proteomics MCP* 2005; **4**: 310–27.

303. Larsen MR, Thingholm TE, Jensen ON, Roepstorff P, Jørgensen TJD. Highly Selective Enrichment of Phosphorylated Peptides from Peptide Mixtures Using Titanium Dioxide Microcolumns. *Mol Cell Proteomics MCP* 2005; **4**: 873–86.

304. Montoya A, Beltran L, Casado P, Rodríguez-Prados J-C, Cutillas PR. Characterization of a Tio_2 Enrichment Method for Label-Free Quantitative Phosphoproteomics. *Methods San Diego Calif* 2011; **54**: 370–8.

305. Wickham H. *Ggplot2: Elegant Graphics for Data Analysis*. 2nd Ed. 2016. Cham: Springer International Publishing : Imprint: Springer, 2016.

306. Bates D, Mächler M, Bolker B, Walker S. Fitting Linear Mixed-Effects Models Using **Lme4**. *J Stat Softw* 2015; **67**.

307. Lüdecke D. Ggeffects: Tidy Data Frames of Marginal Effects from Regression Models. *J Open Source Softw* 2018; **3**: 772.

308. Schmittgen TD, Livak KJ. Analyzing Real-Time PCR Data by the Comparative CT Method. *Nat Protoc* 2008; **3**: 1101–8.

309. Campitelli E. Ggnewscale: Multiple Fill and Color Scales in Ggplot2. 2022.

310. Wilke CO. Cowplot: Streamlined Plot Theme and Plot Annotations for “Ggplot2.” 2020.

311. Carlson M. Org.Mm.Eg.Db: Genome Wide Annotation for Mouse. 2019.

312. Yu G, Wang L-G, Han Y, He Q-Y. Clusterprofiler: An R Package for Comparing Biological Themes Among Gene Clusters. *Omics J Integr Biol* 2012; **16**: 284–7.

313. Yu G. Enrichplot: Visualization of Functional Enrichment Result. 2022.

314. Luo W, Brouwer C. Pathview: An R/Bioconductor Package for Pathway-Based Data Integration and Visualization. *Bioinforma Oxf Engl* 2013; **29**: 1830–1.

315. Ashburner M, Ball CA, Blake JA, *Et Al.* Gene Ontology: Tool for the Unification of Biology. *Nat Genet* 2000; **25**: 25–9.

316. Scorilas A, Kyriakopoulou L, Katsaros D, Diamandis EP. Cloning of a Gene (SR-A1), Encoding for a New Member of the Human Ser/Arg-Rich Family of Pre-Mrna Splicing Factors: Overexpression in Aggressive Ovarian Cancer. *Br J Cancer* 2001; **85**: 190–8.

317. Schrödinger L, Delano W. The Pymol Molecular Graphics System, Version 2.5. 2020.

318. Ashkenazy H, Abadi S, Martz E, *Et Al.* Consurf 2016: An Improved Methodology to Estimate and Visualize Evolutionary Conservation in Macromolecules. *Nucleic Acids Res* 2016; **44**: W344-350.

319. Chothia C, Lesk AM. The Relation Between the Divergence of Sequence and Structure in Proteins. *EMBO J* 1986; **5**: 823–6.

320. Vähätupa M, Prince S, Vataja S, *Et Al.* Lack of R-Ras Leads to Increased Vascular Permeability in Ischemic Retinopathy. *Invest Ophthalmol Vis Sci* 2016; **57**: 4898–909.

321. Li F, Sawada J, Komatsu M. R-Ras-Akt Axis Induces Endothelial Lumenogenesis and Regulates the Patency of Regenerating Vasculature. *Nat Commun* 2017; **8**: 1720.

322. May U, Prince S, Vahatupa M, *Et Al.* Resistance of R-Ras Knockout Mice to Skin Tumour Induction. *Sci Rep* 2015; **5**: 11663.

323. Uhlen M, Fagerberg L, Hallstrom BM, *Et Al.* Proteomics. Tissue-Based Map of the Human Proteome. *Science* 2015; **347**: 1260419.

324. Thul PJ, Akesson L, Wiking M, *Et Al.* A Subcellular Map of the Human Proteome. *Science* 2017; **356**.

325. Rodriguez-Viciana P, Warne PH, Dhand R, *Et Al.* Phosphatidylinositol-3-OH Kinase as a Direct Target of Ras. *Nature* 1994; **370**: 527–32.

326. Marte BM, Rodriguez-Viciana P, Wennström S, Warne PH, Downward J. R-Ras Can Activate the Phosphoinositide 3-Kinase But Not the MAP Kinase Arm of the Ras Effector Pathways. *Curr Biol* 1997; **7**: 63–70.

327. Berrier AL, Mastrangelo AM, Downward J, Ginsberg M, Laflamme SE. Activated R-Ras, Rac1, PI 3-Kinase and Pkcepsilon Can Each Restore Cell Spreading Inhibited by Isolated Integrin Beta1 Cytoplasmic Domains. *J Cell Biol* 2000; **151**: 1549–60.

328. Self AJ, Caron E, Paterson HF, Hall A. Analysis of R-Ras Signalling Pathways. *J Cell Sci* 2001; **114**: 1357–66.

329. Hansen M, Prior IA, Hughes PE, *Et Al.* C-Terminal Sequences in R-Ras Are Involved in Integrin Regulation and in Plasma Membrane Microdomain Distribution. *Biochem Biophys Res Commun* 2003; **311**: 829–38.

330. Holly SP, Larson MK, Parise LV. The Unique N-Terminus of R-Ras is Required for Rac Activation and Precise Regulation of Cell Migration. *Mol Biol Cell* 2005; **16**: 2458–69.

331. Goldfinger LE, Ptak C, Jeffery ED, Shabanowitz J, Hunt DF, Ginsberg MH. RLIP76 (Ralbp1) is an R-Ras Effector that Mediates Adhesion-Dependent Rac Activation and Cell Migration. *J Cell Biol* 2006; **174**: 877–88.

332. Ito Y, Oinuma I, Katoh H, Kaibuchi K, Negishi M. Sema4D/Plexin-B1 Activates GSK-3beta Through R-Ras GAP Activity, Inducing Growth Cone Collapse. *EMBO Rep* 2006; **7**: 704–9.

333. Oinuma I, Ishikawa Y, Katoh H, Negishi M. The Semaphorin 4D Receptor Plexin-B1 is a Gtpase Activating Protein for R-Ras. *Science* 2004; **305**: 862–5.

334. Crowley SD, Gurley SB, Herrera MJ, *Et Al.* Angiotensin II Causes Hypertension and Cardiac Hypertrophy Through its Receptors in the Kidney. *Proc Natl Acad Sci* 2006; **103**: 17985–90.

335. Xue B, Pamidimukkala J, Hay M. Sex Differences in the Development of Angiotensin II-Induced Hypertension in Conscious Mice. *Am J Physiol-Heart Circ Physiol* 2005; **288**: H2177–84.

336. Dimmeler S, Dernbach E, Zeiher AM. Phosphorylation of the Endothelial Nitric Oxide Synthase at Ser-1177 is Required for VEGF-Induced Endothelial Cell Migration. *FEBS Lett* 2000; **477**: 258–62.

337. Mckenzie C, Macdonald A, Shaw AM. Mechanisms of U46619-Induced Contraction of Rat Pulmonary Arteries in the Presence and Absence of the Endothelium. *Br J Pharmacol* 2009; **157**: 581–96.

338. The International Mouse Phenotyping Consortium, Dickinson ME, Flenniken AM, *Et Al.* High-Throughput Discovery of Novel Developmental Phenotypes. *Nature* 2016; **537**: 508–14.

339. Lerman LO, Kurtz TW, Touyz RM, *Et Al.* Animal Models of Hypertension: A Scientific Statement from the American Heart Association. *Hypertension* 2019; **73**.

340. Barsha G, Denton KM, Mirabito Colafella KM. Sex- and Age-Related Differences in Arterial Pressure and Albuminuria in Mice. *Biol Sex Differ* 2016; **7**: 57.

341. Cox BF, Bishop VS. Neural and Humoral Mechanisms of Angiotensin-Dependent Hypertension. *Am J Physiol* 1991; **261**: H1284-1291.

342. Zimmerman MC, Lazartigues E, Lang JA, *Et Al.* Superoxide Mediates the Actions of Angiotensin II in the Central Nervous System. *Circ Res* 2002; **91**: 1038–45.

343. Pechanova O, Vrankova S, Cebova M. Chronic L-Name-Treatment Produces Hypertension by Different Mechanisms in Peripheral Tissues and Brain: Role of Central Enos. *Pathophysiology* 2020; **27**: 46–54.

344. Padmanabhan S, Melander O, Johnson T, *Et Al.* Genome-Wide Association Study of Blood Pressure Extremes Identifies Variant Near UMOD Associated with Hypertension. Schork NJ, Ed. *Plos Genet* 2010; **6**: E1001177.

345. Graham LA, Padmanabhan S, Fraser NJ, *Et Al.* Validation of Uromodulin as a Candidate Gene for Human Essential Hypertension. *Hypertension* 2014; **63**: 551–8.

346. Chamorro-Jorganes A, Grande MT, Herranz B, *Et Al.* Targeted Genomic Disruption of H-Ras Induces Hypotension Through a NO-Cgmp-PKG Pathway–Dependent Mechanism. *Hypertension* 2010; **56**: 484–9.

347. Sandberg K, Ji H. Sex Differences in Primary Hypertension. *Biol Sex Differ* 2012; **3**: 7.

348. Furchgott RF, Zawadzki JV. The Obligatory Role of Endothelial Cells in the Relaxation of Arterial Smooth Muscle by Acetylcholine. *Nature* 1980; **288**: 373–6.

349. Fountain JH, Lappin SL. Physiology, Renin Angiotensin System. In: *Statpearls*. Treasure Island (FL): Statpearls Publishing, 2022.

350. Renna NF, De Las Heras N, Miatello RM. Pathophysiology of Vascular Remodeling in Hypertension. *Int J Hypertens* 2013; **2013**: 1–7.

351. Dinh QN, Drummond GR, Sobey CG, Chrissobolis S. Roles of Inflammation, Oxidative Stress, and Vascular Dysfunction in Hypertension. *Biomed Res Int* 2014; **2014**: 406960.

352. Laurent S. Arterial Wall Hypertrophy and Stiffness in Essential Hypertensive Patients. *Hypertension* 1995; **26**: 355–62.

353. Griffin SA, Brown WC, Macpherson F, *Et Al.* Angiotensin II Causes Vascular Hypertrophy in Part by a Non-Pressor Mechanism. *Hypertension* 1991; **17**: 626–35.

354. Wirth A, Wang S, Takefuji M, *Et Al.* Age-Dependent Blood Pressure Elevation is Due to Increased Vascular Smooth Muscle Tone Mediated by G-Protein Signalling. *Cardiovasc Res* 2016; **109**: 131–40.

355. Safran M, Rosen N, Twik M, *Et Al.* The Genecards Suite. In: Abugessaisa I, Kasukawa T, Eds. *Practical Guide to Life Science Databases*. Singapore: Springer Nature Singapore, 2021, 27–56.

356. Griffiths GS, Grundl M, Allen JS, Matter ML. R-Ras Interacts with Filamin A to Maintain Endothelial Barrier Function. *J Cell Physiol* 2011; **226**: 2287–96.

357. Casado P, Rodriguez-Prados J-C, Cosulich SC, *Et Al.* Kinase-Substrate Enrichment Analysis Provides Insights Into the Heterogeneity of Signaling Pathway Activation in Leukemia Cells. *Sci Signal* 2013; **6**: Rs6.

358. Wozniak MA, Kwong L, Chodniewicz D, Klemke RL, Keely PJ. R-Ras Controls Membrane Protrusion and Cell Migration Through the Spatial Regulation of Rac and Rho. *Mol Biol Cell* 2005; **16**: 84–96.

359. Daoud F, Arévalo Martinez M, Holmberg J, *Et Al.* YAP and TAZ in Vascular Smooth Muscle Confer Protection Against Hypertensive Vasculopathy. *Arterioscler Thromb Vasc Biol* 2022; **42**: 428–43.

360. He J, Bao Q, Yan M, *Et Al.* The Role of Hippo/Yes-Associated Protein Signalling in Vascular Remodelling Associated with Cardiovascular Disease. *Br J Pharmacol* 2018; **175**: 1354–61.

361. Yu OM, Miyamoto S, Brown JH. Myocardin-Related Transcription Factor A and Yes-Associated Protein Exert Dual Control in G Protein-Coupled Receptor- and Rhoa-Mediated Transcriptional Regulation and Cell Proliferation. *Mol Cell Biol* 2016; **36**: 39–49.

362. Boopathy GTK, Hong W. Role of Hippo Pathway-YAP/TAZ Signaling in Angiogenesis. *Front Cell Dev Biol* 2019; **7**: 49.

363. Dupont S, Morsut L, Aragona M, *Et Al.* Role of YAP/TAZ in Mechanotransduction. *Nature* 2011; **474**: 179–83.

364. Majesky MW. Developmental Basis of Vascular Smooth Muscle Diversity. *Arterioscler Thromb Vasc Biol* 2007; **27**: 1248–58.

365. Yu L, Zhang J, Gao A, *Et Al.* An Intersegmental Single-Cell Profile Reveals Aortic Heterogeneity and Identifies a Novel Malat1+ Vascular Smooth Muscle Subtype Involved in Abdominal Aortic Aneurysm Formation. *Signal Transduct Target Ther* 2022; **7**: 125.

366. Gao P, Gao P, Choi M, *Et Al.* Transcriptome Analysis of Mouse Aortae Reveals Multiple Novel Pathways Regulated by Aging. *Aging* 2020; **12**: 15603–23.

367. Zhang K, Kan H, Mao A, Geng L, Ma X. Single-Cell Analysis of Salt-Induced Hypertensive Mouse Aortae Reveals Cellular Heterogeneity and State Changes. *Exp Mol Med* 2021; **53**: 1866–76.

368. Mount PF, Kemp BE, Power DA. Regulation of Endothelial and Myocardial NO Synthesis by Multi-Site Enos Phosphorylation. *J Mol Cell Cardiol* 2007; **42**: 271–9.

369. Uchio-Yamada K, Yasuda K, Monobe Y, Akagi K, Suzuki O, Manabe N. Tensin2 is Important for Podocyte-Glomerular Basement Membrane Interaction and Integrity of the Glomerular Filtration Barrier. *Am J Physiol-Ren Physiol* 2020; **318**: F1520–30.

370. Cho A-R, Uchio-Yamada K, Torigai T, *Et Al.* Deficiency of the Tensin2 Gene in the ICGN Mouse: An Animal Model for Congenital Nephrotic Syndrome. *Mamm Genome Off J Int Mamm Genome Soc* 2006; **17**: 407–16.

371. Ashraf S, Kudo H, Rao J, *Et Al.* Mutations in Six Nephrosis Genes Delineate a Pathogenic Pathway Amenable to Treatment. *Nat Commun* 2018; **9**: 1960.

372. Shatat IF, Becton LJ, Woroniecki RP. Hypertension in Childhood Nephrotic Syndrome. *Front Pediatr* 2019; **7**: 287.

373. Giri A, Hellwege JN, Keaton JM, *Et Al.* Trans-Ethnic Association Study of Blood Pressure Determinants in Over 750,000 Individuals. *Nat Genet* 2019; **51**: 51–62.

374. Wain LV, Vaez A, Jansen R, *Et Al.* Novel Blood Pressure Locus and Gene Discovery Using Genome-Wide Association Study and Expression Data Sets from Blood and the Kidney. *Hypertens Dallas Tex 1979* 2017: HYPERTENSIONAHA.117.09438.

375. Kichaev G, Bhatia G, Loh P-R, *Et Al.* Leveraging Polygenic Functional Enrichment to Improve GWAS Power. *Am J Hum Genet* 2019; **104**: 65–75.

376. Sakaue S, Kanai M, Tanigawa Y, *Et Al.* A Cross-Population Atlas of Genetic Associations for 220 Human Phenotypes. *Nat Genet* 2021; **53**: 1415–24.

377. Barton AR, Sherman MA, Mukamel RE, Loh P-R. Whole-Exome Imputation Within UK Biobank Powers Rare Coding Variant Association and Fine-Mapping Analyses. *Nat Genet* 2021; **53**: 1260–9.

378. Hafizi S, Gustafsson A, Oslakovic C, *Et Al.* Tensin2 Reduces Intracellular Phosphatidylinositol 3,4,5-Trisphosphate Levels at the Plasma Membrane. *Biochem Biophys Res Commun* 2010; **399**: 396–401.

379. Takino J-I, Sato T, Nagamine K, Hori T. The Inhibition of Bax Activation-Induced Apoptosis by Rasgrp2 Via R-Ras-PI3K-Akt Signaling Pathway in the Endothelial Cells. *Sci Rep* 2019; **9**: 16717.

380. Oertli B, Han J, Marte BM, *Et Al.* The Effector Loop and Prenylation Site of R-Ras Are Involved in the Regulation of Integrin Function. *Oncogene* 2000; **19**: 4961–9.

381. Stulić M, Jantsch MF. Spatio-Temporal Profiling of Filamin A RNA-Editing Reveals ADAR Preferences and High Editing Levels Outside Neuronal Tissues. *RNA Biol* 2013; **10**: 1611–7.

382. Retailleau K, Arhatte M, Demolombe S, *Et Al.* Arterial Myogenic Activation Through Smooth Muscle Filamin A. *Cell Rep* 2016; **14**: 2050–8.

383. Jain M, Mann TD, Stulić M, *Et Al.* RNA Editing of Filamin A Pre-Mrna Regulates Vascular Contraction and Diastolic Blood Pressure. *EMBO J* 2018; **37**: E94813.

384. Gardel ML, Nakamura F, Hartwig JH, Crocker JC, Stossel TP, Weitz DA. Prestressed F-Actin Networks Cross-Linked by Hinged Filamins Replicate Mechanical Properties of Cells. *Proc Natl Acad Sci U S A* 2006; **103**: 1762–7.

385. Fritsch RM, Saur D, Kurjak M, *Et Al.* Insp3r-Associated Cgmp Kinase Substrate (IRAG) is Essential for Nitric Oxide-Induced Inhibition of Calcium Signaling in Human Colonic Smooth Muscle. *J Biol Chem* 2004; **279**: 12551–9.

386. Ha JM, Kim YW, Lee DH, *Et Al.* Regulation of Arterial Blood Pressure by Akt1-Dependent Vascular Relaxation. *J Mol Med Berl Ger* 2011; **89**: 1253–60.

387. Iaccarino G, Ciccarelli M, Sorriento D, *Et Al.* AKT Participates in Endothelial Dysfunction in Hypertension. *Circulation* 2004; **109**: 2587–93.

388. Lee MY, Gamez-Mendez A, Zhang J, *Et Al.* Endothelial Cell Autonomous Role of Akt1: Regulation of Vascular Tone and Ischemia-Induced Arteriogenesis. *Arterioscler Thromb Vasc Biol* 2018; **38**: 870–9.

389. Di Maira G, Brustolon F, Pinna LA, Ruzzene M. Dephosphorylation and Inactivation of Akt/PKB is Counteracted by Protein Kinase CK2 in HEK 293T Cells. *Cell Mol Life Sci CMLS* 2009; **66**: 3363–73.

390. Iwashita S, Kobayashi M, Kubo Y, *Et Al.* Versatile Roles of R-Ras GAP in Neurite Formation of PC12 Cells and Embryonic Vascular Development. *J Biol Chem* 2007; **282**: 3413–7.

391. Li H, Prever L, Hsu MY, *Et Al.* Phosphoinositide Conversion Inactivates R-RAS and Drives Metastases in Breast Cancer. *Adv Sci* 2022; **9**: 2103249.

392. Landry CR, Levy ED, Michnick SW. Weak Functional Constraints On Phosphoproteomes. *Trends Genet TIG* 2009; **25**: 193–7.

393. Wiredja DD, Koyutürk M, Chance MR. The KSEA App: A Web-Based Tool for Kinase Activity Inference from Quantitative Phosphoproteomics. Valencia A, Ed. *Bioinformatics* 2017; **33**: 3489–91.

394. Rincón-Arano H, Rosales R, Mora N, Rodriguez-Castañeda A, Rosales C. R-Ras Promotes Tumor Growth of Cervical Epithelial Cells: R-Ras Promotes Cervical Tumor Growth. *Cancer* 2003; **97**: 575–85.

395. Nakada M, Niska JA, Tran NL, Mcdonough WS, Berens ME. Ephb2/R-Ras Signaling Regulates Glioma Cell Adhesion, Growth, and Invasion. *Am J Pathol* 2005; **167**: 565–76.

396. Lien M-Y, Chang A-C, Tsai H-C, *Et Al.* Monocyte Chemoattractant Protein 1 Promotes VEGF-A Expression in OSCC by Activating ILK and MEK1/2 Signaling and Downregulating Mir-29c. *Front Oncol* 2020; **10**: 592415.

397. Giuliani N, Lunghi P, Morandi F, *Et Al.* Downmodulation of ERK Protein Kinase Activity Inhibits VEGF Secretion by Human Myeloma Cells and Myeloma-Induced Angiogenesis. *Leukemia* 2004; **18**: 628–35.

398. Roberts RE. The Role of Rho Kinase and Extracellular Regulated Kinase-Mitogen-Activated Protein Kinase in Alpha2-Adrenoceptor-Mediated Vasoconstriction in the Porcine Palmar Lateral Vein. *J Pharmacol Exp Ther* 2004; **311**: 742–7.

399. Kim J, Lee YR, Lee C-H, *Et Al.* Mitogen-Activated Protein Kinase Contributes to Elevated Basal Tone in Aortic Smooth Muscle from Hypertensive Rats. *Eur J Pharmacol* 2005; **514**: 209–15.

400. Touyz RM, El Mabrouk M, He G, Wu XH, Schiffrin EL. Mitogen-Activated Protein/Extracellular Signal-Regulated Kinase Inhibition Attenuates Angiotensin II-Mediated Signaling and Contraction in Spontaneously Hypertensive Rat Vascular Smooth Muscle Cells. *Circ Res* 1999; **84**: 505–15.

401. Kanehisa M, Furumichi M, Sato Y, Ishiguro-Watanabe M, Tanabe M. KEGG: Integrating Viruses and Cellular Organisms. *Nucleic Acids Res* 2021; **49**: D545–51.

402. Hacker BM, Tomlinson JE, Wayman GA, *Et Al.* Cloning, Chromosomal Mapping, and Regulatory Properties of the Human Type 9 Adenylyl Cyclase (ADCY9). *Genomics* 1998; **50**: 97–104.

403. Gros R, Ding Q, Chorazyczewski J, Pickering JG, Limbird LE, Feldman RD. Adenylyl Cyclase Isoform–Selective Regulation of Vascular Smooth Muscle Proliferation and Cytoskeletal Reorganization. *Circ Res* 2006; **99**: 845–52.

404. Matsumoto T, Wakabayashi K, Kobayashi T, Kamata K. Functional Changes in Adenylyl Cyclases and Associated Decreases in Relaxation Responses in Mesenteric Arteries from Diabetic Rats. *Am J Physiol-Heart Circ Physiol* 2005; **289**: H2234–43.

405. Nelson CP, Rainbow RD, Brignell JL, *Et Al.* Principal Role of Adenylyl Cyclase 6 in K+ Channel Regulation and Vasodilator Signalling in Vascular Smooth Muscle Cells. *Cardiovasc Res* 2011; **91**: 694–702.

406. Liu Z, Khalil RA. Evolving Mechanisms of Vascular Smooth Muscle Contraction Highlight Key Targets in Vascular Disease. *Biochem Pharmacol* 2018; **153**: 91–122.

407. Jeong H-W, Nam J-O, Kim I-S. The COOH-Terminal End of R-Ras Alters the Motility and Morphology of Breast Epithelial Cells Through Rho/Rho-Kinase. *Cancer Res* 2005; **65**: 507–15.

408. Xu Q, Zhuo K, Zhang X, Zhang Y, Xue J, Zhou M-S. Oxytocin-Induced Endothelial Nitric Oxide Dependent Vasorelaxation and ERK1/2-Mediated Vasoconstriction in the Rat Aorta. *Korean J Physiol Pharmacol Off J Korean Physiol Soc Korean Soc Pharmacol* 2022; **26**: 255–62.

409. Nicholson CJ, Singh K, Saphirstein RJ, *Et Al.* Reversal of Aging-Induced Increases in Aortic Stiffness by Targeting Cytoskeletal Protein-Protein Interfaces. *J Am Heart Assoc* 2018; **7**: E008926.

410. Koch C, Papadopoulou-Marketou N, Chrousos G. Overview of Endocrine Hypertension. In: *Endotext [Internet]*. South Dartmouth (MA): Mdtext.Com, 2020.

411. Pepe J, Cipriani C, Sonato C, Raimo O, Biamonte F, Minisola S. Cardiovascular Manifestations of Primary Hyperparathyroidism: A Narrative Review. *Eur J Endocrinol* 2017; **177**: R297–308.

412. Cicala MV, Mantero F. Hypertension in Cushing's Syndrome: from Pathogenesis to Treatment. *Neuroendocrinology* 2010; **92**: 44–9.

413. Xu R, Höß C, Swiercz JM, *Et Al.* A Semaphorin-Plexin-Rasal1 Signaling Pathway Inhibits Gastrin Expression and Protects Against Peptic Ulcers. *Sci Transl Med* 2022; **14**: Eabf1922.

414. Kashihara T, Sadoshima J. Role of YAP/TAZ in Energy Metabolism in the Heart. *J Cardiovasc Pharmacol* 2019; **74**: 483–90.

415. Miller E, Yang J, Deran M, *Et Al.* Identification of Serum-Derived Sphingosine-1-Phosphate as a Small Molecule Regulator of YAP. *Chem Biol* 2012; **19**: 955–62.

416. Seawright JW, Sreenivasappa H, Gibbs HC, *Et Al.* Vascular Smooth Muscle Contractile Function Declines with Age in Skeletal Muscle Feed Arteries. *Front Physiol* 2018; **9**: 856.

417. Schiller HB, Hermann M-R, Polleux J, *Et Al.* B1- and Av-Class Integrins Cooperate to Regulate Myosin II During Rigidity Sensing of Fibronectin-Based Microenvironments. *Nat Cell Biol* 2013; **15**: 625–36.

418. Kinashi T, Katagiri K, Watanabe S, Vanhaesebroeck B, Downward J, Takatsu K. Distinct Mechanisms of Alpha 5beta 1 Integrin Activation by Ha-Ras and R-Ras. *J Biol Chem* 2000; **275**: 22590–6.

419. Althoff TF, Offermanns S. G-Protein-Mediated Signaling in Vascular Smooth Muscle Cells - Implications for Vascular Disease. *J Mol Med Berl* 2015; **93**: 973–81.

420. Cormick G, Ciapponi A, Cafferata ML, Belizán JM. Calcium Supplementation for Prevention of Primary Hypertension. *Cochrane Database Syst Rev* 2015: CD010037.

421. Baksi SN, Abhold RH, Speth RC. Low-Calcium Diet Increases Blood Pressure and Alters Peripheral But Not Central Angiotensin II Binding Sites in Rats: *J Hypertens* 1989; **7**: 423–7.

422. Tohidi M, Hatami M, Hadaegh F, Azizi F. Triglycerides and Triglycerides to High-Density Lipoprotein Cholesterol Ratio Are Strong Predictors of Incident Hypertension in Middle Eastern Women. *J Hum Hypertens* 2012; **26**: 525–32.

423. Kawamoto R, Tabara Y, Kohara K, Kusunoki T, Abe M, Miki T. Interaction Between Serum Uric Acid and Triglycerides in Relation to Prehypertension in Community-Dwelling Japanese Adults. *Clin Exp Hypertens* 2014; **36**: 64–9.

424. Høstmark AT, Tomten SE, Berg JE. Serum Albumin and Blood Pressure: A Population-Based, Cross-Sectional Study. *J Hypertens* 2005; **23**: 725–30.

425. Hu H, Sparrow D, Weiss S. Association of Serum Albumin with Blood Pressure in the Normative Aging Study. *Am J Epidemiol* 1992; **136**: 1465–73.

426. Takase H, Sugiura T, Ohte N, Dohi Y. Urinary Albumin as a Marker of Future Blood Pressure and Hypertension in the General Population. *Medicine (Baltimore)* 2015; **94**: E511.

427. Liao H-W, Saver J, Yeh H-C, *Et Al.* Low Fasting Glucose and Future Risks of Major Adverse Outcomes in People without Baseline Diabetes or Cardiovascular Disease: A Systematic Review and Meta-Analysis. *BMJ Open* 2019; **9**: E026010.

428. Henry P, Thomas F, Benetos A, Guize L. Impaired Fasting Glucose, Blood Pressure and Cardiovascular Disease Mortality. *Hypertension* 2002; **40**: 458–63.

429. Blake JA, Baldarelli R, Kadin JA, *Et Al.* Mouse Genome Database (MGD): Knowledgebase for Mouse-Human Comparative Biology. *Nucleic Acids Res* 2021; **49**: D981–7.